Title

Wavefunction Mapping and Magnetic Field Response of Electrostatically Defined Graphene Quantum Dots

Author

Ge, Zhehao

Publication Date

2023

UNIVERSITY OF CALIFORNIA
SANTA CRUZ

WAVEFUNCTION MAPPING AND MAGNETIC FIELD RESPONSE OF ELECTROSTATICALLY DEFINED GRAPHENE QUANTUM DOTS

A dissertation submitted in partial satisfaction
of the requirements for the degree of

DOCTOR OF PHILOSOPHY

in

PHYSICS

by

Zhehao Ge

September 2023

The Dissertation of Zhehao Ge is approved:

Professor Jairo Velasco Jr., Chair

Professor David Lederman

Professor Sergey Syzranov

Peter Biehl
Vice Provost and Dean of Graduate Studies

Table of Contents

LIST OF FIGURES

LIST OF TABLES

LIST OF ABREVIATIONS

0D	Zero Dimension/Dimensional
1D	One Dimension/Dimensional
2D	Two Dimensions/Dimensional
3D	Three Dimensions/Dimensional
AFM	Atomic Force Microscope/Microscopy
AC	Alternating Current
B	Magnetic Field
BLG	Bilayer Graphene
DC	Direct Current
DOS	Density of States
e	Electron Charge

h	Planck’s Constant
$\hbar$	Reduced Planck’s Constant
LDOS	Local Density of States
MLG	Monolayer Graphene
k_B	Boltzmann’s Constant
QD	Quantum Dot
STM	Scanning Tunneling Microscope/Microscopy
STS	Scanning Tunneling Spectroscopy
TB	Tight-binding
TLG	Trilayer Graphene
UHV	Ultra-high Vacuum

Abstract

WAVEFUNCTION MAPPING AND MAGNETIC FIELD RESPONSE OF
ELECTROSTATICALLY DEFINED GRAPHENE QUANTUM DOTS

by

Zhehao Ge

QDs are mesoscopic objects with 3D quantum confinement, which are often called artificial atoms due to their discrete energy levels. Over the past several decades, a tremendous amount of research has been done on semiconductor QDs, which made them one of the most well-studied QD systems and a testbed for studying rich quantum phenomena that can be hosted in QD systems. But more recently, a new type of QD that is based on atomically thin graphene materials attracted the attention of the condensed matter physics community because of the unique electronic structures hosted by graphene materials. Compared to conventional semiconductor QDs, graphene QDs offer a distinctive platform to study the interplay between quantum confinement, relativistic quantum phenomena, and non-trivial band geometrical properties. Such properties cannot be investigated in conventional semiconductor QDs.

During my Ph.D. study, my research focused on investigating the electronic structure and magnetic field response of these relatively new graphene QDs. To experimentally probe graphene QD states, I used an unconventional but very powerful in-situ graphene QD creation and probing technique with STM, which enabled us to gain information of graphene QD states with atomic scale spatial resolution and meV

energy resolution. Such capability of our experimental approach enabled us to gain insights on graphene QD states that are out of reach with conventional electron transport measurements. In this dissertation, I will include experimental findings from four graphene QD projects that I participated in during my Ph.D. study. This includes the observation of giant orbital magnetic moments and paramagnetic shift in MLG QDs due to their relativistic nature (chapter 5), the effect of Berry curvature and Fermi surface symmetry on the spatial distribution of BLG QD wavefunctions (chapter 6), giant valley Zeeman splitting in TLG QDs due to the giant topological orbital magnetic moment hosted in this system (chapter 7), and the unambiguous direct visualization of the relativistic quantum scars in stadium shaped MLG QDs (chapter 8). These results demonstrate that unique quantum phenomena can be achieved in graphene QDs due to the interplay between quantum confinement, relativistic quantum phenomena, and non-trivial band geometrical properties.

Acknowledgements

I had a great time as a Ph.D. student at UC Santa Cruz over the last six years. I had the luck to be able to learn and perform cutting-edge research in a lab with state-of-the-art instruments but also be able to enjoy the spectacular scenery and biking routes in Santa Cruz while outside the lab. I am also deeply grateful for all the great people I have met either in person or just through Zoom during my Ph.D. study. I would like to take this chance to give my acknowledgement to all of you.

First, I would like to thank my advisor Prof. Jairo Velasco Jr. for his guidance and support during my Ph.D. study. I really enjoyed discussing research ideas with him during my Ph.D. years, and I also appreciate that he gave me lots of freedom to choose between different research projects based on my own interest. Jairo is a high standard scientist, from him, I learned many important qualities to be a good researcher such as being hard-working, being extra careful while handling any experimental instruments, always targeting the highest quality experimental data, being objective while interpreting experimental data, and so many more. Jairo also helped me to be a good communicator, I learned many things from him on how to write a good scientific manuscript and make a great presentation. Besides, Jairo also provided much guidance on my career development. So, I will always feel indebted to him.

Next, I would like to thank all the Velasco group members that I have encountered during my Ph.D. study. I want to especially thank Frederic Joucken, Eberth Arturo Quezada-Lopez, John Davenport and Peter Polizogopoulos. Fred and Arturo both trained me on how to use the STM in our lab. And a lot of my initial

research projects during my Ph.D. study were done with them together. I also really enjoyed discussing physics or other things while we were crowded in the STM room:) From Fred, I also learned many technical stuffs about instruments and graphene physics, which turned out to be very helpful for my research projects. Then Johnny taught me how to fabricate 2D material devices, and I worked closely with him on graphene TFET projects in my first year. I am just grateful that we are both still alive after the cryostat accident that happened in my first year, I am sure we both learned a lot from this experience. Finally, I want to thank Peter for working closely with me on many different types of STM projects after Fred and Arturo both left the lab. And I am also grateful for lots of help Peter provided to me outside the lab. Besides these special thanks, I also want to thank Junyan Liu and Albert Chen, from whom I learned many sample fabrication tricks in my first year. And I also want to thank Carlos Gonzalez and Dongyi Liu for their help on sample fabrication or STM experiments. Then I also want to thank Tianhui Zhu and Qirong Yao for the great discussions we had on STM experiments.

I also want to thank many students and postdocs from the nearby labs or on the main campus for your help during my Ph.D. study. I want to thank Toyanath Joshi for helping me fill liquid helium for our STM during 2020-2021 when I was the only member in our group. I want to thank Anh Nguyen for providing us the G/NiF$_2$ samples, helping with STM liquid helium refill, and many interesting discussions on sample fabrications. I want to thank Ryan van Haren and Beck Sharif for their efforts on managing the liquid helium recovery system. I want to thank Brian Giraldo for helping us set up the Ar/H_2 annealing system. I want to thank Hem Prasad Bhusal for the many discussions we had on sample fabrications. I want to thank Maverick McLanahan for his help on fixing the wire bonder sometimes. I also want to thank Shijun Sun, Siyu Zhu and Kejun Li for discussing many interesting physics problems.

Next, I would like to give my thanks to the UCSC faculties and staffs who provided much help to my Ph.D. study. First, I want to especially thank Prof. David Lederman. David shared lots of research resources in his lab with our lab, which is a crucial component of the successful running of our STM experiments. David also has tremendous knowledge about lab equipment, I can always get some help and learn something from him when I get broken lab equipment. In addition, David also put lots of effort into managing the helium recovery system, from whom I also learned a lot about this system. Then I also want to thank Prof. Arthur Ramirez for letting us use the wire bonder in his lab and always being willing to let us borrow some liquid nitrogen from his lab when we got into a liquid nitrogen shortage emergency. I also want to thank Prof. Nobuhiko Kobayashi for letting us use the tube furnace in his lab for Ar/H_2 annealing. I also want to thank Tom Yuzvinsky for teaching me how to use the SEM and NPGS system on campus for e-beam lithography. I also want to thank Prof. Sergey Syzranov, Prof. Aiming Yan, Prof. Aris Alexandradinata and Prof. Yuan Ping for the many insightful discussions we had on different types of projects. Finally, I want to thank the Hummingbird Computational Cluster team for providing computational resource and supports, which made my graphene QD TB simulations possible.

I also would like to give my thanks to my research project collaborators outside UCSC. I want to especially thank Sergey Slizovskiy and Prof. Vladimir Fal’ko from University of Manchester for providing theoretical support for several of my graphene QD projects, they always provided us with great insight into our experimental findings. Then I want to thank Jesse Balgley, Jackson Butler and Prof. Erik Henriksen from Washington University in St. Louis for providing us G/$RuCl_3$ samples for STM measurements. I also want to thank Prof. Diego R. da Costa from Universidade Federal do Ceará and Prof. Tony Low from University of Minnesota for collaborating with us on our BLG QD project. Finally, I want to thank Anton Graf, Joonas Keski-Rahkonen and Prof. Eric Heller from Harvard University for some great discussions we had on our recent stadium shaped MLG QD results.

Finally, I want to give my deepest thanks to my family for the unconditional love and support they gave me throughout my whole life!

To My Parents

Chapter 1 Introduction

Dimensionality plays an important role in determining an electron system's properties. As an example, Figure 1.1 shows a schematic illustration of the effect of dimensionality on an electron system's DOS. Starting from a continuous DOS in a 3D material, by applying quantum confinement in additional dimensions, the DOS of the electron system can have narrower peaks. Finally, quantized energy levels can be reached once 3D quantum confinement is achieved, which is similar to the case of an atom. Such 0D electron systems with 3D quantum confinement are also called QDs and will be the focus of this dissertation. More specifically, my PhD research is focused on the electronic structure and magnetic field response of QDs that are engineered from 2D electron systems hosted in the graphene material family, including MLG, BLG and TLG. To perform such studies, I used a novel STM technique that can create electrostatically defined graphene QDs in-situ with unprecedently deep and sharp electrostatic potential wells and probe the quantum states of the created QDs with both meV energy resolution and atomic spatial resolution. This powerful technique allowed us to investigate several unique properties of graphene QD states that other experiments are unable to probe.

In this chapter, I will first provide some brief background of semiconductor QDs, which is a similar system to graphene QDs but much more well studied. Then I will introduce the electronic structures of graphene systems and highlight some of their unique properties that will be interesting for QD studies. Finally, I will lay out the structure of this dissertation.

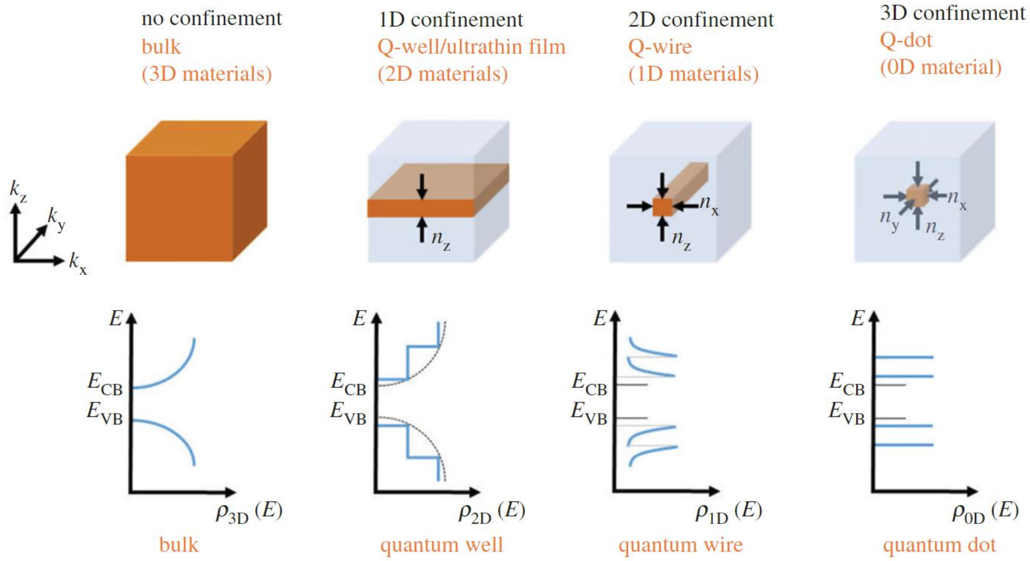

Figure 1.1 Effect of Dimensionality on Electronic Density of States. This figure is cited from reference[1]. The top row shows the schematic of materials with different dimensionalities, the bottom row shows the schematic of the electronic density of states of the corresponding material with certain dimensionality.

1.1 Semiconductor Quantum Dots

QD study is a very big research field and highly interdisciplinary. There exist many different types of QDs and people also focus on various different subjects for QD research. Because of this reason, I do not intend to and am not able to cover every aspect of earlier QD studies. Instead, I will only choose those most related to my research to be covered in this introduction, namely the electronic properties of QDs that are engineered from a 2D electron gas. For this specific direction, the most well studied QDs are semiconductor QDs, which can be achieved through applying additional 2D quantum confinement to the 2D electron gas embedded in semiconductor heterojunctions. Etching and electrostatic gating are two common ways to achieve such additional 2D quantum confinement. Figure 1.2a shows some example semiconductor

QDs with different shapes that were created through etching[2], in this case the physical boundary enacts the quantum confinement. On the other hand, Figure 1.2b shows an array of semiconductor QDs that were created through local electrostatic gating from patterned surface electrodes[3], here the quantum confinement is from electrostatic potential wells.

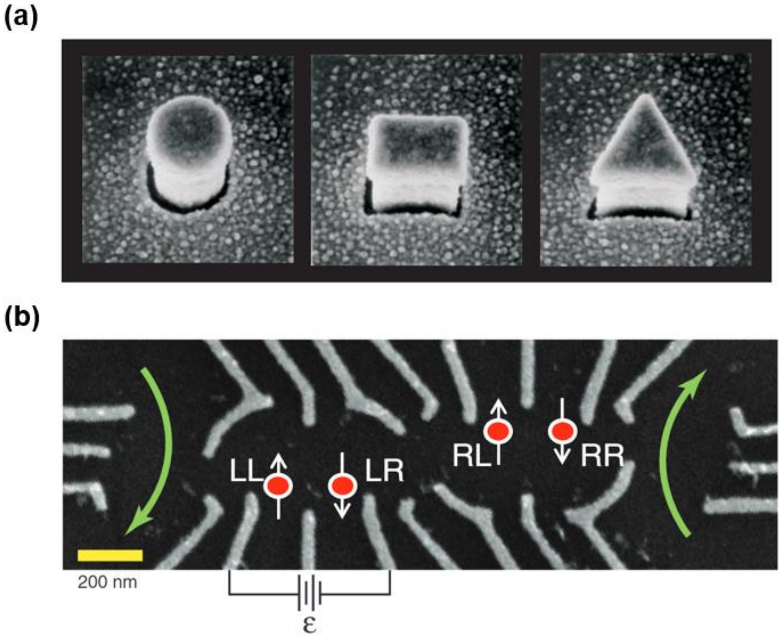

Figure 1.2 Experimental Creation of Semiconductor QDs. (a) Scanning electron microscope images of etched semiconductor QDs. Image adapter from reference[2]. (b) Scanning electron microscope image of patterned surface electrodes on semiconductor 2D electron gas, which can electrostatically define semiconductor QDs. Here an array of four semiconductor QDs were electrostatically created. This image is adapted from reference[3].

Semiconductor QDs are a versatile platform to study and potentially utilize emergent quantum phenomena in low-dimensional quantum systems. The versatility mainly comes from the fact that we have substantial freedom to control the size, shape, and location of semiconductor QDs with the nanofabrication techniques mentioned above. This allows us to tune the energy level of QD states and create QD arrays with arbitrary distribution. In addition, quantized charge numbers in semiconductor QDs can also be achieved through the single electron transport process that arises from the Coulomb blockade effect in QDs[4]. This allows the realization of semiconductor QDs that contain only a few or even a single electron and precise control of the occupation of QD states[2]. All of these capabilities enable the design of semiconductor QD systems that are suitable for the realization and investigation of various model quantum systems and quantum technologies. Below, I will provide some examples.

One well-known model quantum system that can be realized with semiconductor QDs is atomic systems[5,6]. Atoms and QDs have many similarities, for example, they are both systems with 3D quantum confinement and show quantized energy levels. Because of this, QDs are often referred to as artificial atoms. Figure 1.3a shows a famous early day experimental result[2,7] that demonstrated the shell filling of few-electron semiconductor QDs, which highlighted their similarities to real atoms. But there also exists other differences between these artificial atoms and real atoms, which makes it interesting to investigate artificial atoms. Firstly, the artificial atoms realized in semiconductor QDs are 2D, this can give rise to different degeneracies of the quantum states, and that is why they have different magic numbers (number of electron fillings that cause an enhanced additional energy as shown in Figure 1.3b) compared to real atoms. Secondly, the sizes of QDs are several orders larger than real atoms. This makes QD states have a stronger magnetic field response compared to real atomic states. Just as an example, the typical *B* strength needed for an atomic state to acquire a magnetic flux quantum ($\phi_0 = h/e$) is on the order of 10^5 T, but only on the order of 1 T for QD states. Finally, the confinement potential types are usually different between semiconductor QDs and real atoms. In real atoms, the confinement potential is a Coulomb potential. But for semiconductor QDs, the confinement potential is usually close to a harmonic oscillator potential. This made semiconductor QDs a suitable experimental platform to explore the Fock-Darwin states (Figure 1.3b) that are associated with a 2D quantum harmonic oscillator in a magnetic field[2,8,9].

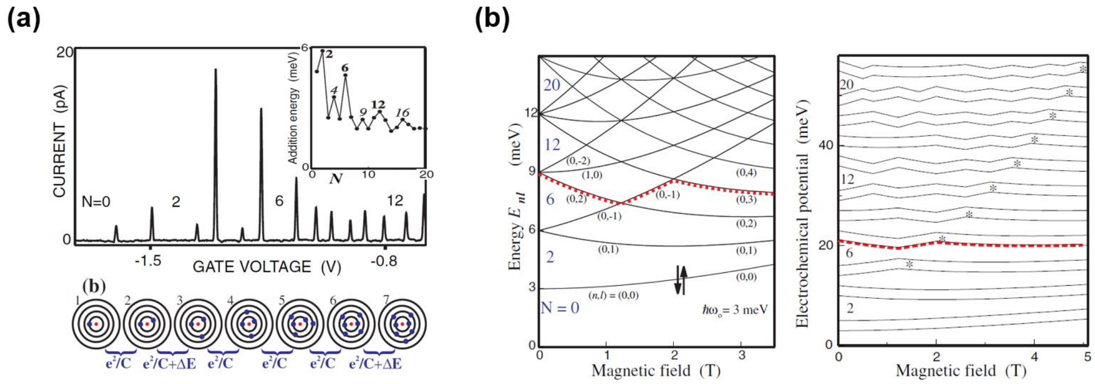

Figure 1.3 Shell Filling and Fock-Darwin States Observed in Semiconductor QDs. (a) Shell filling that resembles an atom were observed in semiconductor QDs through single electron transport. Image adapted from reference[2]. (b) Comparison between theoretical Fock-Darwin spectra and experimentally measured electrochemical potential of a semiconductor QD in a magnetic field. Image adapter from reference[2].

Apart from artificial atomic systems, semiconductor QDs can also be used to realize artificial molecular systems[10-13] and quantum chaotic systems[14,15]. Artificial molecular systems can be realized by creating two semiconductor QDs that are coupled with each other, the energy splitting between the bonding and anti-boning states, a hallmark of molecular systems, have been experimentally observed in such coupled QD systems[13] (Figure 1.4a). Quantum chaotic systems can be realized by creating semiconductor QDs with non-integrable confinement boundary geometries such as a stadium shape (Figure 1.4b), the signatures of quantum chaos have been revealed in the peak shape and statistics of the conductance across these non-integrable semiconductor QD systems[16,17].

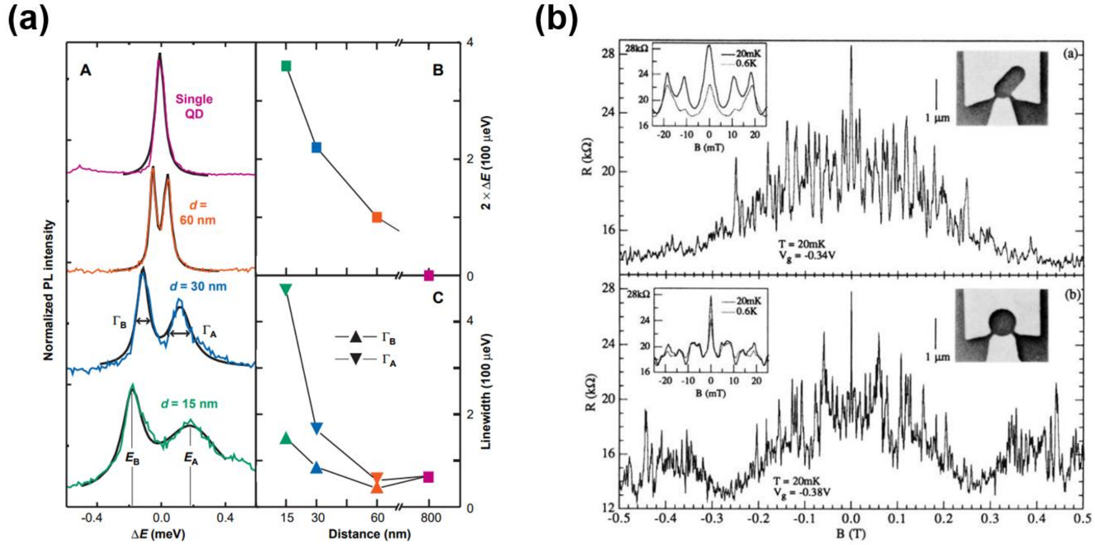

Figure 1.4 Artificial Molecules and Quantum Chaos Realized with Semiconductor QDs. (a) Photoluminescence spectra revealed the formation of bonding and antibonding states in coupled semiconductor QDs, which mimics a molecular systems. Image adapted from reference[13]. (b) Signatures of quantum chaos were observed in the conductance fluctuation of non-circular electrostatically defined semiconductor QDs. Image adapted from reference[17].

Semiconductor QDs are also promising for application in various quantum technologies such as quantum computation, quantum sensing and quantum simulation[18]. For example, the charge quantum degree of freedom hosted in few-electron semiconductor QDs can be utilized for charge sensing[19] and charge qubit-based quantum computation[20,21]. Then the spin quantum degree of freedom hosted in few-electron semiconductors QDs can be used for magnetic field sensing[22], spin qubit-based computation[3,23-27] and Fermi-Hubbard model simulation[28].

1.2 Graphene Systems

Although semiconductor QDs have demonstrated a lot of interesting quantum phenomena and potential applications in quantum technology as discussed in section 1.1, a new type of QD that is based on the quantum confinement of the 2D electron gas in graphene systems caught the condensed matter physics research community's attention recently[29-72]. One reason is because graphene QDs offer a unique platform to explore various quantum phenomena that cannot be hosted in semiconductor QDs. This is because the charge carriers in graphene systems can host many unique properties that do not exist in semiconductor 2D electron gases such as the existence of an additional valley degree of freedom, zero effective mass, and chirality[73]. Thus, graphene QDs offer the opportunity to observe emergent quantum phenomena due to the quantum confinement of these unusual 2D electron gas that exists in graphene systems. Another reason is because graphene QDs are expected to host long spin coherence time, which makes them attractive to be used in spin-based quantum computation. The spin decoherence of spin qubits in semiconductor QDs are mainly from spin-orbit interaction and hyperfine coupling with nuclear spins, but these two mechanisms are strongly suppressed in graphene QDs[74]. This is because graphene materials are purely carbon based, thus have very weak spin-orbit coupling compared to conventional semiconductor systems. In addition, 99% of natural carbon consists of nuclear spin-free ^{12}C, as a result, hyperfine coupling is also strongly suppressed in graphene QDs.

In the sections below, I will review some important properties of the electronic structures of three different graphene systems, including MLG, BLG and TLG.

1.2.1 Monolayer Graphene

MLG is an atomically thin sheet of graphite, its first successful isolation onto insulating substrate was achieved by Novoselov and Geim in 2004 with the Scotch tape method[75,76]. Soon after, a lot of unique physical phenomena were observed in MLG such as the existence of massless Dirac fermions[76], quantum Hall effect with π Berry phase[77] and Klein tunneling[78]. These discoveries soon stimulated the fast growth of research on Van der Waals 2D materials[79], which now is a very large research field in both condensed matter physics and materials science. Many interesting properties of MLG are due to its unique electronic structure. The tight-binding model is one of the most important models to describe MLG's electronic structure, which surprisingly was first studied all the way back to 1947 by Wallace[80], almost 60 years before the experimental isolation of MLG. Below, I will review the tight-binding model of MLG, which is based on two reviews by McCaan[81,82].

The general tight-binding model for a crystal has the following formalism:

$$H\Psi_j = E_j S \Psi_j \tag{1.1}$$

where H and S are the integral matrix and overlap matrix, respectively. E_j and Ψ_j are the energy and wavefunction of the jth electronic band, which can be determined from the secular equation:

$$\det\left(H - E_j S\right) = 0 \tag{1.2}$$

The integral matrix and overlap matrix can be generally expressed as:

$$H_{mm'} = \langle \Phi_\mathrm{m} | \mathcal{H} | \Phi_{m'} \rangle \, ; S_{mm'} = \langle \Phi_\mathrm{m} | \Phi_{m'} \rangle \tag{1.3}$$

Here $\mathcal{H}$ is the Hamiltonian of the crystal and Φ_m are the Bloch states that form the basis of the tight-binding Hamiltonian H. For a crystal with M atomic orbitals per primitive unit cell, there exists M of these basis vectors Φ_m and M different electronic bands. And Φ_m can be constructed from the M different atomic orbital states ϕ_m that exists in a primitive unit cell as following:

$$\Phi_m(\vec{k},\vec{r}) = \frac{1}{\sqrt{N}}\sum_{i=1}^{N} e^{i\vec{k}\cdot\vec{R}_{m,i}}\phi_m(\vec{r}-\vec{R}_{m,i}) \tag{1.4}$$

Here $\vec{k}$ and $\vec{r}$ are the wave vector and position vector of the Bloch state, respectively. $\vec{R}_{m,i}$ is the position vector of the mth atomic orbit in the ith unit cell. And N is the unit cell number of the crystal.

Figure 1.5a shows the honeycomb atomic structure of MLG, it has a triangular lattice with two sublattices carbon atom A and B in each primitive unit cell. $\vec{a}_1$ and $\vec{a}_2$ denotes one possible set of primitive lattice vectors for MLG, whose values are:

$$\vec{a}_1 = \left(\frac{a}{2},\frac{\sqrt{3}a}{2}\right), \qquad \vec{a}_2 = \left(\frac{a}{2},-\frac{\sqrt{3}a}{2}\right). \tag{1.5}$$

Here a is the lattice constant of MLG lattice, and $a = 2.46$ Å. The lattice constant a and carbon-carbon bond length a_{CC} has a connection $a = \sqrt{3}a_{CC}$. And Figure 1.5b shows the reciprocal lattice of MLG with primitive reciprocal lattice vectors:

$$\vec{b}_1 = \left(\frac{2\pi}{a},\frac{2\pi}{\sqrt{3}a}\right), \qquad \vec{b}_2 = \left(\frac{2\pi}{a},-\frac{2\pi}{\sqrt{3}a}\right). \tag{1.6}$$

The first Brillouin zone is a hexagon as indicated by the shaded area in Figure 1.5b with high symmetry points Γ, K_+, K_- and M.

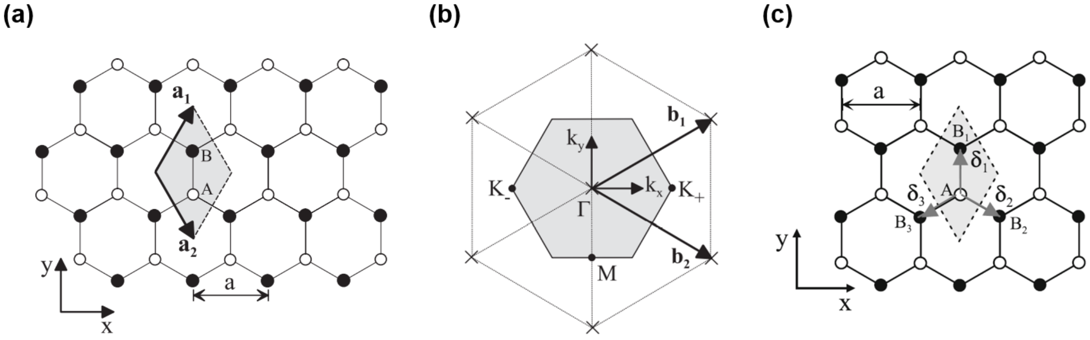

Figure 1.5 MLG atomic structure. (a) Schematic of MLG's atomic structure and its primitive lattice vectors. Image adapted from reference[82]. (b) Schematic of MLG's reciprocal lattice. The shaded hexagon is its first Brillouin zone. Image adapted from reference[82]. (c) Schematic of the three nearest hopping vectors $\vec{\delta_l}$ for MLG. Image adapted from reference[81].

Following the general tight-binding formalism described above, we can first construct the transfer integral matrix (H) and overlap matrix (S) for MLG then calculate the electronic bands of MLG. There exist two carbon atoms in MLG's primitive unit cell, and each carbon atom contributes one p_z atomic orbit to form the electronic bands that are to our interest, here we label these two atomic orbits as A and B. With this information, we expect a 2×2 matrix for both the H and S for MLG. Below, I show the derivation of the matrix elements for H and S. We first look at the diagonal matrix elements for H:

$$H_{AA} = \frac{1}{N} \sum_{i=1}^{N} \sum_{j=1}^{N} e^{i\vec{k}\cdot(\vec{R}_{A,j} - \vec{R}_{A,i})} \langle \phi_A(\vec{r} - \vec{R}_{A,i}) | \mathcal{H} | \phi_A(\vec{r} - \vec{R}_{A,j}) \rangle, \quad (1.7)$$

$$\approx \frac{1}{N}\sum_{i=1}^{N}\langle \phi_A(\vec{r}-\vec{R}_{A,i})|\mathcal{H}|\phi_A(\vec{r}-\vec{R}_{A,i})\rangle, \tag{1.8}$$

$$= \varepsilon_A \tag{1.9}$$

Here the approximation means we only consider the contribution from the same site, and $\varepsilon_A = \langle \phi_A(\vec{r}-\vec{R}_{A,i})|\mathcal{H}|\phi_A(\vec{r}-\vec{R}_{A,i})\rangle$ is the onsite energy of the sublattice A. Similarly, for the other diagonal matrix element, we can get

$$H_{BB} \approx \frac{1}{N}\sum_{i=1}^{N}\langle \phi_A(\vec{r}-\vec{R}_{A,i})|\mathcal{H}|\phi_A(\vec{r}-\vec{R}_{A,i})\rangle = \varepsilon_B \tag{1.10}$$

For intrinsic MLG, we can take $\varepsilon_A = \varepsilon_B = 0$. Now let us derive the off-diagonal matrix elements of H:

$$H_{AB} = \frac{1}{N}\sum_{i=1}^{N}\sum_{j=1}^{N} e^{i\vec{k}\cdot(\vec{R}_{B,j}-\vec{R}_{A,i})}\langle \phi_A(\vec{r}-\vec{R}_{A,i})|\mathcal{H}|\phi_B(\vec{r}-\vec{R}_{B,j})\rangle, \tag{1.11}$$

$$\approx \frac{1}{N}\sum_{i=1}^{N}\sum_{l=1}^{3} e^{i\vec{k}\cdot\vec{\delta}_l}\langle \phi_A(\vec{r}-\vec{R}_{A,i})|\mathcal{H}|\phi_B(\vec{r}-\vec{R}_{A,i}-\vec{\delta}_l)\rangle, \tag{1.12}$$

$$= -\gamma_0 f(\vec{k}) \tag{1.13}$$

Here the approximation means we only consider the nearest neighbor hopping, the three possible nearest hopping for MLG and their associated $\vec{\delta}_l$ are shown in Figure 1.5c. With these given $\vec{\delta}_l$, we can get

$$f(\vec{k}) = e^{i\frac{k_y a}{\sqrt{3}}} + 2e^{-i\frac{k_y a}{2\sqrt{3}}}\cos\left(\frac{k_x a}{2}\right) \tag{1.14}$$

and $\gamma_0 = -\langle \phi_A(\vec{r} - \vec{R}_{A,i}) | \mathcal{H} | \phi_B(\vec{r} - \vec{R}_{A,i} - \vec{\delta}_l) \rangle$ is the hopping energy between the nearest carbon atoms, which is around 3.033 eV for MLG. Similarly, for the other off-diagonal matrix element, we can get

$$H_{BA} = H_{AB}^* \approx -\gamma_0 f^*(\vec{k}) \tag{1.15}$$

Now we have got all the matrix elements for H. Following the similar approximation procedure, we get all the matrix elements for S as below:

$$S_{AA} = S_{BB} \approx 1, \qquad S_{AB} \approx s_0 f(\vec{k}), \qquad S_{BA} \approx s_0 f^*(\vec{k}) \tag{1.16}$$

Here $s_0 = \langle \phi_A(\vec{r} - \vec{R}_{A,i}) | \phi_B(\vec{r} - \vec{R}_{A,i} - \vec{\delta}_l) \rangle$ is the overlap of nearest neighbor orbitals, which is around 0.129 for MLG. Since we have got both H and S for MLG, now we can calculate the electronic band structure of MLG by solving the secular equation as shown in Equation 1.2. It is fairly easy to write down the analytical expression of MLG's tight-binding band structure, which is shown below:

$$E_{\pm}(\vec{k}) = \frac{\pm\gamma_0 |f(\vec{k})|}{1 \mp s_0 |f(\vec{k})|} \tag{1.17}$$

Figure 1.6a shows the 3D plot of MLG's electronic band structure according to Equation 1.17. MLG's conduction band and valance band have the largest energy separation at the Γ point of its Brillouin zone, but its conduction band and valence band touch with each other at the K_+ and K_- points of its Brillouin zone. These two points are also called K_+/K_- valleys. For intrinsic MLG, its Fermi level lies at the energy where this band touching happens. As shown in Figure 1.6b, MLG's low energy bands around its intrinsic Fermi level are distributed around two distinct K_+/K_- valleys and have a linear energy dispersion, which is similar to the energy momentum dispersion of an ultra-relativistic particle such as a photon. These linear low energy bands and their touching points are also called Dirac cones and Dirac points, respectively, because they can be approximately described by a massless Dirac equation, which I will show below. As a result, MLG hosts massless Dirac fermions and is a unique experimental platform to study relativistic quantum phenomena. In chapter 5, I will discuss the relativistic effect on the orbital magnetic moments of QD states hosted in MLG QDs.

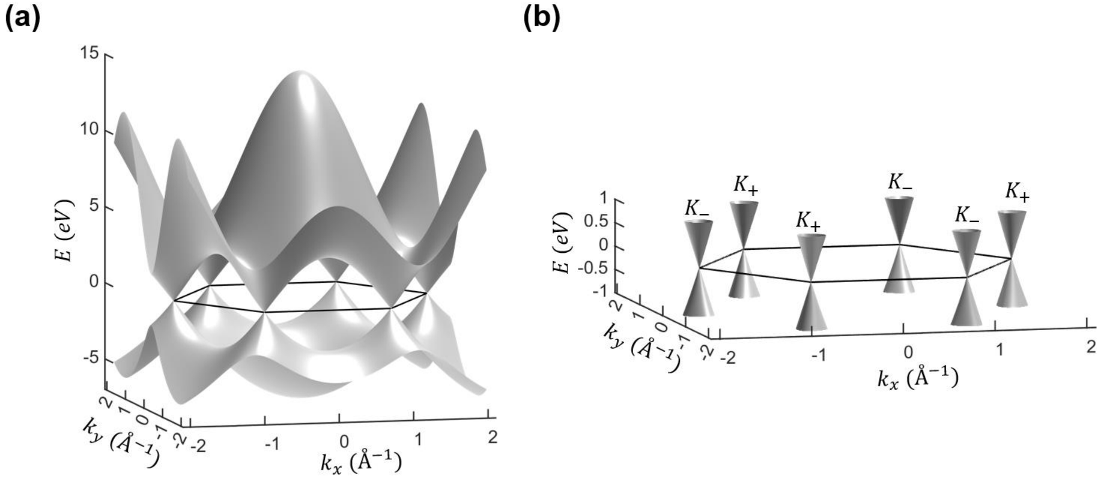

Figure 1.6 Band structure of MLG. (a) Full energy MLG band structure calculated from the tight-binding model. The black hexagon is the boundary of MLG's first Brillouin zone. (b) Low energy cuts of the full MLG band structure shown in (a).

MLG's two distinct K_+ and K_- valleys as shown in Figure 1.6b are located at

$$\vec{K}_\xi = \xi \left(\frac{4\pi}{3a}, 0 \right) \tag{1.18}$$

in the reciprocal space. Here ξ is the valley index, its value can be ± 1. Let us define

$$\vec{p} = \hbar \left(\vec{k} - \vec{K}_\xi \right) \tag{1.19}$$

, which is a small momentum defined around $K_{\pm}$. Using this newly defined momentum, we can rewrite Equation 1.14 as

$$f(\vec{k}) = e^{ip_y a/\sqrt{3}\hbar} + 2e^{-ip_y a/2\sqrt{3}\hbar} \cos\left(\frac{2\pi\xi}{3} + \frac{p_x a}{2\hbar}\right) \tag{1.20}$$

Expanding $f(\vec{k})$ to the first order of $\vec{p}$, we can get

$$f(\vec{k}) \approx -\frac{\sqrt{3}a}{2\hbar}(\xi p_x - ip_y) \tag{1.21}$$

Using Equation 1.21, we can rewrite MLG's transfer integral matrix around $K_{\pm}$ as

$$H_{\xi} = v_F \begin{pmatrix} 0 & \xi p_x - ip_y \\ \xi p_x + ip_y & 0 \end{pmatrix} \tag{1.22}$$

, where $v_F = \frac{\sqrt{3}a\gamma_0}{2\hbar} \approx 10^6\ \mathrm{m/s}$ is MLG's Fermi velocity around $K_{\pm}$ points. With approximation to the first order of $\vec{p}$, the overlap matrix S can be approximated as a unit matrix because the linear expansion term of the off-diagonal elements of S won't be reflected in MLG's band structure around $K_{\pm}$ to the first order of $\vec{p}$. Because of this, we can describe MLG's low energy band structures near $K_{\pm}$ by

$$H_{\xi}\psi = E\psi \tag{1.23}$$

The eigen energies and eigen states of Equation 1.23 can be write down as

$$E_{\pm}^{\xi} = \pm v_F p, \qquad \psi_{\pm}^{\xi} = \frac{1}{\sqrt{2}}\begin{pmatrix} 1 \\ \pm\xi e^{i\xi\varphi} \end{pmatrix} e^{i\vec{p}\cdot\vec{r}/\hbar} \tag{1.24}$$

Here ± represents the conduction band and valence band. These two-component eigenfunctions of MLG's low energy bands mimic the spinor of a spin-1/2 particle. In fact, such analogy can be made by understanding the full polarization of the Bloch wave intensity onto the A and B sublattices as spin up and spin down states as schematized in Figure 1.7. We call this a pseudospin degree of freedom.

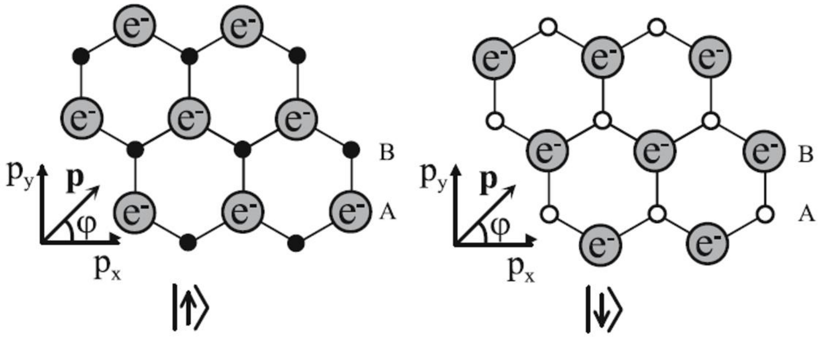

Figure 1.7 Schematic of the Pseudospin Degree of Freedom in MLG. The full electron density polarization on the two inequivalent MLG sublattices can be viewed as pseudospin up and pseudospin down states, respectively. Image adapted from reference**[81]**.

With such an understanding, we can also rewrite MLG's low energy effective Hamiltonian (Equation 1.22) as

$$H_\xi = v_F\left(\xi\sigma_x p_x + \sigma_y p_y\right) \tag{1.25}$$

, where σ_x and σ_y are the spin Pauli matrices. Such representation of MLG's low energy effective Hamiltonian shows a close analogy to the Hamiltonian of a massless Dirac fermion, but with an effective speed of light $v_F \approx \frac{c}{300}$, where c is the speed of light. Equation 1.25 also indicates the pseudospin and momentum of MLG's low energy wavefunctions are locked with each other. The helicity operator[83]

$$h = \frac{\vec{\sigma}\cdot\vec{p}}{|\vec{p}|} \tag{1.26}$$

, which is equivalent to the chirality operator in the massless case, can be used to characterize such pseudospin-momentum lock-in. For K_+ valley, we can get

$$h\psi = \frac{\vec{\sigma} \cdot \vec{p}}{|\vec{p}|}\psi = \frac{H_{K_+}\psi}{\hbar v_F |\vec{p}|} = \frac{E_\pm(\vec{p})\psi}{\pm E_\pm(\vec{p})} = \pm\psi \tag{1.27}$$

So h has two eigen values: $+1$ for the conduction band and -1 for the valence band, which means the pseudospin are parallel and antiparallel to the momentum in these two bands, respectively. This indicates the massless Dirac fermions in MLG are not only relativistic but also chiral (helical is the more proper name, but people usually call it chiral in the literature, so I will stick to the same nomenclature).

Such chirality of MLG's low energy bands is responsible for many interesting quantum phenomena. For example, it can give rise to a non-zero geometrical phase[84,85] (i.e., Berry phase ϕ_{Berry}) for any adiabatic evolution along a closed path that encloses MLG band's Dirac point. As shown in Figure 1.8a, MLG band's Berry phase is connected to the solid angle Ω subtended by its pseudospin during a cyclic evolution as[86,87]

$$\phi_{Berry} = \frac{\Omega}{2} \tag{1.27}$$

With MLG's parallel or antiparallel pseudospin-momentum lock-in, MLG's Berry phase around a Dirac point is quantized and $\phi_{Berry} = \pi$. In addition, as shown in Figure 1.8b-c, the chirality of MLG's low energy bands can also give rise to Klein tunneling[88], which is a relativistic quantum phenomenon that a particle always has 100% transmission probability across a potential barrier with any depth and length when the particle has perpendicular incidence.

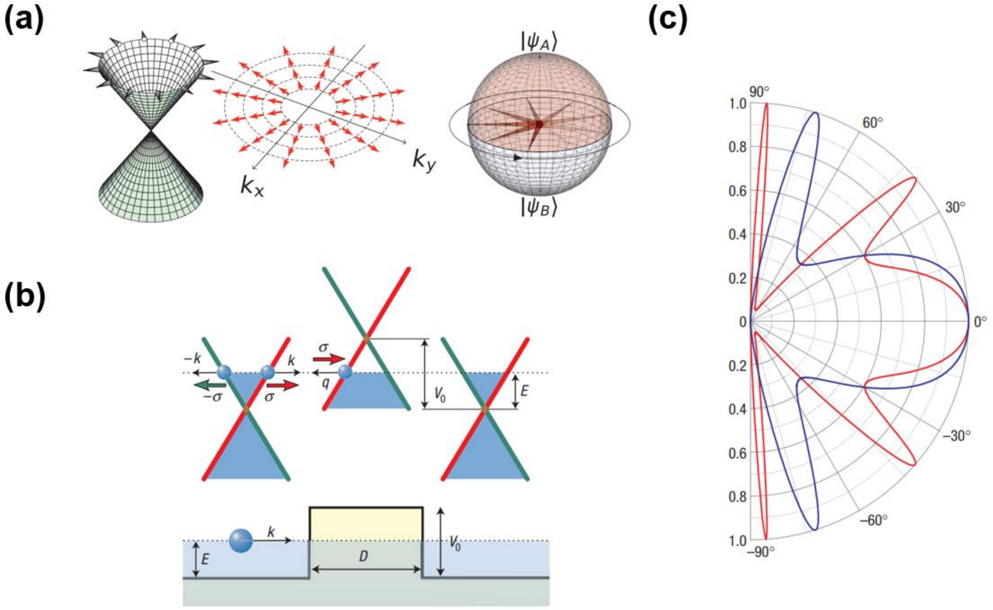

Figure 1.8 Chiral Fermion and Klein Tunneling in MLG. (a) Schematic of the pseudospin momentum lock-in of MLG bands and the 2π solid angle subtended by MLG's pseudospin by one winding in the momentum space around the Dirac point. Image adapted from reference[87]. (b) Schematic of the band diagram and potential barrier for the transmission across a potential barrier problem with MLG n-p-n junction. Image adapted from reference[88]. (c) Calculated transmission probability at different incidence angles with the set up shown in (b) for MLG n-p-n junction. The main message is the universal 100% transmission probability across the potential barrier at vertical incidence, which is the Klein paradox. Image adapted from reference[88].

1.2.2 Bernal Stacked Bilayer Graphene

In the previous section, we discussed the electronic structure of MLG. In this section, we switch to Bernal stacked bilayer graphene (BLG). The tight-binding model of BLG reviewed in this section is also based on a review by McCaan[82].

As shown in Figure 1.9, BLG is essentially a stack of two sheets of MLG that are offset from each other. BLG has the exact same lattice as MLG, which also means BLG has the same reciprocal lattice and Brillouin zone as MLG (see Figure 1.5b). There exists four sublattices in BLG's primitive unit cell, which are named as A_1, B_1,

A_2 and B_2 in Figure 1.9. Two of the four sublattices (B_1 and A_2) are on top of each other, their position is also called the dimer site. The other two sublattices' positions are also called non-dimmer site.

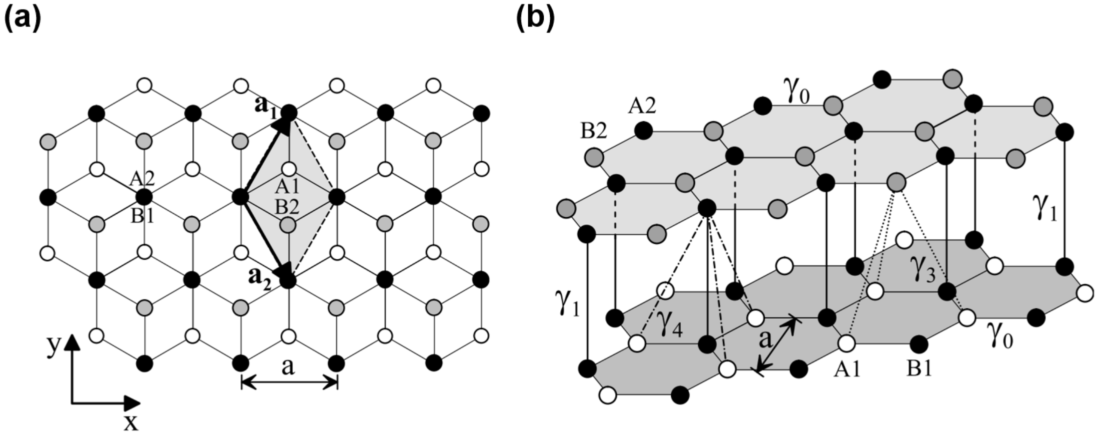

Figure 1.9 BLG atomic structure and tight-binding hopping parameters. (a) Schematic of the top-view of the BLG atomic structure and its primitive lattice vector. Image adapted from reference[82]. (b) Schematic of the 3D view of the atomic structure of BLG and its associated tight-binding hopping parameters. Image adapted from reference[82].

Following the procedure as we showed in section 1.2.1, we can similarly derive the transfer integral matrix H and overlap matrix S for BLG tight-binding model. Because of the doubled atomic orbital states in BLG's primitive unit cell, we expect a 4×4 matrix for H and S for BLG. In addition to the in-plane nearest neighbor hopping γ_0 as we discussed in MLG, there are three additional interlayer nearest neighbor hopping terms need to be considered in BLG's tight-binding model. As shown in Figure 1.9b, these three additional hopping terms are $\gamma_1 = \langle \phi_{A_2} | \mathcal{H} | \phi_{B_1} \rangle$: the hopping between the nearest interlayer carbon atoms both at the dimmer site; $\gamma_3 = -\langle \phi_{A_1} | \mathcal{H} | \phi_{B_2} \rangle$: the hopping between the nearest interlayer carbon atoms both at the non-dimmer site; and

$\gamma_4 = \langle \phi_{A_1} | \mathcal{H} | \phi_{B_2} \rangle = \langle \phi_{B_1} | \mathcal{H} | \phi_{B_2} \rangle$: the hopping between the nearest interlayer carbon atoms with one at the dimmer site and one at the non-dimmer site. With these new hopping terms, BLG's tight-binding Hamiltonian can be written as below:

$$H_{BLG} = \begin{pmatrix} \varepsilon_{A_1} + U/2 & -\gamma_0 f(\vec{k}) & \gamma_4 f(k) & -\gamma_3 f^*(\vec{k}) \\ -\gamma_0 f^*(\vec{k}) & \varepsilon_{B_1} + U/2 & \gamma_1 & \gamma_4 f(\vec{k}) \\ \gamma_4 f^*(\vec{k}) & \gamma_1 & \varepsilon_{A_2} - U/2 & -\gamma_0 f(\vec{k}) \\ -\gamma_3 f(\vec{k}) & \gamma_4 f^*(\vec{k}) & -\gamma_0 f^*(\vec{k}) & \varepsilon_{B_2} - U/2 \end{pmatrix} \tag{1.28}$$

Here $\varepsilon_{A_1}, \varepsilon_{B_1}, \varepsilon_{A_2}$ and ε_{B_2} are the onsite energy for the four sublattices, we can approximate them as 0 for intrinsic BLG although there is a very slight energy difference $\Delta' \approx 0.022$ eV between the dimer site and non-dimer site. And $f(\vec{k})$ is given by Equation 1.14 and identical to MLG. Finally, U is an additional term that describes the interlayer potential difference whose value can be experimentally controlled, for example, by application of an out of plane electric field.

To calculate BLG's full electronic band structures, we also need to know the overlap matrix S. But if we restrict ourselves to BLG's low energy bands, which is what we are interested in, we can approximate S as a unit matrix similar to the MLG case. This means we can directly diagonalize H_{BLG} to get BLG's low energy band structures. Figure 1.10a shows the full BLG band structure calculated in this way with $U = 0$, $\gamma_0 = 3.16$ eV, $\gamma_1 = 0.381$ eV, $\gamma_3 = -0.38$ eV and $\gamma_4 = 0.14$ eV, we have to be careful that we cannot quantitatively trust the energy value of those bands far away from $E = 0$ because we ignored the off-diagonal elements of the overlap matrix, but we can still get a qualitative picture of how BLG's band structure looks like over its whole Brillouin zone. BLG's full band structure generally looks the same as MLG's full band structure (Figure 1.6a), they both have touching conduction band and valance band around the K_+/K_- points and maximum energy separation between the conduction band and valence band at the Γ point. But for BLG, there are in total four electronic bands, which is doubled from the MLG case because of the doubled atomic orbital numbers in BLG's primitive unit cell. In addition, different from MLG's linear energy dispersion around K_+/K_- points, BLG has a trigonally warped band dispersion around K_+/K_- points (Figure 1.10c). In chapter 6, I will discuss the effect of this band trigonal warping on the symmetry of BLG QD wavefunctions.

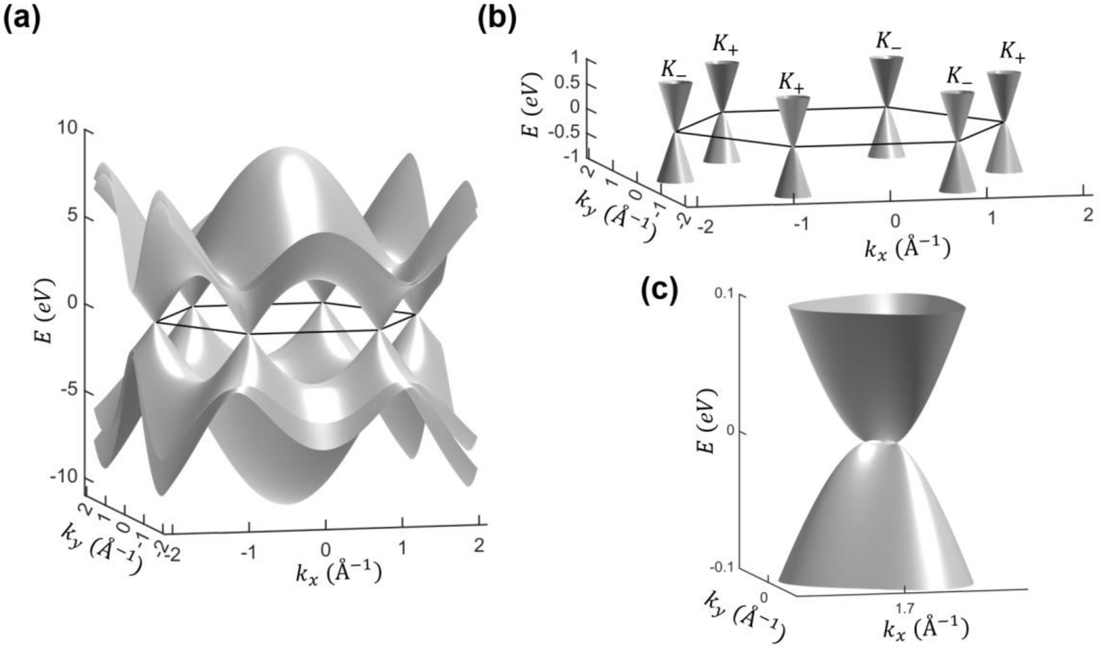

Figure 1.10 Band Structure of BLG. (a) Full energy BLG band structure calculated from the tight-binding model. The black hexagon is the boundary of BLG's first Brillouin zone. (b) Low energy cuts of the full BLG band structure shown in (a). (c) Even lower energy cuts of BLG bands around the K_+ valley shown in (b).

After getting a general picture of BLG's band structure, I will now discuss the properties of BLG's low energy bands in more detail. Similar to MLG, BLG's low energy effective Hamiltonian around K_+/K_- valleys can be achieved by expanding $f(\vec{k})$ around K_+/K_- points. This gives us an effective low energy BLG Hamiltonian:

$$H_{BLG} = \begin{pmatrix} \varepsilon_{A_1} + U/2 & v\pi^\dagger & -v_4\pi^\dagger & v_3\pi \\ v\pi & \varepsilon_{B_1} + U/2 & \gamma_1 & -v_4\pi^\dagger \\ -v_4\pi & \gamma_1 & \varepsilon_{A_2} - U/2 & v\pi^\dagger \\ v_3\pi^\dagger & -v_4\pi & v\pi & \varepsilon_{B_2} - U/2 \end{pmatrix} \tag{1.29}$$

Here $\pi = \xi p_x + ip_y$, $\pi^\dagger = \xi p_x - ip_y$ with the valley index $\xi = \pm 1$, and $v = \sqrt{3}a\gamma_0/2\hbar$ is the same effective velocity we introduced in the MLG case. Then $v_3 = \sqrt{3}a\gamma_3/2\hbar$ and $v_4 = \sqrt{3}a\gamma_4/2\hbar$ are two new effective velocities associated with the hopping parameters γ_3 and γ_4, respectively. Next, by using a Schrieffer–Wolff transformation, BLG's 4×4 low energy effective Hamiltonian can be further reduced to a 2×2 effective Hamiltonian, the details of this procedure can be found in McCaan's reviews[81,82]. Essentially, BLG's low energy bands will be described with an effective Hamiltonian using the two non-dimmer site orbits as the basis. This procedure also indicates BLG's low energy wavefunctions are polarized on the two non-dimmer carbon atoms. After this procedure, BLG's 4×4 low energy effective Hamiltonian now can be expressed as

$$H_{BLG} = H_0 + H_w + H_4 + H_U \tag{1.30}$$

where

$$H_0 = -\frac{1}{2m}\begin{pmatrix} 0 & (\pi^\dagger)^2 \\ (\pi)^2 & 0 \end{pmatrix}, \qquad m = \frac{\gamma_1}{2v^2} \tag{1.31}$$

$$H_w = v_3 \begin{pmatrix} 0 & \pi^\dagger \\ \pi & 0 \end{pmatrix} - \frac{v_3 a}{4\sqrt{3}\hbar} \begin{pmatrix} 0 & (\pi^\dagger)^2 \\ (\pi)^2 & 0 \end{pmatrix}, \tag{1.32}$$

$$H_4 = \frac{2vv_4}{\gamma_1} \begin{pmatrix} \pi^\dagger \pi & 0 \\ 0 & \pi\pi^\dagger \end{pmatrix}, \tag{1.33}$$

$$H_U = \frac{U}{2} \left[\begin{pmatrix} 1 & 0 \\ 0 & -1 \end{pmatrix} - \frac{2v^2}{\gamma_1^2} \begin{pmatrix} \pi^\dagger \pi & 0 \\ 0 & -\pi\pi^\dagger \end{pmatrix} \right]. \tag{1.33}$$

Now let us discuss each effective 2 × 2 Hamiltonian's effect on BLG's low energy band structures. H_0 is the minimum model to describe BLG's low energy bands, which only considers the γ_0 intralayer hopping and γ_1 inter layer hopping. As shown in Figure 1.11a, H_0 results in approximately parabolic shape low energy conduction and valence bands with effective mass $m = \gamma_1/2v^2$ that touch with each other. Similar to MLG, the spinor-like H_0 also gives rise to pseudospin-momentum lock-in for BLG's low energy bands, which means BLG possess massive chiral fermions. But in the BLG case, the full polarization of the Bloch wave onto the two non-dimmer sites at the top and bottom layers forms the pseudospin up and pseudospin down states. In addition, as schematized in Figure 1.11b, BLG pseudospin's winding speed associated with changing momentum direction is twice that of MLG. This gives rise to a doubled solid angle subtended by its pseudospin during a cyclic evolution that encloses K_+/K_- point compared to the MLG case, as a result BLG bands have a 2π Berry phase, which is doubled from MLG's π Berry phase.

Although H_0 captures many fundamental properties of BLG's low energy bands, H_w, originating from the γ_3 hopping, strongly perturbs the symmetry of BLG's low energy bands. As shown in Figure 1.11c, after considering the γ_3 hopping term, BLG's low energy bands are now trigonally warped. Furthermore, at even lower energies ($\lesssim 1$ meV), BLG bands will go over a Lifshitz transition and change from one Fermi surface pocket to four Fermi surface pockets in one valley as shown in Figure 1.11d. Even though H_w strongly altered BLG's low energy band symmetry, BLG's 2π Berry phase is still preserved even with the Lifshitz transition. The three outer Fermi surface pockets each contributes a π Berry phase, but the central Fermi surface pocket contributes a $-\pi$ Berry phase, which still results in a net 2π Berry phase.

H_4 adds another perturbation to BLG's low energy bands, which is resulted from the γ_4 hopping. H_4 can create an asymmetry between the conduction band and valence band as shown in Figure 1.11e, but such asymmetry is very small with the γ_4 hopping strength in BLG, so in many cases we can simply ignore the γ_4 hopping to simply the BLG tight-binding model. But with larger γ_4, the induced asymmetry between the conduction band and valence band can very significant as shown in Figure 1.11f, where we used a γ_4 value five times the actual γ_4 value in BLG.

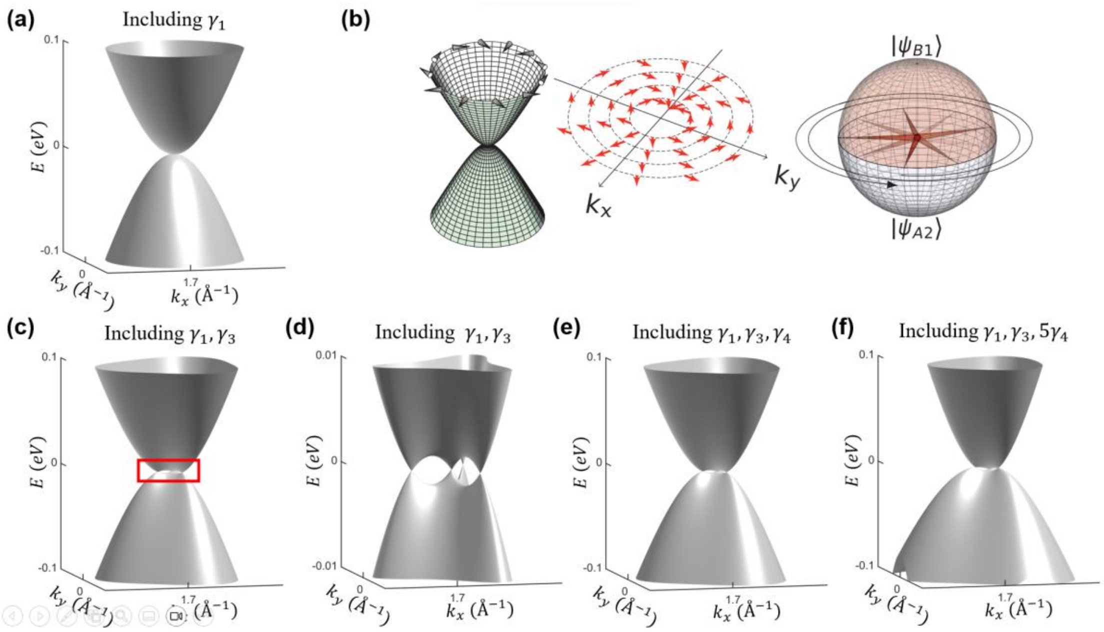

Figure 1.11 Each interlayer hopping term's effect on BLG low energy bands. (a) Calculated low energy BLG bands around the K_+ valley with considering only the γ_1 interlayer hopping. (b) Schematic of the pseudospin momentum lock-in of the low energy BLG bands that only considered γ_1 interlayer hopping and the 2π solid angle subtended by its pseudospin with one winding in the momentum space around the K_+ point. Image adapted from reference[87]. (c-d) Calculated low energy BLG bands around the K_+ valley with considering the γ_1 and γ_3 interlayer hopping. The red box in (c) indicates the zoomed-in energy range shown in (d). (e-f) Calculated low energy BLG bands around the K_+ valley with considering the γ_1, γ_3 and γ_4 interlayer hopping. The γ_4 value used to get (f) is five times the actual value of γ_4 in BLG just to exaggerate γ_4 hopping's effect on low energy BLG bands.

So far, we have discussed all the interlayer hopping parameters' effect on BLG's low energy bands. Next, I will discuss the effect of H_U, which is induced by interlayer potential difference, on BLG's low energy bands. The non-zero interlayer potential difference breaks the inversion symmetry of BLG and can induce a band gap for its low energy bands. For the simplest case (i.e., only considers γ_0, γ_1 hopping and U), the band gap induced by U can be expressed as

$$E_{gap} = \frac{|U|\gamma_1}{\sqrt{\gamma_1^2+U^2}} \tag{1.34}$$

For small $|U|$, $E_{gap} \approx |U|$. The parameter U can be easily controlled in experiment by external out of plane electric fields, which can be implemented by electrostatic gates. This indicates BLG is a unique material that hosts a gate tunable band gap, such band gap tunability opens the door toward electrostatically induced charge confinement, which is crucial for QD studies. Figure 1.12a shows a calculated low energy BLG bands with $U = 60$ meV that only considered γ_0 and γ_1 hopping.

Beyond band gap opening, the inversion symmetry breaking included by the interlayer potential difference U also allows the existence of non-zero Berry curvature Ω in BLG bands. The Berry curvature associated with a Bloch band can generally be expressed as[84]

$$\vec{\Omega}_n(\vec{q}) = \vec{\nabla}_{\vec{q}} \times \left\langle u_n(\vec{q}) \middle| i\vec{\nabla}_{\vec{q}} \middle| u_n(\vec{q}) \right\rangle \tag{1.35}$$

where $u_n(\vec{q})$ is the n-th electronic band's Bloch wavefunction. With Equation 1.35, we can write down the more explicit form for calculating BLG band's Berry curvature[84,89]:

$$\vec{\Omega}(\vec{k}) = i\left[\left\langle \frac{\partial u}{\partial k_x} \middle| \frac{\partial u}{\partial k_y} \right\rangle - \left\langle \frac{\partial u}{\partial k_y} \middle| \frac{\partial u}{\partial k_x} \right\rangle\right] \vec{e}_z \tag{1.36}$$

Figure 1.12b-c shows the calculated Ω that are associated with the BLG bands shown in Figure 1.12a. The Berry curvature of BLG bands has peaks that surround the K_+ point with a ring-like shape, and the Berry curvature signs are opposite between the conduction band and valance band at the K_+ valley. In addition, the Berry curvature signs in the same type of band at the K_- valley are also reversed from the K_+ valley, which is a result of the preservation of time reversal symmetry in BLG that guarantees $\Omega(-k) = -\Omega(k)$.

So far, we ignored the γ_3 hopping when analyzing U's effect on BLG's low energy bands. γ_3 hopping does not impart a significant change in the BLG low energy bands' response to an interlayer potential difference U. Figure 1.12d shows the calculated BLG low energy bands that considered γ_3 hopping with the same $U = 60$ meV as in the $\gamma_3 = 0$ case (Figure 1.12a), apart from trigonal warping of the BLG low energy bands, a band gap with a size similar to the $\gamma_3 = 0$ case is induced by this interlayer potential difference. As shown in Figure 1.12e-f, similar to the $\gamma_3 = 0$ case, these gapped and trigonally warped bands also possess non-zero Berry curvature. Different from the ring-like Berry curvature peak distribution in the $\gamma_3 = 0$ case, the Berry curvature now has three sharp peaks surround the K_+ point. But the Berry curvature sign of the BLG bands still has the same valley and conduction/valence band dependence as in the $\gamma_3 = 0$ case. In chapter 6, I will discuss the effect of gapped BLG band's non-zero Berry curvature on the spatial distribution of BLG QD wavefunctions.

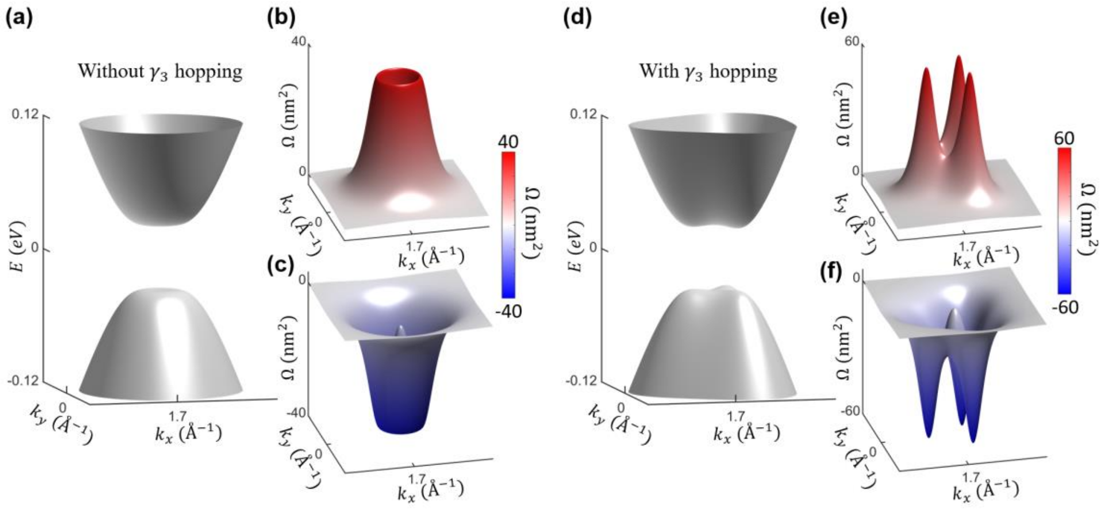

Figure 1.12 Gapped BLG bands and its associated Berry curvature. (a) Calculated BLG bands around K_+ point with an interlayer potential difference $U = 60\ \mathrm{meV}$. γ_3 hopping is not considered here. (b) The calculated Berry curvature of the conduction band shown in (a). (c) The calculated Berry curvature of the valence band shown in (a). (d) Calculated BLG bands around K_+ point with an interlayer potential difference $U = 60\ \mathrm{meV}$. γ_3 hopping is considered here. (e) The calculated Berry curvature of the conduction band shown in (d). (f) The calculated Berry curvature of the valence band shown in (d).

Berry curvature is a fundamental property of electronic bands, it determines the Berry phase picked up by a quantum state associated with the electronic bands by[84]

$$\phi_{Berry} = \int_S \vec{\Omega}(\vec{k}) \cdot d\vec{S} \tag{1.37}$$

, where S is the surface enclosed by the closed path of a cyclic adiabatic evolution in momentum space. In the MLG and ungapped BLG cases, their electronic bands' Berry curvature can be understood as a delta function at the K_+/K_- points or the four legs in the BLG case with Lifshitz transition, which will give rise to a quantized π or 2π Berry phase in MLG and ungapped BLG, respectively. But for gapped BLG, its Berry curvature has a distribution in momentum space, which gives the possibility of continuously tuning the Berry phase of a quantum state by controlling its closed path in momentum space[56,90,91]. In addition, the integration of Berry curvature divided by 2π over the whole Brillouin zone determines the Chern number[84], which is a topological invariant, of an electronic band, thus Berry curvature also plays an important role in understanding the topological property of electronic bands. Finally, non-zero Berry curvature can also give rise to many interesting quantum phenomena such as anomalous Hall effect and orbital magnetism[84].

1.2.3 Bernal Stacked Trilayer Graphene

In the previous two sections, we showed MLG hosts low energy electronic bands with linear energy dispersion, which made it suitable for investigating relativistic quantum phenomena, and BLG hosts low energy electronic bands with gate tunable band gap that can also host non-zero Berry curvature. In this section, I will show Bernal stacked trilayer graphene (TLG) can be a platform to host the physics that exists in both MLG and BLG with its mixed MLG-like and BLG-like low energy electronic bands.

Figure 1.13a shows the atomic structure and hopping terms of TLG[92], similar to BLG, TLG is a stack of MLG sheets. But different from the BLG case, with three MLG layers, there naturally exists another type of stacking for trilayer graphene, which is the rhombohedral stacking[93-95]. Figure 1.13b shows the difference between Bernal stacked trilayer graphene and rhombohedral stacked trilayer graphene, they are often referred to as ABA-TLG and ABC-TLG, respectively. During my PhD study, I only studied QDs that are based on ABA-TLG, which is the more stable stacking of TLG, so I plan to only review the electronic structure of ABA-TLG. For those who are interested in the electronic structure of ABC-TLG, referenc[93-95] can be a good starting point. For simplicity, I will refer to ABA-TLG just as TLG later on.

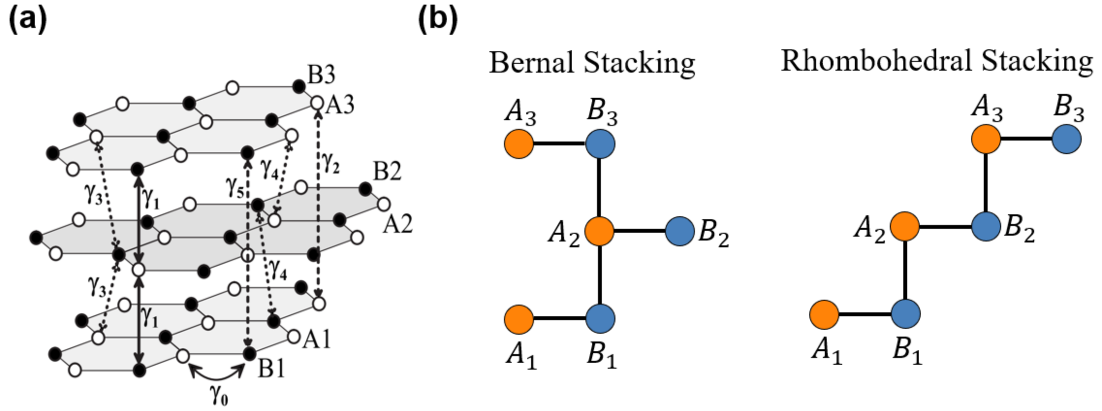

Figure 1.13 TLG atomic structure and tight-binding hopping parameters. (a) Schematic of the 3D view of the atomic structure of TLG and its associated tight-binding hopping parameters. Image adapted from reference[92]. (b) Schematic of the difference between the unit cell of Bernal stacked trilayer graphene (TLG) and Rhombohedral stacked trilayer graphene.

As shown in Figure 1.13a, in addition to those hopping terms we have already introduced in MLG and BLG, there exists two additional hopping terms $\gamma_2 = \langle \phi_{A_1} | \mathcal{H} | \phi_{A_3} \rangle$: the hopping between the top layer and bottom layer carbon atoms both at the non-trimmer site, and $\gamma_5 = \langle \phi_{B_1} | \mathcal{H} | \phi_{B_3} \rangle$: the hopping between the top layer and bottom layer carbon atoms both at the trimmer site. Similar to the BLG case, there is an intrinsic onsite energy difference between the trimmer site carbon atoms and non-trimmer site carbon atoms $\Delta_{AB} = \varepsilon_{trimmer} - \varepsilon_{nontrimmer}$. But different to the BLG case, such small energy difference plays an important role in determining the low energy electronic structure of TLG, which we will show later. With these newly defined parameters, we can write down the TLG tight-binding Hamiltonian as[92]:

$$H_{TLG} = \begin{pmatrix} \varepsilon_{A_1} & -\gamma_0 f(\vec{k}) & \gamma_4 f(k) & -\gamma_3 f^*(\vec{k}) & \dfrac{\gamma_2}{2} & 0 \\ -\gamma_0 f^*(\vec{k}) & \varepsilon_{B_1} + \Delta_{AB} & \gamma_1 & \gamma_4 f(\vec{k}) & 0 & \dfrac{\gamma_5}{2} \\ \gamma_4 f^*(\vec{k}) & \gamma_1 & \varepsilon_{A_2} + \Delta_{AB} & -\gamma_0 f(\vec{k}) & \gamma_4 f^*(\vec{k}) & \gamma_1 \\ -\gamma_3 f(\vec{k}) & \gamma_4 f^*(\vec{k}) & -\gamma_0 f^*(\vec{k}) & \varepsilon_{B_2} & -\gamma_3 f(\vec{k}) & \gamma_4 f^*(\vec{k}) \\ \dfrac{\gamma_2}{2} & 0 & \gamma_4 f(\vec{k}) & -\gamma_3 f^*(\vec{k}) & \varepsilon_{A_3} & -\gamma_0 f(\vec{k}) \\ 0 & \dfrac{\gamma_5}{2} & \gamma_1 & \gamma_4 f(\vec{k}) & -\gamma_0 f^*(\vec{k}) & \varepsilon_{B_3} + \Delta_{AB} \end{pmatrix} \tag{1.38}$$

Similar to the BLG case, we approximate the overlap matrix S as a unit matrix. Then we get the eigenvalues and eigenstates of TLG bands by numerically diagonalize H_{TLG} shown in Equation 1.38. Figure 1.14a shows the calculated TLG bands' energy dispersion over the whole Brillouin zone, it's generally the same as the MLG and BLG cases, the only noticeable difference is now TLG has in total six bands. Similarly, TLG's low energy bands are distributed around the K_+ and K_- points of its Brillouin zone. Figure 1.14b-c shows the calculated TLG low energy bands around the K_+ valley, we notice it has both MLG-like and BLG-like bands, and they are both gapped. To note, we did not include any interlayer potential difference here. The gap opening in the TLG case is due to its intrinsic inversion symmetry breaking. If we take sublattice A_2 as the inversion point, A_1, A_3 and B_2 do not have the corresponding inversion symmetric sublattices.

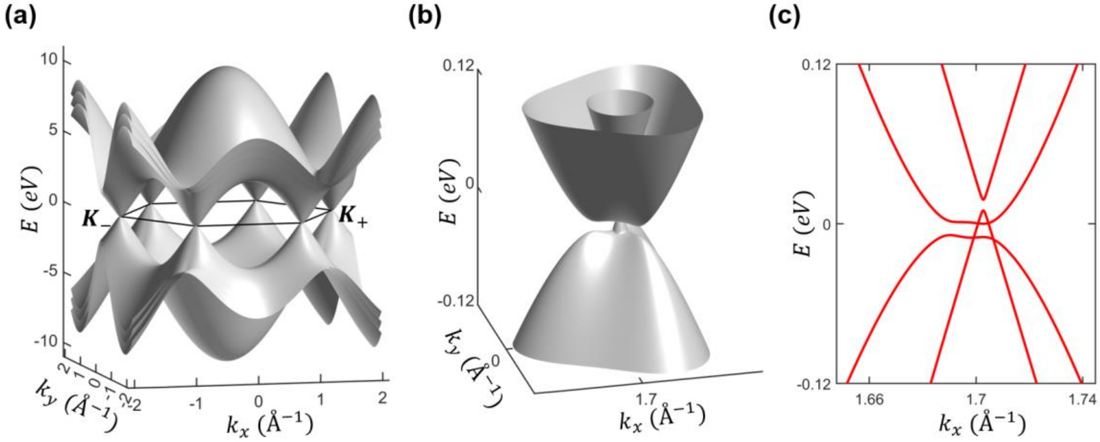

Figure 1.14 Band Structure of TLG. (a) Full energy TLG band structure calculated from the tight-binding model. The black hexagon is the boundary of TLG's first Brillouin zone. (b) Lower energy TLG bands around the K_+ valley shown in (a). (c) Line cut along the k_x direction at $k_y = 0$ for the low energy TLG bands shown in (b).

So far, we have only visually observed the similarity between the low energy TLG bands and low energy MLG and BLG bands, but we can actually more formally prove TLG's low energy bands indeed have an equivalence with low energy MLG and BLG bands. Similar to the MLG and BLG case, for TLG's low energy bands around the K_+/K_- valley, we can describe them with an effective Hamiltonian give below[92]:

$$H_{TLG} = \begin{pmatrix} 0 & v\pi^\dagger & -v_4\pi^\dagger & v_3\pi & \frac{\gamma_2}{2} & 0 \\ v\pi & \Delta_{AB} & \gamma_1 & -v_4\pi^\dagger & 0 & \frac{\gamma_5}{2} \\ -v_4\pi & \gamma_1 & \Delta_{AB} & v\pi^\dagger & -v_4\pi & \gamma_1 \\ v_3\pi^\dagger & -v_4\pi & v\pi & 0 & v_3\pi^\dagger & -v_4\pi \\ \frac{\gamma_2}{2} & 0 & -v_4\pi^\dagger & v_3\pi & 0 & v\pi^\dagger \\ 0 & \frac{\gamma_5}{2} & \gamma_1 & -v_4\pi^\dagger & v\pi & \Delta_{AB} \end{pmatrix} \tag{1.39}$$

, where the effective velocities and $\pi/\pi^\dagger$ are defined in the same way as in the BLG case. By performing a unitary transformation, we can rewrite this effective Hamiltonian with a new basis $(\psi_{A_1} - \psi_{A_3})/\sqrt{2}$, $(\psi_{B_1} - \psi_{B_3})/\sqrt{2}$, $(\psi_{A_1} + \psi_{A_3})/\sqrt{2}$, ψ_{B_2}, ψ_{A_2}, and $(\psi_{B_1} + \psi_{B_3})/\sqrt{2}$. With this new basis, TLG's low energy effective Hamiltonian given in Equation 1.39 can be rewritten as[92]:

$$H_{TLG} = \begin{pmatrix} -\frac{\gamma_2}{2} & v\pi^\dagger & 0 & 0 & 0 & 0 \\ v\pi & -\frac{\gamma_5}{2} + \Delta_{AB} & 0 & 0 & 0 & 0 \\ 0 & 0 & \frac{\gamma_2}{2} & \sqrt{2}v_3\pi & -\sqrt{2}v_4\pi^\dagger & v\pi^\dagger \\ 0 & 0 & \sqrt{2}v_3\pi & 0 & v\pi & -\sqrt{2}v_4\pi \\ 0 & 0 & -\sqrt{2}v_4\pi & v\pi^\dagger & \Delta_{AB} & \sqrt{2}\gamma_1 \\ 0 & 0 & \gamma_1 & -\sqrt{2}v_4\pi^\dagger & \sqrt{2}\gamma_1 & \frac{\gamma_5}{2} + \Delta_{AB} \end{pmatrix} \tag{1.40}$$

It forms two blocks, the upper block and lower block look exactly like the low energy effective Hamiltonian for MLG (Equation 1.22) and BLG (Equation 1.29), respectively. This result formally proved the equivalence between TLG's low energy bands and MLG and BLG's low energy bands. We can use the following effective Hamiltonian to describe the effective MLG bands in TLG[92]:

$$H_{MLG}^{eff} = \begin{pmatrix} -\frac{\gamma_2}{2} & v\pi^\dagger \\ v\pi & -\frac{\gamma_5}{2} + \Delta_{AB} \end{pmatrix} \tag{1.41}$$

For the effective BLG block, it can be further reduced to a 2×2 matrix following the same procedure we mentioned in the real BLG case to describe the effective BLG bands in TLG. To the first order, we can get[92,96]:

$$H_{BLG}^{eff} = -\frac{1}{2m}\begin{pmatrix} 0 & (\pi^\dagger)^2 \\ (\pi)^2 & 0 \end{pmatrix} + \sqrt{2}v_3 \begin{pmatrix} 0 & \pi^\dagger \\ \pi & 0 \end{pmatrix} + \begin{pmatrix} \frac{\gamma_2}{2} & 0 \\ 0 & 0 \end{pmatrix} + \cdots \tag{1.42}$$

, where $m = \gamma_1/\sqrt{2}v^2$.

From the effective MLG Hamiltonian (Equation 1.41) and effective BLG Hamiltonian (Equation 1.42) that we derived from TLG, we can see exactly what tigh-binding parameters determine the gap opening of the effective MLG and BLG bands in intrinsic TLG. γ_2, γ_5 and Δ_{AB} together determines the band gap of the effective MLG band. But for the effective BLG band, only γ_2 determines its band gap. This argument can be directly visualized by calculating low energy TLG bands without considering γ_2, γ_5 and Δ_{AB} or considering only one of these parameters (Figure 1.15). We can see γ_2, γ_5 and Δ_{AB} all can open a band gap in the effective MLG band, but only γ_2 can open a band gap in the effective BLG band, which agrees with the discussion we had above.

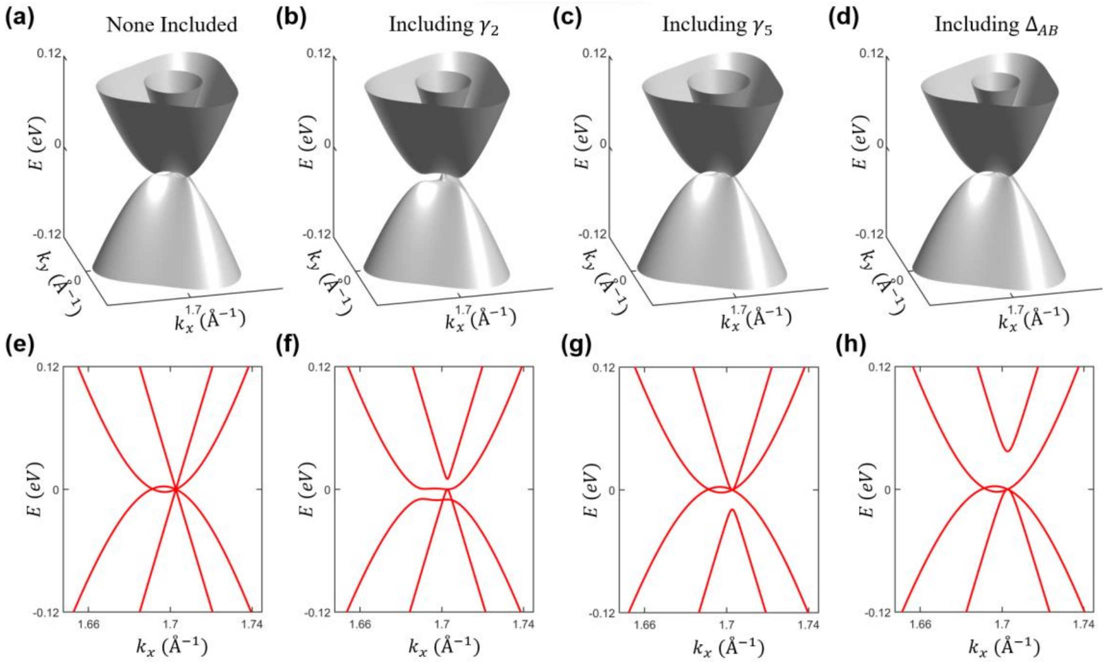

Figure 1.15 Effect of γ_2, γ_5 and Δ_{AB} on TLG low energy bands. (a) Low energy TLG bands around the K_+ point without considering γ_2, γ_5 and Δ_{AB}. (b-d) Low energy TLG bands around the K_+ point with considering the γ_2 hoping (b), γ_5 hoping (c) and onsite

energy difference Δ_{AB} (d), respectively. (e-h) Line cut along the k_x direction at $k_y = 0$ for the low energy TLG bands shown in (a-d), respectively.

The gap opening in TLG's effective MLG bands is quite unique because a band gap cannot be opened for real MLG's linear Dirac bands simply by an external electric field like in the BLG case. So, I will focus on this gapped effective MLG band in TLG and provide detailed discussion of this gapped effective MLG band. According to TLG's effective MLG Hamiltonian (Equation 1.41), the gap size Δ of this effective MLG band can be expressed as

$$\Delta = \left|\Delta_{AB} + \frac{\gamma_2 - \gamma_5}{2}\right| \tag{1.43}$$

The exact values of these parameters are hard to be experimentally determined, there usually exists many inconsistencies between experimentally extracted or theoretically calculated values[96-100]. But from earlier works, we can still get a rough idea of the order of magnitude of these values. Based on early graphite studies[100], the values of these parameters are $\gamma_2 \approx -0.02\ \mathrm{meV}$, $\gamma_5 \approx 0.038\ \mathrm{meV}$, and $\Delta_{AB} \approx 0.037\ \mathrm{meV}$, which leads to a gap size $\Delta = 8$ meV for the effective MLG bands in TLG. As we can see, Δ_{AB} is on the same order of γ_2 and γ_5, as a result, Δ_{AB} plays an important role in determining the gap size and gap sign of the effective MLG bands of TLG. This is quite different from the BLG case where we can ignore the Δ_{AB} term because it does not have much effect on BLG's low energy bands.

One important consequence of the gap opening of TLG's effective MLG bands is that these bands now can also possess non-trivial band geometrical properties such as non-zero Berry curvature. Electronic bands with non-zero Berry curvature also possess non-zero orbital magnetic moment $\vec{\mu}(\vec{k})$, which is another intrinsic property associated with electronic bands' geometrical properties[84]. This orbital magnetic moment can be expressed as[84]

$$\vec{\mu}(\vec{q}) = -i\frac{e}{2\hbar}\langle\vec{\nabla}_{\vec{q}}u_n(\vec{q})| \times [H(\vec{q}) - \varepsilon(\vec{q})]|\vec{\nabla}_{\vec{q}}u_n(\vec{q})\rangle \tag{1.44}$$

, where $H(\vec{q}) = e^{-i\vec{q}\cdot\vec{r}}He^{i\vec{q}\cdot\vec{r}}$ is the q-dependent Hamiltonian and $\varepsilon(\vec{q})$ is the band energy. With this definition, the orbital magnetic moment associated with gapped MLG bands can be analytically expressed as[101]

$$\vec{\mu}_{Eff_{MLG}}(\vec{k}) = \frac{e}{\hbar}\frac{\Delta}{\left[\left(\frac{\Delta}{\hbar v_F}\right)^2 + 4|\vec{k}|^2\right]}\vec{e}_z \tag{1.45}$$

From Equation 1.45, we can see the orbital magnetic moment direction depends on the gap sign of the effective MLG band and it has a peak value at the Dirac point $k = 0$. And this peak value can be expressed as[101]

$$\mu_{peak} = \frac{e\hbar}{2m^*}, \qquad m^* = \frac{\Delta}{2v_F^2} \tag{1.46}$$

Here m^* is the effective mass of gapped MLG band at its band edge. With the gap value $\Delta \approx 8$ meV we estimated for the effective MLG bands in TLG, this leads to an effective mass $m^* \approx 0.0007m_e$, where m_e is the electron mass. This effective mass is extremely small. And the maximum orbital magnetic moment associated with the effective MLG band will be $\mu_{peak} \approx 1421\mu_B$ (μ_B is the Bohr magneton), which is extremely large. In chapter 7, I will show the influence of such giant orbital magnetic moment of weakly gapped effective MLG bands on the magnetic field response of TLG QD states.

1.3 Outline of the Dissertation

In section 1.2, we reviewed many unique properties of the electronic structure of MLG, BLG and TLG. During my PhD study, I used a low temperature STM to characterize the electronic structure and magnetic field response of electrostatically defined QD based on the graphene systems covered in section 1.2. This includes MLG QDs, BLG QDs and TLG QDs. With these different types of graphene QD systems, I was able to investigate many types of interesting physics problems and observe varieties of quantum phenomena that arose from the interplay between quantum confinement and those unique properties of the electronic structure of graphene systems that we discussed in section 1.2. In this section, I will lay out the structure of this dissertation.

In chapter 2, I will introduce some fundamentals of low temperature STM, which is the experimental tool that I use to create and measure graphene QDs. In this chapter, I will especially explain how we use STM to create electrostatically defined graphene QDs with unprecedently sharp potential wells, which distinguished our works from similar works. Apart from this, I will also focus on explaining how we perform magnetic field resolved STS measurements with the STM in our lab.

In chapter 3, I will give a brief review of the fabrication of graphene devices that are suitable for STM graphene QD studies. In this chapter, I will extensively explain the surface cleaning procedure of our fabricated graphene devices to ensure the high possibility of finding a large enough pristine graphene area in STM for QD studies.

In chapter 4, I will introduce some numerical simulation tools that can model experimental graphene QDs, which provided tremendous help on the understanding of my experimental findings on graphene QDs during my PhD study. I will especially focus on explaining the tight binding model of graphene QDs and how to implement and solve it with a python package called Pybinding[102].

In chapter 5, I will show the results of my PhD study on the magnetic field response of single and coupled MLG QDs. As discussed in section 1.2.1, MLG is a platform that hosts relativistic quantum phenomena due to its linear Dirac bands. Together with the idea of artificial atoms and molecules introduced in section 1.1 for QDs, these single and coupled MLG QDs can be thought of as artificial relativistic atoms and molecules, respectively. In this chapter, I will uncover some unique magnetic field responses of 2D artificial relativistic atoms and molecules.

In chapter 6, I switch to my PhD study on the wavefunction mapping of BLG QD states. As discussed in section 1.2.2, BLG's low energy bands can be gapped by external out of plane electric field. This also makes BLG's low energy bands possess non-zero Berry curvature, which is a property missing in MLG. In addition, BLG's low energy bands has strong trigonal warping effect thus have a unique triangular Fermi surface, which is very different from the circular Fermi surface in MLG case. As a result, BLG QDs offer a unique platform to investigate the effect of Berry curvature and Fermi surface symmetry on QD states. In this chapter, I will show the effect of trigonal warping and Berry curvature of BLG bands on the spatial distribution of BLG QD wavefunctions.

In chapter 7, I will show my PhD study on the magnetic field response of TLG QD states. As discussed in section 1.2.3, TLG low energy bands host both an effective MLG band and an effective BLG band. I will emphasize its effective MLG band, which is weakly gapped and thus different from a real MLG band. Such weakly gapped MLG bands possess extremely large orbital magnetic moments. In this chapter, I will show how such giant orbital magnetic moments influence the magnetic field response of the TLG QD states that are associated with the quantum confinement of its effective MLG bands.

In chapter 8, I will switch to back to the MLG system, but this time I will show my PhD study on the wavefunction mapping of non-circular MLG QDs. In chapters 5-7, my studies are all focused on circular QDs although based on different graphene systems. As introduced in section 1.1, non-circular QDs, for example, stadium shaped QDs can be used to investigate quantum chaos. One important phenomenon in quantum chaos is the wavefunction scarring[103] (i.e., enhanced wavefunction probability density along unstable classical periodic orbit). But the experimental visualization of such an effect is so far elusive for real quantum systems. In this chapter, I will show our results on the wavefunction mapping of stadium shaped MLG QDs, targeting to unambiguously visualize the wavefunction scarring effect in a real quantum system.

In chapter 9, I will give a brief outlook of future research directions with the STM in-situ local doping technique that I used in graphene QD studies.

Chapter 2 Scanning Tunneling Microscope (STM)

2.1 Introduction

STM is the experimental tool that I used to create and probe electrostatically defined graphene QDs during my PhD study. In this chapter, I will introduce some fundamentals of STM theories and its operation that are necessary to perform graphene QD STM experiments and interpret the acquired STM data.

2.1.1 Working Principle of STM

The fundamental working principle of STM is electron tunneling. When a sharp conductive probe (i.e., STM tip) is brought extremely close to but still not in contact with a conductive surface, an electron current can flow between the surface and probe if a bias voltage is applied between them as schematized in Figure 2.1a. Here the current flow is governed by the electron tunneling across the vacuum barrier between the surface and probe as shown in Figure 2.1b, which is fundamentally different from conventional electron transport in a conductive material. Based on the Bardeen[104] and Tersoff-Hamman[105,106] theory, the current flow (I) between the STM tip and sample can be expressed as:

$$I(V_S, \vec{r}) \propto \int_{\mu}^{\mu+eV_S} LDOS(E, \vec{r}) e^{-\frac{z}{\lambda}} dE \tag{2.1}$$

Here V_S is the bias voltage applied between the STM tip and sample, $\vec{r}$ is the location of the STM tip on the sample, μ is the chemical potential of the sample, z is the distance between the STM tip and sample, and λ is the effective local decay length. To make Equation 2.1 valid for describing STM experiments, some assumptions must be made.

In the Bardeen picture, it is assumed that the $LDOS$ of the STM tip is a constant and has no energy dependence. In the Tersoff-Hamman theory, it is assumed that the wavefunction of the STM tip apex has an s-wave form. These assumptions indicate that the STM tip calibration will be a crucial step to help get reliable STM data for proper interpretation. I will discuss the details of the STM tip calibration procedures that I used in section 2.3.1 below.

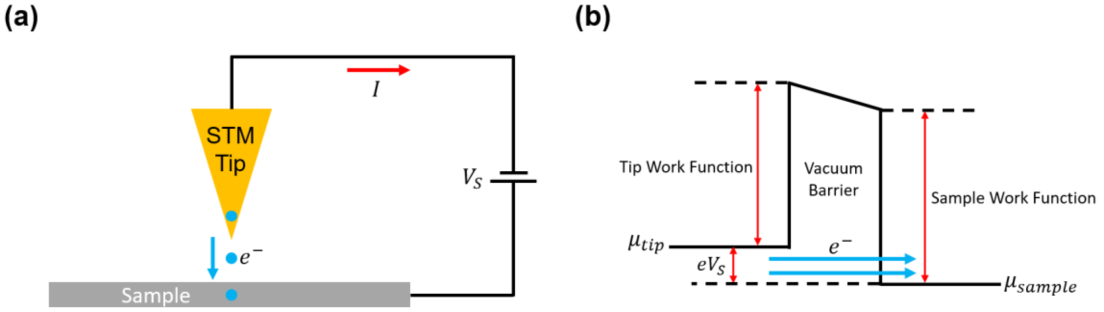

Figure 2.1 Electron tunneling in STM. (a) Schematic of the current flow between an STM tip and sample by applying a bias voltage V_S between them. The current flow is assisted by the electron tunneling across the vacuum barrier between the STM tip and sample as depicted by the blue arrow. (b) Schematic of the potential barrier between the STM tip and sample. The vacuum potential barrier is determined by the sample and tip work functions. The chemical potential difference between the STM tip and sample is determined by the applied V_S between them. Electrons can tunnel from occupied states from one side to the unoccupied states on the other side as depicted by the blue arrows.

For conventional low-temperature STM, there exists two major modes. One is the scanning tunneling microscopy (STM) mode, and the other one is the scanning tunneling spectroscopy (STS) mode. The STM mode utilizes the exponential dependence of the tunneling current on tip-sample distance as shown in Equation 2.1, which gives STM high sensitivity on measuring the sample topography. Typically, in the STM mode, the tunneling current is used as a feedback signal and kept at a constant by adjusting the z-piezo length during the scan. The sample topography can be extracted from the z-piezo length at every location. But one thing to note is that, for samples with strong spatial $LDOS$ variation, it is very common that the spatial $LDOS$ pattern and the topography will be convoluted with each other using the constant current STM mode. Different form the STM mode, the STS mode utilizes the dependence of the tunneling current on sample $LDOS$. During the STS mode, typically the tip sample distant is kept as a constant, then we sweep the V_S and measure differential conductance dI/dV_S at every bias voltage scanned. According to Equation 2.1, we can get

$$\frac{dI}{dV_S}(V_S,\vec{r}) \propto LDOS(\mu + eV_S,\vec{r}). \tag{2.2}$$

As a result, with the STS mode, the dI/dV_S spectra directly reflect the sample $LDOS$ spectra. But something we need to pay attention to in Equation 2.2 is that here we assumed μ and λ have no V_S dependence. However, for graphene QDs or more generally graphene-based systems, these two parameters both have strong dependence on V_S and can cause significant features in their dI/dV_S spectra. To properly understand the graphene QD STS data that I will show in the later chapters, it is crucial to get a more complete picture of what happens during the STS measurement on graphene QDs. So I will provide some more detailed discussions of the STS of graphene and graphene QDs below.

First, I will discuss the consequence of V_S dependence of μ on graphene STS. When μ has V_S dependence due to tip gating, the measured differential conductance dI/dV_S will be modified from Equation 2.2 and have the following expression

$$\frac{dI}{dV_S}(V_S,\vec{r}) \propto \left(1+\frac{\partial\mu}{\partial(eV_S)}\right) LDOS(\mu+eV_S,\vec{r}) - \frac{\partial\mu}{\partial(eV_S)} LDOS(\mu,\vec{r}) \qquad (2.3)$$

As we can see, the differential conductance at V_S now has contributions from the sample $LDOS$ at both $\mu + eV_S$ and μ, and their relative contribution factor depends on the value of $\partial\mu/\partial(eV_S)$. The general property of $\partial\mu/\partial(eV_S)$ is that its magnitude is negatively correlated with $LDOS$ at the Fermi level. For common metallic samples, because of the high $LDOS$ near their Fermi level, $\partial\mu/\partial(eV_S)$ almost vanishes, so we can recover the conventional dI/dV_S spectra expression as shown in Equation 2.2. But for graphene and graphene QDs, there exists many energy ranges with very low $LDOS$. As a result, when the Fermi level lies around those low $LDOS$ energy ranges, $\partial\mu/\partial(eV_S)$ cannot be ignore anymore. To get the exact value of $\partial\mu/\partial(eV_S)$, we need to use the quantum capacitance model[107], which accounts for the Fermi level energy shift when electrostatically gating the system. I will not show details how this model works here, but interested readers can check out the supplementary information of reference[50] as an example.

Next, I will discuss the effect of V_S dependence of λ on graphene STS. The effective local decay length λ in general is expected to have V_S dependence, because at different V_S, the effective vacuum tunneling barrier height is different. But such an effect can normally be ignored in graphene STS measurement. Firstly, it's because the vacuum tunneling barrier height is on the order of 5 eV, which depends on the work function of graphene[108]. This value is much larger than the typical V_S range applied during graphene STS measurement (smaller than -0.5 V to 0.5 V), so the change of λ

is expected to be small during the STS measurement. Secondly, even if we still consider the tunneling barrier height change during the STS measurement, the change of the effective λ will be smooth and gradual, so it will not cause any sharp features in the dI/dV_S spectra that might complicate STS data interpretation.

However, for graphene STS, there exists another mechanism that can significantly and abruptly change the value of λ when V_S is above certain threshold. This is phonon-assisted inelastic electron tunneling process[109,110]. In short, when V_S approaches the energy of certain graphene phonon modes, new inelastic electron tunneling channels will open in addition to the elastic tunneling channel as schematized in Figure 2.2a. For graphene, its inelastic electron tunneling process can have a significantly enhanced λ compared to its elastic electron tunneling process. Figure 2.2 b shows an experimentally measured λ as a function of V_S for MLG STS[109], the effective local decay length significantly increases when $|V_S|$ approaches ~60 mV, which is close to the energy of graphene out-of-plane acoustic K phonon[111]. As a result, graphene dI/dV_S spectra typically show a sudden enhancement of dI/dV_S signals once $|V_S|$ reaches ~60 mV. This can create a gap-like feature near $V_S = 0$ as shown in Figure 2.2 c, which is often referred to as a phonon gap. In my graphene QD studies, I typically limited the V_S window within the elastic electron tunneling only range, which is around -60 mV to 60 mV. This avoids the complication by the unwanted inelastic electron tunneling processes. When measuring STS for such relatively small V_S window, I typically use a set point of around $I = 1$ nA at $V_S = -60$ mV.

To illustrate the discussions made in the above two paragraph more clearly, Figure 2.3 shows an experimentally measured color map of gate-resolved STS acquired on pristine MLG area. The gate independent dark feature around $V_S = 0$ is the phonon gap we discussed before. Near $V_G = 0$ V, there exists some bright features in the color map, which comes from STM tip induced MLG QD, which I will discuss in more detail in section 2.3.1. As we can see, there exists two bright features that disperse different with V_G as marked by the yellow arrows. These two features are from the same tip induced MLG QD states due to the V_S dependence of μ of MLG sample, they are from the $LDOS(\mu + eV_S)$ contribution and $LDOS(\mu)$ contribution to the dI/dV_S signal as shown in Equation 2.3.

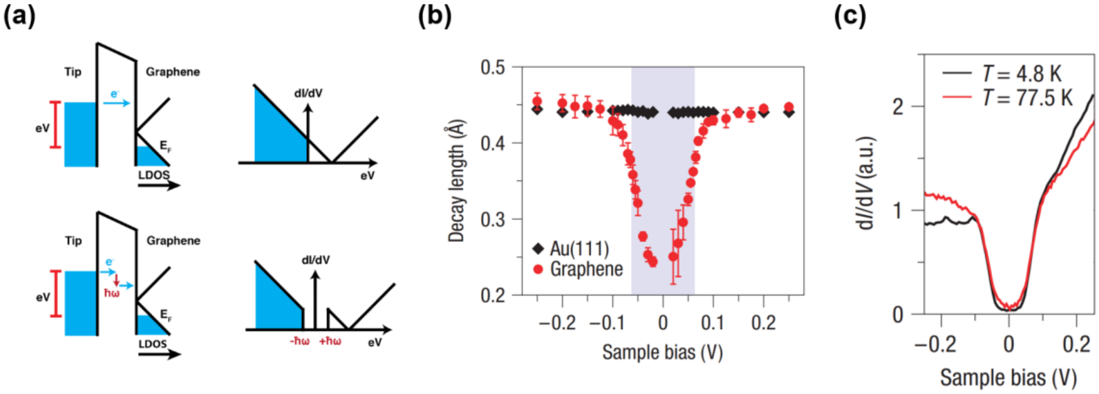

Figure 2.2 Phonon assisted inelastic electron tunneling into graphene. (a) Schematic of the difference between elastic (top row) and inelastic electron tunneling process into graphene (bottom row) and their corresponding STS features. Image adapted from reference[112]. (b) Experimentally measure effective decay length λ for MLG STS. Image adapted from reference[109]. (c) Typical experimental dI/dV_S spectra for MLG, which features a symmetric gap around $V_S = 0$. Image adapted from reference[109].

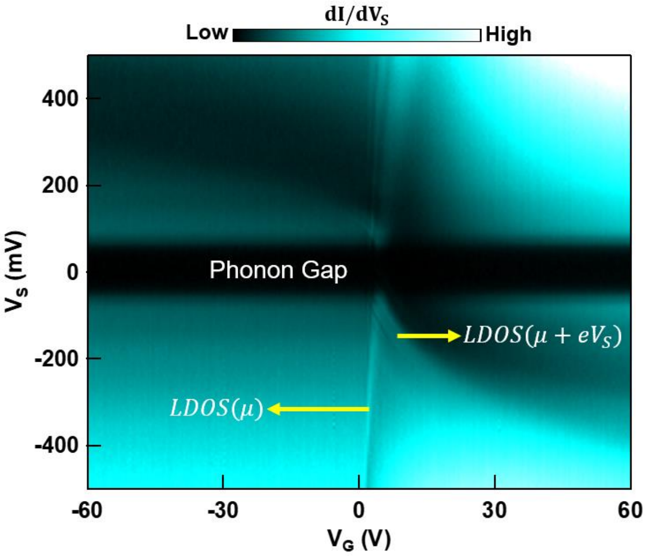

Figure 2.3 Gate-resolved STS on a pristine MLG sample. The set point used to acquire the dI/dV_S spectrum was $I = 1$ nA, $V_S = -500$ mV with a 5 mV ac modulation.

2.1.2 Structure of the Createc LT-STM

In section 2.1.1 I discussed the theoretical working principle of STM, in this section I will show how to implement these working principles in a real lab by introducing the structure of the Createc LT-STM, which is a commercial STM that I use for my PhD studies.

Figure 2.4a shows the structure of the Createc LT-STM in our lab. It is composed of four major parts, which are the STM chamber, liquid helium (LHe) cryostat, load-lock, preparation chamber, and load-lock chamber. Below I will describe the major functions of each part. Firstly, the STM chamber is where the STM head is placed, and we do all the STM measurements in this chamber. I will provide more details of the STM head later. The STM chamber has the best vacuum of the whole STM system, its vacuum is typically better than 1×10^{-10} mbar, which is achieved through a combined ion pump/titanium sputtering pump system. This vacuum level is in the UHV range, which is a crucial part of realizing the vacuum tunnel barrier in the STM theory. The major function of the LHe cryostat is to keep the STM head at around LHe boiling temperature, which is around 4.2 K at atmosphere pressure. Such a low temperature can reduce thermal broadening of the sample $LDOS$ and the thermal noise of electronics, which is important for getting high quality STS data. Next, the major function of the preparation chamber is to perform sample surface treatments such as UHV annealing and Ar sputtering before introducing a sample into the STM chamber. The vacuum of this chamber typically is slightly above 1×10^{-10} mbar when no operation happens, which is also achieved through a combined ion pump/titanium sputtering pump system. Finally, the load-lock chamber is mainly served as a buffer that connects the atmospheric and UHV environments. UHV systems typically cannot be directly exposed to atmospheric environment because certain adsorbates from atmosphere such as water can be very difficult to remove and prevent reaching UHV later without baking the chamber walls. But for the load-lock chamber, UHV is not required, so it will not have such a problem. The vacuum in the load-lock chamber is achieved through a combined turbo pump and roughing pump system, which can achieve a vacuum around 1×10^{-8} mbar. UHV system opened to such a vacuum level will have no issue going back to UHV later without baking the system. So, all samples from the atmospheric environment are first introduced into the load-lock chamber before being moved into UHV.

Now, I will provide some more details of the STM head. Figure 2.4b shows a photo of the STM head. The STM head contains a tip holding slot and a sample holding slot. The tip holding slot has only one electrical connection, which is grounded. The sample holding slot has five electrical connection pins, which can be connected to external sources. Apart from these, the STM head also contains a coarse xyz piezo system, a fine xyz piezo system, a mechanical suspension system and a superconducting magnet. The STM tip is fixed at the bottom of the fine piezo, which controls the STM tip's xyz position with ~1 pm precision. Such high precision control of the tip position is a prerequisite of performing STM measurements. Although the fine piezo has high precision, its scanning range is quite narrow, the xy dimension it can scan is around 700 nm (with a 10x gain), and the z dimension it can scan is around 17nm (with a 1x gain). Because of this, the fine piezo is mounted on a coarse xyz piezo system, which can move across the xyz dimensions with cm ranges but with a lower precision for the position control. Next, the mechanical suspension system is composed of three springs. During STM measurements, the STM head is suspended by these three springs, which can damp out most high frequency mechanical noises. In our STM, the mechanical vibration noise picked up by the STM can be reduced below 10 pm. Finally, the STM head of our system also contains a superconducting coil, which can serve as a magnet when current is flowing through the coil. The maximum magnetic field can be reached is ~2 T for this superconducting coil in our STM.

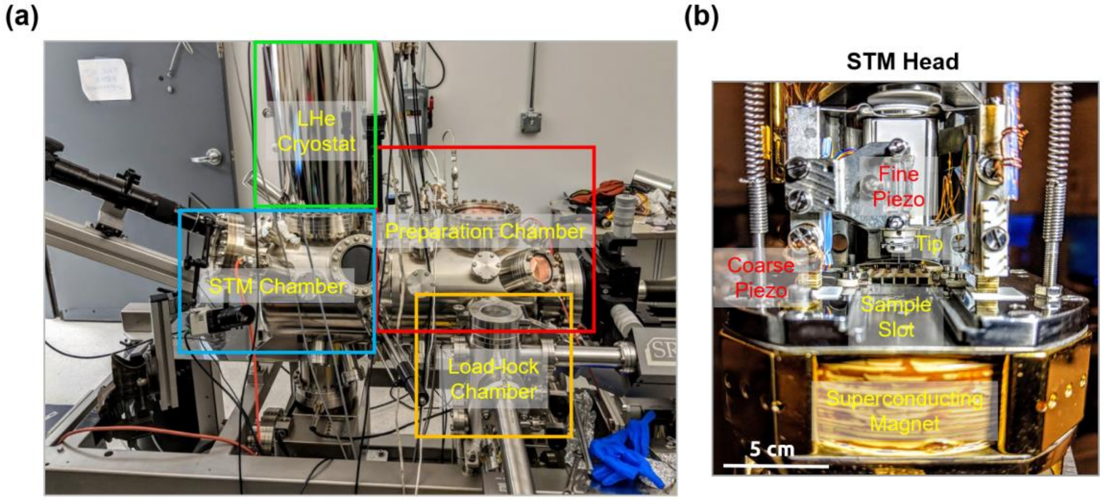

Figure 2.4 Structure of the Createc LT-STM. (a) Photograph of the whole structure of the Createc LT-STM in our lab. (b) Photograph of the STM head in the Createc LT-STM in our lab.

2.2 Basic STM Operations

In section 2.1, I have introduced the working principle of STM and showed the structure of a real STM. In this section, I will introduce some basic STM operations that are frequently used in my PhD studies.

2.2.1 STM Tip Preparation and Calibration

As mentioned in section 2.1.1, tip calibration is a crucial step to get reliable STM/STS data. In this section, I will briefly describe how I prepare and calibrate STM tips for graphene QD studies.

Most of the STM tips that I used for graphene QD studies were made of tungsten (W), only one tip I have used was made of platinum-iridium (Pt-Ir). I did not notice any obvious difference between W tips and Pr-Ir tips for graphene QD studies. Since almost all my studies were done with W tips, here I will only describe how the W tips were made in my experiments. The general idea of making W tips is using electrochemical etching. We use sodium hydroxide (NaOH)/deionized (DI) water solution as the electrolyte (mass ration between NaOH and DI water is 1:12.5), and we use a straight W wire as the anode and a circularly looped copper wire as the cathode. During the electrochemical etching, we put the circular copper cathode right at the NaOH electrolyte surface and dip the W wire slightly into the NaOH electrolyte as shown in Figure 2.5a. Then we apply an 8 V DC voltage between the W anode and copper cathode to start the etching of the W wire, typically the current during the etching is maintained around 15 mA. During the etching process, we closely monitor the part of the W wire that is dipped into the NaOH electrolyte. Once this part is detached from the above W wire, we immediately turn the applied DC voltage to zero. Then the etching process is done. Normally, a very sharp W tip can be achieved through this process, the tip end can be as narrow as several hundred nanometers. Figure 2.5b shows the optical image of an example etched W tip.

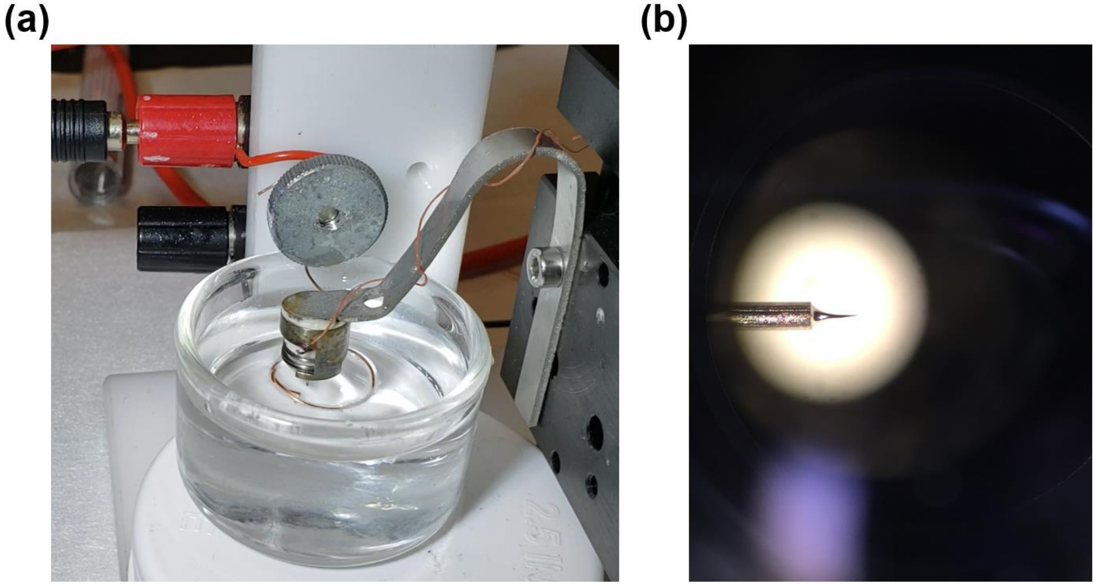

Figure 2.5 Electrochemical etching for W tip fabrication. (a) A photograph of the W tip etching set up. (b) An optical microscope image of an etched W tip. The W wire diameter is 300 μm.

After the successful etching of a W tip, I typically will rinse it with DI water and IPA then blow dry it with nitrogen gas. After this, I will bring the W tip into the STM system. For a newly etched W tip, I will perform a combined Ar sputtering and UHV annealing as shown in Figure 2.6 before bringing it into the STM chamber and using it. I typically will do two rounds of UHV annealing at 550 C for about 1 minute before and after the Ar sputtering. For the Ar sputtering, I typically set the Ar ion source to 1.7 kV with 10 mA emission and adjust the Ar inlet pressure to around 6×10^{-5} mbar. And I usually will do the Ar sputtering at two different sides of the W tip for about 25 minutes at each side. After these steps, finally I will bring the W tip into the STM chamber and put it into the tip slot on the STM head for tip calibration.

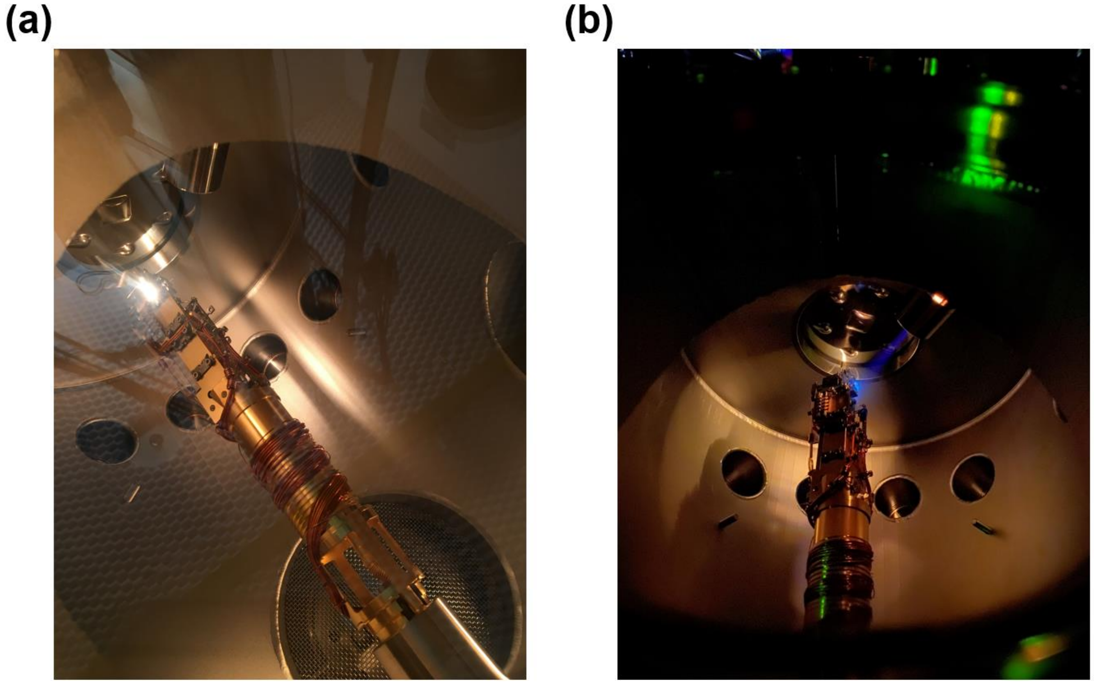

Figure 2.6 STM tip UHV annealing and Ar sputtering. (a) A photograph of a W tip under UHV annealing. The very bright spot is the glowing from the heating source, and the W tip is right above it. (b) A photograph of a W tip under Ar sputtering. The blue jet is the Ar ion beam, which is aimed at the W tip.

So far, I have shown how to fabricate a new STM tip. Next, I will describe the STM tip calibration procedure that I use for graphene QD studies. I perform my STM tip calibrations on the Au (111) surface, which possesses a well-understood 2D surface-state band that can be used for tunneling spectra calibration[109,113]. During the tip calibration, the first step I do is to make sure the STM is in a status that the current noise is below 0.5% at 1 nA, -700 mV set point and we can acquire stable topography images with good spatial resolution for the Au (111) surface. Figure 2.7a shows an example good topography image for Au (111) surface, we should be able to clearly resolve the Au (111) terraces and the so called herringbone structure, which is a result of the Au (111) surface reconstruction[113]. This step can typically be done by a combination of pulsing the tip with $\pm$ 10 V bias voltage and poking the tip into the Au (111) surface with 9 to 100 Å depth. If the tip is really bad and cannot achieve a stable status, we may try the UHV annealing and Ar sputtering I described earlier. If it still does not work, we may have to make a new tip. Most of the time, we do not have to go through the latter two steps to get a stable STM tip that can produce a good topography image on Au(111).

The second step of my tip calibration procedure is to check the poke shape and make sure it is circular, which is crucial for creating graphene QDs with good circular symmetry. I typically will first check the poke shape by poking the tip into the Au (111) surface with 35 Å depth and make sure it is not extremely off from a circular shape. Then I will check the shape of 9 Å pokes, and make sure they are very circular as the one shown in Figure 2.7b. This step can normally be done by randomly poking the tip into Au (111) surface with different depth (15~100 Å) and duration (0.1~60 seconds).

The final step of my tip calibration procedure is to calibrate the tunneling spectra[109,113] and make sure a sharp step appears at around -500 mV, where the Au (111) 2D surface-state band onsets[113], and most of the dI/dV_S spectra is flat. Figure 2.7c shows an example calibrated dI/dV_S spectra on Au (111) surface. During this step, I always applied a 9 Å poke with 0.1 second duration and check the tunneling spectra after every poke until a good spectrum like the one in Figure 2.7c appears. Then I will check the shape of the poke and confirm its circular like the one in Figure 2.7b.

If the poke shape is not circular, we can either repeat step three or go back to step two depending on how bad the shape is.

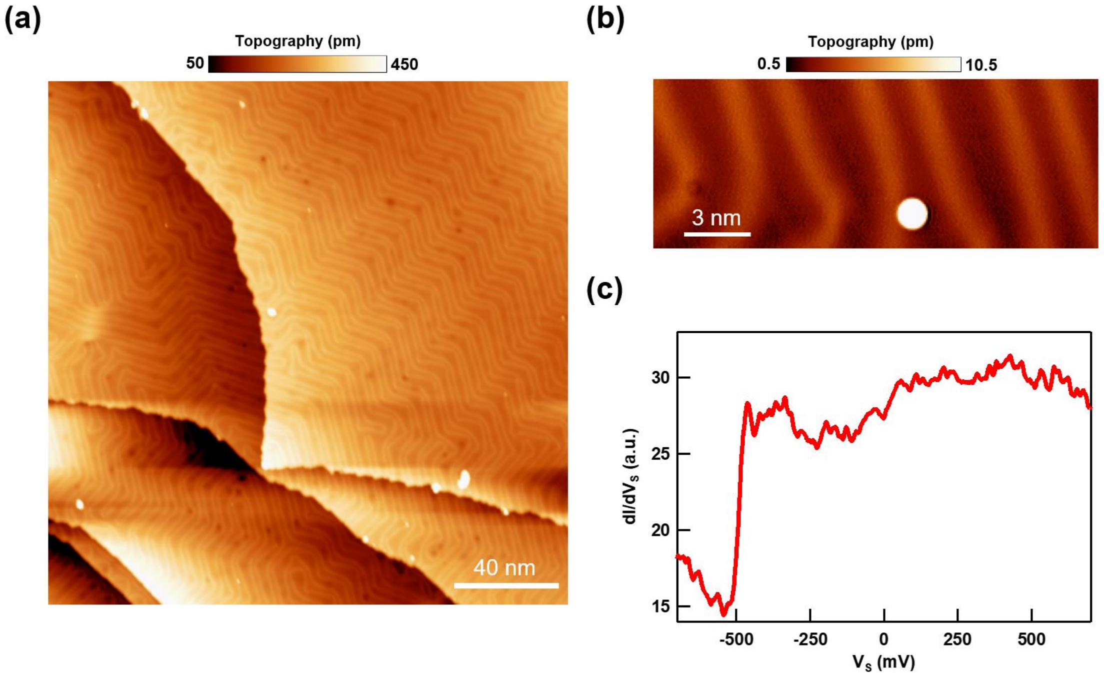

Figure 2.7 STM tip calibration on Au (111) surface. (a) A stable and well spatially resolved STM topography of the Au (111) surface. The zigzagging features are the surface reconstruction of the Au (111) surface. The set point used to acquire the topography was $I = 0.1$ nA, $V_S = -700$ mV. (b) STM topography after a 9 Å, 0.1 second poke, a circular protrusion was left on the Au (111) surface. The set point used to acquire the topography was $I = 0.05$ nA, $V_S = -700$ mV. (c) STS of the Au (111) surface with a well calibrated STM tip. The set point used to acquire the dI/dV_S spectrum was $I = 1$ nA, $V_S = -700$ mV with a 7 mV ac modulation.

2.2.2 Scanning Tunneling Spectroscopy (STS) and dI/dV_S Mapping

STS measurements is the major technique that I use to characterize the electronic structure of graphene QDs. As described in section 2.1.1, STS can probe the $LDOS$ of the sample with ultra-high spatial resolution, even atomically resolved $LDOS$ can be measured. Such capability of STS can provide valuable information of the electronic structure of graphene QDs that other experimental techniques cannot probe. In this section, I will briefly describe how we realize STS measurements and some other extended STS techniques such as gate resolved STS, spatially resolved STS and dI/dV_S mapping in our experiments.

According to Equation 2.2, the differential conductance dI/dV_S can provide $LDOS$ information of the sample. In experiments, we use a standard lock-in technique to measure the tunneling current I and dI/dV_S at the same time. In addition to the DC bias voltage V_S, we add a small AC modulation $\tilde{V}_{ac}$ to the bias voltage. As a result, the total tunneling current I will be

$$I\left(V_S + \tilde{V}_{ac}\right) \approx I(V_S) + \frac{dI}{dV_S}(V_S)\tilde{V}_{ac} \tag{2.4}$$

, which contains a DC current and an AC current. The AC current strength, which can be picked up by a lock-in, is proportional to the dI/dV_S value at V_S, so current I and dI/dV_S can be measured at the same time. In my experiments, the frequency of the AC signal I use is typically 704 Hz, and the time constant I choose on the lock-in is 30 ms. But if I notice the dI/dV_S signal picked up by the lock-in is too noisy, I usually will try adjusting the AC signal frequency or increasing the lock-in time constant to 100 ms.

For graphene QDs, it is useful to perform STS at different locations of the QDs and at different gate voltages (V_G). Two common STS measurements that I performed to characterize the electronic structure of graphene QDs are the gate resolved STS (which we usually call it gate sweep for simplicity) and spatially resolved STS along a line (which we usually call it line scan for simplicity). To perform gate sweeps, we typically keep the STM tip at the same location of the graphene QD while adjusting the applied V_G during the measurement. We automated such measurement by using a python script (see appendix A) that can control V_G and dI/dV_S spectra measurement. Then for the line scan, we normally keep V_G at a constant and perform a series of dI/dV_S spectra measurement along a line across the graphene QD, such a measurement is also automated by a python script that can control the tip position and dI/dV_S spectra measurement (see appendix A). By combining the ideas behind gate sweep and line scan, we can also do automated gate resolved line scan and spatially resolved gate sweep.

Another useful measurement for characterizing the electronic structure of graphene QDs is constant bias dI/dV_S mapping. The main idea behind such a measurement is that the $LDOS$ of a sample has a relation with its wavefunctions ψ as

$$LDOS(E,\vec{r}) = \sum_{\nu} |\psi_\nu(\vec{r})|^2 \, \delta(E - E_\nu). \tag{2.5}$$

As a result, we can get insight into the spatial distribution of graphene QD wavefunctions by performing constant bias dI/dV_S mapping. In experiment, when performing constant bias dI/dV_S mapping, we keep the applied V_S and the set point for current I a constant while recording the dI/dV_S signals picked up by the lock-in. We typically also use a python script (see appendix A) to automate a series of dI/dV_S mappings at different V_S or V_G. But one thing I want to point out is that with the constant current as feedback, because of the strong spatially varying $LDOS$ for graphene QDs, the tip sample distant z will not be a constant during the measurement according to Equation 2.1. Because of this, the constant bias dI/dV_S map $dI/dV_S(V_S,\vec{r})$ is not directly proportional to $LDOS(\mu + eV_S,\vec{r})$, instead

$$\frac{dI}{dV_S}(V_S,\vec{r}) \propto \frac{LDOS(\mu + eV_S,\vec{r})}{|\int_{\mu}^{\mu+eV_S} LDOS(E,\vec{r})dE|}. \tag{2.6}$$

As a result, regions with generally lower $LDOS$ can have unproportionally enhanced dI/dV_S signals in the constant bias dI/dV_S maps. This is an important consideration for our modelling of QD states. I will discuss this in more detail in chapters 4 and 6.

2.2.3 Magnetic Field Resolved STS

Using the capability of performing gate resolved and spatially resolved STS as discussed in section 2.2.2, a lot of information can be gained for graphene QD states with STM. As mentioned in section 2.1.2, our STM can also apply an external magnetic field up to the sample, this gives us one more tuning knob for studying graphene QD states. Compared to the gate sweep and line scan measurements as described in section 2.2.2, magnetic field resolved STS (which I call it B sweep) is less straight forward, so I decide to use an independent section to describe how we realize B sweep for graphene QDs in our experiments.

One reason why B sweep is more difficult to realize in our experiments is because the STM head will drift when the magnetic field is turned on and finally can touch the cryogenic box with a magnetic field as small as 0.2 T. This will bring in lots of mechanical vibration noise into the STM head and prevent us from doing measurements. We believe the movement in the STM is due to magnetic fields from other nearby components. As shown in Figure xxx, the superconducting magnet is attached to the STM head for our STM. As a result, when the magnetic field is turned on, the superconducting coil will interact with nearby magnetic materials such as the permanent magnets of the ion-pump in the STM chamber and drift away from its original position. We partially solve this problem by adding iron plates outside the STM chamber as shown in Figure 2.8 to counter the interaction between the superconducting magnet and other magnetic materials. With the configuration shown in Figure 2.8, we can increase the magnetic field up to 1.2 T without the STM head touching the cryogenic box.

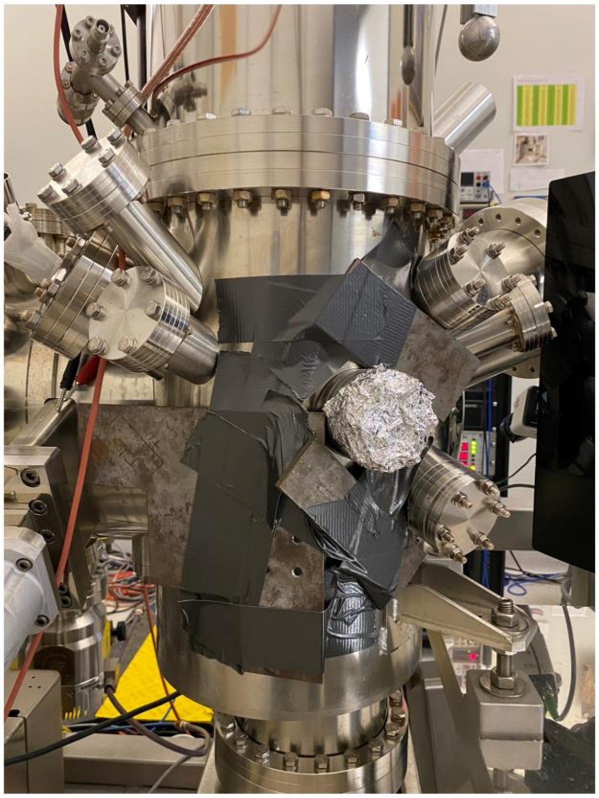

Figure 2.8 STM head drift correction. A photograph of the STM chamber with several iron plates attached to it, which can reduce the STM head drift when a magnetic field is applied.

Another reason B sweep is less straight forward to realize compared to gate sweeps and line scans is that the fine piezo in our STM responses to external magnetic field, which can cause a relative drift between the STM tip and sample in all x, y and z directions. But the good news is that such drift is systematic and not random, so we can correct these drifts during the measurement. For the drift in the z direction, the feedback system in the STM can automatically correct such drift in the constant current mode. But in gate sweep measurements, we still need to wait several seconds to let the STM tip position stabilize in the z direction due to the tip inertia before starting an STS measurement after every magnetic field change. For the drift in the x and y directions, I typically will first get the xy drift values in several magnetic fields by tracking the position change of some distinctive features on the sample. Then I will use these acquired xy drift values to correct the tip position during the B sweep measurement by assuming the xy drift is linearly changing between each tested magnetic field values. Similar to the gate sweep and line scan, B sweep in my experiments are also automated by a python script. Appendix A shows an example python script that can be used to perform B sweep measurement between 0 and 0.4 T for graphene QD states, which incorporated the ideas mentioned above to avoid the tip drift issue in a magnetic field.

2.3 In-situ Creation of Electrostatically Defined Graphene QDs

In section 2.2, we discussed several important STM measurement techniques that can be used to investigate the electronic structure and magnetic field response of graphene QDs. In this section, I will talk about how to in-situ create electrostatically defined graphene QDs that can be probed with these STM measurement techniques. Two in-situ graphene QD creation techniques were used in my PhD studies. One uses the local gating effect from the sharp STM tip to create graphene QDs, the other one uses localized boron nitride defect charges to electrostatically induce graphene QDs. Below, I will describe more details of these two techniques.

2.3.1 Tip Gating Induced Graphene QDs

The tip gating technique has been widely used in graphene QD STM experiments to locally create MLG QDs[50-52,55,59], BLG QDs[56] and TLG QDs[61]. In this section, I will briefly discuss the mechanism behind this technique and how to optimize tip-induced graphene QDs for measurements.

As schematized in Figure 2.9a, the sharp STM tip can serve as a local electrostatic gate and induce a local electrostatic doping profile $\Delta n(r)$ in the graphene sample right beneath the STM tip. This doping profile $\Delta n(r)$ can be thought of as an extra doping in addition to the global sample doping n_0 that can be controlled by a back gate. The depth and width of $\Delta n(r)$ depends on the tip apex shape, tip-sample work function difference and the V_S applied between the tip and sample. Typically, it is impossible to know the tip apex shape as a priori. But following the tip calibration procedure described in section 2.3.1, we can normally assume the tip apex has certain degree of circular symmetry, thus the tip-induced doping profile can be approximated as circularly symmetric. But for the depth and width of the doping profile $n(r)$, it can vary from experiments to experiments. Usually, it is more practical to treat them as some unknown parameters when doing theoretical modeling and tune these parameters to get the best fitting between experiment and theory.

Regardless of the details of the depth and width of tip induced doping profile $\Delta n(r)$, the back gate can be used to tune and optimize the depth and sharpness of the graphene QD confinement potential profile $U(r)$. After considering the back gate controlled global sample doping n_0, the total spatial doping profile can be approximated as $n(r) = n_0 + \Delta n(r)$. For graphene systems, they typically have the lowest density of states near the charge neutrality point. As a result, at locations where graphene is close to charge neutral ($n = 0$), the confinement potential will have the strongest response to doping change (i.e., $\partial\mu/\partial n$ is large). Because of this, as schematized in Figure 2.9b, with the same tip induced doping profile $\Delta n(r)$, sharpest and deepest confinement potential will be achieved when the global doping is tuned to a condition such that $n = 0$ crosses around the half-maximum of the spatial doping variation. This condition is equivalent to tuning the system to a circular p-n junction configuration. When global doping is over p-doped or over n-doped then p-n junction does not exist in the graphene system. In these cases, the confinement potential will be less deep and less sharp compared to the p-n junction scenario.

The creation and probing of tip-induced graphene QDs are relatively easy and straightforward, we simply perform a gate sweep measurement, then tip induced graphene QD states can be revealed in dI/dV_S spectra at gate voltages that give the optimal confinement potential for graphene QDs. Figure 2.3 shows an example gate sweep done on a pristine MLG area, bright and sharp features appear at V_G slight larger than zero, which corresponds to STM tip induced MLG QD states. But one obvious drawback of this technique is that we can only probe the QD states at the center of graphene QDs because of the mechanism of how such QDs are formed are tied to the tip and thus will move with the tip.

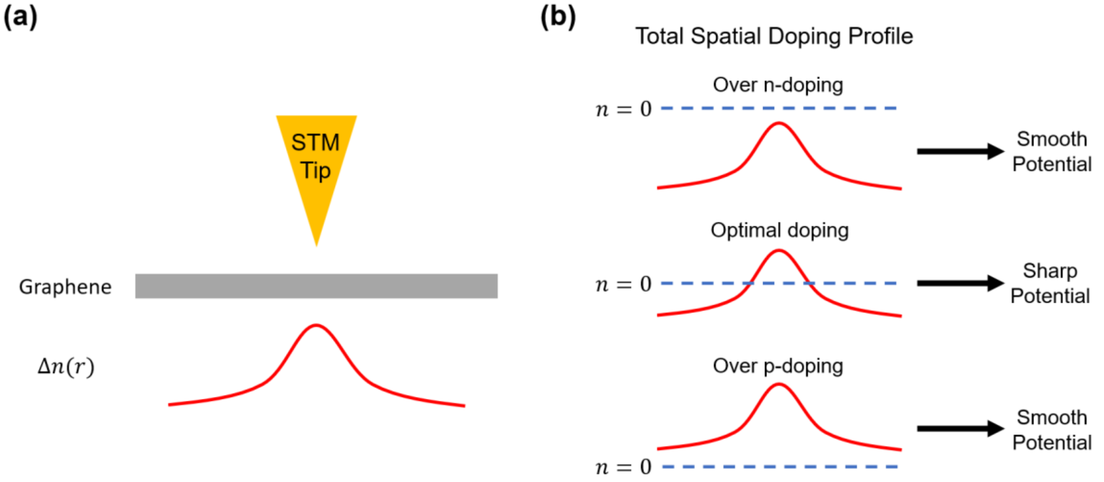

Figure 2.9 Tip induced local doping and optimizing graphene QD confinement potential. (a) Schematic of STM tip's local gating effect, which can induce a local doping profile beneath the STM tip in graphene systems. (b) Schematic of the doping condition that can result in sharper confinement potential for graphene QDs. The red line indicates the total spatial doping profile $n(r)$, the blue dashed line indicates the charge neutral line.

2.3.2 Hexagonal Boron Nitride (hBN) Defect Charge Induced Graphene QDs

As mentioned in section 2.3.1, one major drawback of using tip gating effect to create graphene QDs is that we are not able to probe the graphene QD states away from the dot center. But with hBN defect charge induced graphene QDs, such an issue can be avoided. In this section, I will describe how to in-situ create and optimize hBN defect charge induced graphene QDs with STM.

The creation of hBN defect charge induced graphene QDs involves a STM tip bias pulsing technique[53,114] that can ionize hBN defects and create nanometer scale localized hBN defect charges to electrostatically induce graphene QDs. This technique so far has been demonstrated to work with graphene/hBN heterostructures, I will give details on how to make such samples in chapter 3. Figure 2.10 shows the general procedure of how this STM tip bias pulsing works. As depicted in Figure 2.10a, the first step of this technique is to apply a large gate voltage (V_G) between the graphene sample and silicon back gate while the STM is in the constant current mode with the feedback loop closed. In the second step, we will open the feedback loop and lift the STM tip up from its original position by around 1 to 2 nm, then a large bias voltage (V_S~5 V) will be applied between the STM tip and graphene sample for 1 to 2 minutes. We call this step the tip bias pulsing. During this step, it is believed that hBN defects can be ionized by the large local electric field from the STM tip. But because of the back gate electric field, hBN defect charges can migrate and finally accumulate at the hBN/SiO_2 interface until the back gate electric field is fully screened by the accumulated hBN defect charges as depicted in Figure 2.10b. Based on this picture, one conclusion we can get is that the amount of accumulated hBN defect charges depends on the magnitude of V_G applied during the tip bias pulsing step. After the tip bias pulsing step, we will bring down V_S to its normal value and go back to the constant current mode with feedback loop closed. As depicted in Figure 2.10c, the accumulated hBN defect charges can create a local doping in the graphene sample. Then by adjusting the global sample doping level with back gate, we can finally achieve a p-n junction structure that can be used for graphene QD studies as depicted in Figure 2.10d. With well calibrated STM tips, graphene QDs with good circular symmetry usually can be created by this tip bias pulsing technique without much difficulty. One thing to note is that Figure 2.10 only depicted the p-type graphene QD creation. But by reversing the sign of applied V_G during the tip bias pulsing step, a n-type graphene QD can also be created.

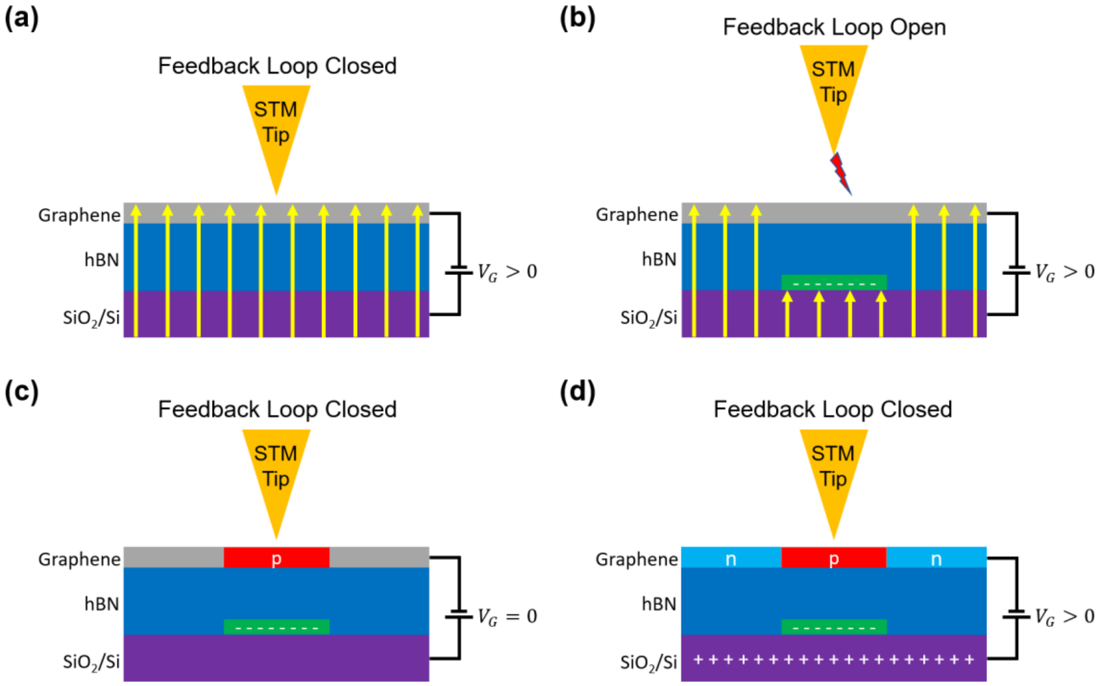

Figure 2.10 STM tip bias pulsing technique for graphene QD creation. (a)-(d) Schematic of the STM circuit and sample status before (a), during (b) and after (c-d) the tip bias pulsing. The yellow arrows depict the electric field between silicon back gate and graphene/hBN heterostructure. The lightning symbol depicts a bias pulse is applied. The green square depicts the accumulated hBN defect charges.

The tip bias pulse procedure described above involves only one time tip bias pulse, so I will refer to it as one-step tip pulsing technique from now on. This one-step tip pulsing technique was invented by my PhD advisor and his colleagues during his postdoc years while they were studying hBN defects with STM[114,115]. They first used this technique to in-situ create and probe MLG QDs with STM and successfully imaged the wavefunctions of MLG QD states[53], which was not achievable with tip-induced MLG QDs. Soon after, a research group at NIST picked up this technique and performed STM studies on hBN defect charge induced MLG QDs with magnetic fields, which resulted in many interesting discoveries[57,58,68]. Although the one-step tip pulsing technique worked relatively well for MLG QDs, people (which includes me) soon noticed difficulty extending this technique to created BLG QDs that can host clear QD states[64]. The major issue here is that due to the higher density of states and stronger screening of BLG compared to MLG, BLG QDs created by the one-step tip pulsing technique do not have deep and sharp enough confinement potential well to host well separated QD states.

In order to improve the depth and sharpness of the potential well of these tip bias pulsing created graphene QDs, we made two improvements to our experiments compared to those earlier related STM works. The first improvement we made is that we reduced the hBN thickness for our graphene/hBN heterostructures. Previous works used graphene/hBN devices with 60-100 nm thick hBN, but we reduced the hBN thickness down to 15-20 nm. This is motivated by the hypothesis that the tip bias pulsing created hBN defect charges are accumulated at the hBN/SiO_2 interface. With such an assumption, we expect using thinner hBN can reduce the distance between graphene sample surface and accumulated hBN defect charges, which should reduce the fringe electric fields between them and result in shaper potential change near the p-n junction boundary.

The second improvement we made is that we modified the one-step tip pulsing technique to a two-step tip pulsing technique. The general motivation behind this modification is to enhance the doping contrast inside and outside the graphene QDs, so that we can get deeper potential wells. Figure 2.11 shows the general idea behind this two-step tip pulsing technique. During the tip bias pulsing step, the tip-sample distance can affect the area size of accumulated hBN defect charges. In general, the closer the tip is to the graphene sample surface the larger graphene areas can be doped by the tip pulsing technique. Following this idea, we added a doping background creation step to the original one-step tip pulsing technique. For example, if we want to create a p-type graphene QD, we will first do a tip bias pulse at negative V_G with the tip relatively close to the sample surface, this can create a larger area of accumulated positive hBN defect charges during the tip bias pulsing step (Figure 2.11a) and result in a large n-doped graphene area after the tip bias pulsing step (Figure 2.11b). Then we will reverse V_G to positive values and do a second tip bias pulse, but this time the tip is lifted farther away from the graphene surface so that negative hBN defect charges can only accumulate in a smaller area (Figure 2.11c), which can give rise to a small p-doped graphene region surrounded by the larger n-doped graphene background created by the first tip bias pulse (Figure 2.11d). The advantage of this two-step tip pulsing technique compared to the one-step tip pulsing technique is that we can perform the tip pulsing step at relatively low gate voltages (for example, at -60 V and $+\ 60$ V), to achieve the same doping contrast inside and outside the graphene QD. Notably, we would need to apply a 120 V gate voltage with the one-step tip pulsing technique to achieve a similar effect. Graphene devices are much more susceptible to have dielectric breakdown issues at such high V_G, thus the two-step voltage pulsing technique enables access to new potentials.

With the combination of these two improvements, we are able to create graphene QDs with much deeper and shaper potential wells than earlier works. Such improvement of the graphene QD potential wells in our experiments enabled us to observe many new phenomena in MLG QDs, BLG QDs and TLG QDs. I will show some of our findings on hBN defect charge induced MLG QDs and BLG QDs in chapters 5,6 and 8. In addition, the enhanced potential well depth and sharpness also reduces the tip gating effect on the STM measurements of such hBN defect charge induced graphene QDs, which somewhat is a problem for such studies pointed out by some earlier works[59,69].

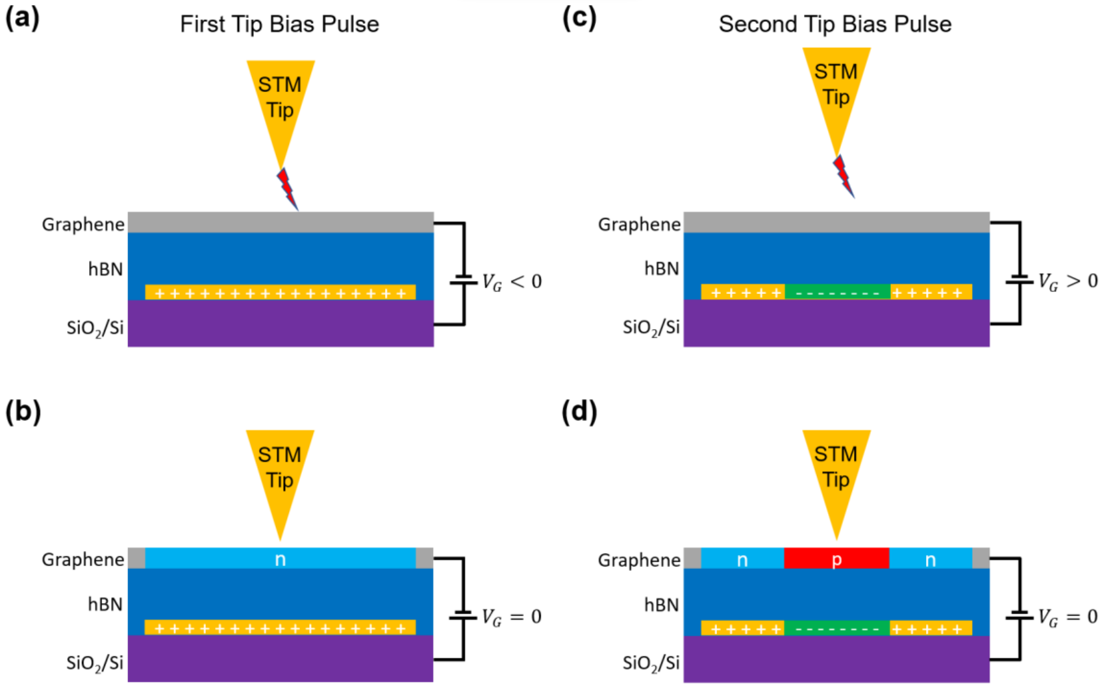

Figure 2.11 Two-step tip pulsing technique for p-type graphene QD creation. (a)-(b) Schematic of the STM circuit and sample status during (a) and after (b) the first tip bias pulsing. A large n-doped graphene area can be created after the first tip pulsing. (c)-(d) Schematic of the STM circuit and sample status during (a) and after (b) the second tip bias pulsing. A smaller p-doped graphene area surrounded by the n-doped background can be created after the second tip pulsing.

Chapter 3 Graphene Device Fabrication

As mentioned in section 2.3.2 of chapter 2, the STM tip bias pulsing technique for the in-situ creation of graphene QDs so far has only been demonstrated to work with graphene/hBN devices. In this chapter, I will briefly describe how to fabricate graphene/hBN devices that are suitable for graphene QD studies with STM.

3.1 Graphene/Hexagonal Boron Nitride (hBN) Heterostructure Assembly

The first step to make a graphene/hBN device is to fabricate a graphene/hBN heterostructure. In my experiments, I used a polymer-based Van der Waals 2D material stacking technique that was originally developed by Zomer[116] and revised by several elder PhD students in our research group[117,118] and other research groups[112] to fabricate graphene/hBN heterostructures for STM studies. This transfer technique involves a polymer named methyl methacrylate (MMA), so I will refer to this technique as MMA transfer technique. Below I will describe the details of this MMA transfer technique that I used in my experiments.

3.1.1 Substrate Preparation and Mechanical Exfoliation

The first step of this MMA transfer technique is to prepare graphene and hBN flakes, which will both be prepared by the standard mechanical exfoliation technique that uses the Scotch® Magic™ tape[75]. The hBN samples will be exfoliated on 285 nm SiO_2/Si substates as shown in Figure 3.1a, and the graphene samples will be exfoliated on MMA/transparent tape/glass slide substrates as shown in Figure 3.1b. I typically cut the SiO_2/Si substates to around 1 cm × 1 cm size and will rinse them with acetone and isopropyl alcohol (IPA) subsequently then blow dry them with nitrogen gas before using them for hBN exfoliation. Then the MMA/transparent tape/glass slide substate is prepared by spin coating a thin layer of MMA on top of hand-made transparent tape/glass slide substrate with a size of around $2.5\ \text{cm} \times 2.5\ \text{cm}$. During the spin coating step, I typically will drop 5 to 7 drops of MMA/methyl isobutyl ketone (MIBK) solution with a 1:12 mass ratio onto the transparent tape/glass slide substrate and try to evenly cover the whole substrate with MMA/MIBK solution, then I will start the spin-coating with a 1300 rpm rotation speed for 70 seconds. I typically will wait ~12 hours before using the freshly spin coated MMA/transparent tape/glass slide substrate for graphene exfoliation.

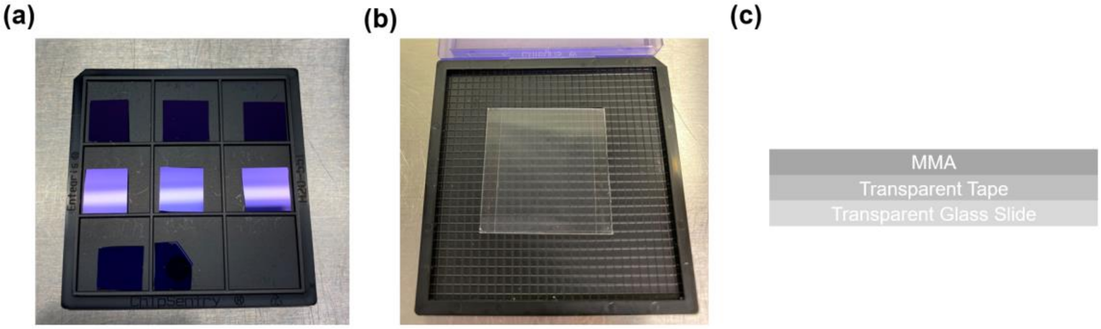

Figure 3.1 Prepared substrates for graphene and hBN exfoliation. (a) A photograph of cut and cleaned 285 nm SiO_2/Si substrate. (b) A photograph of transparent tape/glass slide substrate that is spin-coated with a thin layer of MMA. (c) Schematic side view of the of the MMA/transparent tape/glass slide substrate shown in (b).

Now I will briefly describe the mechanical exfoliation step for graphene and hBN samples. I will first describe the hBN exfoliation. I typically will grab 2 to 3 small hBN bulk parent crystals as shown in Figure 3.2a and put them onto an around 12 cm long Scotch® Magic™ tape to start the hBN crystal cleaving step. During the hBN cleaving step, I will try to evenly cover the hBN crystals over the tape with the least amount of tape folding. I noticed by limiting the tape folding number can help yield larger area hBN flakes during the exfoliation step. After the hBN cleaving step, I will gently press the scotch tape that is covered with hBN crystals onto as many prepared SiO_2/Si substrates as possible as shown in Figure 3.2b. Then I will use a cotton Q-tip to scrub over the SiO_2/Si substrates with a mild force several times before starting the hBN exfoliation. During the hBN exfoliation step, I usually try to separate the tape from the SiO_2/Si substrate slowly, which is believed to help get larger hBN flakes. It typically takes me around 5 seconds to complete this exfoliation step over one SiO_2/Si substrate. After this step, I will anneal these after exfoliation SiO_2/Si substrates in air at 500 ℃ for 2 hours. Then I will use an optical microscope to find hBN flaks that are suitable for my experiments. I typically use hBN flakes with a size larger than 50 μm × 50 μm and look blue and free of adsorbates in the optical microscope. Figure 3.2c shows an example identified hBN flake that is suitable for my studies.

The graphene exfoliation procedure, in general, is the same as the hBN exfoliation. I also use around 12 cm long Scotch® Magic™ tape to first grab some graphite from graphite parent crystals as shown in Figure 3.2e. But the graphite cleaving step is a bit different from the hBN cleaving step. During the graphite cleaving step, instead of trying to cover the whole scotch tape evenly with graphite crystals, I will observe the scotch tape under while light after every cleaving and try to identify spots with semi-transparent large grey area on the tape. Once such spot is identified, I normally will stop the graphite cleaving and press the scotch tape piece that contains the identified large grey spot onto the prepared MMA/transparent tape/glass slide substrate. Figure 3.2f shows an image of a scotch tape that contains such large grey spot (marked by a yellow circle) and is pressed onto an MMA/transparent tape/glass slide substrate. Similar to the hBN exfoliation, I will use a cotton Q-tip scrub over the scotch tape several times then slowly separate it from the MMA substrate. It typically takes me 45 to 60 seconds to complete this step. After this step, I will identify graphene flakes that are suitable for my experiments under an optical microscope. The layer number of the graphene flake can be extracted from the green color contrast between the sample and MMA substrate. For thin graphene samples, such green color contrast is linearly proportional to the graphene layer numbers, which is around 3.5% for each layer. I typically use graphene flakes that are larger than 50 μm × 50 μm and free of adsorbates for my experiments. Figure 3.2g shows an example identified BLG flake that is suitable for my experiments.

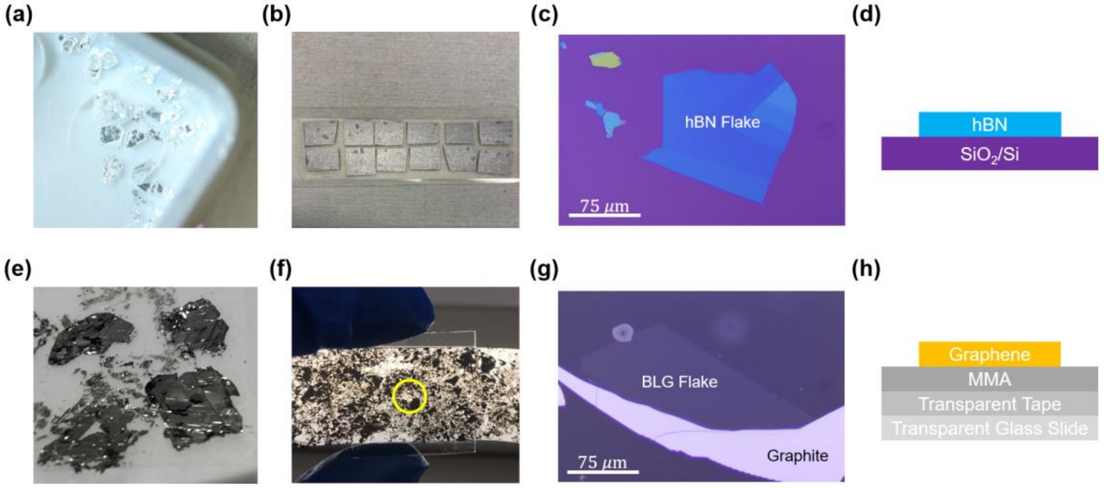

Figure 3.2 Graphene and hBN exfoliation. (a) A photograph of some bulk parent hBN crystals. (b) A photograph of a scotch tape after the hBN cleaving step that is pressed onto multiple SiO$_2$/Si substrates. (c) An optical microscope image of an identified hBN flake suitable for STM experiments. (d) Schematic of the side view of the sample shown in (c). (e) A photograph of some parent graphite crystals. (f) A photograph of a scotch tape after the graphite cleaving step that is pressed onto an MMA/transparent

tape/glass slide substrate. The yellow circle highlights the large semi-transparent grey graphite spot. (g) An optical microscope image of an identified BLG flake that is suitable for STM experiments. (h) Schematic of the side view of the sample shown in (g).

3.1.2 Graphene/hBN Stack Assembly

After getting the suitable graphene and hBN flakes, the next step is to stack them together. This step is the core of the fabrication of graphene/hBN heterostructures and realized with a stack assembly stage built by our lab. Figure 3.3a shows the structure of the stack assembly stage that I use. It mainly consists of three parts: Bottom sample stage, top sample stage and optics. The bottom sample stage is equipped with a Peltier pad, an XY micromanipulator, a rotation stage and two goniometers, which can be used to control the temperature of the sample holder, x and y positions of the sample, rotation of the sample and the tilting of the sample stage in the x and y directions, respectively. Then, the top sample stage is equipped with a hollow sample holder for optics purpose and an XYZ micromanipulator that can control the x, y and z positions of the top sample. Finally, the optics part includes an optical microscope and a CCD camera that is connected to a computer. This enables the visualization of micrometer scale samples during the stack assembly, which is crucial for the alignment of top and bottom samples and the control of the contact speed between the top and bottom samples.

After introducing the structure of the stack assembly stage, now I will briefly describe the procedure that I use to stack graphene and hBN flakes together. The first step I typically do is to adjust the alignment between the top sample holder plane and bottom sample holder plane to almost parallel by adjusting the two goniometers equipped on the bottom sample stage. After this, I will put the SiO_2/Si chip that contains the targeted hBN flake onto the bottom sample holder and fix the MMA/transparent tape/glass slide substrate that contains the targeted graphene flake onto the hollow top sample holder. Next, I will use the optical microscope to locate the targeted graphene and hBN flakes and bring them to roughly the same position, then I will bring them closer by lowering the top sample holder. After this, I will do some fine adjustments of the relative positions and rotations between the graphene and hBN flakes until they get into a desired configuration. Then I will keep bringing down the top sample holder until the MMA substrate touches the silicon chip, which can be easily determined by the color change of the silicon chip (from purple to yellow). After this, I will keep bringing down the top sample holder but very slowly and observe the movement of the contact front of the regions where the MMA substrate has touched the silicon chip at the same time until the contact front is about 50 to 100 μm to the targeted graphene and hBN flakes that are aligned but not in contact yet. Now, I will increase the bottom sample holder temperature to around 40 ℃ and wait until the contact front moves across the whole graphene and hBN flakes. At this point, the graphene and hBN flakes are already in contact with each other as schematized in Figure 3.3b. And Figure 3.3c shows an optical microscope image taken during the stack assembly step, which shows the BLG and hBN flakes shown in Figure 3.2 are brought into contact with each other. Then I will increase the bottom sample holder temperature to around 60 ℃ and wait about 5 minutes before turning off the heating and let the sample holder to cool down. Once the bottom sample holder temperature drops below 30 ℃, I will slowly bring up the top sample holder and make sure the MMA of stacked graphene/hBN area is always in contact with the silicon chip until the silicon chip is picked up by the MMA/transparent tape/glass slide substrate, which indicates the end of the graphene/hBN stack assembly step.

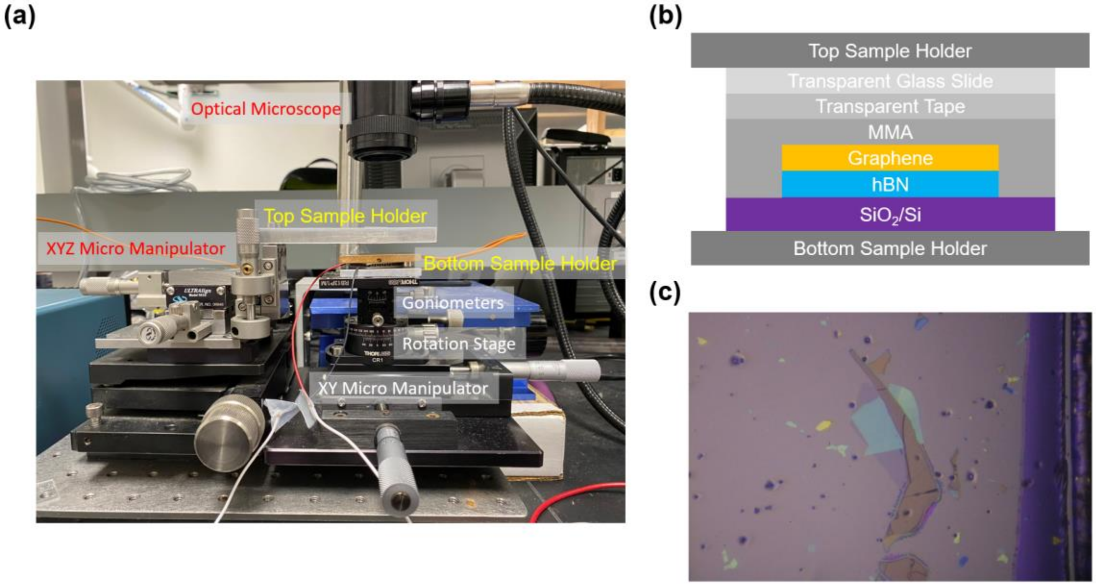

Figure 3.3 Graphene/hBN stack assembly. (a) A photograph of the stack assembly stage built in our lab. (b) Schematic of the side view of the graphene and hBN sample status when they are brought in contact during the stack assembly step. (c) An optical microscope image of the BLG and hBN flakes shown in Figure 3.2 are brought into contact with each other during the stack assembly step. Regions with yellow background in the image are the regions where MMA and silicon chip are in contact.

3.1.3 MMA Removal

After the graphene/hBN stack assembly step, the desired graphene/hBN heterostructure is still covered by MMA. In the next step, we will use dichloromethane (DCM) to dissolve the unwanted MMA layer. To do that, I typically will first put the MMA covered graphene/hBN stack into a room temperature DCM bath as schematized in Figure 3.4a and keep it there for at least 15 minutes. Then I will heat the DCM bath to around 50 ℃ and keep it at this temperature for around 15 minutes. After this, I will turn off the heat and let the DCM cool down for at least 15 minutes. Finally, I will bring the silicon chip out from the DCM bath. During this step, I will keep a steady flow of IPA solution rinsing over the silicon chip during the whole process and avoid the silicon chip getting dry with DCM solution on top. After these steps, the MMA layer should have mostly been removed, and we can get an exposed graphene/hBN heterostructure that rests on the SiO_2/Si substrate as schematized in Figure 3.4b. And Figure 3.4c shows an optical microscope image of the assembled BLG/hBN stack shown in Figure 3.3c after the MMA removal step, most of the BLG flakes in direct contact with the silicon chip as shown in Figure 3.3c has rolled up or been removed, which is very common.

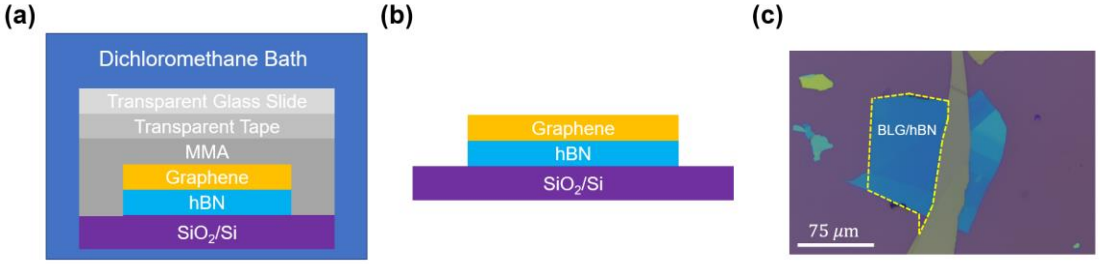

Figure 3.4 MMA layer removal. (a) Schematic of removing the MMA layer on top of the assembled graphene/hBN stack with a dichloromethane bath. (b) Schematic of the grapehen/hBN heterostructure after the MMA dissolving step in DCM bath. (c) An optical microscope image of the assembled BLG/hBN stack shown in Figure 3.3c after the MMA dissolving step in DCM. The area encircled by a yellow dashed line indicates the BLG/hBN heterostructure area.

3.1.4 MMA Pick-up Technique

So far, I have discussed the original MMA transfer technique that was developed earlier. During my PhD study, I discovered an alternative of this MMA transfer technique, which I will refer to as MMA pick-up technique. The main difference between the original MMA transfer technique and the MMA pick-up technique is in the sample contact step. For the original MMA transfer technique, the bottom sample holder is heated first to 40℃ then to 60 ℃ during the sample contact step. But for the MMA pick-up technique, the bottom sample holder is kept below 20℃ and we will only use mechanical force to push forward the contact front. This change has a significant consequence on how strongly the MMA is stuck to the silicon chip. Following the original MMA transfer technique, MMA will stick very well to the silicon chip and cannot be easily separated from the silicon chip again. But following the MMA pick-up technique, the MMA only weakly sticks to the silicon chip and can be easily removed from the silicon chip again. This change together with many other recently developed 2D material pick-up techniques[119,120] motivated me to try using the Van der Waals force between 2D materials to use a 2D material on the MMA substrate to pick up another 2D material on the silicon chip, and it turned out works.

Figure 3.5 schematized the fabrication of a graphene/hBN heterostructure with the MMA pick-up technique. A double side tape is added between the silicon chip and bottom sample holder so that the whole silicon chip will not be picked up during the separation of MMA from the silicon chip, which is another modification to the original MMA transfer technique. In order to make a graphene/hBN heterostructure that rests on a SiO_2/Si substrate as shown in Figure 3.4b, we can follow the original MMA transfer technique to transfer the picked-up graphene/hBN heterostructure onto the silicon chip. For the fabrication of graphene/hBN heterostructures, this MMA pick-up technique does not have much advantage compared to the original MMA transfer technique. But if we want to study more complex heterostructures such as heterostructures involving multiple layers of different materials or twist-angle controlled samples, the MMA pick-up technique can provide some advantages. With the MMA transfer technique, we need to go through the polymer dissolving step after every time we stack two materials together. As a result, if we want to add a third layer on top of the fabricated 2D material stack as shown in Figure 3.4b, the interface between the third layer material and the original 2D material stack can have a lot of contamination from the MMA residue. But with the MMA pick-up technique, we will not have such an issue because all the interfaces of the fabricated 2D material stack will never been exposed to MMA.

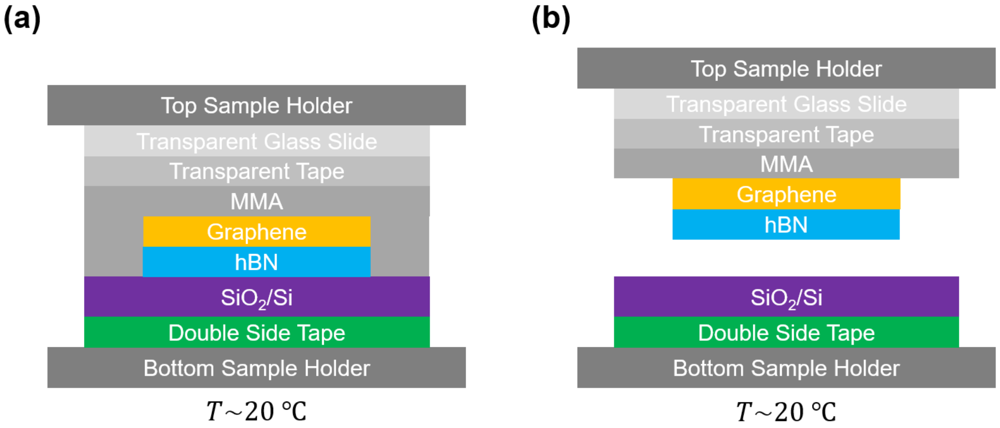

Figure 3.5 Graphene/hBN stack assembly with MMA pick-up technique. (a) Schematic of the setup of the MMA pick-up technique when graphene and hBN flakes are brought into contact. The bottom sample holder is kept at around 20 °C. (b) Schematic of a hBN flake is picked up from the silicon chip by a graphene flake on the MMA substrate by separating the MMA from the silicon chip after the graphene and hBN flakes have made contact.

3.2 Electrode Fabrication and Sample Mounting

After getting the graphene/hBN heterostructure, we need to fabricate electrical contacts to make it into a device. For STM studies, we only need two electrical contacts. One contact is to graphene, which is for applying the bias voltage between the STM tip and graphene. The other contact is to silicon back gate, which is for applying the back gate voltage between the silicon back gate and graphene. I will first describe how we make the electric contact for graphene. Instead of using the more conventional e-beam lithography to pattern electrical contacts to graphene samples, we use a commercial metal stencil mask[121,122] to do that. The main reason for this choice is to help improve the surface cleanness of the graphene/hBN sample because with the stencil mask technique we can avoid the graphene surface being exposed to polymer resists. Figure 3.6 shows the general procedure of how we fabricate electrical contact to graphene. We first locate the target graphene/hBN heterostructure through the hole of the stencil mask, then we adjust the stencil mask to a position such that only a small corner of the graphene/hBN sample is exposed to the hole of the stencil mask. Then we evaporate a thin layer of chromium (Cr) and gold (Au) subsequently through thermal evaporation. I typically evaporate a 7 nm thick Cr and 100 nm to 200 nm thick Au. After this step, the stencil mask can be removed, and an electrical contact has been made to the graphene/hBN sample.

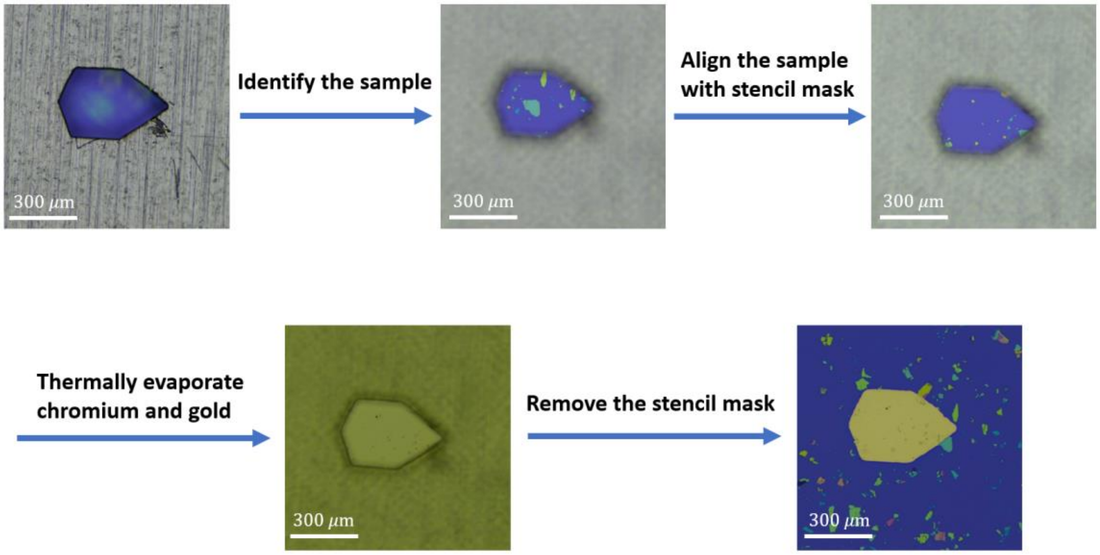

Figure 3.6 Procedure of making electrical contacts to graphene/hBN heterostructure with a stencil mask.

Before showing the how we make the electrical contact to the silicon back gate, I will show how we mount the graphene/hBN device onto the STM sample holder. Figure 3.7 shows a graphene/hBN device mounted onto the STM sample holder. We use a metal clamp to mechanically fix the graphene/hBN sample onto the STM sample holder. Normally, the touching point between the silicon chip edges and the metal clamp (the red circled area in Figure 3.7) will have electric contact that is good enough for a back gate. As a result, we do not have to make an additional electrode for applying gate voltages. We can directly apply the gate voltage through the metal STM sample holder. Then for applying bias voltages, we connect the evaporated Cr/Au electrode to one of the STM electrode pad through wire bonding, then V_S can be applied through there. We find it is very difficult to bond wires to the metal/ceramic electrode pad provided by Createc, so we typically stick a tantalum foil (marked by the green circle in Figure xxx) onto the electrode pad with silver paste. It is very easy to wire bond to the tantalum foil.

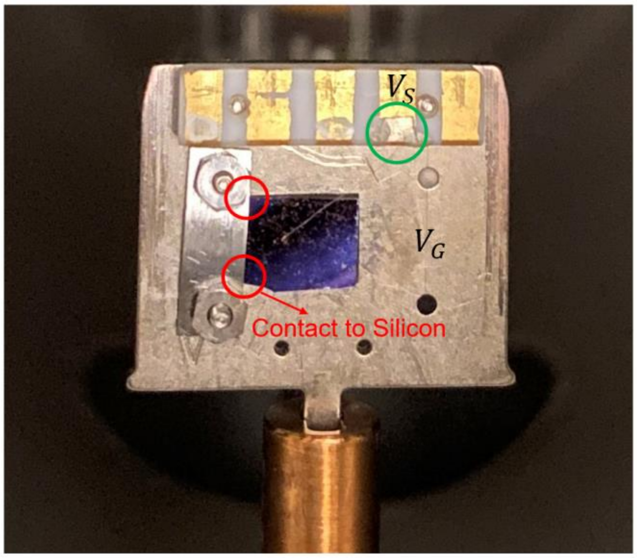

Figure 3.7 Graphene/hBN sample mounting onto the STM sample holder.

3.3 Sample Surface Cleaning

Sample surface cleanness is crucial for STM experiments as STM is an extremely sensitive surface probe, any adsorbates on the sample surface can affect the experimental results or even prevent the STM experiments from starting. Because of this reason, one important step toward the successful execution of STM graphene QD studies is to obtain large adsorbates free graphene surfaces. In this section, I will briefly describe the procedures we take to improve the surface cleanness of fabricated graphene/hBN devices.

3.3.1 Ar/H_2 Annealing

Although most MMA can be removed from the graphene surface after the MMA removal step described in section 3.1.3, we find a few nanometers thick MMA layer usually will remain on the graphene surface and cannot be dissolved, possibly due to the strong bonding between graphene and MMA. This is a well-known issue when graphene surface has been exposed to polymers, but previous studies demonstrated Ar/H_2 annealing can help remove this type of thin layer of polymer residue on the graphene surface[123]. Figure 3.8 shows an early day result that I got during the second year of my PhD study while I was testing the Ar/H_2 annealing for graphene/hBN samples. It shows a comparison between the typical AFM topography image of the same graphene/hBN sample before and after 3 hours of annealing in a 10% H_2 concentration Ar/H_2 forming gas at 340 ℃. As shown in Figure 3.8a, the graphene surface is typically very rough caused by the MMA residue layer, the surface topography root mean square (RMS) is typically above 350 pm for a $200\ \mathrm{nm} \times 200\ \mathrm{nm}$ window. As shown in Figure 3.8b, after the Ar/H_2 annealing, lots of MMA residue starts to be removed from the graphene surface. The graphene surface RMS can go down to around 60 pm for a $200\ \mathrm{nm} \times 200\ \mathrm{nm}$ window in those polymer-free region. By annealing the graphene/hBN sample in Ar/H_2 forming gas at higher temperatures and longer time, we can get a more complete removal of the MMA residue. Now, I typically anneal the graphene/hBN samples in Ar/H_2 forming gas at 400℃ for 12 to 16 hours. In addition, I typically will ramp up the temperature from room temperature to 400 ℃ in 3 hours, and let the furnace cool down from 400 ℃ to room temperature longer than 3 hours. In addition to the surface polymer removal during the Ar/H_2 annealing process, high temperature annealing can also improve the graphene/hBN interface quality though the self-cleansing mechanism[124]. Basically, the randomly distributed interface adsorbates can move and be concentrated to a few locations after the high temperature annealing as shown in Figure 3.9. Randomly distributed small blisters at the graphene/hBN interface before Ar/H_2 annealing (Figure 3.9a) are concentrated to fewer spots on the sampler after Ar/H_2 annealing (Figure 3.9b). This interface self-cleansing process is also very important for getting large atomically flat graphene/hBN heterostructure areas.

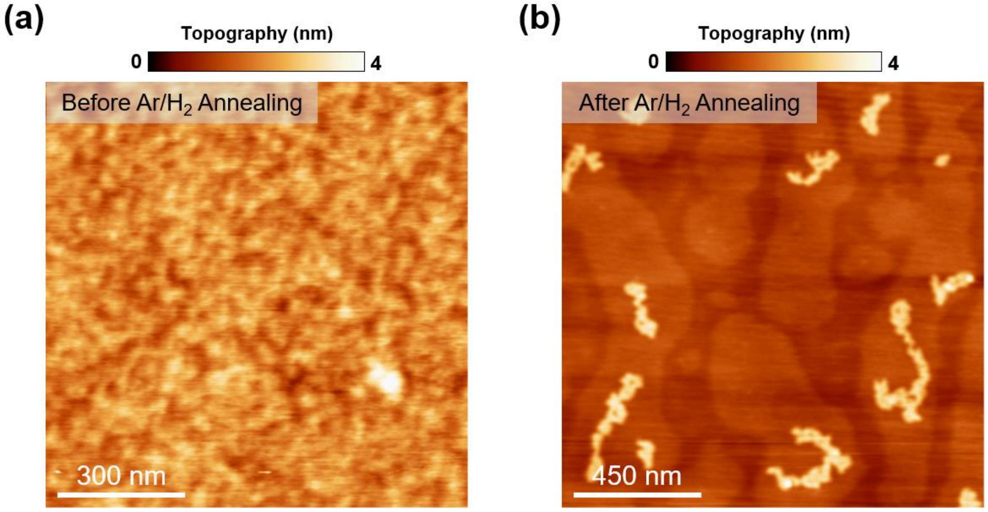

Figure 3.8 MMA polymer residue removal through Ar/H_2 annealing. (a) A typically AFM topography of the graphene surface before Ar/H_2 annealing. (b) An AFM topography of the graphene surface after Ar/H_2 annealing showing the removal of MMA residues. The annealing was done in a 10% H_2 concentration Ar/H_2 forming gas at 340 ℃ for 3 hours. AFM topography in (a) and (b) were both taken by the non-contact AFM mode of an Asylum Research Cypher-S AFM from Oxford Instruments.

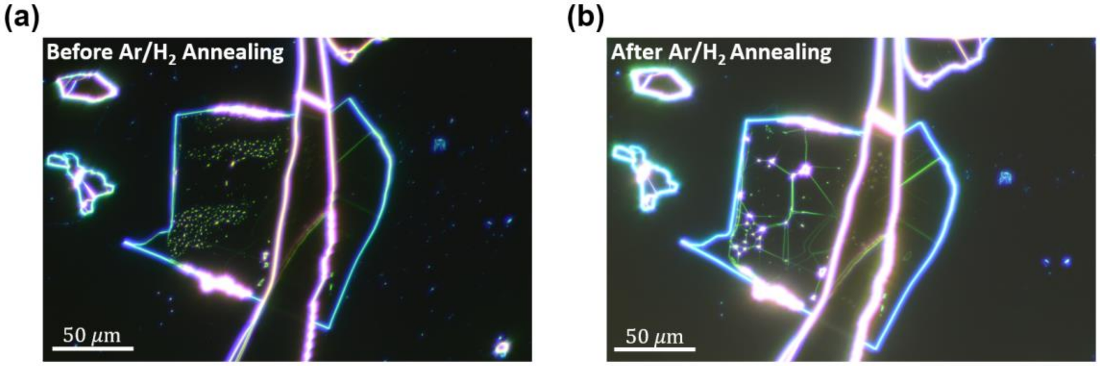

Figure 3.9 Graphene/hBN interface self-cleansing. (a)-(b) Dark field optical microscope images of the same BLG/hBN heterostructure shown in Figure 3.4c before (a) and after (b) 400 ℃ Ar/H_2 annealing.

3.3.2 AFM Tip Cleaning

Although the Ar/H_2 annealing process can remove a lot of MMA surface residues on the graphene/hBN heterostructures, we find somehow it is still not enough to enable us to easily find large atomically flat graphene/hBN heterostructure areas in STM. Earlier studies demonstrated by sweeping the graphene surface with an AFM tip thought the contact AFM mode can further remove surface polymer residues and improve interface quality[122,125]. So after the Ar/H_2 annealing step, we perform sequential scans in contact mode with a setpoint of 0.2 V, scanning speed of ~15 μm/sec, and 1024×1024 pixels resolution to sweep one or multiple $30\ \mu m \times 30\ \mu m$ regions of the graphene/hBN heterostructure by an Asylum Research Cypher-S AFM from Oxford Instruments with Econo-ESP-Au tips (spring constant $\sim 0.2\ N/m$) from Oxford Instruments. Figure 3.10 shows a comparison between the contact mode AFM topography acquired from the first pass and the 13th pass during the ATM tip cleaning process of the BLG/hBN sample shown in Figure 3.4c. Clear streaky features due to surface polymer residues appear in the AFM topography from the first pass (Figure 3.10a), but such streaky features disappeared in the AFM topography from the 13th pass (Figure 3.10b), which is an indication of further surface polymer residue removal.

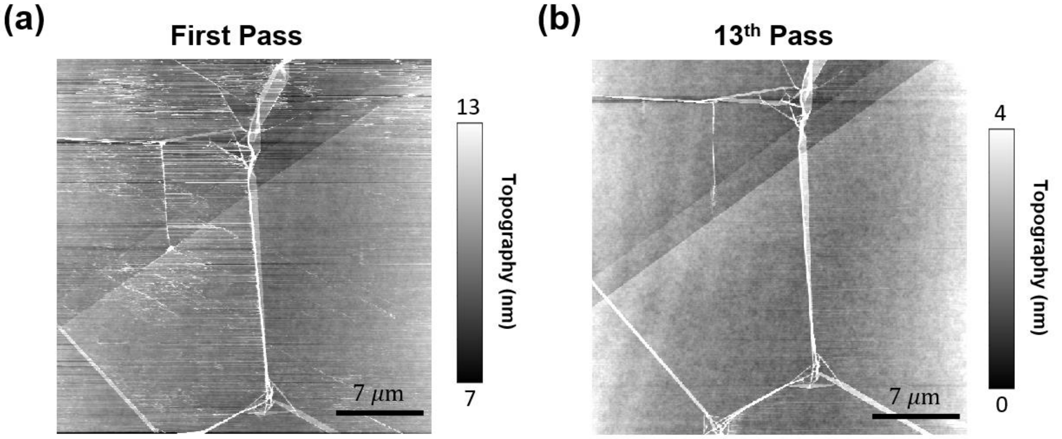

Figure 3.10 Contact mode AFM topography evolution during the ATM tip cleaning process. (a) Initial AFM topography acquired through AFM contact mode, denoted as first pass. (b) AFM topography acquired though contact mode during the 13th pass at the same region that is shown in (a).

3.3.3 UHV Annealing

After the AFM tip cleaning process, we are close to the end of the surface cleaning process for graphene/hBN samples for STM studies. Next, we will mount the graphene/hBN device onto the STM sample holder as shown in Figure 3.7 and bring it into UHV. Then we will do a final round of annealing in UHV as shown in Figure 3.11a at 400 ℃ for 6 to 10 hours in the preparation chamber of our STM system. Typically, the preparation chamber pressure can spike to as high as around 3×10^{-8} mbar at the beginning of the UHV annealing, but such high pressure normally will only last several tens of minutes, and very quickly the preparation chamber pressure can drop back to the 10^{-9} mbar range. Typically, the preparation chamber pressure can drop below

3×10^{-10} mbar at the end of the UHV annealing process. After the UHV annealing, we can finally bring the sample into the STM chamber and perform graphene QD studies. Figure 3.11b shows a photograph of the STM tip approached on the BLG/hBN sample shown in Figure 3.4c. With the high spatial resolution of our STM's optical setup, we can target the STM tip to land on those AFM tip cleaned areas, which is very helpful. With a good sample, we can typically land the STM tip on an at least $200\ \text{nm} \times 200\ \text{nm}$ atomically flat area with one or two attempts. The high cleanness of our graphene/hBN samples contributed a lot to preserving the calibrated STM tip status, which I believe contributed a lot to the high quality of the STM data we can get on graphene QD measurements.

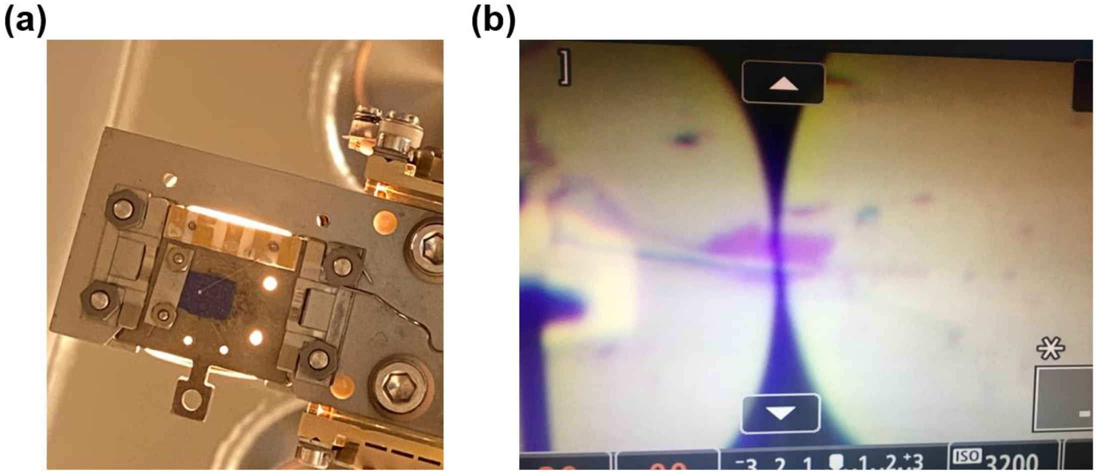

Figure 3.11 UHV annealing and STM tip approach for graphene/hBN devices. (a) A photograph of a graphene/hBN devices mounted on the STM sample holder is under 400 ℃ UHV annealing in the preparation chamber. (b) A photograph of the STM tip is approached to a adsorbates free area on the BLG/hBN sample shown in Figure 3.4c.

Chapter 4 Graphene QD Simulation

In chapter 2 and chapter 3, I discussed the experimental tools and techniques that I used to investigate graphene QDs. In this chapter, I will briefly describe how to numerically simulate graphene QD systems so that we can compare experimentally acquired data with theoretical results. Throughout my PhD this has proven to be a powerful tool for understanding the physics behind our experimental observations.

4.1 Tight-binding Model of Graphene QDs

As discussed in chapter 1, the electronic structure of graphene systems can be described by TB model. By a slight modification, graphene TB model can also be used to describe electrostatic graphene QDs. To achieve this, we modify each carbon atom's onsite energy according to graphene QD's confinement potential well. Taking MLG QD as an example, its TB Hamiltonian can be written as

$$H = \sum_{i} V(\vec{R}_i^A) a_i^{\dagger} a_i + \sum_{i} V(\vec{R}_i^B) b_i^{\dagger} b_i - \sum_{<i,j>} \gamma_0 (a_i^{\dagger} b_j + b_j^{\dagger} a_i) \qquad (4.1)$$

Here $a_i^{\dagger}(a_i)$ and $b_i^{\dagger}(b_i)$ are the creation (annihilation) operators for electrons on sublattice A and B at site $\vec{R}$, respectively. γ_0 is the nearest neighbor hopping parameter for MLG, and $< i, j >$ denotes only the nearest neighbor hopping is considered. The electrostatic MLG QD can be defined through varying the onsite energy V of carbon atoms at position $\vec{r} = \vec{R}_i$ according to its electrostatic confinement potential well $V(\vec{r})$. By replacing $V(\vec{r})$ to a constant, the MLG QD TB Hamiltonian will reduce to the MLG TB Hamiltonian. In this special case, the system preserves translational symmetry so its eigen wavefunctions can be described by Bloch states. This enabled us to reduce the

MLG TB Hamiltonian to a 2×2 matrix with crystal momentum $\vec{k}$ as a variable. Such a procedure can also reduce the BLG and TLG TB Hamiltonian to a 4×4 and 6×6 matrix, respectively. The small matrix size of MLG, BLG and TLG TB Hamiltonians made it computationally not difficult to get their eigen energies and eigen wavefunctions. However, in the graphene QD case, $V(\vec{r})$ is not a constant anymore and the system lacks translational symmetry. As a result, we are not able to reduce the graphene QD TB Hamiltonian to a small matrix by utilizing Bloch states as in the pristine graphene cases. Instead, the matrix size of the graphene QD TB Hamiltonian can be extremely large. For example, the matrix size can be around $30\, million \times 30\, million$ for an electrostatic MLG QD defined on a finite MLG mesh with 500 nm radius. Now, it is not trivial to solve such graphene QD TB Hamiltonians with giant matrices. But luckily, there already exists algorithms[126,127] and packages[102,128,129] to handle such giant Hamiltonian quantum systems. Benefited from this, I was able to use a python package named Pybinding[102], which has the kernel polynomial method[127] implemented into it, to simulate different types of graphene QD systems based on their TB models. Such numerical simulation capability provided tremendous help to the understanding of our experimental observations. Below, I will give a brief description of how to use this package to simulate the LDOS of MLG QDs, BLG QDs and TLG QDs. More details about the Pybinding package can be found in the PhD thesis of the author of this package[130].

4.1.1 Building A Graphene Mesh

The first step to use Pybinding to simulate graphene QDs is to create a finite size graphene mesh. We can use the Lattice function of the Pybinding package to define the primitive lattice vectors, sublattices and hopping terms of the graphene system we want to build. Below is an example code that defines the MLG TB model.

```
def monolayer_graphene():
   a = 0.24595   # [nm] unit cell length
   a_cc = 0.142  # [nm] carbon-carbon distance
   t0 = -3.03      # [eV] nearest neighbour hopping
   lat = pb.Lattice(a1=[a, 0],
                    a2=[a/2, a*sqrt(3)/2])
   lat.add_sublattices(('A', [0.1*a_cc, -a_cc+0.1*a_cc, 0]),
                       ('B', [0.1*a_cc, 0.1*a_cc, 0]))
   lat.add_hoppings(
      # inside the main cell
      ([0,  0], 'A', 'B', t0),
      # between neighboring cells
      ([-1, 1], 'B', 'A', t0),
      ([0, 1], 'B', 'A', t0),
   )
   lat.min_neighbors = 2
   return lat
```

Figure 4.1a shows the MLG lattice defined by the code above, $\vec{a}_1$ and $\vec{a}_2$ are the primitive lattice vectors of MLG, and the two sublattices of MLG are labeled as A and B. Next, we can use the Model function in Pybinding package to define a finite size graphene mesh, the mesh shape and size can be arbitrary defined. And this function will also automatically create the associated TB Hamiltonian of the defined graphene mesh. Figure 4.1b,c shows two example meshes that can be defined in the Pybinding package using the code showed below, one is a 5 nm × 5 nm MLG mesh (Figure 4.1b), and the other one is circular MLG mesh with 5 nm radius (Figure 4.1c).

```
# Create a 5nm x 5nm square mesh
def rectangle(width, height):
    x0 = width / 2
    y0 = height / 2
    return pb.Polygon([[x0, y0], [x0, -y0], [-x0, -y0], [-x0, y0]])
model = pb.Model(monolayer_graphene(), rectangle(width=5, height=5))

#Create a 5 nm radium circular mesh
def circle(radius):
    def contains(x, y, z):
        return np.sqrt((x/1)**2 + y**2) < radius
    return pb.FreeformShape(contains, width=[2*radius, 2*radius])
model = pb.Model(monolayer_graphene(), circle(radius=5))
```

In actual electrostatic graphene QD simulations, I typically use a circular graphene mesh with several hundred nanometers radius to avoid the mesh boundary's effect on the graphene QD defined at the mesh center. Taking similar procedures, we can also define a finite size BLG sheet and TLG sheet with the Pybinding package, example codes can be found in Appendix B.

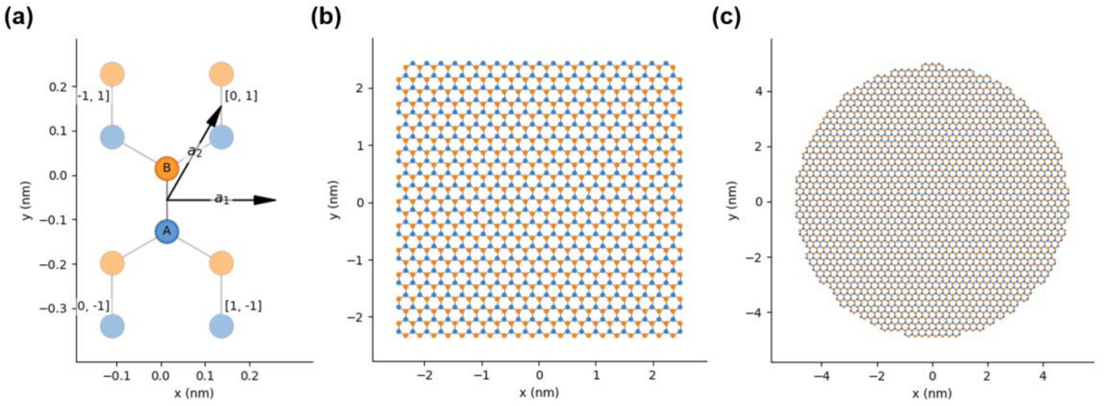

Figure 4.1 Define finite size MLG mesh in Pybinding. (a) The MLG lattice defined in Pybinding. (b) A 5 nm × 5 nm square MLG mesh defined in Pybinding. (c) A 5 nm radium circular MLG mesh defined in Pybinding.

4.1.2 Define the Graphene QD

After building a finite size graphene mesh, the next step to simulate graphene QDs with the Pybinding package is to define the electrostatic graphene QD that we want to simulate in the finite size graphene mesh. This can be done by using the onsite_energy_modifier function of the Pybinding package to adjust the onsite energy of the graphene mesh's carbon atoms according to the electrostatic confinement potential well of the graphene QD that we want to simulate. To match the simulation conditions with experiments, I typically will use the extracted confinement potential well from experimental line scan data to define the graphene QD potential well in the simulation. Taking BLG QD as an example, Figure 4.2 shows an experimentally measured dI/dV_S spectra along a line across the center of an hBN defect charge induced BLG QD. From such data, we can extract the potential well and band gap of the BLG QD. Then we can implement the extracted potential well and band gap to the BLG QD model with the following code:

```
f='BLG_Potential.txt'
            aa = np.loadtxt(f, skiprows=0, usecols=(0)) #distance (nm)
            b = np.loadtxt(f, skiprows=0, usecols=(1))*1+0.015 #potential (eV)
def wavy(delta):
    @pb.onsite_energy_modifier
    def f(sub_id,x,y):
        p=0
        u=0
        r=np.sqrt(x**2+y**2)
        for i in range(0,len(aa)-1,1):
            u=u+(np.heaviside(r-aa[i],0.5)+np.heaviside(aa[i+1]-r,0.5)-1)*((r-
aa[i])*(b[i+1]-b[i])/(aa[i+1]-aa[i])+b[i])
        if sub_id == 'A1':
            return delta + u
        if sub_id == 'B1':
            return delta + u
```

```
        if sub_id == 'A2':
            return -delta + u
        if sub_id == 'B2':
            return -delta + u
    return f
model = pb.Model(bilayer_graphene(), circle(radius=250), wavy(delta=0.03))
```

The code above defines a BLG QD with a potential well extracted from Figure 4.2 and a band gap of 60 meV on a 250 nm BLG mesh. Here the BLG_Potential.txt file saves the extracted BLG QD potential, and A_1, B_1 and A_2, B_2 are the BLG sublattices on the top layer and bottom layer of BLG, respectively.

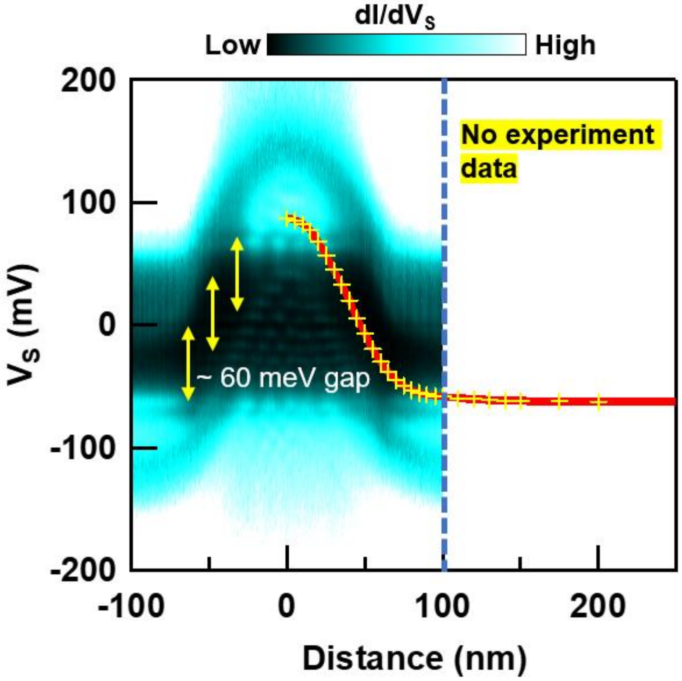

Figure 4.2 Extracting potential well and band gap of BLG QDs. dI/dV_S spectra along a line that crosses the center of a BLG QD. The yellow crosses and the red curve correspond to the extracted potential profile of the BLG QD at $V_G = -5$ V. The potential profile outside 100 nm is extrapolated from the tendency of the extracted potential profile from center to 100 nm. The yellow double-sided arrows indicate the size of the band gap of the BLG QD at $V_G = -5$ V. The STS set point used to acquire the data was $I = 1.5$ nA, $V_S = -200$ mV with a 3 mV ac modulation.

4.1.3 $LDOS$ Calculation

As mentioned earlier, Pybinding has the kernel polynomial method[127] included in its package. Kernel polynomial method can calculate a large quantum system's $LDOS$ in the whole energy range but only at one real space location at a time. One main advantage of the kernel polynomial method is its computational efficiency because of its high numerical stability, the computational time with this method scales linearly with the sparse matrix size[130]. But kernel polynomial method is an approximate technique and cannot give exact eigenvalue and eigenstate solutions. An energy broadening to the $LDOS$, which is defined by the user, is always included in the calculation. This is different from the Lanczos method[126,128], which is another algorithm commonly used for solving large sparse matrix but can give exact eigenvalues and eigenstates. But the Lanczos method has lower computational efficiency compared to the kernel polynomial method due to the numerical instability of this algorithom[130]. In addition, for large sparse matrix, the Lanczos method typically is used to calculate the exact eigenvalues and eigenstates in a narrow energy range, which is not quite compatible with the nature of STS data. With all these considerations, the kernel polynomial method is a more suitable algorithm for solving graphene QD TB Hamiltonians to compare with experimental STM graphene QD data.

To implement the kernel polynomial method for solving the $LDOS$ of a defined graphene QD, we can conveniently use the kpm.calc_ldos() function in the Pybinding package. An example code is given below:

```
kpm = pb.kpm(model)
```

```
ldos = kpm.calc_ldos(energy=np.linspace(-0.2, 0.2, 2000), broadening=0.002, position=[0,0])
```

Here ‘model’ is the graphene QD TB Hamiltonian, which we discussed how to define in Pybinding in section 4.1.2. With the above code, the $LDOS$ at the graphene QD center in energy range -200 meV to 200 meV with a 2 meV energy broadening will be calculated.

A very nice feature of the kernel polynomial method is that the calculation of $LDOS$ at different locations can be easily parallelized for computation, which can significantly reduce the computation time needed to get a full spatially and energetically resolved $LDOS(E, r)$ for the simulated graphene QD. I use the ‘Pool’ function of the multiprocessing package included in Python to implement the parallel computation. Example full codes for simulating spatially resolved $LDOS$ spectra along a line across the QD center with parallel computing for MLG QDs, BLG QDs and TLG QDs are included in Appendix B. I typically do such simulations on the Hummingbird Computational Cluster[131] at UCSC with 24 to 72 CPUs for each simulation. By assembling the calculated $LDOS$ at different locations and different energies together, we can get simulated $LDOS$ spectra along a line and $LDOS$ map at a constant energy, which can be used to compare with experimentally measure line scan data and dI/dV_S map data for graphene QDs. But when comparing these data, especially between simulated $LDOS$ maps and experimentally measure dI/dV_S maps, we need keep in mind that to get a better matching between experiments and simulations, the simulated $LDOS$ map need to be adjusted according to Equation 2.6 to compensate the tip-sample distance change effect during the dI/dV_S map measurements as discussed in section 2.2.2. Examples of such $LDOS$ map intensity adjustments to get better matching between experiments and simulations can be found in chapter 6 and chapter 8.

4.1.4 Magnetic field simulation

The graphene TB QD model can also be used to simulate magnetic field effects. This can be done through the Peierls substitution[130,132] for hopping parameters t: $t \rightarrow te^{i\frac{2\pi}{\Phi_0}\int_n^m \vec{A}_{nm}\cdot d\vec{l}}$, where Φ_0 is the magnetic flux quantum, $\vec{A}_{nm}$ is the magnetic vector potential along the path between sites n and m. The Peierls substitution to graphene QDs can be done through the hopping_energy_modifier function in Pybinding, below shows an example code:

```
def constant_magnetic_field(B):
    @pb.hopping_energy_modifier
    def function(energy, x1, y1, x2, y2):
        # the midpoint between two sites
        y = 0.5 * (y1 + y2)
        # scale from nanometers to meters
        y *= 1e-9
        # vector potential along the x-axis
        A_x = B * y
        # integral of (A * dl) from position 1 to position 2
        peierls = A_x * (x1 - x2)
        # scale from nanometers to meters (because of x1 and x2)
        peierls *= 1e-9
        # the Peierls substitution
        return energy * np.exp(1j * 2*pi/phi0 * peierls)
    return function
```

4.1.5 Scaled Graphene QD TB Model

Although the kernel polynomial method is computationally very efficient to solve the $LDOS$ of quantum systems with large sparse matrix such as those graphene

QDs defined on a several hundred nanometer graphene mesh. For even larger quantum systems, such as graphene QDs defined on a micrometer scale graphene mesh, it will still be very challenging and time consuming to solve the $LDOS$ of such systems with the kernel polynomial method. For these even large graphene QD TB models, one can use a scaled graphene TB model technique[133], which can help reduce the TB model matrix size but still very well maintain the low energy physics we want to investigate. The procedure behind of scaled graphene TB model is quite simple, we simply adjust the lattice constant a and hopping parameters t as following:

$$a \to s \cdot a, \qquad t \to \frac{t}{s} \tag{4.2}$$

Here s is the scaling factor. Taking MLG as an example, the energy bands of the scaled MLG model at energies $|E| \ll 3\pi\gamma_0/s$ will remain the same as the real MLG bands. This technique is quite useful for the TB simulation for stadium shaped MLG QDs that I will discuss in chapter 8 because these systems are several times larger than those single graphene QD systems, which will take a very long time to simulate without the scaling technique. Even with a scaling factor 2, the computational time can be reduced by about 4 times.

4.2 Continuum Model of Graphene QDs

In the previous section, I described the TB model of graphene QDs and how to numerically solve it with the Pybinding package. Although the graphene QD TB model can very well reproduce experimental observations, very often the physics of the observation can still be unclear with only the TB model result. This is because the TB simulation for graphene QDs in some sense is just like running an experiment but on a computer, we simply input all the parameters into a giant matrix then wait for the results output by the simulation. In this chapter, I will introduce the continuum model of graphene QDs and briefly describe how to numerically solve it. Different from the TB model, continuum model can usually provide us more insights into the physics behind the experimental observations. For example, we can get quantum number resolved $LDOS$ for graphene QDs with the continuum model but cannot with the TB model.

Below I will use MLG QD as an example to demonstrate how the continuum model works for graphene QDs. The procedures I describe below are based on what I learned from earlier MLG QD works[53,134,135] that involves MLG QD continuum model. The continuum model of MLG QDs is based on the low energy effective Hamiltonian of MLG as described in section 1.2, without magnetic field, its continuum model Hamiltonian can be expressed as

$$H_{MLG\ QD}^{\xi} = v_F\left(\xi\sigma_x p_x + \sigma_y p_y\right) + V \tag{4.3}$$

Here ξ is the valley index and V is the QD potential well. Since MLG has spatial inversion symmetry, the QD states in the two valleys will have the exact same properties. From now on, I will only work with the K_+ valley, which has $\xi = 1$. With circularly symmetric potential well $V(r)$, the above MLG QD Hamiltonian will be more conveniently to work in the polar coordinates and can be rewritten as

$$H_{MLG\ QD} = \begin{pmatrix} V(r) & -i\hbar e^{-i\theta}(\partial_r - \frac{i}{r}\partial_\theta) \\ -i\hbar e^{i\theta}(\partial_r + \frac{i}{r}\partial_\theta) & V(r) \end{pmatrix} \tag{4.4}$$

The above Hamiltonian commutes with operator $J_z = L_z + \hbar\sigma_z/2$, as a result the ansatz of the above Hamiltonian can be written as

$$\psi(r,\theta) = \frac{1}{\sqrt{r}}\begin{pmatrix} u_A(r)e^{i\left(m-\frac{1}{2}\right)\theta} \\ iu_B(r)e^{i\left(m+\frac{1}{2}\right)\theta} \end{pmatrix} \tag{4.5}$$

Operator J_z mimics the total angular momentum operator, the difference here is that the pseudospin of MLG is acted as the real electron spin. And the above ansatz gives an eigenvalue of $m\hbar$ for J_z, so m is the total angular quantum number, which should have half-integer values. Next, insert the above ansatz into the eigenvalue equation for the Hamiltonian shown in Equation (4.4), we can separate the angular and radial variables and get

$$\begin{pmatrix} V(r) & \hbar v_F\left(\partial_r + \frac{m}{r}\right) \\ \hbar v_F\left(-\partial_r + \frac{m}{r}\right) & V(r) \end{pmatrix}\begin{pmatrix} u_A(r) \\ u_B(r) \end{pmatrix} = E\begin{pmatrix} u_A(r) \\ u_B(r) \end{pmatrix} \tag{4.6}$$

The above differential equation can be solved with the finite difference method, which essentially approximate the continuous eigenfunctions $u(r)$ with values u_i on a discrete but dense lattice, here i is the lattice index, and approximate ∂_r by

$$\partial_r \approx \frac{1}{2\delta}(u_{i+1} - u_{i-1}) \tag{4.7}$$

, where δ is the distance between two lattice points. With N lattice points, the 2×2 matrix shown in Equation (4.6) will be approximated by a $2N \times 2N$ sparse matrix. Then the differential equation problem can be transformed into the eigenvalue problem of the $2N \times 2N$ sparse matrix, which can be conveniently solved with a Python program with the eigenvalue solvers included in the SciPy package. An example code can be found in Appendix C. After getting the eigenvalues and eigenfunctions of the differential equation (4.6), we can then calculate quantum number resolved $LDOS$ of the simulated MLG QD with

$$LDOS_m(E) = \sum_\nu |u_\nu(r)|^2 \delta(E - E_\nu) \tag{4.8}$$

, where m is the total angular quantum number and ν labels the radial eigenstates for fixed m. In practice, we can typically approximate $\delta(E - E_\nu)$ with a Lorentzian function with peak half maximum width Γ and add a spatial smooth to $|u_\nu(r)|^2$ with Gaussian broadening to reduce fast spatial oscillations from numerical artefacts if necessary.

So far, we have discussed the continuum model of MLG QD without a magnetic field. To simulate the magnetic field effect, we just have to replace $\vec{p}$ with $\vec{p} + e\vec{A}$ in the MLG QD Hamiltonian shown in Equation (4.4), where $\vec{A}$ is the magnetic field vector potential. For a spatially uniform magnetic field B, its vector potential in the polar coordinates can be written as

$$A_r = 0, \qquad A_\theta = \frac{Br}{2} \tag{4.9}$$

And this gives us

$$H_{MLG\ QD}(B) = \begin{pmatrix} V(r) & -i\hbar e^{-i\theta}\left(\partial_r - \frac{i}{r}\partial_\theta + \frac{eBr}{2\hbar}\right) \\ -i\hbar e^{i\theta}\left(\partial_r + \frac{i}{r}\partial_\theta - \frac{eBr}{2\hbar}\right) & V(r) \end{pmatrix} \tag{4.10}$$

It is evident that the MLG QD Hamiltonian in magnetic field still commutes with J_z, as a result, the ansatz shown in Equation (4.5) still works for MLG QD in a magnetic field. Inserting it into Equation (4.10), we can get $H(r)$ as

$$\begin{pmatrix} V(r) & \hbar v_F(\partial_r + \frac{m}{r} + \frac{eBr}{2\hbar}) \\ \hbar v_F(-\partial_r + \frac{m}{r} + \frac{eBr}{2\hbar}) & V(r) \end{pmatrix} \begin{pmatrix} u_A(r) \\ u_B(r) \end{pmatrix} = E \begin{pmatrix} u_A(r) \\ u_B(r) \end{pmatrix} \quad (4.11)$$

We can then use the same procedure described for MLG QD without magnetic field to numerically solve the differential equation (4.11) and get quantum number resolved $LDOS$ for MLG QDs in a magnetic field. Appendix C shows an example Python code that can be used to calculate angular quantum number resolved $LDOS(E,r)$ in a magnetic field with the MLG QD continuum model. Figure 4.3 shows an example result for the $LDOS(E,r)$ of MLG QD states with and without a magnetic field, the splitting between the initially degenerate plus and minus angular quantum number states in a magnetic field can be visualized.

A similar procedure to the one I described above also works for BLG QDs if trigonally warping is not considered[136]. An example code for simulating the $LDOS(E,r)$ of BLG QDs is also included in Appendix C. But when trigonal warping is considered, the BLG QD Hamiltonian no longer has circular symmetry, as a result, we cannot separate the angular and radial parts of the BLG QD wavefunctions. We can still simulate BLG QDs with the continuum model in this case[137], but it will become a bit more complicated to do so.

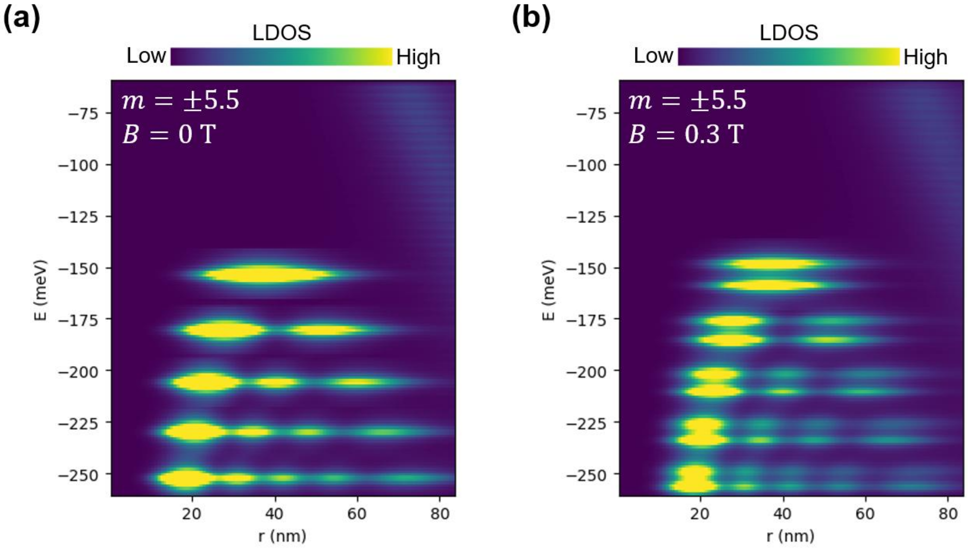

Figure 4.3 Angular quantum number resolved $LDOS(E,r)$ calculated from the MLG QD continuum model for $m = \pm 5.5$ MLG QD states in $B = 0$ T (a) and $B = 0.3$ T (b). The potential well used for the MLG QD is $V(r) = -0.03r^2$ $\mathrm{meV/nm^2}$.

Chapter 5 Giant Orbital Magnetic Moments and Strong Paramagnetic Shift in MLG QDs

In chapter 1, we introduced the electronic structure of MLG and pointed out that it hosts massless Dirac fermions that feature a linear energy dispersion and can be used as a platform to investigate relativistic quantum phenomena. Following the idea of artificial atoms and molecules for semiconductor QDs introduced in chapter 1, single and coupled MLG QDs offer the opportunity to study artificial atoms and molecules in the ultrarealistic regime. In this chapter, I will present our results on the unique magnetic field responses observed in single and coupled MLG QDs due to their relativistic nature by using the in-situ graphene QD creation and probing technique described in chapter 2. The results shown in this chapter have been published in reference[63].

5.1 Introduction

MLG is an ideal platform for studying relativistic quantum phenomena because it hosts massless Dirac fermions[76] and has high gate tunability. As a result, multiple relativistic quantum phenomena have been demonstrated with MLG such as Klein tunneling[78,88] and atomic collapse[138,139]. Such phenomena are important not only for fundamental research but also for technological applications. For example, Klein tunneling renders MLG pn junctions highly transparent, which makes MLG an outstanding platform for electron optics applications such as negative refraction[140], Veselago lensing[141], and beam collimation[142,143].

QDs are often referred to as artificial atoms because of their atomic-like electronic structure[5,6]. They have been widely studied over the last 40 years in semiconductors and have provided immense fundamental insight[2,27,144] . Recently, the confinement of massless Dirac fermions in electrostatically defined QDs has been achieved in MLG[50-55,57,59,69,145]. Different from semiconductor QDs formed with massive Schrödinger fermions, QDs populated by massless Dirac fermions can be viewed as artificial relativistic atoms, thus offering a unique opportunity to study atomic properties in the ultra-relativistic regime (particle speed close to lightspeed).

For such artificial relativistic atoms, the usual relationship between orbital magnetic moment ($\vec{\mu}$) and angular momentum ($\vec{L}$) for atomic states ($\vec{\mu} = g\mu_B\vec{L}/\hbar$, μ_B is Bohr magneton, $\hbar$ is Dirac's constant, g is Landé g-factor) is invalid. This is because massless Dirac fermions disobey the non-relativistic relationship between velocity and momentum, $\vec{p} = m\vec{v}$. Instead, $\vec{\mu}$ is given by the area of the atomic orbit (πr^2) multiplied by the electrical current ($\frac{-ev_D}{2\pi r}$), which results in $\vec{\mu} = -e\vec{v}_D \times \vec{r}/2$. Because of this, the large and constant Dirac velocity $\vec{v}_D$ together with a sizable atomic orbital radius $\vec{r}$ can produce extremely large $\vec{\mu}$ for artificial relativistic atoms. One direct consequence of this large $\vec{\mu}$ is a giant Zeeman splitting for artificial atomic orbital states in a magnetic field (B), which can potentially be useful for sensing. Such properties of artificial relativistic atoms, however, have not been experimentally demonstrated to date.

In this chapter, I will show B dependent STS of gate-tunable single and coupled MLG QDs to unravel the unique B responses of artificial relativistic atoms and molecules. For single MLG QD states, we observed large linear splitting in B, which evidenced the giant $\vec{\mu}$ of these states. And we further studied the angular quantum number and gate dependence of the MLG QD $\vec{\mu}$ and found good agreement with theory. For coupled MLG QD states, we found the linear splitting in B was quenched. Instead, a B^2 dependent energy shift towards lower energy was observed due to the existence of a strong paramagnetic shift in relativistic atomic systems. These phenomena underscore the uniqueness of MLG QDs compared to conventional semiconductor QDs.

5.2 Magnetic Field Response of Single MLG QDs

5.2.1 Experiment Setup

We study MLG QDs defined by electrostatically induced circular pn junctions with a scanning tunneling microscope (STM) as schematized in Figure 5.1a. The circular MLG pn junction is created in a monolayer graphene or 14.1° twisted bilayer graphene/hBN heterostructure resting on a SiO_2/Si chip with the in-situ graphene QD creation technique described in section 2.3.2. The STM tip is grounded, a bias voltage V_S together with an ac voltage V_{ac} is applied between the STM tip and graphene to measure dI/dV_S spectra. And a back gate voltage V_G can be applied between the p-doped silicon and graphene to tune the MLG QD potential and doping. In addition, an out of plane magnetic field can be applied to the whole device.

Although Klein tunneling[78,88] makes it difficult to confine massless Dirac fermions, their oblique incidence onto the circular pn junction boundary (schematized in Figure 5.1b) avoids the 100% transmission occurring at normal incidence. This allows for the formation of quasi-bound states in MLG QDs, which have been confirmed in previous experiements[50,53-55,57,59,69,145]. In zero B, the clockwise and counterclockwise quasi-bound states possessing the same radial quantum number (n) and angular quantum numbers ($\pm m$) are degenerate due to time reversal symmetry. The directions of their $\vec{\mu}$, however, are opposite (Figure 5.1c). Thus, by applying an external B, the degeneracy between the clockwise and counterclockwise quasi-bound states is lifted through an orbital Zeeman effect (Figure 5.1d), leading to a splitting energy $\Delta E = 2|\vec{\mu} \cdot \vec{B}|$. This linear orbital Zeeman splitting can be used to measure $\vec{\mu}$ of MLG QD states.

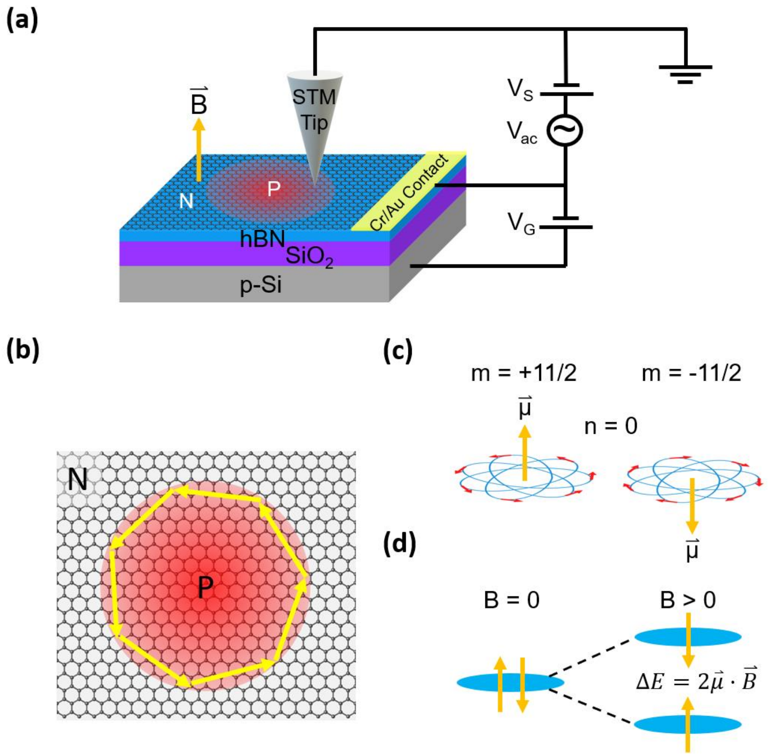

Figure 5.1 Experimental set up and orbital Zeeman splitting of MLG QD states. (a) Schematic of the experimental setup. (b) Schematic of the confinement of massless Dirac fermions in a circular MLG pn junction. (c) Schematic of the orbital magnetic moments of MLG QD states. The blue lines are the calculated semiclassical orbits of

$n = 0$, $m = \pm 11/2$ MLG QD states in a parabolic potential well $U(r) = -0.01r^2$ meV/nm^2. The red arrows indicate the direction of the trajectory. The orange arrows indicate the orientation of the orbital magnetic moments. (d) Schematic of the orbital Zeeman splitting of MLG QD states in a finite magnetic field. The blue ovals and orange arrows represent the energy levels and the orbital magnetic moment orientations of MLG QD states, respectively.

5.2.2 The Importance of Increasing QD Potential Well Sharpness

Due to the unique band topology near graphene's Dirac point, there exists step-like splitting from a Berry phase jump of MLG QD states in the presence of a critical magnetic field (B_C).[57,135] This step-like splitting obscures linear orbital Zeeman splitting and thus compromises the measurement of $\vec{\mu}$ for MLG QD states. In a quadratic potential well $U(r) = \kappa r^2$, the critical field for the step-like splitting is $B_c = \frac{2m\hbar\kappa}{e\varepsilon}$,[135] where m and ε are the angular quantum number and energy of MLG QD states, respectively. Therefore, increasing the sharpness of the potential well (κ) and accessing QD states with high angular quantum number (m) can increase B_c, thus reducing the deleterious effect that Berry phase induced step-splitting imposes on the measurement of $\vec{\mu}$.

To quantitively support the above discussion, we calculated the $LDOS$ as a function of energy and B for MLG QDs with quadratic potential wells that have different sharpness. Figure 5.2a,b shows the m resolved $LDOS(E,B)$ for MLG QDs calculated with the continuum model of MLG QD described in section 4.2, the B_c necessary for a Berry phase jump at different energies are represented by the red line in each $LDOS(E,B)$ plot. When $B < B_c$, the degenerate QD states show a linear splitting. But when $B > B_C$, the linear splitting trend for the QD states gradually stops and step-like splitting emerges. Although the linear splitting can still be observed in m resolved $LDOS(E,B)$ for the smooth potential well (Figure 5.2a), when summing m together (which is more relatable to experiments), the linear splitting pattern is washed out by the step-like splitting from other states with different m. Figure 5.2c,d show the$m$ summed $\partial^2 LDOS/\partial E^2(E,B)$ at $d = 40$ nm calculated with the TB model of MLG QD described in section 4.1. Evidently, linear splitting cannot be resolved in the smooth potential well (Figure 5.2c) but can still be resolved in the sharp potential well (Figure 5.2d).

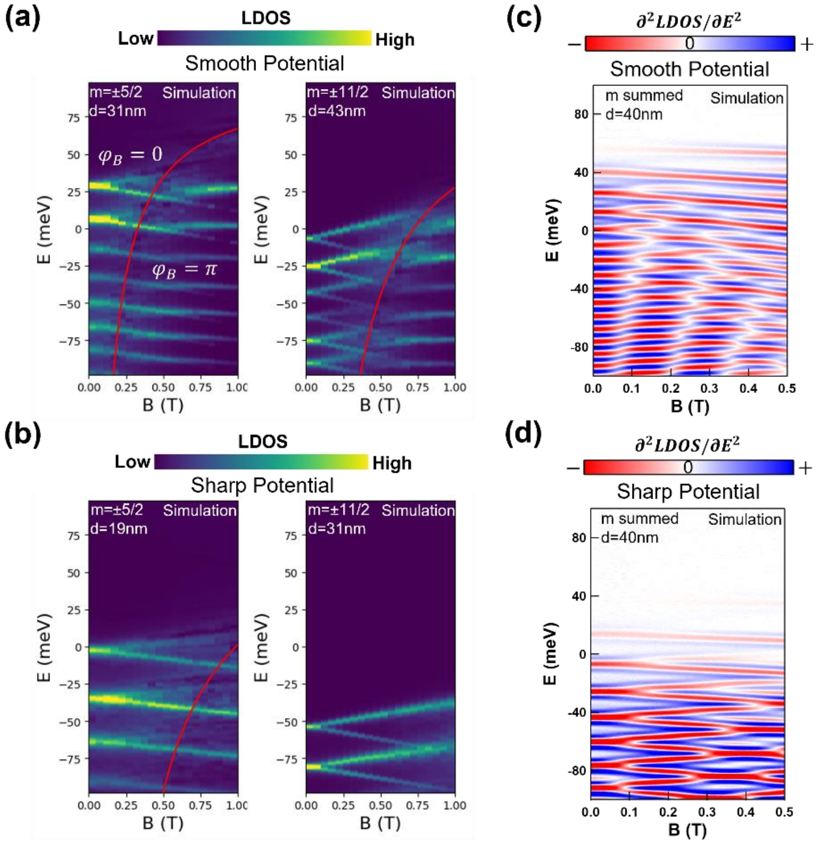

Figure 5.2 The influence of potential well sharpness for observing orbital Zeeman splitting. (a)-(b) Calculated m resolved $LDOS(E,B)$ for MLG QD states with $m = \pm 5/2$ and $m = \pm 11/2$ at certain locations in a parabolic potential well $U(r) = \kappa r^2 +$

b, where $\kappa = -0.01\ \mathrm{meV/nm^2}$ for the smooth potential and $\kappa = -0.03\ \mathrm{meV/nm^2}$ for the sharp potential, and $b = 100$ meV for both potentials. The red line represents the theoretical critical magnetic field B_c necessary for the onset of a Berry phase jump for graphene QD states. (c)-(d) Calculated m summed $\partial^2 LDOS/\partial E^2(E,B)$ for graphene QD states at 40 nm away from the center. The potential well parameters for the smooth and sharp potentials are the same as in (a).

In order to create MLG QDs with sharp potential wells, we use the two-step tip bias pulsing technique described in section 2.3.2 on samples with reduced hexagonal boron nitride (hBN) thickness (detailed tip bias pulsing procedure can be found in Appendix xxx). Figure 5.3a shows a typical dI/dV_S spectra along a line across the center of a circular pn junction created with this technique on a large angle (14.1°) twisted bilayer graphene (tBLG)/hBN sample. By tracking the graphene charge neutrality point (marked by white dots in Figure 5.3a), we estimate the potential variation to be 200~300 meV across 100 nm. This is 2~3 times sharper than previous works that utilized a related tip pulsing technique[53,57,59,69]. Figure 5.3b shows a comparison of dI/dV_S point spectra at $d = 0$ nm and 40 nm of the MLG QD shown in Figure 5.3a. Evidently, the dI/dV_S peaks are much sharper off center than at the QD center. This is because near the QD boundary, states with larger m are concentrated, which correspond to Dirac fermions propagating tangentially to the pn junction, resulting in a stronger reflection and hence better confinement[53,54]. For the remainder of this work, we will focus on these large m states hosted in circular MLG QDs. Figure 5.4 shows two example constant bias dI/dV_S maps of MLG QDs created with our two-step tip pulsing technique that has very good circular symmetry.

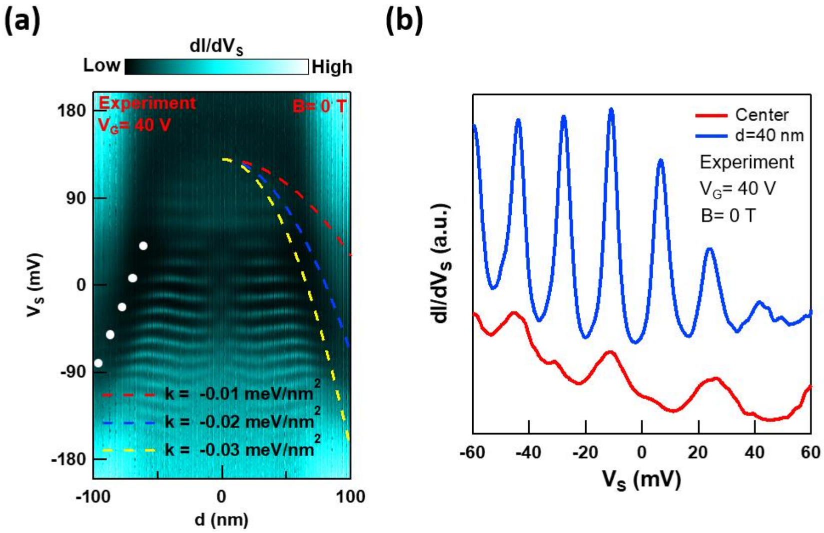

Figure 5.3 MLG QDs with sharp potential wells. (a) Experimentally measured $dI/dV_S(V_S, d)$ at $V_G = 0$ V along a line across the center of a circular graphene pn junction that has a sharp potential well. Colored dashed lines are quadratic potential wells with different κ values. The set point used to acquire the tunneling spectra was $I = 1$ nA, $V_S = -200$ mV, with a 2 mV ac modulation. (b) dI/dV_S point spectra at the center and at 40 nm away from the center of the circular graphene pn junction as shown in (a). The set point used to acquire the tunneling spectra was $I = 1$ nA, $V_S = -60$ mV, with a 2 mV ac modulation.

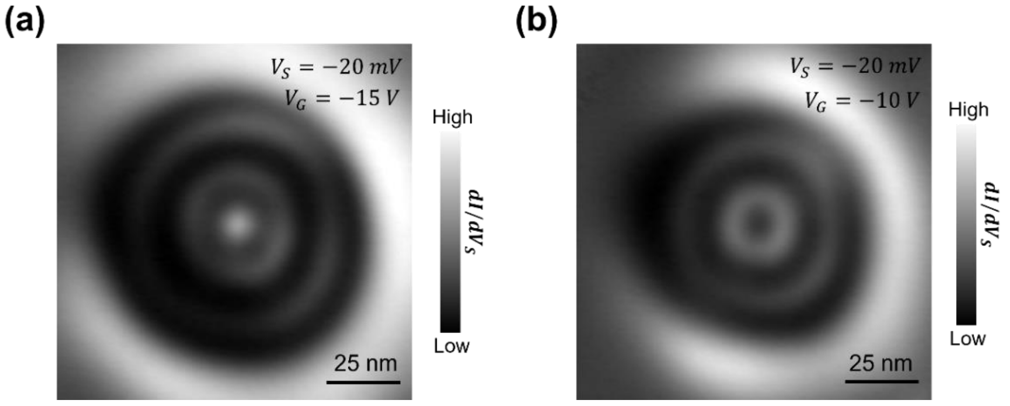

Figure 5.4 dI/dV_S maps of the circular graphene pn junction. (a)-(b) dI/dV_S maps measured from the circular graphene pn junction as shown in Figure 5.5a at $V_G = -15$ V (a) and $V_G = -10$ V (b). The tunneling parameters used to get the dI/dV_S are both $I = 0.1$ nA, $V_S = -20$ mV with a 2 mV ac modulation in (a) and (b).

5.2.3 Observation of Linear Orbital Zeeman Splitting

We now study the response of our MLG QDs with a sharp potential well to a perpendicular B. Figure 5.5a,b shows the comparison of $dI/dV_S(V_S, d)$ measured across the center of another MLG QD with a sharp potential well in $B = 0$ T and 0.2 T. Splitting patterns are clearly seen in $B = 0.2$ T as dimples near the QD boundary where high m states concentrate. Figure 5.5c shows the evolution of dI/dV_S point spectra at $d = 40$ nm in various B, the splitting and merging of MLG QD states can be seen as B increases. To visualize this behavior more clearly, $dI/dV_S(V_S, B)$ with high B resolution was acquired and is shown in Figure 5.5d. These data were taken from the same MLG QD shown in Figure 5.5a,b at $d = 40$ nm, here $d^3I/dV_S^3(V_S, B)$ are presented to enhance the visibility of dI/dV_S peaks. We observe a clear linear splitting for each QD state. We attribute this behavior to the orbital Zeeman splitting of MLG QD states. And these experimental findings are all in good agreement with simulations based on the TB model described in section 4.1 for MLG QDs with a quadratic potential well (Figure 5.5e-h), thus further supporting our qualitative understanding. The slight deviations visible between experiment and simulation at negative energies are likely due to the deviation of the experimental potential from the quadratic potential used in our simulation.

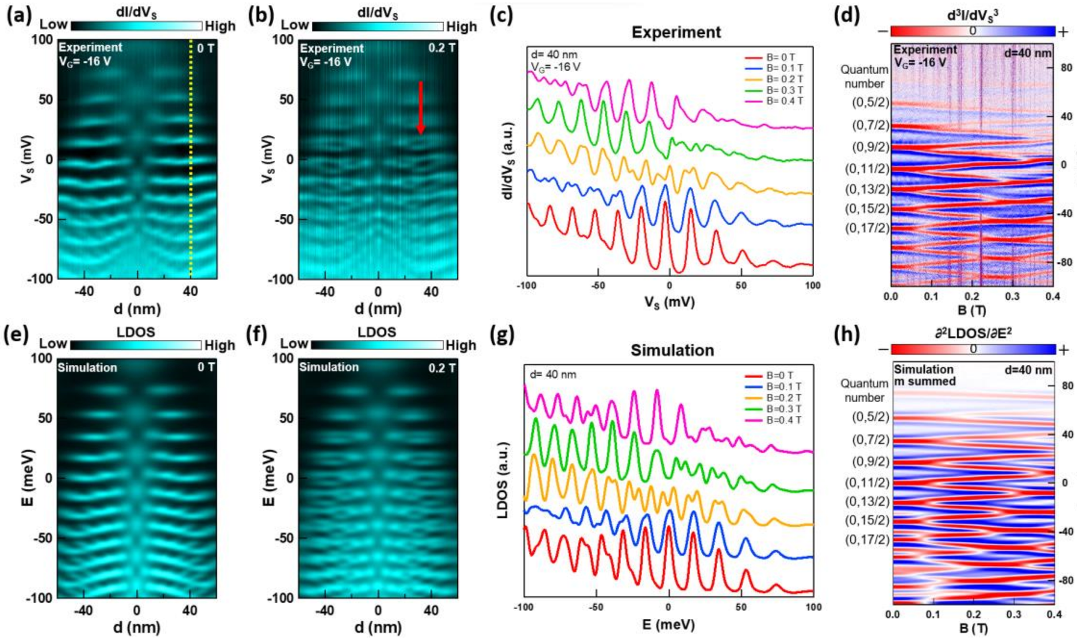

Figure 5.5 Experimental observation of linear orbital Zeeman splitting. (a)-(b) Experimentally measured $dI/dV_S(V_S,d)$ at $V_G=-16$ V in $B=0$ T (a) and $B=0.2$ T (b) along a line across the center of a circular graphene pn junction with a sharp potential well. This pn junction is different from the junction shown in Figure 5.3. The red arrow indicates the splitting of one QD state. (c) dI/dV_S point spectra measured at $d=40$ nm and at $V_G=-16$ V in various magnetic fields from 0 T to 0.4 T with a 0.1 T step. (d) $d^3I/dV_S^3(V_S,B)$ at $V_G=-16$ V at $d=40$ nm as indicated by the yellow dashed lines in (a). The quantum number (n,m) corresponds to radial and angular quantum number, respectively. (e)-(f), Simulated $LDOS(E,d)$ for a MLG QD in $B=0$ T (e) and $B=0.2$ T (f) with $U(r)=-0.03r^2$ meV/nm^2 $+\,160$ meV. (g) Simulated $LDOS$ at $d=40$ nm in various magnetic fields from 0 T to 0.4 T for the same MGL QD in (e) and (f). (h) Simulated $\partial^2LDOS/\partial E^2(E,B)$ at $d=40$ nm for the same GQD in (e) and (f). The quantum number (n,m) corresponds to radial and angular quantum number, respectively.

5.2.4 Angular Quantum Number Dependence of $\vec{\mu}$

After confirming the existence of orbital Zeeman splitting, we extract $\vec{\mu}$ of our artificial relativistic atom and study its angular quantum number dependence. To do this, we first assign the radial and angular quantum number of MLG QD states in $dI/dV_S(V_S,d)$ data following an approach used in a previous work[57], an example is shown in Figure 5.6a. Next, we compare both the energies where the MLG QD state appears in the $dI/dV_S(V_S, B)$ data and the locations where the $dI/dV_S(V_S, B)$ data was taken with the $dI/dV_S(V_S, d)$ data to assign the quantum numbers to the QD states in $dI/dV_S(V_S, B)$ measurements. Figure 5.6 shows an example compassion between the $dI/dV_S(V_S, B)$ data and $dI/dV_S(V_S, d)$ data to assign quantum numbers to MLG QD states in the $dI/dV_S(V_S, B)$ data. For the state in $dI/dV_S(V_S, B)$ at $d = 25$ nm near $V_S = 0$ mV, it is in between the (0,9/2) and (1,5/2) state, and in the $dI/dV_S(V_S, B)$ data, we see the linear splitting is different from other states, which we think is caused by a mixing effect of the two QD states. These type of states in the $dI/dV_S(V_S, B)$ data, were not considered for orbital magnetic moment extraction and quantum number assignment.

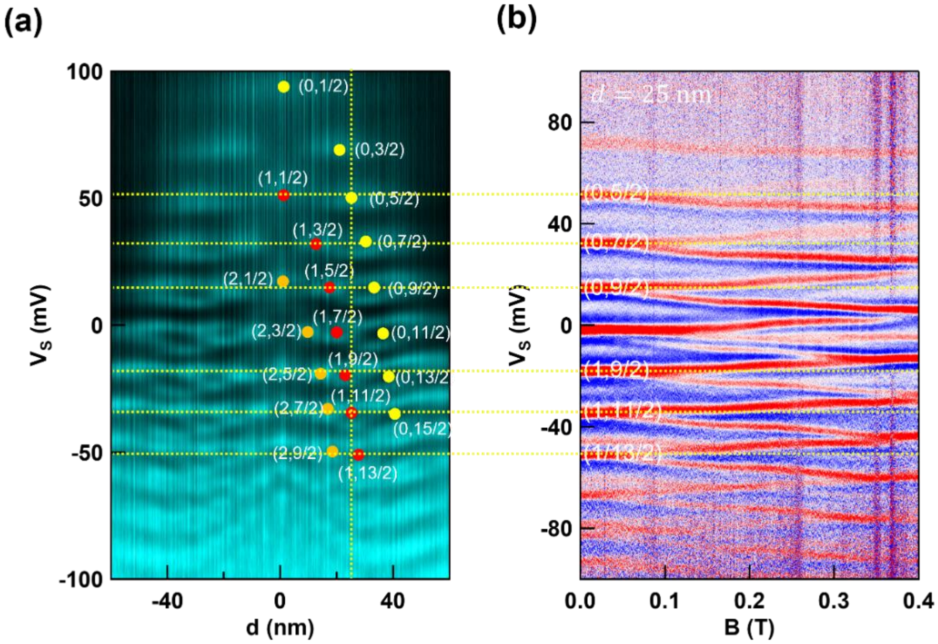

Figure 5.6 Quantum number assignment for MLG QD states in $d^3I/dV_S^3(V_S, B)$ measurements. (a) The same $dI/dV_S(V_S, d)$ data measured at $V_G = -16$ V in $B =$

0.2 T as shown in Figure 5.5b with radial and angular quantum numbers assigned to the MLG QD states. The first and second number in the parenthesis corresponds to the radial and angular quantum numbers, respectively. (b) $dI^3/dV_S^3(V_S, B)$ data measured at $d = 25$ nm for the dot shown in (a) with $V_G = -16$ V. The horizontal yellow dashed lines correspond to the energies of the MLG QD states in $B = 0$ T at $d = 25$ nm, the vertical dashed line in (a) corresponds to the position where (b) was taken. The quantum numbers of QD states in (b) can be assigned by checking quantum numbers of the graphene QD states at the intersection points of the vertical and horizontal dashed lines in (a).

Following the procedure described above, we can assign both the radial and angular quantum numbers (n, m) for MLG QD states shown in Figure 5.5d,h. By using the simple consideration discussed in Figure 5.1d ($\Delta E = 2|\vec{\mu} \cdot \vec{B}|$), $\vec{\mu}$ of MLG QD states can then be extracted from the slopes of ΔE as a function of B. Figure 5.7a shows the extracted $\Delta E(B)$ and corresponding linear fits for QD states with different m at $V_G = -16$ V, a clear increase in slope is seen for states with larger m. The magnitude of $\vec{\mu}$ (μ) as a function of m extracted from the slopes of linear fits in Figure 5.7a is plotted in Figure 5.7b. An increase from $\sim 200\mu_B$ to $\sim 500\mu_B$ for μ is seen when m is increased from 2.5 to 10.5.

Next, we compare our experimentally extracted μ with theory. Approximately, the measured μ are on the order of $300\mu_B$. This value agrees well with the μ of a current loop ($\mu = \frac{ev_F r}{2}$) for a charge flowing with MLG's Fermi velocity $v_F = 10^6$ m/s and with a loop radius $r = 35$ nm. For a more formal comparison we calculated m resolved $LDOS(E, B)$ with the continuum model described in section 4.2 for MLG QDs with quadratic potential wells, some results are shown in Figure 5.7c-e. From such plots, we can extract μ for MLG QD states with different quantum numbers, the extracted μ for states with $n = 0$ and $m = 2.5$ to 10.5 are plotted in Figure 5.7b.

We notice the experimental results (red triangles) do not overlay any individual theory curve (empty circles). Additionally, experimental results at larger m appear closer to theoretical curves calculated with a smaller $|\kappa|$. Akin to the discrepancy discussed for Figure 5.5, the discrepancy seen here is likely caused by the deviation of the experimental potential from a quadratic potential at negative V_S as depicted in Figure 5.8. Nonetheless for both experiment and theory, a clear increase in μ is seen with increasing m.

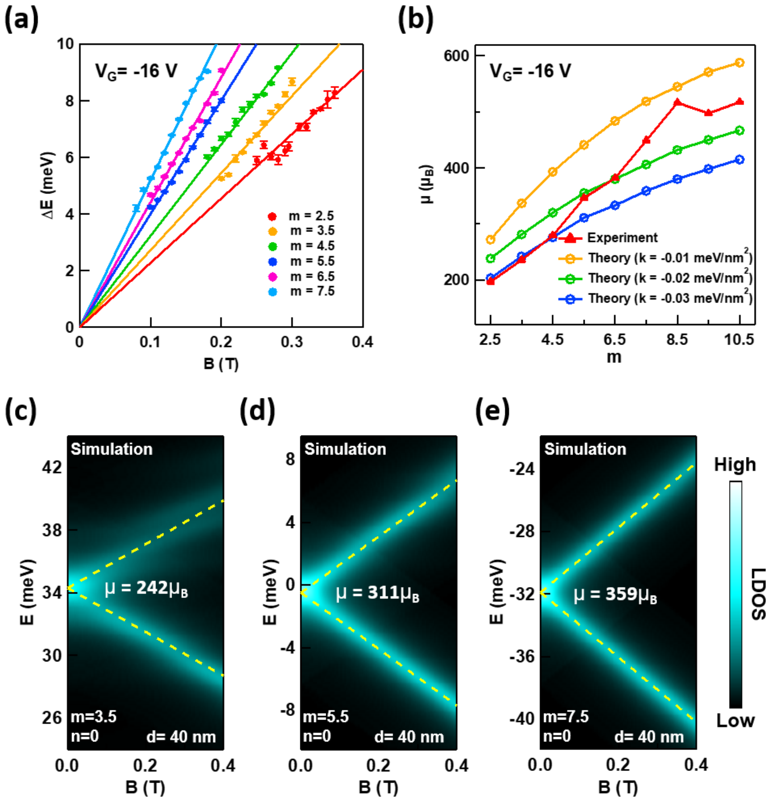

Figure 5.7 Angular quantum number dependence of magnetic moments of MLG QD states. (a) Experimentally extracted orbital Zeeman splitting energy at various B and the linear fits for MLG QD states with different m and $n = 0$ at $V_G = -16\,\mathrm{V}$. (b) Comparison between experimentally extracted $\mu(m)$ at $V_G = -16$ V and theoretically calculated $\mu(m)$ for MLG QD states with parabolic potential wells $U(r) = \kappa r^2$. (c)-(e) Calculated m resolved $LDOS(E, B)$ at $d = 40$ nm for QD states with $n = 0$ and

$m = 3.5$ (c), $m = 5.5$ (d) and $m = 7.5$ (e) in a MLG QD with $U(r) = -0.03r^2\ \mathrm{meV/nm^2} + 160\ \mathrm{meV}$. Yellow dashed lines indicate the theoretical orbital Zeeman splitting size with the μ given in each plot. Error bars in (a) reflect one standard error of the peak position in Gaussian multi-peak fitting. Error bars in (b) reflect one standard error of the slope in weighted linear fitting.

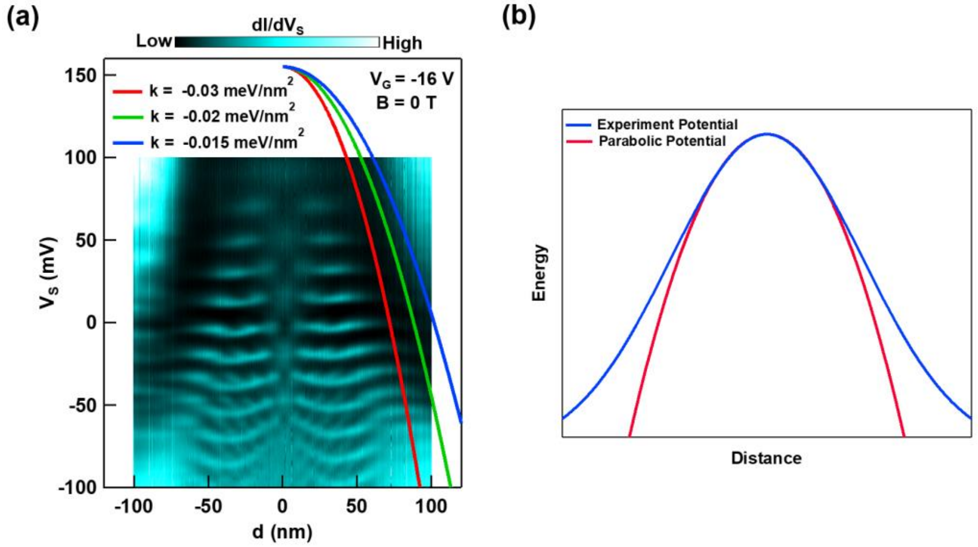

Figure 5.8 Deviation between experimental potential well and parabolic potential well. (a) Experimentally measured $dI/dV_S(V_S, d)$ for the same QD shown in Figure 5.5a at $V_G = -16$ V along a line across the center of a circular MLG pn junction. Colored lines are quadratic potential wells with different κ values. The set point used to acquire the tunneling spectra was $I = 1$ nA, $V_S = -200$ mV, with a 2 mV ac modulation. (b) Schematic of the deviation between experimental potential well and parabolic potential well at more negative energies. The experimental potential well deviates from parabolic potential well at more negative energies, and the actual QD radius will be larger than the parabolic potential well. This explains the faster increase of experimentally measured μ than the theoretical values for graphene QDs with a quadratic potential well.

5.2.5 Gate Dependence of $\vec{\mu}$

We now explore the gate dependence of μ for our artificial relativistic atoms. Figure 5.9a-c shows $dI/dV_S(V_S, d)$ measured at $V_G = -20$ V, -10 V and 0 V in $B = 0.2$ T for the same QD in Figure 5.5a. The potential well sharpness of MLG QDs in our experiments can be tuned by V_G. Apparently as the potential well sharpness increases with increasing V_G, the splitting energy reduces. Figure 5.9d shows the experimentally extracted $\Delta E(B)$ for the $n = 0, m = 5.5$ QD state at various V_G, $dI^3/dV_S^3(V_S, B)$ data at these V_G are shown in Figure 5.10. A clear increase in slope is seen as V_G is decreased, indicating an enhancement of μ when reducing V_G. To see this more quantitatively, we plot extracted μ values as a function of m in Figure 5.9e for MLG QD states with different m measured at various V_G. The extracted μ are generally smaller at larger V_G (sharper potential well) for all QD states.

The observed gate tuning of μ can be understood as a result of orbital size tuning of MLG QD states with V_G: sharper dots at larger V_G have current loops with smaller radius. In contrast to nonrelativistic atoms, μ for relativistic atoms is governed by the orbital radius instead of the angular momentum. Therefore, it is uniquely possible to tune μ of our artificial relativistic atom by V_G while maintaining the same quantum numbers. These results are also supported by the theoretically calculated $\mu(m)$ for MLG QDs with different potential well sharpness (Figure 5.7b).

We now compare the observed μ in MLG QDs with that of other systems. The value of μ observed in this work are orders of magnitude larger than those observed in natural atoms[146] and semiconductor QDs[147-149], and are also several times larger than those observed in Bernal-stacked bilayer graphene (BLG) QDs[37,66] (Table 5.1). Although similar μ values have been observed in Bernal-stacked trilayer graphene (TLG) QDs[61], the findings in this work have several distinctions/advantages. Briefly, MLG QDs can achieve similar μ with a smaller QD size and maintain linear splitting within a larger B range compared to TLG QDs.

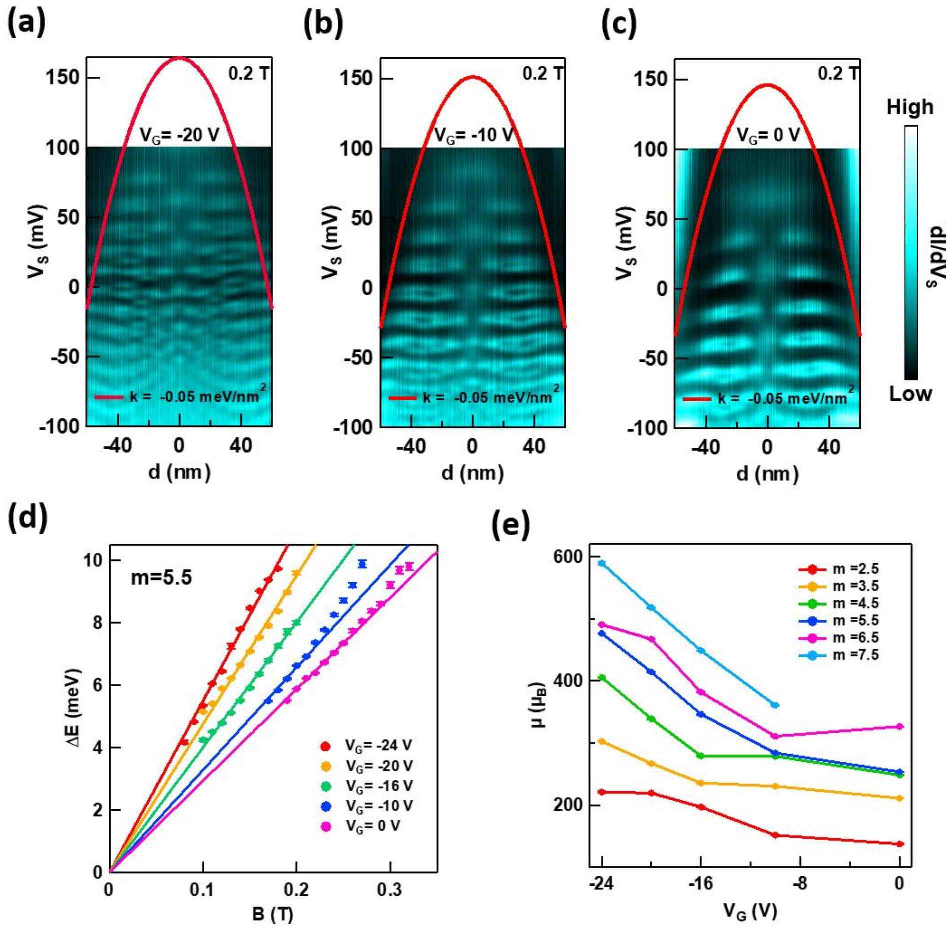

Figure 5.9 Gate dependence of magnetic moments of MLG QD states. (a)-(c) Experimentally measured $dI/dV_S(V_S,d)$ at $V_G = -20$ V (a), $V_G = -10$ V (b) and $V_G = 0$ V (c) in $B = 0.2$ T along a line across the center of the same circular MLG pn junction shown in Figure 5.5a. The red curve in each plot represents a parabolic potential well with $\kappa = -0.05\ \mathrm{meV/nm^2}$ and is a guide for the eye to aid comparison between potential well sharpness variation between different V_G. (d) Experimentally extracted orbital Zeeman splitting energy at various B and the corresponding linear fits for MLG QD states with $n = 0, m = 5.5$ at different V_G. (e) Experimentally extracted μ for MLG QD states with different m and $n = 0$ at different V_G. Error bars in (d) reflect one standard error of the peak position in Gaussian multi-peak fitting. Error bars in (e) reflect one standard error of the slope in weighted linear fitting.

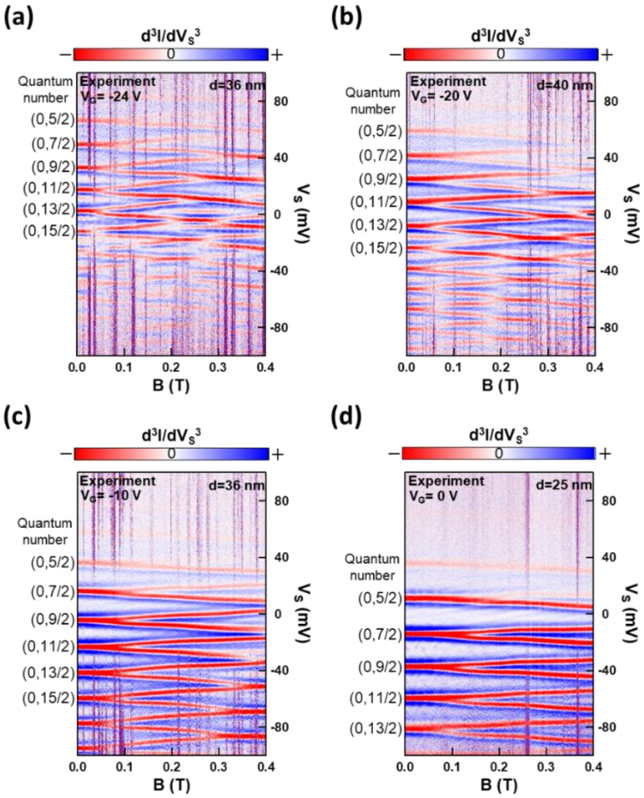

Figure 5.10 $d^3I/dV_S^3(V_S,B)$ plot at different V_G. (a) $d^3I/dV_S^3(V_S,B)$ at $V_G = -24$ V and at $d = 36$ nm. (b) $d^3I/dV_S^3(V_S,B)$ at $V_G = -20$ V and at $d = 40$ nm. (c) $d^3I/dV_S^3(V_S,B)$ at $V_G = -10$ V and at $d = 36$ nm. (d) $d^3I/dV_S^3(V_S,B)$ at $V_G = 0$ V and at $d = 25$ nm. The quantum number (n,m) in (a)-(d) corresponds to radial and angular quantum number, respectively.

Systems	**Observed maximum effective μ**
Natural Atoms	On the order of several μ_B for their ground states and not highly excited states[146]
Self-assembled InP QDs[147]	$\sim 17.3\mu_B$ ($\sim$2.0 meV/T)
Self-assembled InAs/GaAs QDs[148]	$\sim 18.5\mu_B$ ($\sim$2.1 meV/T)
Self-assembled InGaAs/GaAs QDs[149]	$\sim 19.5\mu_B$ ($\sim$2.3 meV/T)
STM tip induced BLG QDs[66]	$\sim 86\mu_B$ ($\sim$10 meV/T)

Few-carrier BLG QDs[37]	$\sim 45\mu_B$ ($\sim$5 meV/T)
STM tip induced TLG QDs[61]	$\sim 525\mu_B$ ($\sim$61 meV/T)
This work (MLG QDs)	$\sim 600\mu_B$ ($\sim$70 meV/T)

Table 5.1 Comparison of measured μ values from different types of systems. For works in which μ values are not given directly, we convert the observed Zeeman splitting ΔE in B to an effective μ through the definition $\mu = \frac{\Delta E}{2B}$.

5.2.6 Potential Applications in Magnetic Field Sensor Arrays

The extremely large orbital Zeeman splitting observed in our MLG QDs ($\sim$23 to 58 meV/T) together with their nanometer scale sizes offers a unique opportunity to fabricate magnetometer arrays with nanometer scale spatial resolution, which is difficult to achieve for the current state of the art[150,151]. The smallest unit of such structure is an uncoupled double MLG QD as shown in Figure 5.11a. We calculated $\partial^2 LDOS/\partial E^2(E, d)$ for double MLG QDs that are separated by 200 nm and with potential wells that are similar to our experiment with the TB model described in section 4.1. The left and right MLG QDs are exposed to a uniform 0.2 T and 0.3 T, respectively. Energy splitting near the pn junction boundary is seen in both MLG QDs (Figure 5.11b), but the splitting energy is ~ 50% larger for the right MLG QD that is exposed to a larger B. The simulation result thus demonstrates the possibility to achieve $\sim$100 nm spatial resolution for B sensing with MLG QD arrays.

To experimentally demonstrate the capability of B sensing for a double graphene QD, we created a double circular MLG pn junction that is separated by 200 nm with our tip pulsing technique (detailed procedure see Appendix xxx). Figure

5.11c shows a comparison between the $d^3I/dV_S^3(V_S, d)$ along a line across the center of both QDs in 0 T and 0.3 T. In $B = 0.3$ T, similar to Figure 5.11b, a splitting for states near the edge of the QD is clearly seen in both QDs, hence demonstrating the possibility of B sensing for a double graphene QD structure. Furthermore, the linear splitting of graphene QD states persists for the double QD structure (Figure 5.11d). In our current experimental setup, we are unable to create a spatially varying B, thus precluding a test of the spatial resolution depicted by our simulation (Figure 5.11b). Earlier works have demonstrated the ability of probing electronic structures of graphene in magnetic fields with TFET[152], thus it is possible to make magnetometer array with MLG QD array TFET device, which can be more flexible for different types of magnetic field measurements and also more suitable for applications.

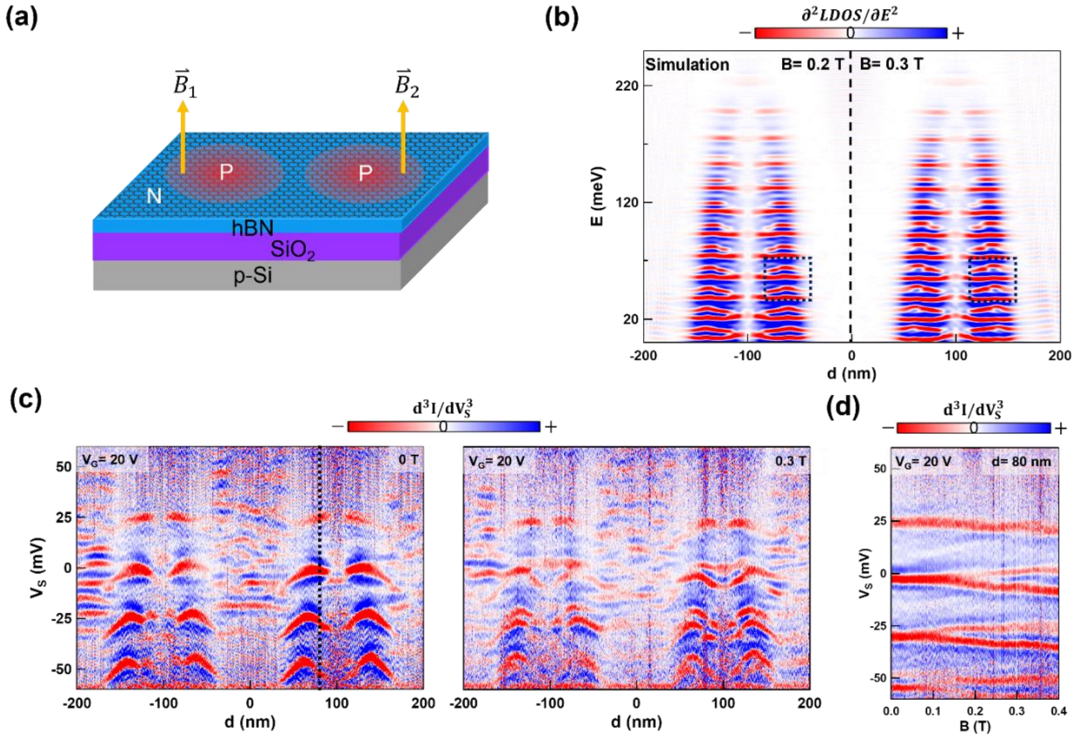

Figure 5.11 Demonstration of a magnetic field sensor array based on double MLG QDs. (a) Schematic of the simplest magnetic field sensor array based on two MLG QDs. The left and right MLG QDs are exposed to a uniform out of plane magnetic field with intensity B_1 and B_2, respectively. (b) Simulated $\partial^2 LDOS/\partial E^2(E,d)$ for a double MLG QD separated by 200 nm along a line across the centers of both QDs. The intensity of the out of plane magnetic field is 0.2 T and 0.3 T for $d < 0$ and $d > 0$, respectively. The black dashed boxes highlight the orbital Zeeman splitting energy difference between the states in the left and right MLG QDs. (c) Experimentally measured $d^3I/dV_S^3(V_S,d)$ at $V_G = 20$ V in $B = 0$ T and $B = 0.3$ T for experimentally created double MLG QDs that are separated by 200 nm. (d) $d^3I/dV_S^3(V_S,B)$ at $V_G = 20$ V and at $d = 80$ nm as indicated by the black dashed line in (c). d^3I/dV_S^3 values in (c)-(d) were numerically calculated from the dI/dV_S acquired through a lock-in measurement and smoothed with a 2 mV box average. The set point used to acquire the tunneling spectra in (c)-(d) was $I = 1$ nA, $V_S = -60$ mV, with a 2 mV ac modulation.

5.3 Magnetic Field Response of Coupled Double MLG QDs

5.3.1 General Properties

Having thoroughly investigated μ of single MLG QDs, below we study the B response of coupled double MLG QDs, which can be viewed as artificial relativistic molecules[65]. These structures were created on a MLG/hBN sample by fabricating two circular p-doped regions with centers separated by 150 nm with our two-step tip voltage pulsing technique (detailed procedure see Appendix xxx). Figure 5.12a shows a $d^3I/dV_S^3(V_S,d)$ plot measured along a line across the centers of two dots in $B = 0$ T at $V_G = 0$ V, the red and blue patterns in the plot correspond to dI/dV_S peaks and valleys, respectively. Three distinct regions can be identified and labeled as (i), (ii), and (iii) in Figure 5.12a. At region (i), the energy spacing between dI/dV_S peaks are half of those at regions (ii) and (iii); and at region (iii) different nodal patterns appear compared to region (ii). These features are distinct from uncoupled double MLG QDs made with a similar fabrication technique as shown in Figure 5.11.

Next, we map the B response of our coupled MLG QDs. Plots of $d^3I/dV_S^3(V_S, B)$ measured at the three distinct regions of the coupled dots are shown in Figure 5.12b-e. First, we notice at region (i) the QD states display a positive energy shift that is proportional to B^2, such behavior is more evident in a zoom in (Figure 5.12c). The parabolic energy shift observed here is $\sim 20\ \mathrm{meV/T^2}$. Secondly, in region (ii) we encounter a linear splitting resembling the observation in single MLG QDs (Figure 5.12d). Finally, region (iii) reveals a distinct behavior compared to the other regions, a staggered pattern for dI/dV_S peaks (Figure 5.12e).

These observations are all qualitatively reproduced with the TB model described in section 4.1 for a coupled double MLG QD. Figure 5.13a shows the simulated $\partial^2 LDOS/\partial E^2(E, d)$ for a coupled double MLG QD with two dots separated by 140 nm, we clearly see the double splitting of QD states near at the far ends of the double dot similar to Figure 5.12a. As shown in Figure 5.13b,c the disappearance of linear splitting and existence of paramagnetic shift is also reproduced for these double split states. Meanwhile, as shown in Figure 5.13d, the linear splitting still exists for QD states closer to QD center, which also agrees with the experiment. Finally, as shown in Figure 5.13e, the half energy shift of the QD states at the center between two dots is also reproduced by our TB model. But we also notice there exists some quantitative discrepancy between the TB model results and experimental results. First, we notice the paramagnetic shift reproduced in the TB model ($\sim 3\ \mathrm{meV/T^2}$) is smaller than the experimental observation ($\sim 20\ \mathrm{meV/T^2}$). Next, the magnetic field at which the QD states at $d = 0$ nm show energy shift for the first time is larger in the TB model results

($B \approx 200\,\mathrm{mT}$) than in the experimental results ($B \approx 100\,\mathrm{mT}$). These quantitative discrepancies are most likely caused by the difference between the exact 2D potential of coupled MLG QDs in the experiment and the potential used in the TB model.

To attain an intuitive understanding of our experimental observations, we consider semiclassical orbits within strongly coupled double MLG QDs. For QD states in a single MLG QD, their semiclassical orbits can be approximated as circular orbits. Once two QD states strongly couple, the circular orbits of individual QD states merge into a figure-eight orbit. Such an orbit is schematized by the yellow rings embedded in a double MLG QD in Figure 5.12f. The arrows indicate the reversed current flow directions of the two rings of the figure-eight orbit. Note that the single-dot states with the same direction of circulations on the dot couple only weakly (e.g., by potential gradient) due to the counter-propagation of states at the touching dot edges. Closer to each individual QD center, we expect QD states have a smaller radius and are decoupled thus forming circular orbits, as depicted by green rings in Figure 5.12f. In our experiment, regions (i) and (iii) correspond to QD states with figure-eight orbits, and region (ii) corresponds to QD states with circular orbits. With this understanding in hand, the half energy spacing observed at region (i) compared to region (ii) is due to the length of the figure-eight orbit being twice that of the circular orbit. This is because according to the semiclassical quantization rule the energy spacing between MLG QD states is $\Delta E = \frac{hv_F}{L}$, where h is Planck's constant, v_F is the graphene Fermi velocity and L is the semiclassical orbit length. Consequently, the large B induced linear splitting observed at region (ii) can be explained by the large $\vec{\mu}$ of circular orbits akin to uncoupled MLG QDs.

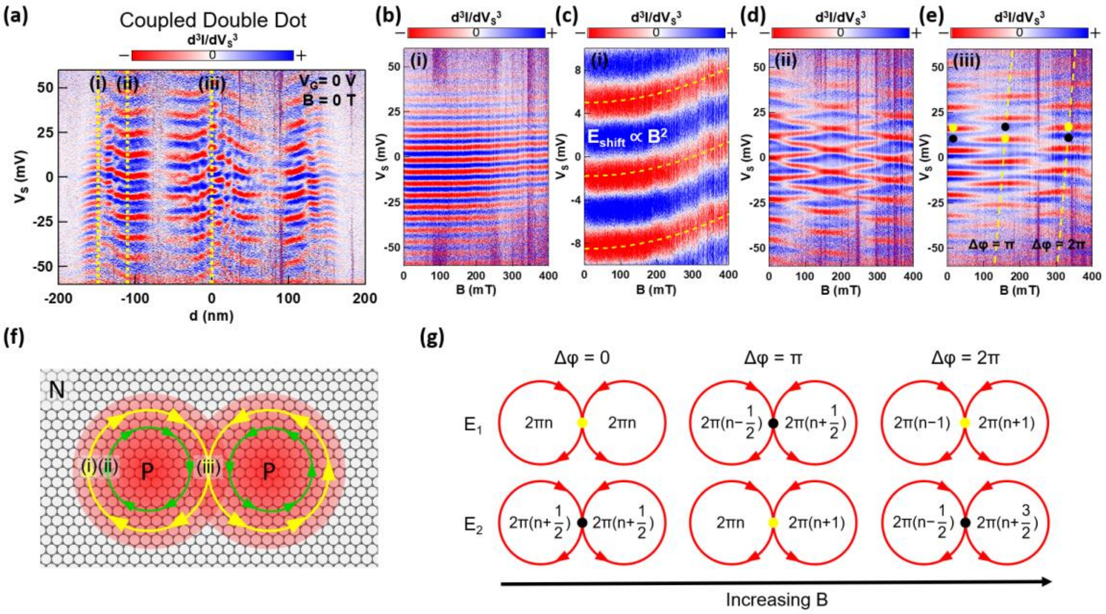

Figure 5.12 Paramagnetic shift and Aharonov–Bohm (AB) effect in coupled double GQDs. (a) Experimentally measured $d^3I/dV_S^3(V_S,d)$ at $V_G = 0$ V in $B = 0$ T for coupled double MLG QDs that are separated by 150 nm. (b) $d^3I/dV_S^3(V_S,B)$ measured at $V_G = 0$ V at $d = -150$ nm corresponding to region (i) in (a). (c) Zoom in of (b) around $V_S = 0$. (d) $d^3I/dV_S^3(V_S,B)$ measured at $V_G = 0$ V at $d = -110$ nm corresponding to region (ii) in (a). (e) $d^3I/dV_S^3(V_S,B)$ measured at $V_G = 0$ V at $d = 0$ nm corresponding to region (iii) in (a). Yellow dashed lines indicate approximate B, at which the circular orbits pick up an integer number of π AB phase. d^3I/dV_S^3 values in (a)-(e) were numerically calculated from the dI/dV_S acquired through a lock-in measurement. The set point used to acquire the tunneling spectra in (a)-(e) was $I = 1$ nA, $V_S = -60$ mV, with a 2 mV ac modulation. (f) Schematic of coupled double MLG QD, and figure-eight and circular orbits, a degenerate time-reversed figure-eight orbit also exists but is not shown here for clarity. (g) Schematic of the constructive (represented by yellow dot) and destructive (represented by black dot) interference at the center of the figure-eight orbit for different energy levels and its tuning by B through AB effect.

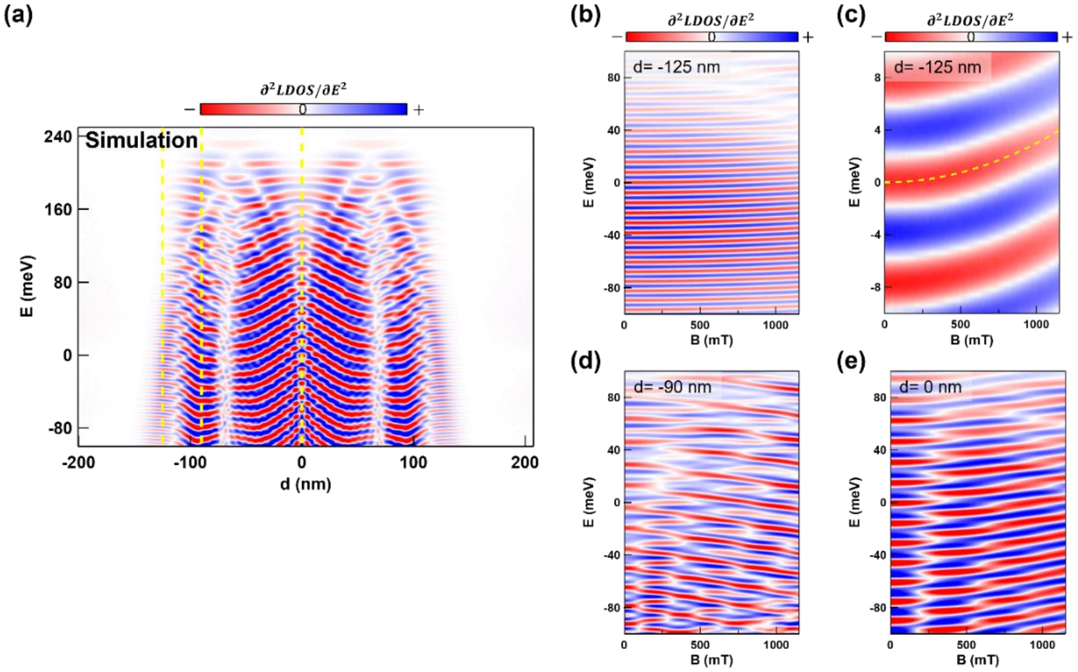

Figure 5.13 TB simulation results for a coupled double MLG QD. (a) Simulated $\partial^2 LDOS/\partial E^2(E,d)$ for a coupled double MLG QD with two dots separated by 140 nm. (b)-(e) Simulated $\partial^2 LDOS/\partial E^2(E,B)$ for the double dot shown in (a) at $d = -125$ nm (b,c), $d = -90$ nm (d) and $d = 0$ nm (e), these locations are indicated by yellow dashed lines in (a). The yellow dashed line in (c) indicates the parabolic energy shift of QD states in B, with a shifting rate of 3 $\mathrm{meV/T^2}$.

5.3.2 Van Vleck Paramagnetic Shift

We now discuss how the unique B response observed in region (i) corresponds to the emergence of a Van Vleck paramagnetic shift, due to the relativistic nature of our artificial molecule. Because each of the two rings of the figure-eight orbit have reversed current flow directions, their $\vec{\mu}$ are in opposite directions but with the same magnitude. Therefore, the net $\vec{\mu}$ of an entire figure-eight orbit will be zero, hence explaining the disappearance of linear splitting in B at regions (i) and (iii). Moreover, the positive parabolic energy shift for holes observed at region (i) is caused by a Van

Vleck paramagnetic shift, which is a second order perturbative B response[153]. Classically, this effect stems from a Lorentz force that expands (contracts) orbits with μ aligned (anti-aligned) to B, resulting in an increase (decrease) of μ. The quenching of the first order B effect in figure-eight orbits helps the detection of this second order effect. Importantly, for non-relativistic systems such as natural atoms[154] and semiconductor QDs[147,148,154], a Larmor diamagnetic shift due to the change of electron orbital velocity in B also exists and is usually stronger than the Van Vleck paramagnetic shift. However, for MLG QDs, the Larmor diamagnetic shift is absent because of the constant velocity of massless Dirac fermions. Alternatively, this can be understood as resulting from the graphene Hamiltonian in B lacking a B^2 term that produces Larmor diamagnetism in non-relativistic systems. Such a B induced response is thus unique to ultra-relativistic artificial atoms and molecules.

5.3.3 Aharonov–Bohm effect

Finally, we discuss the origin of the staggered red stripe patterns in $dI^3/dV_S^3(V_S, B)$ plot at region (iii) and attribute them to Aharonov–Bohm (AB) oscillations occurring at region (iii). When a particle returns to its original position after traveling along a closed path, constructive (destructive) interference leading to enhanced (reduced) $LDOS$ occurs if the action along the closed path $\frac{1}{\hbar}\oint \boldsymbol{p} \cdot d\boldsymbol{q}$ equals an even (odd) number of π. Here $\boldsymbol{p}$ and $\boldsymbol{q}$ are the canonical momentum and position coordinates. As shown in Figure 5.12g, two distinct eigen energies exist for figure-eight orbits with constructive (yellow dot) and destructive (black dot) interference at the figure-eight orbit center, respectively. This is because charges return to this location after traveling half of a figure-eight orbit. By applying an external B, the AB effect causes the pickup of additional phases ($\Delta\varphi = \frac{-e\Phi_B}{\hbar}$, where Φ_B is the magnetic flux through each circular segment) with opposite signs for the two circular orbits flowing in opposite directions. As a result, the energy level of the figure-eight orbit does not change in B to first order, but the interference type at the figure-eight orbit center switches depending on the amount of $\Delta\varphi$ picked up by each circular segment (Figure 5.12g). This explains the staggered pattern observed at region (iii) (Figure 5.12e), where red and blue stripes (corresponding to constructive and destructive interference, respectively) alternate at a constant V_S in B. This observed AB oscillation in the $LDOS$ intensity of coupled MLG QDs can also be potentially used for B sensing.

Finally, to further support our interpretation, we compared the assigned $\Delta\varphi$ in Figure 5.12e with the expected AB phase pick-up based on our experimental double dot geometry. For QD states around $V_S = 0$ mV as shown in Figure 5.12e, the first dI/dV_S intensity flip occurs at around $B_1 = 150\ \mathrm{mT}$. Next, by checking where the double splitting of QD states first appears in Figure 5.12a, we can estimate the radius of the circular segment of the corresponding figure-eight orbit for the states around $V_S = 0$ mV to be $r_0 \approx 65\ \mathrm{nm}$. Thus, the corresponding AB phase for the circular segments of figure-eight orbits when dI/dV_S intensity flip occurs for the first time can be estimated as $\Delta\varphi_1 = \frac{eB_1\pi r_0^2}{\hbar} \approx 0.96\pi$, which is close to the expected π phase picking up.

5.4 Conclusions

In conclusion, we use magnetic field resolved STS successfully observed giant $\vec{\mu}$ and large orbital Zeeman splitting in artificial relativistic atoms formed with single MLG QDs. We also observed strong Van Vleck paramagnetic shifts and AB oscillations in artificial relativistic molecules formed with coupled double MLG QDs. Our findings add fundamental insight into relativistic quantum phenomena in solid state systems and pave the way towards new modalities of B sensing that utilizes massless Dirac fermions. Furthermore, the phenomena observed in this work stem from long lived states near MLG QD boundaries; thus, resembling persistent currents in metallic rings[155,156]. Notably, our work demonstrates the potential for realizing giant and tunable persistent currents in MLG QDs. Such currents can potentially be used in quantum information processing[157] and quantum simulation[158].

Chapter 6 Visualizing the Effect of Fermi Surface Symmetry and Berry Curvature Sign on BLG QD Wavefunctions

In the previous chapter, we studied the unique B response of MLG QDs due to their relativistic nature. In this chapter, I will switch to BLG QDs, which is an equally interesting system compared to MLG QDs. As introduced in chapter 1, different from circularly symmetric low energy MLG bands, low energy BLG bands have a three-fold rotational (C_3) symmetry. In addition, an out of plane electric field can induce a band gap and non-zero Berry curvature in BLG bands, which is a property that also does not exist in MLG. These attributes make BLG QDs a unique platform to investigate the effect of Fermi surface symmetry and non-zero Berry curvature on QD states. In this chapter, I will present our results on the wavefunction mapping of BLG QDs that were created with the two-step tip bias pulsing technique described in chapter 2. We discovered that the spatial distribution of BLG QD wavefunctions can reveal both the Fermi surface symmetry and Berry curvature sign of BLG bands. The results shown in this chapter have been published in reference[60].

6.1 Introduction

The visualization and manipulation of electronic states in quantum materials is of fundamental interest and has the potential for quantum information processing technologies[159,160]. Among the numerous quantum material platforms that are under consideration for these advanced technologies BLG is highly attractive because it possesses an electric field tunable band gap[161]. This unique material property permits the realization of electrostatic QDs with pristine boundaries and high flexibility to enable charge carrier confinement and QD state formation[31,32]. In addition, BLG QDs have long spin decoherence lifetimes[74], controllable quantum degrees of freedom[30,36], and nontrivial band topology[162]. These traits are all favorable for quantum information technology. At the time of this study, experimental progress with BLG QDs interfaced with hBN have just achieved spin-valley resolved single electron charging[30,64] and magnetic field controlled valley splitting[30,36], which are important steps towards BLG QD's application in quantum information. More recently, spin and valley blockade[70,71], and long spin and valley relaxation times were experimentally demonstrated[43,48]. These new experimental advances with BLG QDs not only brought BLG QDs closer to application in quantum information technology, but also showed how fast BLG QD research is advancing. Apart from these achievements, the understanding of BLG QD wavefunction is also important, because it determines the energy spectrum and allowable transitions between QD states. These energetics govern the preparation, manipulation, and readout of quantum information[163]. At the time of this study, theoretical predictions for BLG QD wavefunction shape were abundant[134,136,137,164-166], but the experimental validation of these predictions was still lacking.

6.2 Wavefunction Mapping and Spatially Resolved STS of BLG QD States

In this work, we use a low-temperature STM to probe the wavefunctions of in-situ created BLG QDs. Figure 6.1a shows the schematic of the measurement setup. The STM tip is grounded, a bias voltage V_S together with an ac voltage V_{ac} is applied between the STM tip and BLG QD, which allowed us to perform spatially resolved STS measurements and energy resolved dI/dV_S mappings. The BLG QD here is defined by a circular pn junction, which is created in a BLG/hBN heterostructure with the two-step pulsing technique described in section 2.3.2 (detailed procedure can be found in Appendix E). In addition, a back gate voltage V_G can be applied to tune the doping and potential well of BLG QD.

To avoid the influence of adsorbates in our studies we create circular BLG pn junctions in at least $200 \times 200\ \mathrm{nm}^2$ adsorbate free regions. Figure 6.1b shows the topography of one such region. Figure 6.1c shows an atomically resolved topography at the center of the region where a circular BLG p-n junction was created. Bright topographical features that form a triangular lattice are clearly visible, as expected for BLG[167,168]. We overlay the atomic structure of BLG in this panel and use it to identify three of the four atoms within the BLG unit cell: A_{top}, B_{top}, and B_{bottom}. The fourth atom (A_{bottom}) on the bottom layer is obscured by B_{top}. In such a triangular lattice two orientations exist for the apparent triangles, we denote these orientations as α (dashed blue line that encloses B_{top}) and β (dashed yellow line that encloses B_{bottom}).

By performing constant sample bias dI/dV_S maps we can image the wavefunctions of BLG QD states. Figure 6.1d,e shows two dI/dV_S maps taken at two different energies $V_s = -10.5\ \mathrm{mV}$ and $V_s = -12.5\ \mathrm{mV}$ with the same back gate voltage ($V_G = -5\ \mathrm{V}$). A dashed yellow line provides a guide to the eye for the QD boundary. The electronic states outside of the BLG QD exhibit are approximately circularly symmetric, which is consistent with the QD boundary shape. In contrast, the states within the BLG QD display a rich nodal pattern that breaks rotational symmetry. For example, in Figure 6.1d there exists a "Y" shaped feature and three bright nodes around the BLG QD center. On the other hand, the pattern in Figure 6.1e does not have a “Y” shaped feature, instead it contains six bright nodes around the QD center. Despite the difference between the details of these dI/dV_S map patterns, a clear C_3 symmetry is shared between them. And with a closer inspection of these triangular BLG QD wavefunctions, we further notice that their triangular distributions are both aligned with the α triangle orientation of the BLG lattice.

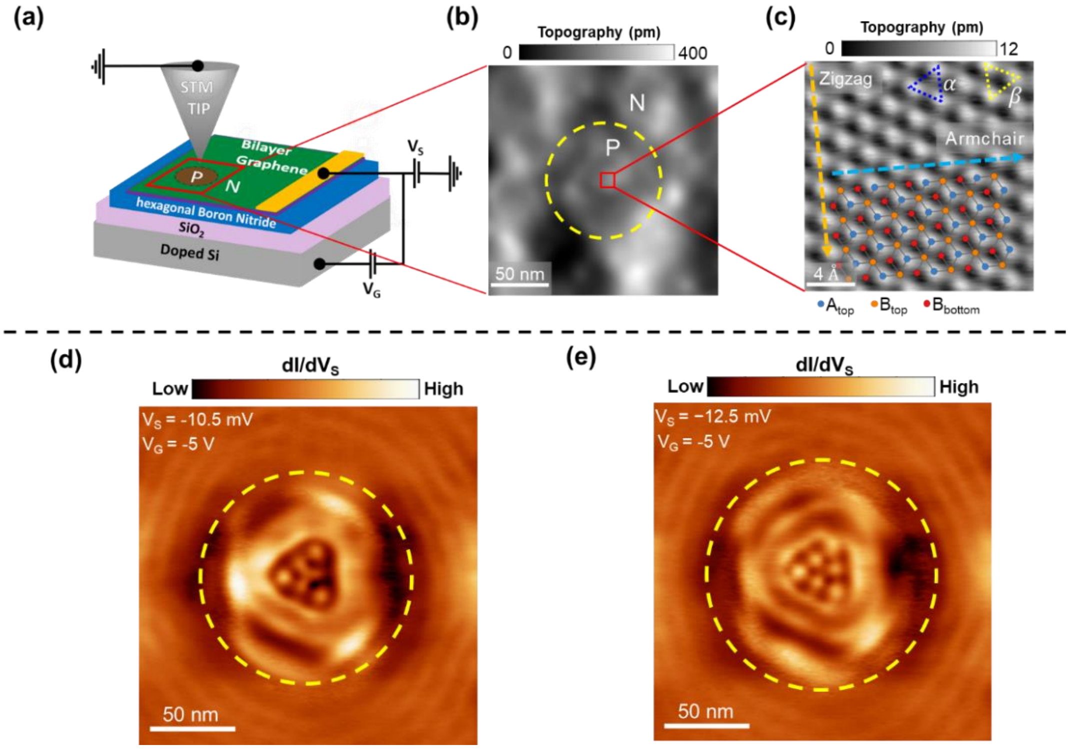

Figure 6.1 Wavefunction mapping of a circular BLG QD. (a) Schematic of a STM tip probing a BLG QD that is defined by a circular p-n junction. (b) BLG topography after the creation of a circular BLG QD. Yellow dashed line denotes the QD boundary. The scanning parameters used to acquire the topography were $V_S = -8.5$ mV, $I = 0.3$ nA. (c) Atomically resolved BLG topography at the QD center, the scanning parameters were $V_S = -100$ mV, $I = 2.5$ nA. BLG crystal structure is overlaid on the topography. The orange and blue arrows indicate the zigzag and armchair directions of BLG structure, respectively. The blue and yellow triangles represent the two possible orientations for the BLG lattice by connecting the three closest bright atoms. (d)-(e) Constant bias dI/dV_S maps of the BLG QD created at the pristine BLG region shown

in (b). The yellow dashed line in (d) and (e) denotes the boundary between p and n doped regions. Scanning parameters used to acquire the data were $V_S = -10.5$ mV (d) and $V_S = -12.5$ mV (e), both with $I = 0.3$ nA and a 2mV ac excitation.

Such an alignment between the BLG QD wavefunction orientation and the α triangle orientation of BLG lattice is not a simple coincidence and highly reproducible. Figure 6.2a,b shows two additional dI/dV$_S$ maps measured from another two different BLG QDs with p-type central doping created with the two-step tip pulsing technique. Triangular QD wavefunction with clear C_3 symmetry is observed in both cases. Figure 6.2c,d shows the atomically resolved topography at the center of the two BLG QDs shown in Figure 6.2a,b, respectively. Although these two BLG QDs were created in the same BLG/hBN sample, the BLG lattice orientations in Figure 6.2c,d are rotated by 180° with respect to each other. We believe this is due to the fact that exfoliated BLG flakes can contain adjacent AB and BA stacked regions[169]. But in both cases, it is clear that the BLG QD wavefunction orientation is aligned with the α triangle of BLG lattice.

To attain a more comprehensive understanding of the spatial distribution for BLG QD states, we further performed spatially resolved STS measurements for BLG QDs. Figure 6.3 shows the color plot of experimentally measured $dI/dV_S(V_S, d)$ for the BLG QD shown in Figure 6.1d,e. These measurements were done along lines that are aligned with the BLG zigzag and armchair directions across the QD center. A distinct nodal level structure with high dI/dV_S amplitude is visible and is surrounded by a dark envelope, which corresponds to the BLG band gap, in each of the two plots. Moreover, for the dI/dV_S spectra taken along the armchair direction (Figure 6.3a), the nodal distribution exhibits an asymmetric dI/dV_S intensity with respect to the QD center. On the other hand, along the zigzag direction (Figure 6.3b), the nodal distribution of the same BLG QD exhibits a clear mirror symmetry with respect to the QD center. Such a difference between QD state distribution along the armchair and zigzag directions is in agreement with the observation of triangular shaped BLG QD wavefunctions aligned with the α triangle of BLG lattice. The well-defined difference seen between the armchair and zigzag directions indicates that the broken rotational symmetry of BLG QD wavefunctions observed in Figure 6.1d,e persists for a wide energy range.

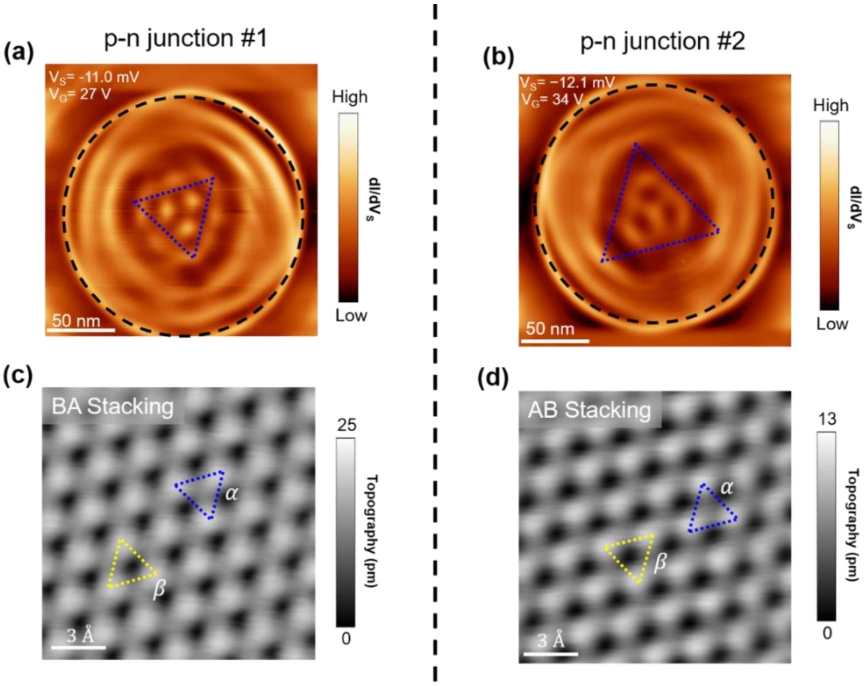

Figure 6.2 Reproducibility of the alignment between BLG QD wavefunction orientation and BLG lattice orientation. (a)-(b) Constant bias dI/dV_S maps of two BLG QDs that were created at two different locations on a BLG/hBN heterostructure. The dI/dV_S map in (a) was taken at $V_G = 27$ V with scanning parameters $I = 0.1$ nA, $V_S = -11.0$ mV, $V_{ac} = 1$ mV. The dI/dV_S map in (b) was taken at $V_G = 34$ V with scanning parameters $I = 0.5$ nA, $V_S = -12.1$ mV, $V_{ac} = 1.5$ mV. The black dashed circle in (a) and (b) denotes the geometry of the BLG p-n junction. The blue dashed triangle in (a)

and (b) indicates the orientation of the triangular BLG QD wavefunction. (c)-(d) Atomically resolved BLG topography at the center of p-n junction#1 and p-n junction#2, respectively. Scanning parameters were $I = 2.0$ nA, $V_S = -60$ mV for (c) and $I = 2.5$ nA, $V_S = -50$ mV for (d). The blue and yellow dashed triangles indicate the α and β triangle of the BLG lattice, respectively, in both (c) and (d).

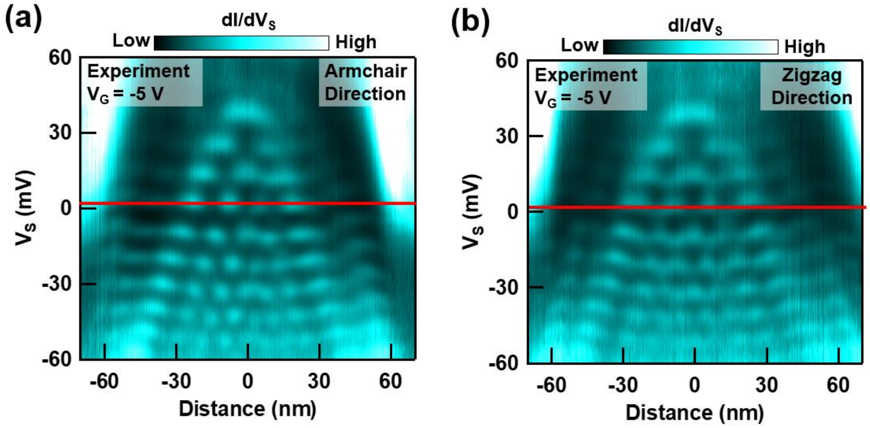

Figure 6.3 Spatially resolved energy levels inside a BLG QD along armchair and zigzag directions. (a)-(b) Measured dI/dV_S spectra along BLG's armchair (a) and zigzag (b) directions at $V_G = -5$ V. The "0" on the horizontal axis in (a) and (b) denotes the center of the QD. The set point used to acquire the tunneling spectra was $I = 1$ nA, $V_S = -60$ mV, with a 2 mV ac modulation

6.3 Origin of the C_3 Symmetry of BLG QD Wavefunctions

Insight into the origin of our observations can be gained by considering the behavior of BLG charges corralled within a circular electrostatic potential well that is defined by a circular p-n junction. This setup has been extensive studied with theories[134,136,164-166] prior to our experimental observations, however, all of them predicted circularly symmetric BLG QD wavefunctions akin to those seen in MLG QDs[53,54,63], which is contradictory to the C_3 symmetrical BLG QD wavefunctions observed in our experiments.

Interestingly, the BLG QD wavefunction observed in our experiments exhibit the same symmetry as those trigonally warped low energy BLG bands when γ_3

hopping is considered as discussed in section 1.2.2. This connection suggests an explanation for our findings and is also supported by a BLG QD theory[137] published several months after our experimental findings, in which the γ_3 hopping is considered. To verify this possibility, we proceeded by using the TB model described in section 4.1 to simulate BLG QDs that incorporate γ_3 hopping and a band gap. The potential well and the size of the band gap used in model were extracted from the experiment as discussed in section 4.1.2, the potential well extraction example given there (Figure 4.2) actually is for the BLG QD shown in Figure 6.1d,e. Figure 6.4 shows the BLG hopping parameter definition and the BLG lattice orientation used in our BLG QD TB model. The BLG armchair and zigzag directions, and the α and β triangles of BLG lattice are well defined in the model.

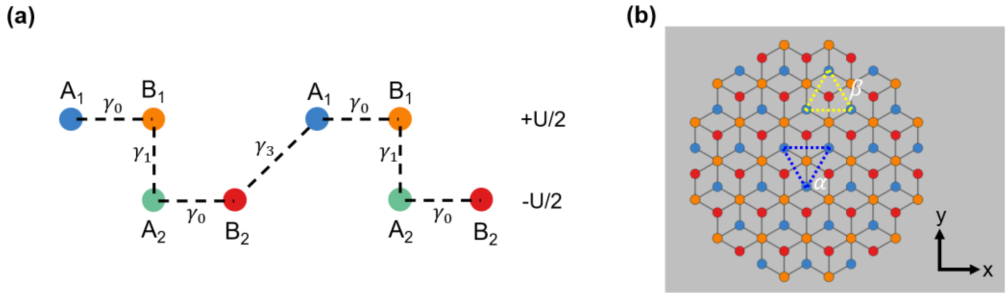

Figure 6.4 Schematics of the included BLG hopping parameters and BLG lattice orientation in our BLG QD TB model. (a) Schematic side view of two BLG unit cells. There are four atoms in the unit cell, A1 and B1 are on the top layer, and A2 and B2 are on the bottom layer. The dashed lines indicate the definitions of all the hopping parameters in the TB model. The $+U/2$ and $-U/2$ indicates the definition of interlayer potential difference in the TB model. (b) Top view of the BLG crystal structure. The atom colors in (b) are the same as in (a). The blue dashed triangle and yellow dashed triangle denote the α and β triangle of the BLG lattice, respectively. The x, y coordinate axis defines the orientation of BLG lattice in the TB model.

Figure 6.5 shows the simulated $LDOS(E,d)$ along BLG armchair (Figure 6.5a) and zigzag (Figure 6.5b) crystallographic directions that cross the QD center. Remarkably, the nodal distribution and dark envelope in the simulated $LDOS(E,d)$ closely resemble the experimentally measured $dI/dV_S(V_S,d)$. Apart from the similar energy spacing between the nodal patterns, the mirror symmetry of the $LDOS$ intensity with respect to the QD center is preserved along the zigzag direction but not along the armchair direction, which is in agreement with our experimental data. We also notice the relative intensity of the bright envelope at the top left and top right corner in the simulated $LDOS(E,d)$ map is obviously much weaker than those in the experimental $dI/dV_S(V_S,d)$ data. This is caused by the tip-sample distance changing during the $dI/dV_S(V_S,d)$ measurement due to the spatially varying $LDOS$ distribution of BLG QDs, which is discussed in more detail in section 2.2.2. Figure 6.6a,b shows the simulation result that considers this tip-sample distance changing effect, which I name it as simulated $dI/dV_S(V_S,d)$. Now extremely bright envelopes similar to the experimental data appear in the simulation result. Figure 6.6c,d shows the comparison between experimental and simulated constant energy dI/dV_S profiles, which more clearly demonstrated the good agreement between experiment and simulation on the mirror asymmetric and mirror symmetric dI/dV_S intensity distribution along BLG armchair (Figure 6.6c) and zigzag (Figure 6.6d) directions, respectively.

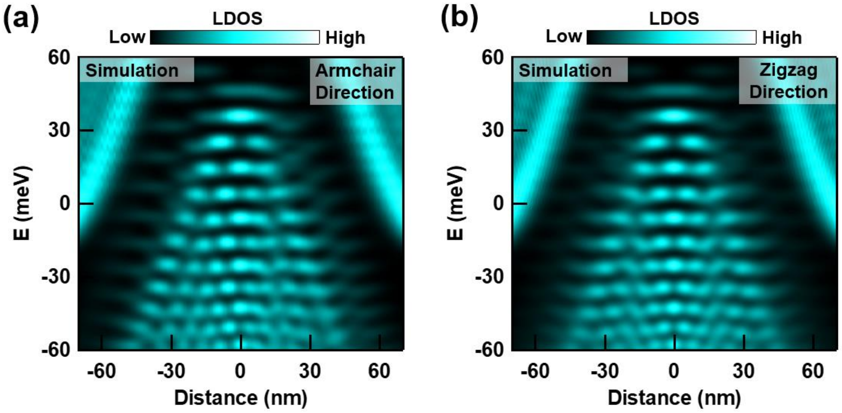

Figure 6.5 Simulated $LDOS(E, d)$ for BLG QD. (a) Calculated $LDOS(E, d)$ along the BLG armchair direction from the negative side to the positive side along the x coordinate axis in Figure 6.4b. (b) Calculated $LDOS(E, d)$ along the BLG zigzag direction from the negative side to the positive side along the y coordinate axis in Figure 6.4b. The “0” on the distance axis in (a) and (b) denotes the QD center. The $LDOS$ in (a) and (b) includes only the contribution from BLG top layer (A1 and B1 sublattices). A constant 60 meV band gap (top layer was set at a higher energy than the bottom layer, $U = +60$ meV) and $\gamma_3 = -0.38$ eV was included in the model.

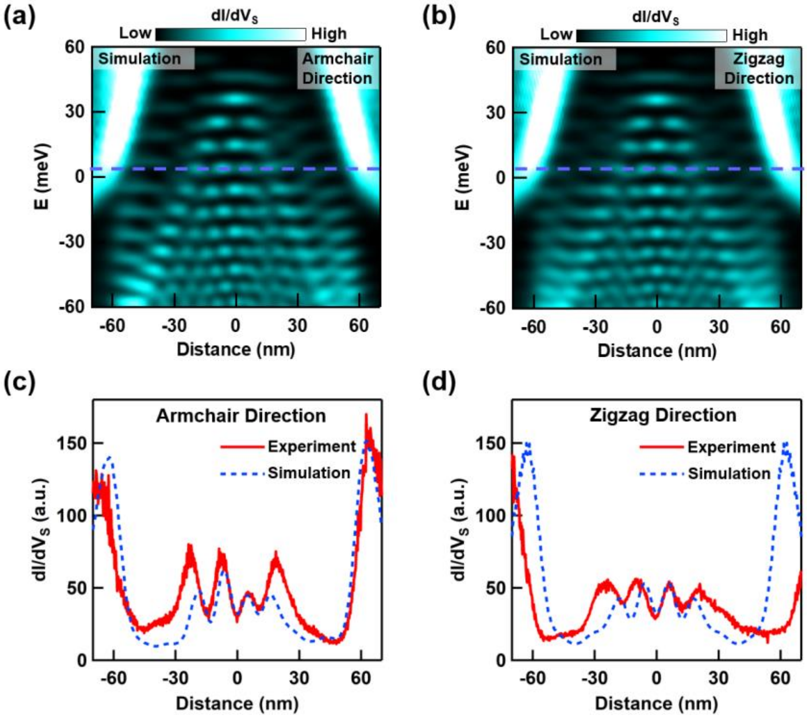

Figure 6.6 Simulated $dI/dV_S(V_S, d)$ for BLG QD and comparison with experiment. (a)-(b) Simulated $dI/dV_S(V_S, d)$ for BLG QD, which is modified from the simulated

$LDOS(V_S, d)$ shown in Figure 6.5 by considering the tip-sample distance change in experiment with Equation 2.6. (c)-(d) Comparison between experimental and simulated constant energy dI/dV_S profile along the BLG armchair (c) and zigzag (d) directions. The experiment dI/dV_S profile was acquired from Figure 6.3 at $V_S = 2$ mV (indicated by the red solid line). The simulated dI/dV_S profile was acquired from (a) and (b) accordingly at $E = 4$ meV (indicated by the blue dashed line).

Apart from the simulated and experimental $dI/dV_S(V_S, d)$, a good agreement is also seen between experimental dI/dV_S maps and simulated constant energy $LDOS$ maps. To ensure that the compared simulated $LDOS$ maps and experimental dI/dV_S maps correspond to the same BLG QD states, the energies chosen for $LDOS$ maps and dI/dV_S maps for comparison are based on matching the nodal structure in the experimental $dI/dV_S(E, d)$ and simulated $LDOS(E, d)$. Figure 6.7 shows some example comparisons. Figure 6.7a,b shows the experimentally measured $dI/dV_S(E, r)$ and calculated $LDOS(E, d)$ along BLG armchair direction for the same BLG QD shown in Figure 6.3 but at $V_G = 0$ V. Then Figure 6.7c-f shows the comparison between experimental dI/dV_S map and calculated $LDOS$ map at the energies of the second dip (Figure 6.7c,d) and the third peak (Figure 6.7e,f) of the central nodal structure in Figure 6.7a,b, whose energies are marked by the red and yellow arrows in Figure 6.7a,b, respectively. A very good agreement is observed between the experimental dI/dV_S maps and simulated $LDOS$ maps. For example, they both have triangular shaped patterns with similar nodal distribution. In addition, the orientations of the triangular patterns in experiment and simulation are both aligned with the α triangle of BLG lattice.

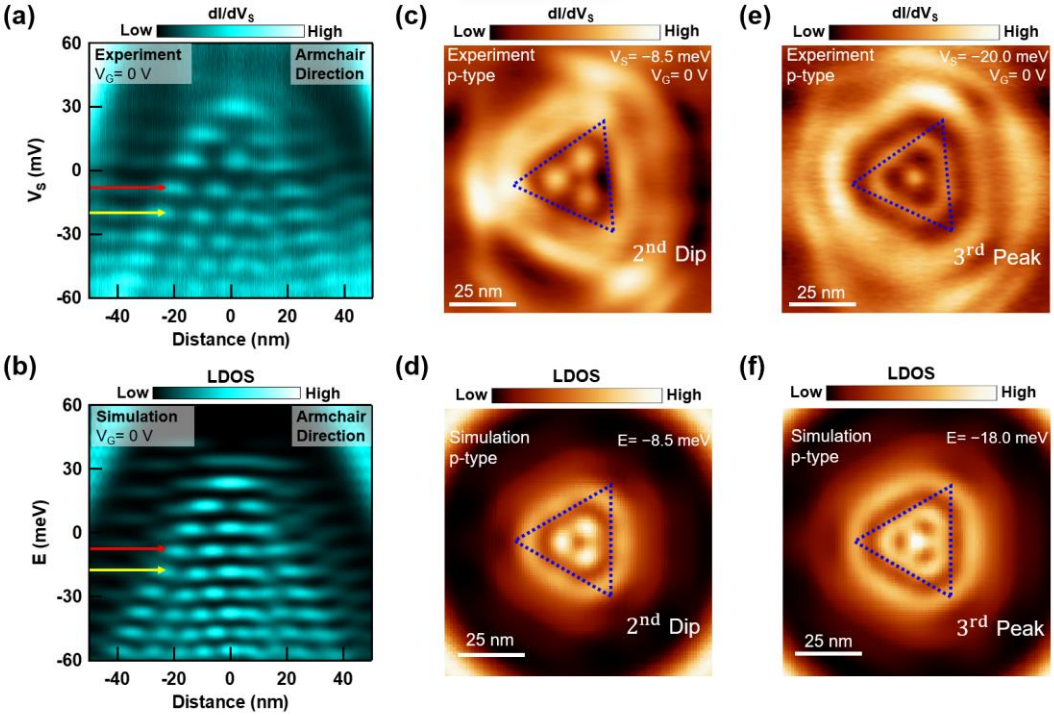

Figure 6.7 Comparison between experimental dI/dV_S maps and simulated $LDOS$ maps for BLG QDs. (a) Experiment $dI/dV_S(V_S, d)$ taken along the BLG armchair direction for the same BLG QD shown in Figure 6.3 but at $V_G = 0$ V. The setpoint used for this measurement was $I = 1$ nA, $V_S = -60$ mV with a 2 mV ac modulation. (b) Simulated $LDOS(E, d)$ along BLG armchair direction for a BLG QD, only A_1 and B_1 sublattice contribution was considered. (c)-(d) Experimental dI/dV_S map (c) and simulated $LDOS$ map (d) for BLG QD states at energies indicated by the red arrow in (a) and (b), respectively. (e)-(f) Experimental dI/dV_S map (e) and simulated $LDOS$ map (f) for BLG QD states at energies indicated by the yellow arrow in (a) and (b), respectively.

Crucially, we found that the agreement between experiment and simulation breaks down if either γ_3 or a band gap is not included in the BLG QD TB model. Figure 6.8a-c shows the calculated $LDOS(E, d)$ along the armchair direction for BLG QDs with the same potential well but with different γ_3 hopping and interlayer potential difference U in the TB model. For $\gamma_3 \neq 0$ and $U \neq 0$ (Figure 6.8a), the calculated $LDOS(E, d)$ reproduce the dark envelope and broken mirror symmetry with respect to the center of the QD as observed in experiment (Figure 6.3a). In contrast, for $\gamma_3 = 0$ and $U \neq 0$ (Figure 6.8b), the calculated $LDOS(E, d)$ does not reproduce the broken mirror symmetry with respect to the QD center. Then for $\gamma_3 \neq 0$ and $U = 0$ (Figure 6.8c), the dark envelope seen in the experiment does not appear in the calculated $LDOS(E, d)$. Figure 6.8d shows the comparison between the extracted constant energy $LDOS$ profiles from Figure 6.8a-c (the energy is indicated by the dashed lines in each figure). Only the constant energy $LDOS$ profile with $\gamma_3 \neq 0$ and $U \neq 0$ agrees with the constant energy dI/dV_S profile extracted from experiment as shown in Figure 6.6c. Therefore, it is necessary to have both trigonal waring ($\gamma_3 \neq 0$) and a band gap ($U \neq 0$) in the TB model to reproduce our experiment results.

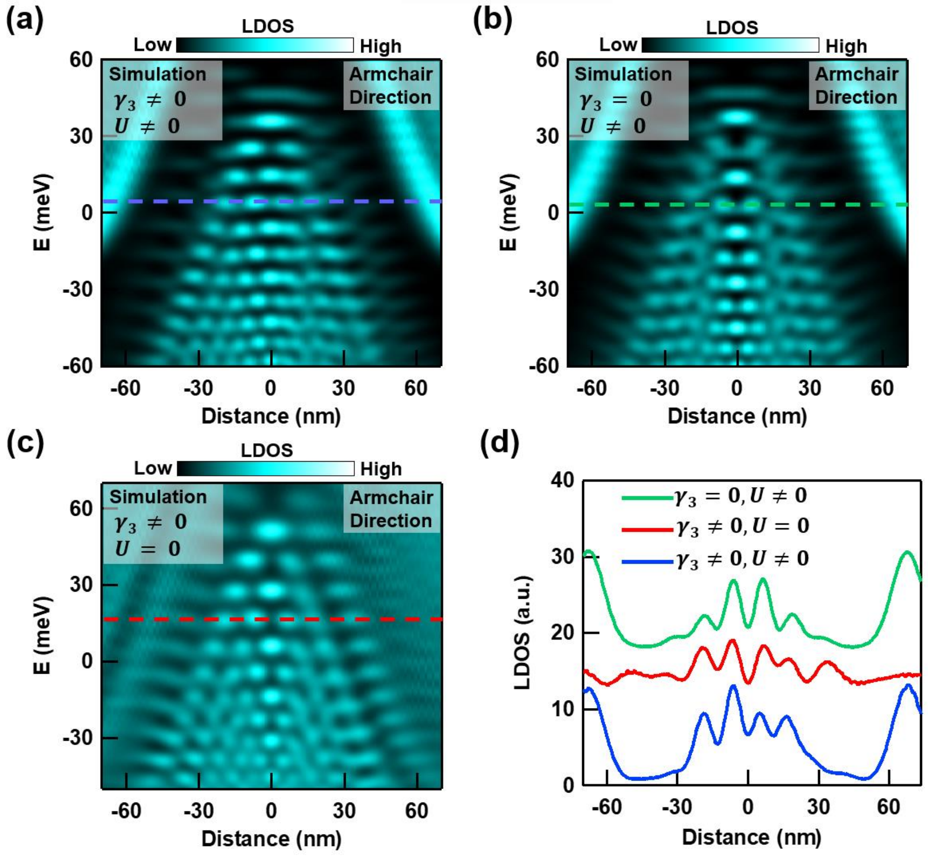

Figure 6.8 Calculated $LDOS(E, d)$ from BLG QD TB models with different γ_3 and U configurations. (a)-(c) Calculated $LDOS(E, d)$ along the BLG armchair direction with $\gamma_3 = -0.38$ eV, $U = 60$ meV (a), $\gamma_3 = 0$, $U = 60$ meV (b), and $\gamma_3 = 0$, $U = 0$ (c). Only the BLG top layer (A1 and B1 sublattices) contribution is considered for $LDOS$. (d) Comparison between the constant energy $LDOS$ line profile from (a)-(c). The energies of the $LDOS$ line profiles are indicated by the blue dashed line in (a), green dashed line in (b) and red dashed line in (c), accordingly.

This conclusion can be further verified by comparing the experimental dI/dV_S maps with calculated constant energy $LDOS$ maps that incorporates different γ_3 and U conditions in the BLG QD TB model. With $\gamma_3 = 0$ and $U = 0$ (Figure 6.9a) or $\gamma_3 = 0$ and $U \neq 0$ (Figure 6.9b), the calculated $LDOS$ maps both have circular symmetry. This does not agree with the observed C_3 symmetry in experimental dI/dV_S maps. When $\gamma_3 \neq 0$ and $U = 0$ (Figure 6.9c), the calculated LDOS map has a weak C_6 symmetry near the center of the BLG QD. This also does not agree with the experiment. Only when $\gamma_3 \neq 0$ and $U \neq 0$ (Figure 6.9d), the experimentally observed C_3 symmetry is reproduced in the calculated $LDOS$ map. To make sure Figure 6.9a-d compares similar BLG QD states, the energy of the fourth peak in the $LDOS$ spectrum at the QD center is used in each case.

By comparing the shape of triangular patterns in simulated $LDOS$ maps with experimental dI/dV_S maps, we can further get insight on the value of the γ_3 hopping term for BLG from our experiment. Figure 6.10 shows one experimental dI/dV_S map and several calculated $LDOS$ maps with different γ_3 values used in the model. By comparing these simulation results with the experiments, we can acquire an upper bound of -0.38 eV and a lower bound of -0.12 eV for the value of γ_3. In addition, we note that our experiment enables the determination of the sign of BLG γ_3 hopping term.

A wrong sign of BLG γ_3 hopping was used in many BLG experimental and theoretical works, a more detailed discussion about this issue can be found in reference[170].

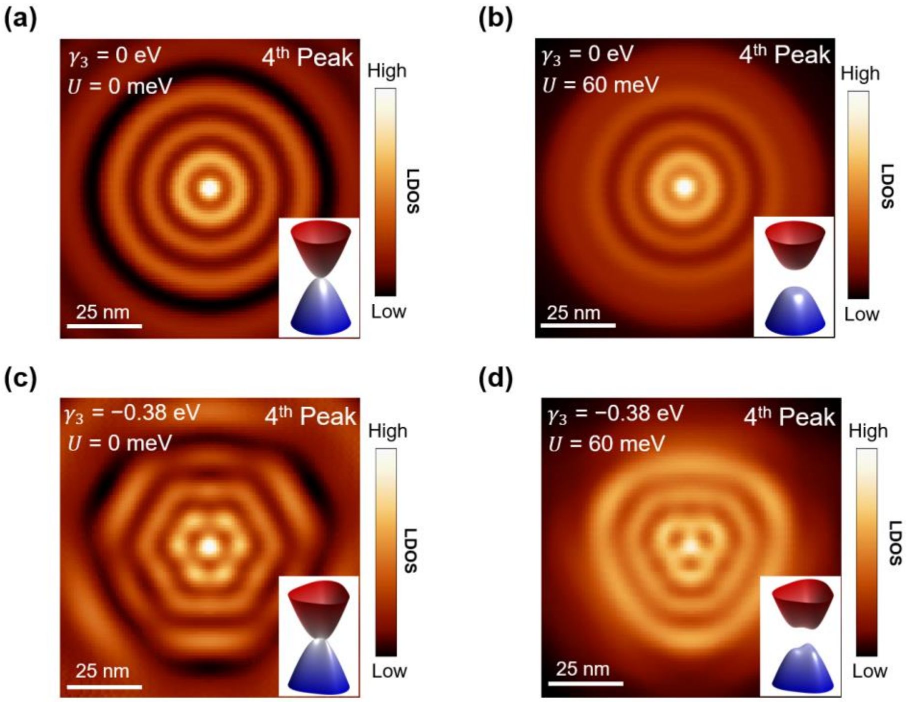

Figure 6.9 Calculated $LDOS$ maps with different γ_3 and U configurations. (a)-(d) Constant energy $LDOS$ map with $\gamma_3 = 0$ and $U = 0$ (a), $\gamma_3 = 0$ and $U = 60$ meV (b), $\gamma_3 = -0.38$ eV and $U = 0$ (c), and $\gamma_3 = -0.38$ eV and $U = 60$ meV (d). The energy of the $LDOS$ maps in (a)-(d) correspond to the fourth $LDOS$ peak at the QD center. Only the LDOS contribution from A_1 and B_1 sublattices are considered. The inset at the bottom right corner in (a)-(d) shows the BLG band structure (energy range is -120 meV to 120 meV) near K valley with the corresponding γ_3 and U values.

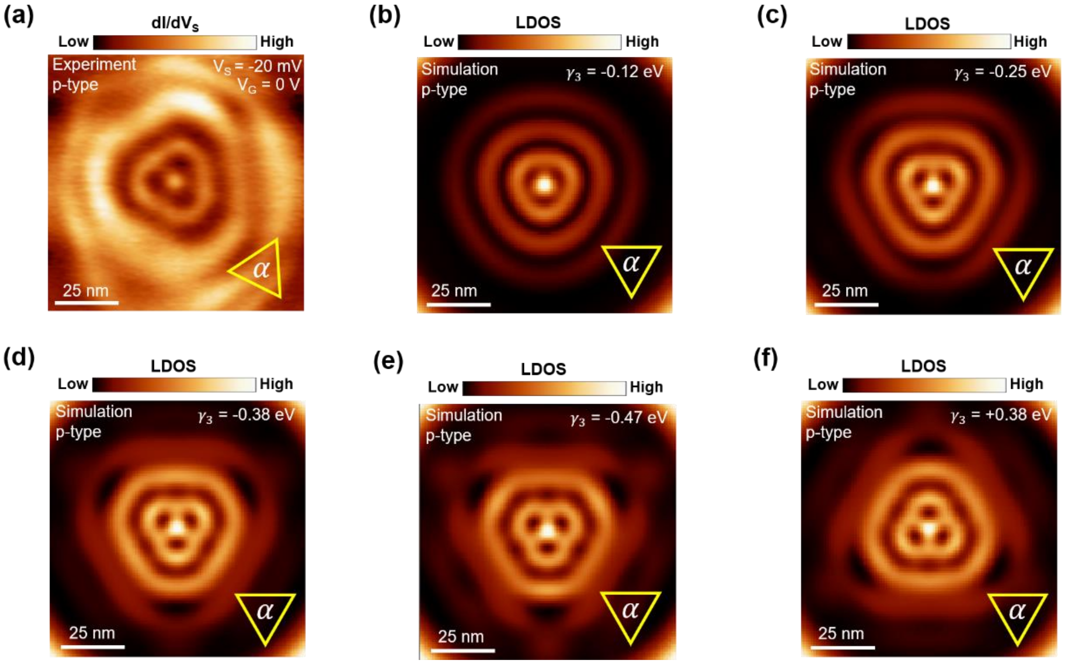

Figure 6.10 Simulated BLG QD $LDOS$ maps with different γ_3 values. (a) The same experimentally measured constant energy dI/dV_S map as shown in Figure 6.7e, the yellow triangle depicts the orientation of the α triangle of BLG lattice. (b)-(f) Simulated $LDOS$ maps for a p-type BLG QD with different γ_3 values in the TB model, the value of γ_3 used for each simulation is shown at the top right corner of each $LDOS$ map. The yellow triangle in (b)-(f) shows the orientation of the α triangle of BLG lattice in the simulation.

6.4 Effect of Berry Curvature Sign on BLG QD Wavefunction Rotation

The observed strong influence of gapped and anisotropic BLG bands for BLG QD states has intriguing implications for accessing the nontrivial band geometrical properties of gapped BLG bands. As discussed in section 1.2.2, gapped BLG bands host non-zero Berry curvatures (Figure 1.12). A very recent STM study demonstrated for the first time that the π Berry phase (another quantity of band geometrical properties) of MLG can be extracted from quantum interference patterns[171]. But up to date, no study has investigated Berry curvature's effect on quantum interference patterns. QD wavefunctions in a sense can be understood as quantum interference patterns within a confinement potential well, as a result, BLG QD with gapped BLG bands offers the opportunity to investigate this problem.

To explore the possible effect of Berry curvature on BLG QD wavefunctions, we start with using TB simulations to calculate the $LDOS$ maps of BLG QDs with p-type and n-type central doping and with different interlayer potential difference polarities ($U > 0$ and $U < 0$). As shown in Figure 6.11a, the different types of QDs with gapped and anisotropic bands enable trapping of low energy holes (upper panel) and low energy electrons (lower panel). Simulated $LDOS$ maps for analogous QDs with the same potential well curvature and gap size but with different polarity for the interlayer potential difference are shown in Figure 6.11b-e. First, we focus on BLG QDs with p-type central doping (Figure 6.11b,c). We find that the orientation of the $LDOS$ distribution for these QDs exhibits a 180^{o} rotation between $U = +60$ meV and $U = -60$ meV. In addition, for $U = +60$ meV, the $LDOS$ pattern is aligned with the α triangle of BLG lattice, while for $U = -60$ meV the $LDOS$ pattern is aligned with the β triangle of BLG lattice. A similar rotation and $LDOS$ pattern alignment with respect to the BLG lattice can also be seen for QDs with n-type central doping when U changes sign (Figure 6.11d,e).

The rotation in the simulated $LDOS$ patterns indicates that a property of BLG has been modified between the different interlayer potential difference polarity configurations. The band structure of BLG does not depend on the interlayer potential difference polarity. In contrast, the Berry curvature of BLG bands does depend on the sign of the interlayer potential difference[84,89,172]. For example, for confined holes, the Berry curvature of BLG's valence band in the K valley is negative for $U = +60$ meV (see inset of Figure 6.11b). The Berry curvature of the same band is positive for $U = -60$ meV (see inset of Figure 6.11c). A similar Berry curvature sign flip can be seen for QDs with n-type central doping as well (insets of Figure 6.11d,e). Here we focus on one valley because the Berry curvature sign flip also occurs in the other valley when the interlayer potential polarity changes. The simulated $LDOS$ patterns in Figure 6.11b-e suggest that the Berry curvature sign of confined quasiparticles has a measurable effect on the spatial distribution of BLG QD wavefunctions.

To experimentally verify this intriguing possibility, we created a circular BLG QD with n-type central doping at the same region where the p-type BLG QD as shown in Figure 6.1d,e was created (detailed QD creation procedure see Appendix E). We used this approach because in our experiment we were unable to modify the polarity of the interlayer potential difference and U is always positive. Nonetheless, our simulations in Figure 6.11b,d reveal a 180° rotation between trapped holes and electrons with $U > 0$. In addition, the $LDOS$ pattern for trapped holes (electrons) is aligned with the α (β) triangle of the BLG lattice. These predictions from the simulations are consistent with the Berry curvature sign flip[84,89,172] for the corresponding bands shown in the insets of Figure 6.11b,d. Notably, Figure 6.12a,b shows the experimentally measured dI/dV_S maps for BLG QDs with p-type and n-type central doping, respectively. In exact agreement with the simulations, the orientations of the dI/dV_S patterns differ by a 180° rotation and they align with the α triangle of the BLG lattice for trapped holes and with the β triangle of the BLG lattice for trapped electrons. Thus, our experiment verified our theoretical prediction about the Berry curvature sign's effect on BLG QD wavefunction orientation.

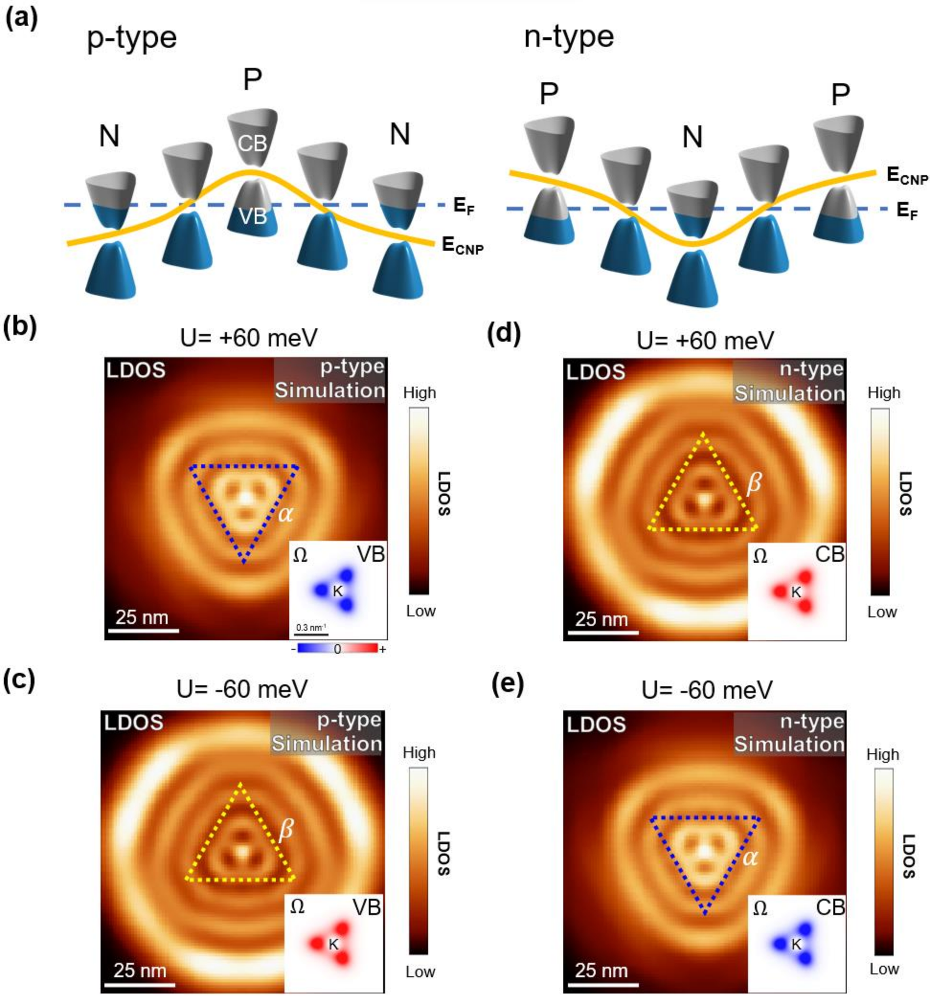

Figure 6.11 Simulated BLG QD $LDOS$ map tracks Berry curvature sign switch of confined charge carriers. (a) Band diagrams for BLG QD with p-type (left panel) and n-type (right panel) central doping. The orange and blue curves indicate the BLG charge neutrality point (E_{CNP}) and Fermi level (E_F), respectively. BLG QDs with p-type and n-type central doping confine holes and electrons, respectively. (b)-(e) Simulated $LDOS$ maps for BLG QDs with p-type and n-type central doping. The potential well and gap size are the same in (b)-(e), but the interlayer potential difference polarity U is $+60$ meV for (b) and (d), and U is -60 meV for (c) and (e). The blue

triangle in (b) and (e) and yellow triangle in (c) and (d) represents the orientation of the α and β triangles of BLG lattice in the TB model, respectively. Inset in (b-c) and (d-e) shows the calculated Berry curvature (Ω) of valence band (VB) and conduction band (CB) near K valley with $U = +60$ meV and $U = -60$ meV, respectively.

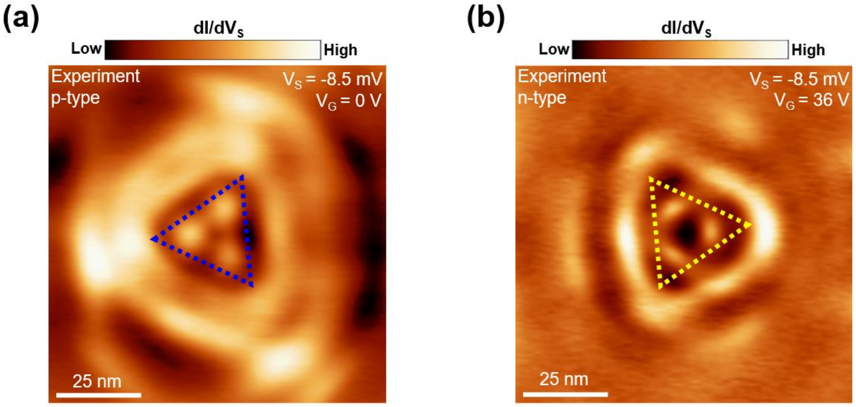

Figure 6.12 Experimental dI/dV_S maps for BLG QDs with different central doping. (a) Experimentally measured dI/dV_S maps for a BLG QD with p-type central doping with scanning parameters $I = 0.3$ nA and $V_{ac} = 2$ mV. (b) Experimentally measured dI/dV_S maps for a BLG QD with n-type central doping with scanning parameters $I = 0.1$ nA and $V_{ac} = 3$ mV. The blue triangle in (a) and yellow triangle in (b) represent the orientations of α and β triangles of BLG lattice, respectively.

Additionally, we further came up a heuristic to predict the orientation of the real space $LDOS$ distribution within a BLG QD. This argument requires knowledge of the Fermi surface orientation in momentum space and the Berry curvature sign of confined charges. Figure 6.13 summarizes the connection between the BLG Fermi surface orientation in momentum space, the BLG QD $LDOS$ distribution in real space, and the corresponding BLG Berry curvature sign for a single valley. Essentially, if the Berry curvature sign of confined charges from a certain band is positive (negative), the orientation of the real space $LDOS$ distribution within a BLG QD can be predicted by rotating the orientation of the associated band's Fermi surface in momentum space clockwise (counterclockwise) by 90°.

By applying this rule to both valleys of BLG bands, we will get the same BLG QD $LDOS$ distribution for the two valley states, which is expected due to the preserved time reversal symmetry in BLG QDs. For trigonally warped low energy BLG bands, the Fermi surface orientations are inverted between different valleys that are within the same band (conduction band or valence band) and remain the same between different bands at the same valley. The sign of the Berry curvature for BLG bands are inverted between different valleys that are within the same band or between different bands at the same valley[84,89,172]. Additionally, the Berry curvature sign will switch if the polarity of the interlayer potential difference is inverted[84,89,172]. This sign switch is depicted on the left side of Figure 6.13b (for $U > 0$) and Figure 6.13c (for $U < 0$). Interestingly, because of the inversion of both the Fermi surface orientation and the Berry curvature sign at different valleys and within the same band, the predicted orientations of $LDOS$ distributions from the two valleys will be the same. This is depicted on the right-hand side of Figure 6.13b,c. Because holes in valence band (electrons in conduction band) are confined in QDs with p-type (n-type) central doping, we can compare the predicted orientations of $LDOS$ distribution from our heuristic with the calculated results in Figure 6.11b-e. And we find the orientation of simulated $LDOS$ pattern agrees with the heuristic prediction in every scenario. But currently, we still do not understand why such heuristic prediction works.

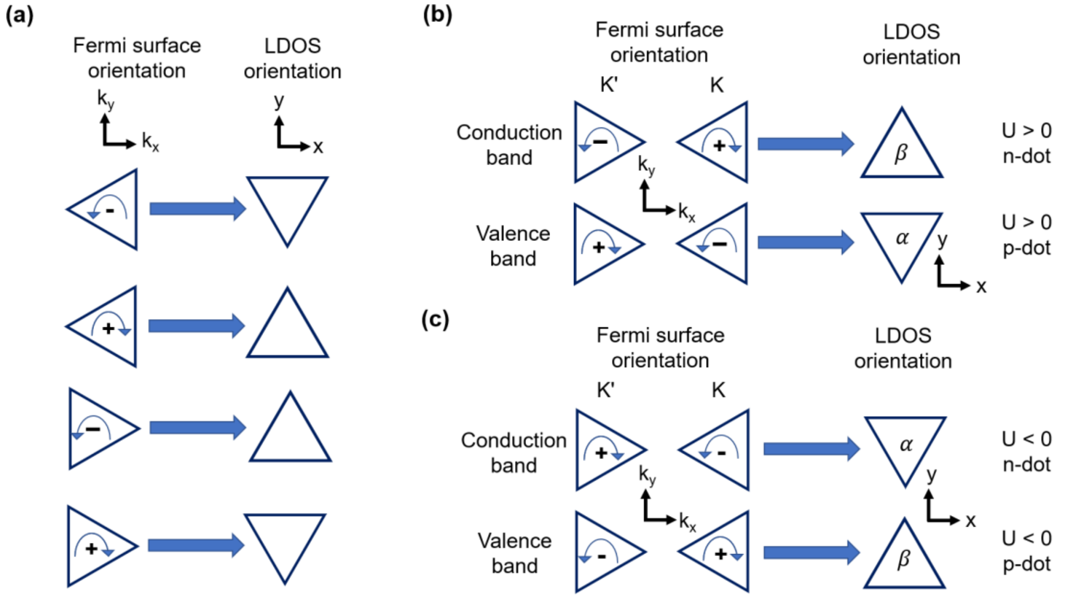

Figure 6.13 Schematic of heuristic for predicting the orientation of the real space $LDOS$ distribution within a BLG QD. (a) Application of heuristic to a single valley with different orientations in momentum space. On the left side, the triangle represents the orientation of BLG's triangular Fermi surface with respect to k_x and k_y axis. The $+$ and $-$ signs inside the triangle represent the Berry curvature sign for the corresponding band. On the right side, the triangle indicates the predicted orientation of the triangular $LDOS$ pattern with respect to x and y axis. (b)-(c) Application of heuristic discussed in (a) to BLG conduction and valence bands in two valleys. Both panels cover the simulated BLG QDs with different central doping type and different interlayer potential polarity ($U > 0$ showed in (b) and $U < 0$ showed in (c)). The left column shows the Fermi surface orientation at the K and K' valleys. The Fermi surface orientations considered here are consistent with TB calculation results with the BLG lattice orientation shown in Figure 6.4b. By applying the heuristic to the K and K' valleys, $LDOS$ patterns with an orientation that is consistent with calculated $LDOS$ patterns in Figure 6.11b-e are yielded.

6.5 Conclusions

In conclusion, we have spatially mapped BLG QD wavefunctions for the first time. We used BLG QD as a platform to demonstrate the effect of Fermi surface symmetry and Berry curvature on the spatial distribution of QD wavefunctions. Our findings showed the trigonal warping of BLG bands have a strong influence on BLG QD states, an aspect missed in most previous BLG QD theories. Additionally, we demonstrated the BLG QD wavefunction orientation can reveal the Berry curvature sign of confined charge carriers. This finding could inspire future works using quantum interference patterns to study the properties of materials that have finite Berry curvature such as semiconducting transition metal dichalcogenides[173] (e.g. MoS_2), topological insulators[174] (e.g. WTe_2) and Weyl semimetals[175-177] (e.g. TaAs). The technical advancements presented here can also potentially be used to study more sophisticated platforms such as double and multiple BLG QDs. The tunable couplings in these systems make them promising for the realization of quantum bits based on spin and valley degrees of freedom[35,72].

Chapter 7 Giant Topological Orbital Magnetic Moment and Valley Splitting in TLG QDs

In chapter 5, we observed linear splitting of MLG QD states in a magnetic field due to their orbital magnetic moments. For MLG QDs, their orbital magnetic moments originate from the probability current of their QD wavefunctions. But in materials with non-trivial band geometrical properties, orbital magnetic moments can also come from self-rotating Bloch waves. To distinguish, such orbital magnetic moments are also called topological orbital magnetic moments due to their close relationship to band topological properties. For intrinsic MLG, their bands are not gapped and do not host such topological orbital magnetic moments. However, as discussed in section 1.2.3, TLG consists of gapped effective MLG bands that can host extremely large topological orbital magnetic moments. In this chapter, I will discuss the influence of such giant topological orbital magnetic moment on the magnetic field response of tip induced TLG QD states. The results shown in this chapter have been published in reference[61].

7.1 Introduction

The orbital magnetic moment stemming from the rotational motion of electrons is ubiquitous in nature. It can be found in a variety of systems from single atoms to complex crystals and can influence the magnetic properties of these systems. In recent years, topological magnetic moments emerging from self-rotating wave packets[84] have been discovered in 2D Van der Waals crystals with broken inversion symmetry[178-182]. Experimental manifestations of the topological magnetic moments have been observed lately, including the valley Zeeman effect,[30,36,37,51,52,162,178-187] spontaneous orbital ferromagnetism,[188,189] and orbital magnetoelectric effects[190-192]. The former is important for valleytronics because it enables control of individual valley states, while the latter two could potentially facilitate new ultra-low power magnetic devices. To harness the valley Zeeman and orbital magnetoelectric effects in 2D crystals, systems with topological magnetic moments both large and tunable via gate modulation are desirable. The possibility to achieve these properties have been separately demonstrated with BLG, offering[162] a tunable valley g-factor $(g_v) \sim 40 - 120$, and moiré superlattices in MLG, with[180] large g_v ~ 2500.

In this work, we will show a giant and gate tunable topological orbital magnetic moment can be realized in naturally occurring Bernal stacked trilayer graphene (TLG) by utilizing its peculiar band structure. As discussed in section 1.2.3, due to the mirror symmetry of TLG (Figure 7.1a), its electronic spectra can be viewed as overlapping bilayer graphene (BLG) and weakly gapped monolayer (MLG) bands[97]. As shown in Figure 7.1a, the antisymmetric wavefunction combination of sublattices A_1 and A_3 (blue shading) and B_1 and B_3 (orange shading) can be mapped onto a new sublattice B and A of an effective MLG lattice that gives rise to effective MLG bands[92]. Because of the γ_2 and γ_5 hopping energy difference and the onsite energy difference between the trimer and non-trimer sites (Δ_{AB}), the effective MLG sublattices have different energies (broken inversion symmetry), leading to a light-mass Dirac spectrum with large topological magnetic moments. A full TB calculation of the TLG band structure in the absence of a perpendicular electric field is plotted in Figure 7.1b, where the effective MLG and BLG bands (both gapped) are indicated by the blue cones and semi-transparent red shells. The gaps and mutual alignment of the effective MLG and BLG bands are both tunable by the encapsulation environment, gating, and doping.

Of the two effective bands in TLG, gapped MLG bands are especially interesting in terms of topological orbital magnetic moment. This is because with a similar gap size, gapped MLG has a much larger topological orbital magnetic moment compared to gapped BLG. Neglecting trigonal warping, the BLG orbital magnetic moment is suppressed by a factor of Δ/γ_1 compared to gapped MLG bands, where Δ is the gap size of gapped MLG and BLG bands and $\gamma_1 \approx 0.381$ eV is the interlayer hopping term introduced in section 1.2 for graphene systems. For small gap size ($\Delta \sim 10$ meV), the topological orbital magnetic moment in gapped MLG bands can be orders of magnitude larger than those in gapped BLG bands.

This feature of gapped MLG bands offers an opportunity to engage states with giant topological magnetic moments[84,180,182]. In addition, the direction of the topological orbital magnetic moment of gapped MLG bands in the two valleys are opposite (schematized in Figure 7.1b), this can lead to a valley splitting in a magnetic field with very large effective valley Landé g-factor g_v. Furthermore, the topological orbital magnetic moments of gapped MLG bands are tunable through tuning the gap size by, for example, a back gate. Figure 7.1c shows the calculated topological orbital magnetic moment distribution in momentum space $M(\vec{k})$ for gapped MLG bands with different gap sizes. The peak values of $M(\vec{k})$ are extremely large and can be tuned from $\sim 800\mu_B$ to $\sim 400\mu_B$ by tuning the gap size from 14 meV to 26 meV. This indicates g_v of the effective MLG band is not only large but also tunable.

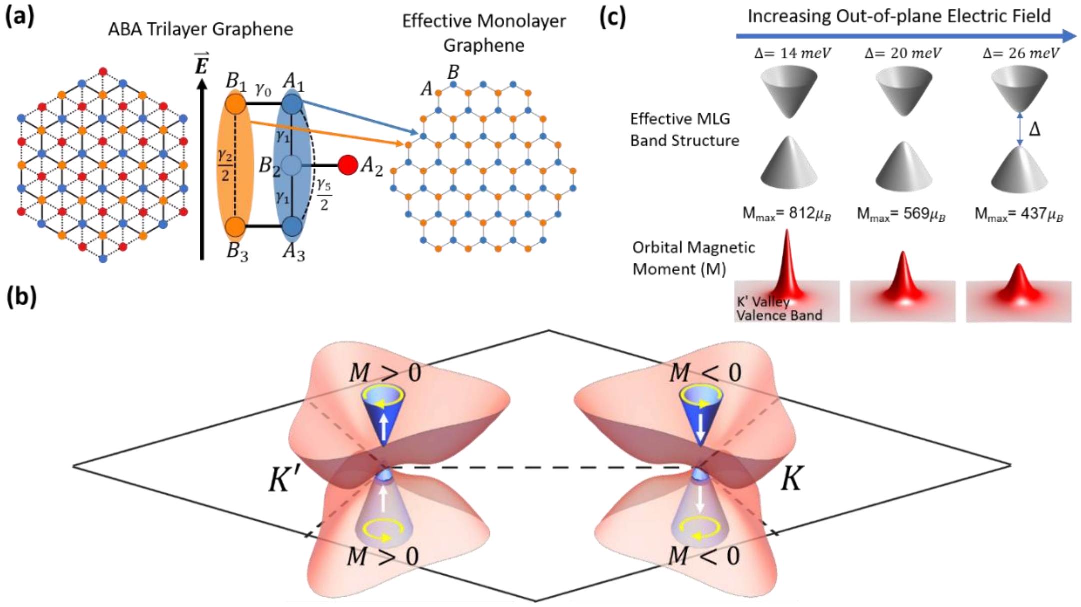

Figure 7.1 Effective MLG band in TLG with giant and tunable topological orbital magnetic moment. (a) Left panel: Top view of the TLG atomic structure. Middle panel: Schematic of the TLG unit cell and hopping parameters. Right panel: Mapping TLG onto an effective MLG lattice. (b) Schematic of the calculated low energy band structure in K and K' valleys for TLG with no external electric field. Blue cones represent the effective MLG bands. The semi-transparent red shells represent the effective BLG bands. The yellow arrows depict the orientation of the self-rotating wave packet in each band and the white arrows correspond to the direction of the topological orbital magnetic moment originating from the self-rotating wave packet. (c) Upper panel: Low energy band structures of the effective gapped MLG with different out-of-plane electric fields applied to TLG. Lower panel: topological orbital magnetic moment in the K' valley valence band of the corresponding gapped MLG bands shown in the upper panel. Here we assumed v_F of the MLG band is 10^6 m/s.

7.2 Gate, Sublattice and Magnetic Field Resolved STS on Pristine TLG

To experimentally verify the giant and gate tunable g_v that possibly exists in TLG's effective MLG bands, we first performed gate and sublattice resolved STS pristine areas of TLG/hBN heterostructures. The TLG/hBN sample used in this study are fabricated with the MMA based transfer technique discussed in section 3.1. During the sample fabrication, TLG and hBN are misaligned intentionally to avoid any spectral reconstruction near the charge neutrality point (CNP)[193], which is the energetic region of interest in our study. The measurement setup for our experiments is shown in the upper panel of Figure 7.2a. The STM tip is grounded, and a bias voltage V_S is applied between the STM tip and TLG to induce a tunneling current. In addition, a back gate voltage V_G is applied between the doped silicon and TLG to institute an out-of-plane electric field that shifts the TLG Fermi energy and modifies the TLG band structure[92]. To avoid influence from adsorbates we performed all STS measurements at the centers of atomically pristine regions that were no smaller than $20 \times 20\ \mathrm{nm}^2$. The lower panel of Figure 7.2a shows a typical atomically resolved topography at the center of such a region where the tunneling spectra were acquired. A clear triangular lattice is visible, which agrees with prior STM studies of ABA TLG supported on metals and SiC[194,195]. Furthermore, no moiré pattern is observed in larger area topography scans (Figure 7.3), thus indicating TLG and hBN are misaligned.

A model atomic structure is overlaid on top of the measured topography in Figure 7.2a that indicates the ABA TLG sublattices. The grey and bright spots correspond to sublattices A_1 and B_1, respectively. Both A_1 and B_1 sublattices reside on the TLG top layer, as shown in Figure 7.1a. In contrast, the dark spot corresponds to sublattice A_2, which resides on the middle layer. Since STM is mostly sensitive to surface states, we expect the tunneling signal from our measurements to consist primarily of contributions from the top TLG layer, hence sublattices A_1 and B_1 will dominate our STS measurements.

Typical gate resolved STS results for sublattices A_1 and B_1 are shown in Figure 7.2b,c, respectively. To reduce the influence of slight deviations from the target sublattice for a single measurement, the tunneling spectra at each gate voltage shown in Figure 7.2b,c correspond to an average of spectra at nine different targeted locations (Figure 7.4 shows the STS results before averaging at some selected V_G). Interestingly, the spectra for sublattice A_1 exhibit a prominent $\mathrm{d}I/\mathrm{d}V_S$ peak (marked by a black dot) that diminishes in intensity and shifts toward the positive bias voltage with decreasing V_G. We find the strong dI/dV_S peak is only present on sublattice A_1 (Figure 7.2b,c). Notably, this feature was absent in previous gate resolved STS studies of ABA TLG.[196,197]

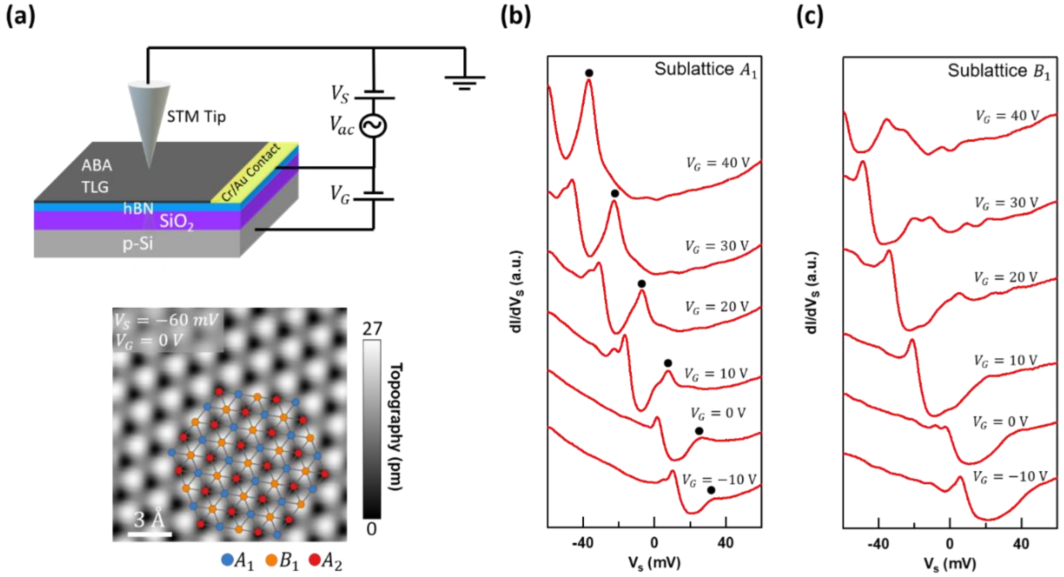

Figure 7.2 Gate and sublattice resolved TLG STS. (a) Upper panel: Schematic of the experimental setup. Lower panel: Atomically resolved topography of a pristine TLG patch at $V_G = 0\,V$, the scanning parameters used are $I = 1$ nA, $V_S = -60$ mV. The TLG atomic structure is overlaid on top of the topography, the definition of the sublattice is consistent with that in Figure 7.1a. (b)-(c) Tunneling spectra at various

gate voltages on sublattice A_1 (b) and B_1 (c). The set point used to acquire the tunneling spectra was $I = 1$ nA, $V_S = -60$ mV, with a 2 mV ac modulation.

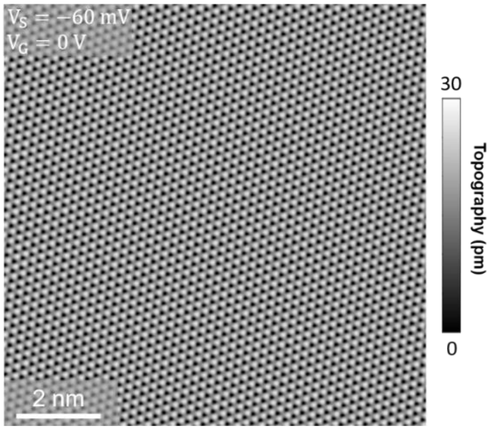

Figure 7.3 $10 \times 10\ \mathrm{nm}^2$ atomically resolved TLG topography. Atomically resolved STM topography of a pristine TLG/hBN area at $V_G = 0\ V$, the scanning parameters used are $I = 1$ nA, $V_S = -60$ mV.

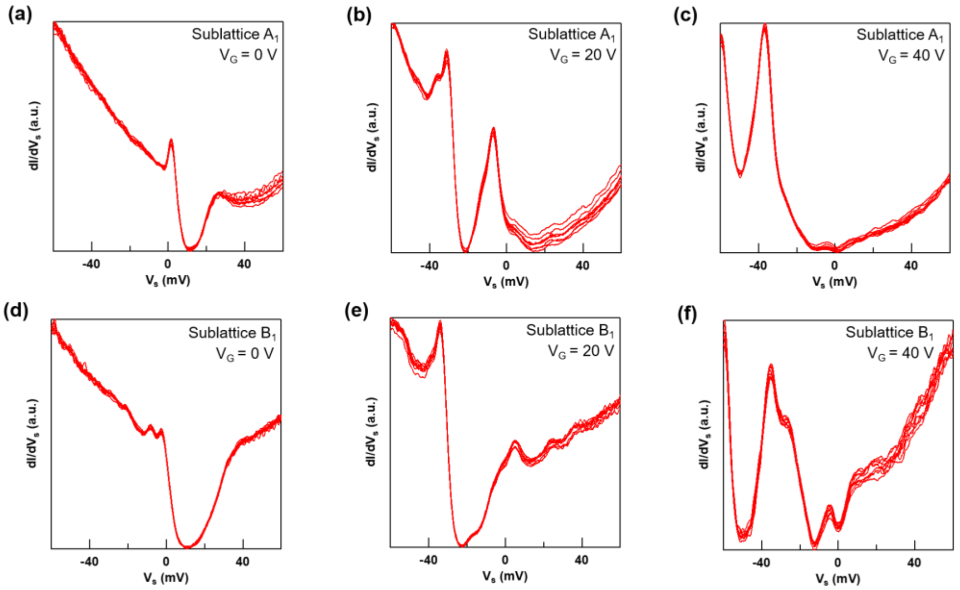

Figure 7.4 Reproducibility of sublattice resolved tunneling spectra. (a)-(c) Tunneling spectra measured from sublattice A₁ distributed at nine different locations within a $1.6 \times 1.6\ \mathrm{nm}^2$ window at $\mathrm{V_G} = 0$ V, $\mathrm{V_G} = 20$ V and $\mathrm{V_G} = 40$ V, respectively. (d)-(f) Tunneling spectra measured from sublattice B₁ distributed at nine different locations within a $1.6 \times 1.6\ \mathrm{nm}^2$ window at $\mathrm{V_G} = 0$ V, $\mathrm{V_G} = 20$ V and $\mathrm{V_G} = 40$ V, respectively. The set point used to acquire the tunneling spectra in (a)-(f) was $I = 1$ nA, $V_S = -60$ mV, with a 2 mV ac modulation.

Intrigued by this finding we next performed gate and sublattice resolved STS on pristine TLG/hBN area in finite out of plane magnetic field B. Our aim was to investigate the possibility of valley splitting in this system. Figure 7.5 shows the experimentally measured tunneling spectra on sublattice A_1 and B_1 at $V_G = 10\ \mathrm{V}$, $20\ \mathrm{V}$, $30\ \mathrm{V}$ and $40\ \mathrm{V}$ with B from $0.1\ \mathrm{T}$ to $0.6\ \mathrm{T}$ with a $0.1\ \mathrm{T}$ interval. The most prominent feature in these data is the strong dI/dV_S peak on sublattice A_1 will split into two as B is increased at all V_G (Figure 7.5a-d). But this behavior not observed on sublattice B_1 (Figure 7.5e-h). In addition, we found lower intensity satellite dI/dV_S peaks emerge on the positive V_s side as B is increased. In contrast to the prominent sublattice dependent peaks, these satellite dI/dV_S peaks were observed on both sublattices at all V_G. Figure 7.6 shows the dependence of the splitting energy ΔE on B extracted from Figure 7.5a-d at different V_G, we find the relationship between ΔE and B generally is not linear at all V_G.

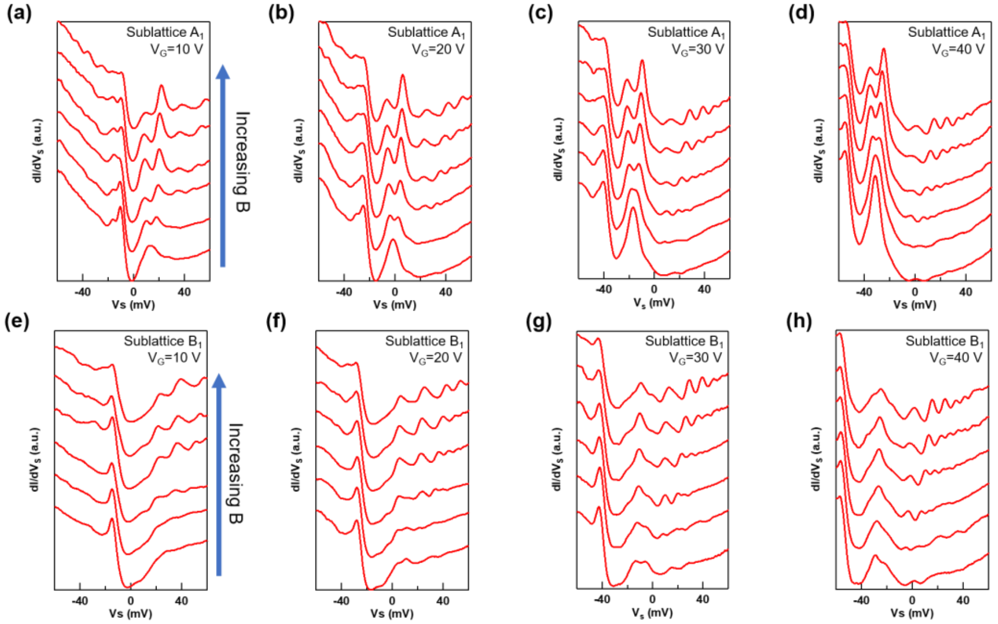

Figure 7.5 B dependent tunneling spectra on sublattice A_1 and B_1 at different V_G. (a)-(d) Tunneling spectra measured from sublattice A_1 at $V_G = 10$ V, $V_G = 20$ V, $V_G = 30$ V and $V_G = 40$ V, respectively. Within each panel, the applied B increases from 0.1 T to 0.6 T with a 0.1 T interval from bottom to top. (e)-(h) Tunneling spectra measured from sublattice B_1 at $V_G = 10$ V, $V_G = 20$ V, $V_G = 30$ V and $V_G = 40$ V, respectively. Within each panel, the applied B increases from 0.1 T to 0.6 T with a 0.1 T interval from bottom to top. The set point used to acquire the tunneling spectra in (a)-(h) was $I = 1$ nA, $V_S = -60$ mV, with a 2 mV ac modulation.

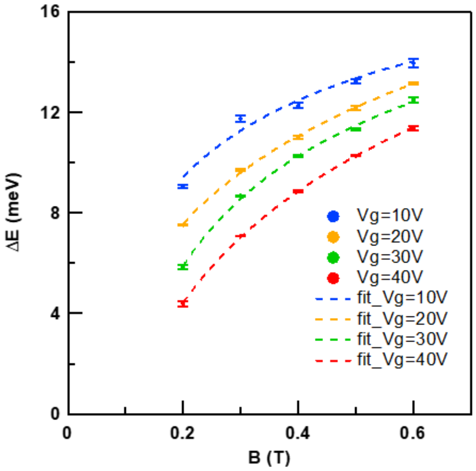

Figure 7.6 dI/dV_S peak splitting energy ΔE as a function of B. The colored dots are the peak splitting energy extracted from Figure 7.5a-d at different B and V_G. The dashed lines are polynomial fits to the extracted splitting energies. The splitting energies are not linearly dependent on B.

7.3 Valley Splitting of Tip-induced TLG QD State

To understand our experimental findings, we consider the local tip gating effect as discussed in section 2.3.1. Due to the capacitive coupling between the STM tip and TLG, a shallow and smooth positive potential well can be induced in TLG, yielding an electrostatically defined QD[50,56]. Thus, the sharp dI/dV_S peak observed in our experiments can be understood as a tip induced TLG QD state. More specifically, this sharp peak arises from the confinement of gapped MLG bands. As depicted in Figure 7.7a, the positive potential well induced by the STM tip raises the energy of valence band MLG states into the band gap, making these states localized and forming a valley degenerate QD state. This emerging QD state can explain the strong dI/dV_S peak on sublattice A_1 (Figure 7.2b) where the gapped MLG states near the valence band edge reside. A comparison between the calculated $LDOS$ for TLG with and without a tip potential well is shown in Figure 7.7b. A strong $LDOS$ peak, which is similar to our experimental observations, appears in the simulation that includes a tip potential well.

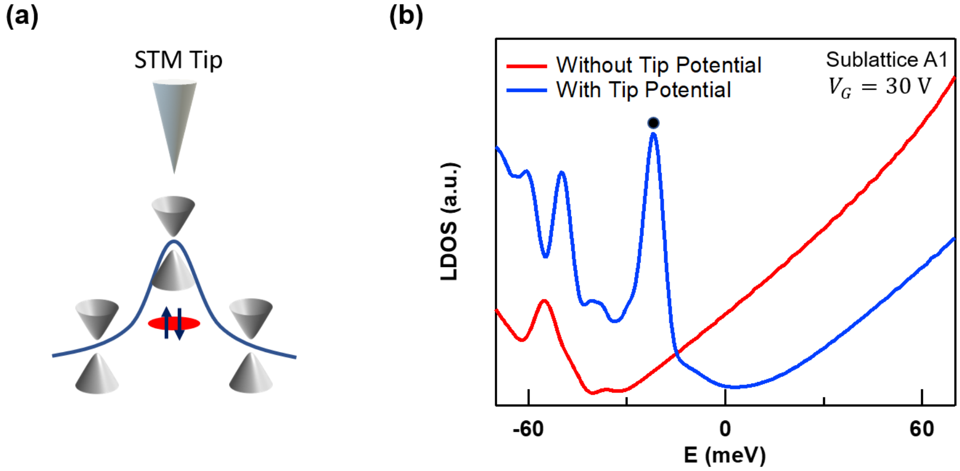

Figure 7.7 Localized state due to tip induced potential well. (a) Schematic of the STM tip included potential well (blue line) and the localized stated (red ellipse) from the confinement of the gapped MLG band. (b) Calculated TB $LDOS$ for sublattice A_1 with and without a tip potential at $V_G = 30$ V. The black dot indicates the tip induced TLG QD state that is observed in our experiment.

Using the tip induced TLG QD picture, the experimentally observed dI/dV_S peak splitting in magnetic field can be understood as a valley splitting of the initially valley degenerate gapped effective MLG QD state in B. As schematized in Figure 7.1b, the topological orbital magnetic moments $M_z(\vec{k}) = \tau \frac{e}{\hbar} \frac{\Delta}{[\Delta/(\hbar v_F)]^2 + 4|\vec{k}|^2}$ (v_F is the Fermi velocity of the MLG bands, $\tau = +1$and -1 for K' and K valley, respectively) of the effective MLG bands in K and K' valleys are both out of plane and with opposite orientations. Thus, an out of plane B will couple to the opposite $\vec{M} = \hat{z}\tau M_z$ of the electrons in the two valleys and generate a valley splitting of the tip induced QD state. Using this simple picture, ΔE can be approximated as $2\left|\vec{M} \cdot \vec{B}\right|$, which can also be expressed as $g_v \mu_B B$. Here μ_B is the Bohr magneton, and g_v is defined as the valley g factor. To demonstrate this argument more convincingly, Figure 7.8 shows the calculated $LDOS(E, B)$ with the continuum model described in section 4.2 for a gapped MLG QD, a linear valley splitting appears only on one of the two MLG sublattices (on which sublattice the splitting appears depends on the gap sign of gapped MLG QD). Such sublattice polarized valley splitting is similar to what we observed in our experiments (Figure 7.5).

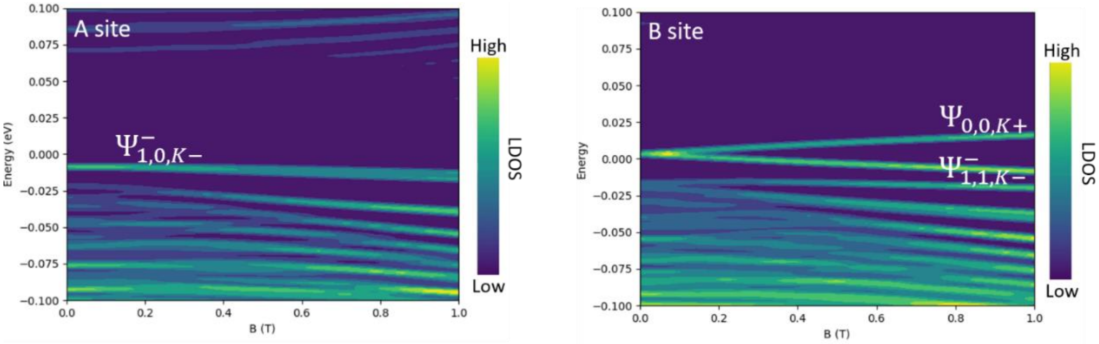

Figure 7.8 Valley splitting of gapped MLG QD states with tip potential. Calculated $LDOS(E, B)$ at the QD center for A and B sublattices. A potential well $V(r) = 50\ e^{-r^2/(2\ (30\ \mathrm{nm})^2)}$ and a gap $\Delta = 30$ meV are use in the gapped MLG QD model.

However, in our experiments, we observed a non-linear dependence between ΔE and B (Figure 7.6), which is contradictory to the linear valley splitting described above. To explain the non-linear valley splitting observed in our experiment, we need to consider the competition between the QD confinement and magnetic field confinement, and the band mixing of TLG's effective MLG and BLG bands when an out of plane electric field exists (Figure 7.9). With increasing B, the magnetic field confinement starts to dominate over the QD confinement, and the valley splitting is expected to gradually start following the splitting between the Landau level (LL) 0- and LL1- of gapped MLG, which is nonlinear as plotted by the green line in Figure 7.10. To fully account for the observed non-linear valley splitting in our experiments, we further consider the influence of the tip potential on LL0- and LL1- (red line in Figure 7.10) as well as the effect from the MLG/BLG band mixing (orange line in Figure 7.10). After incorporating all these effects, the theoretical ΔE (blue line in Figure 7.10) shows good agreement with the experimentally extracted ΔE value (red dots in Figure 7.10).

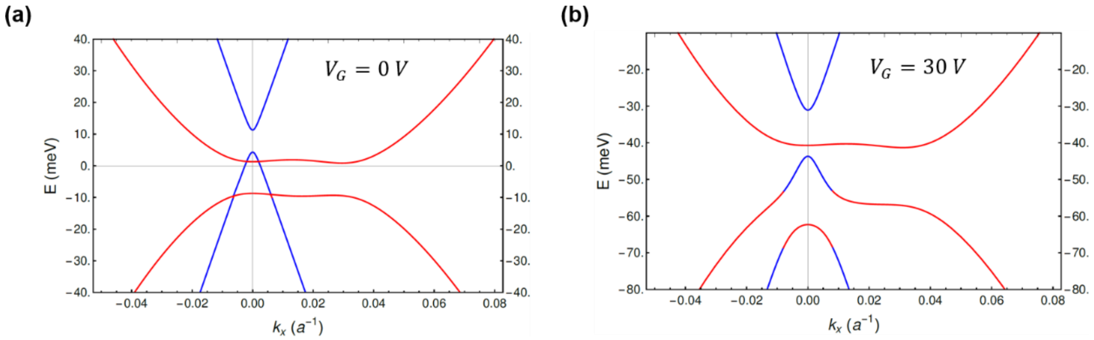

Figure 7.9 Electric field induced band mixing. (a)-(b) Calculated TLG band structure at $V_G = 0$ V (a) and $V_G = 30$ V (b). The blue lines correspond to the effective MLG bands, and the red lines correspond to the effective BLG bands. At $V_G = 30$ V, the valence bands of the BLG and MLG parts mix with each other.

In addition, it is important to note that the tip induced potential well is crucial for the experimental detection of valley splitting in TLG in small B. Although the LL0- and LL1 of gapped MLG mentioned above can host a similar valley splitting effect as seen in our experiments, it cannot be detected in small B without a tip induced potential well. Figure 7.11 shows a comparison between the calculated $LDOS(E, B)$ from the TB model described in section 4.1 for TLG with and without a tip induced potential well at $V_G = 30$ V. In small magnetic fields, the peak splitting that corresponds to the valley splitting can only be clearly visible with a tip induced potential well.

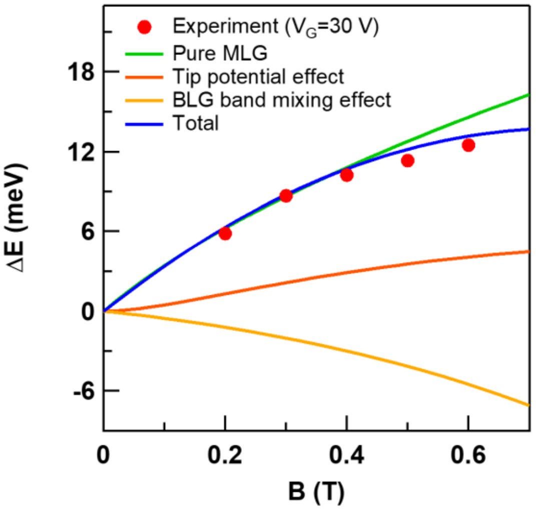

Figure 7.10 Comparison between the experimental and theoretical valley splitting energy at $V_G = 30\ V$. The experimental splitting energy is extracted from Figure 7.5c. The depth and width of the Gaussian potential well used in the theoretical calculation are 50 meV and 40 nm, respectively.

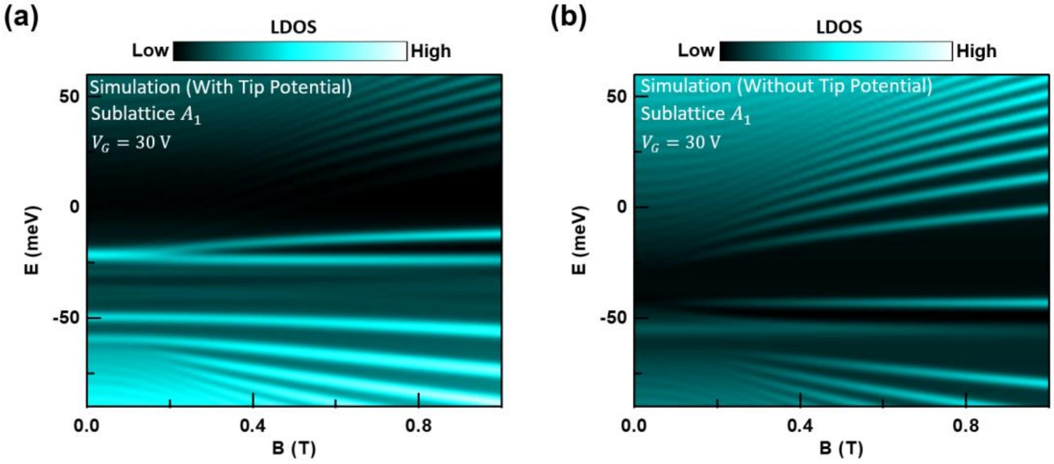

Figure 7.11 Enhanced valley splitting visibility with a tip induced potential well. (a)-(b) Calculated $LDOS(E, B)$ for sublattice A_1 with a tip induced potential well (a) and

without a tip potential well (b). A clear peak splitting is visible at around -25 meV in (a), but non clear peak splitting is visible in (b).

7.4 Giant and Gate Tunable g_v of Tip Induced TLG QD State

Having understood the observed valley splitting in B for TLG, we now discuss its gate tunability. The gap of the effective MLG band depends on the out-of-plane electric field (E$_z$), which can be expressed as $\Delta = \frac{1}{2}\sqrt{\gamma_2^2 + (U_1 - U_3)^2} + \frac{\gamma_5}{2} - \Delta_{AB}$. Here $U_1 - U_3 \propto E_z$ is the interlayer energy difference between the top and bottom layer of TLG. Modulation of this quantity by V_G controls the intensity of the inversion symmetry breaking in the top TLG layer, which leads to a gate tunable MLG gap (Δ). Importantly, this tunable Δ will give rise to tunable topological magnetic moments in MLG bands as shown in Figure 7.1c. Such gate tunable topological magnetic moments can yield a gate tunable g_v.

To study the gate tunable g_v in TLG, we performed $dI/dV_S(V_S, B)$ measurements with high B resolution at different V_G. The upper panel of Figure 7.12a-d shows the experimentally measured $dI^3/dV_S^3(V_S, B)$ at different V_G, the valley splitting state that arises from tip induced TLG QD and Landau level fans can both be observed in these measurements. The lower panel of Figure 7.12a-d shows the zoom-in of the valley splitting state at different V_G from the upper panel of Figure 7.12a-d, the valley splitting is not linearly dependent on B within the full experimentally measured B range but approximately linearly dependent on B in small B. By doing linear fitting to the valley splitting states in small B, we can extract g_v based on the slope of the linear fitting lines. We extracted a g_v value of 1050 ± 72, 722 ± 71,

611 ± 39 and 517 ± 47 for $V_G = 10$ V, 20 V, 30V and 40 V, respectively. These results demonstrated that g_v in TLG is both giant and gate tunable, such combination of large value and high tunability for g_v is unparalleled in previously studied systems[162,180].

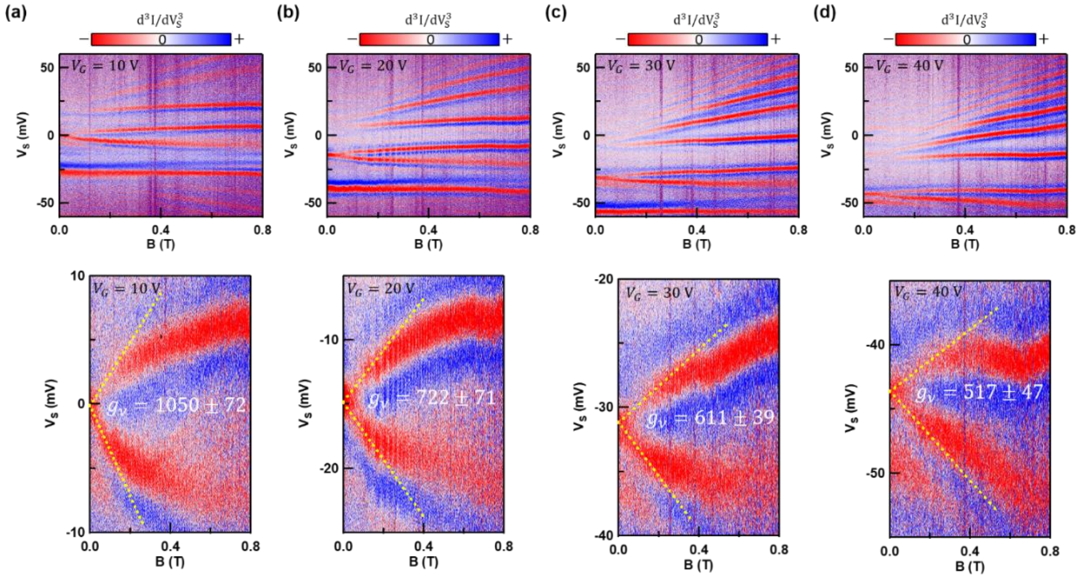

Figure 7.12 Valley g-factor extraction at different V_G. (a)-(d) Experimentally measured d^3I/dV_S^3 (V_S, B) at $V_G = 10$ V (a), $V_G = 20$ V (b), $V_G = 30$ V (c) and $V_G = 40$ V (d). The lower panels in (a)-(d) are a zoom in of the data shown in the upper panel of (a)-(d), respectively. The d^3I/dV_S^3 values are numerically calculated from the dI/dV_S data measured from the lock-in in experiment. The purpose of showing d^3I/dV_S^3 data is to better visualize the peak splitting. The red features in d^3I/dV_S^3 correspond to the dI/dV_S peak. The yellow dashed lines in the lower panel of (a)-(d) are the linear fit to the peak splitting in small B, and g_v is calculated based on the slope of the linear fits. The set point used to acquire the dI/dV_S tunneling spectra in (a)-(d) was $I = 1$ nA, $V_S = -60$ mV, with a 2 mV ac modulation. The STM tip used to acquire the data in (a)-(d) does not have a good atomic resolution for the tunneling spectra.

Before comparing the observed gate tunable g_v with theory, we first extract the gap size Δ for gapped MLG at different V_G. At high B, the effect of magnetic field confinement is more significant than the QD confinement. As a result, Landau levels dominate the tunneling spectra in this regime. In gapped MLG, a zeroth LL (LL0) exists near the band edges of the conduction (labelled LL0+) and valence (labelled LL0-) bands[195]. So, we can use the energy spacing between LL0+ and LL0- to estimate the gap size of the effective MLG bands in our experiment. Figure 7.13a shows an experimentally measured $dI/dV_S(V_S, V_G)$ plot in $B = 1$ T, LLs from the effective MLG bands can be clearly observed. The LLs in the conduction band are labeled up to the 5th LL. We can next extract the dispersion of the LLs as a function of *B*. To do this we acquire a vertical line cut from $dI/dV_S(V_S, V_G)$ measurements in different *B*. Figure 7.13b shows the dispersion of different LLs at $V_G = 40\ V$ and with increasing *B*, note that the horizontal axis is plotted as $\sqrt{B}$. Evidently, the energy dispersions of LL0+ and LL0- are nearly *B* independent. In contrast, the dispersions of the other five LLs are approximately linearly dependent on $\sqrt{B}$ at high *B*. This behavior agrees with the expected LL energy dispersion in MLG[73]. Figure 7.13c shows the extracted band gap size at selected V_G, Δ roughly has a linear dependence on V_G. The extracted Δ are also depicted as doubled sided yellow arrows in Figure 7.13a. Representative tunneling spectra that were used to extract the gap values are shown in Figure 7.14, where the LL0+ and LL0- are indicated by black arrows. These representative spectra were acquired at several different V_G and with $B = 1$ T.

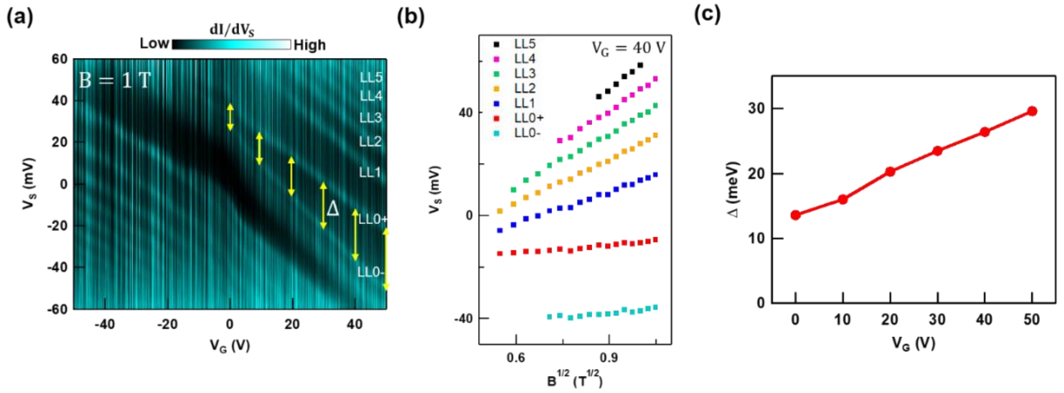

Figure 7.13 Gap size extraction for effective MLG bands. (a) Experimentally measured $dI/dV_S(V_S, V_G)$ in $B = 1$ T at $V_G = 40$ V. The set point used to acquire the tunneling spectra was $I = 1$nA, $V_S = -60$ mV, with a 2 mV ac modulation. The yellow double-sided arrows represent the gap size of the effective MLG bands at different V_G. (b) Extracted LL dispersion at $V_G = 40$ V from $dI/dV_S(V_S, \mathrm{V_G})$ in different B. The extracted LL dispersions are plotted as a function of $\sqrt{B}$. (c) Extracted gap size of the effective MLG bands at different V_G.

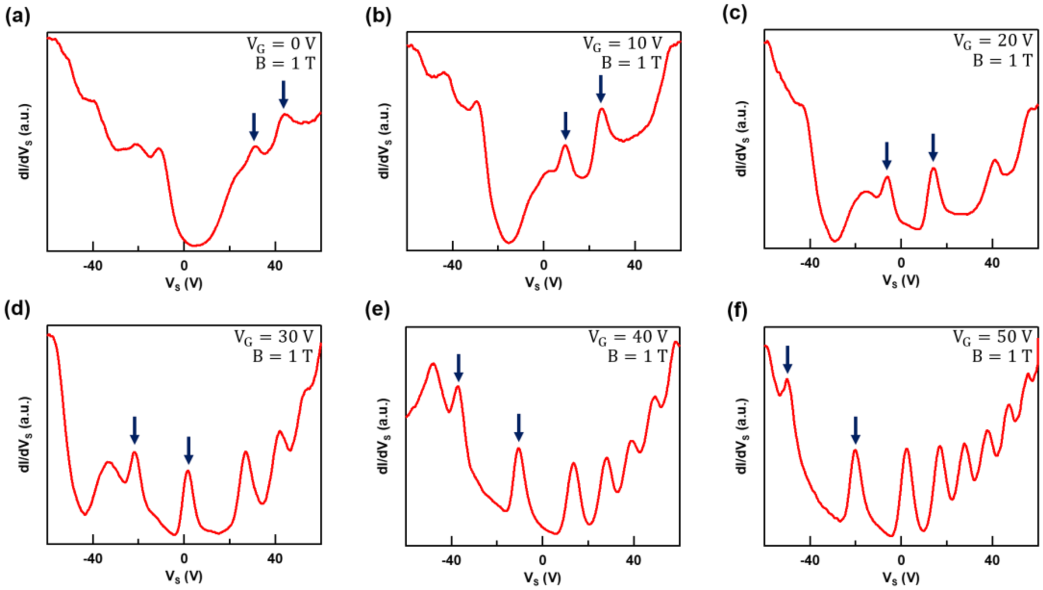

Figure 7.14 Tunneling spectra in $B = 1$ T at different V_G. (a)-(f) Tunneling spectra extracted from Figure 7.13a at $\mathrm{V_G} = 0$ V, 10 V, 20 V, 30 V, 40 V and 50 V, respectively. The LL0+ and LL0- are indicated by black arrows. To reduce noise, each spectrum consists of an average of spectra within a gate voltage range of ± 0.4 V near the targeted V_G. The set point used to acquire the tunneling spectra was $I = 1$nA, $V_S = -60$ mV, with a 2 mV ac modulation.

After getting the gap size Δ of the effective MLG bands at different V_G, we can now proceed to compare the observed gate tunable g_v with theory. In the theory, we use plane wave representation $\psi(\vec{k})$ of the gapped MLG QD state at $B = 0$ T to estimate the valley g-factor as $g_v = \frac{2}{\mu_B} \int M(\vec{k}) \left|\psi(\vec{k})\right|^2 d\vec{k}$, where $M(\vec{k})$ is the topological orbital magnetic moment of gapped MLG. The calculated g_v as a function of Δ for a Gaussian shaped $\psi(\vec{r})$ with a width of 150 nm and 300 nm are shown in Figure 7.15 as a green solid line and blue solid line, respectively. The experimentally extracted g_v as a function of Δ are plotted in Figure 7.15, the experiment and theory display a good agreement. We notice the experimental g_v at small Δ (i.e., small V_G) agrees better with theory that corresponds to larger Gaussian width for $\psi(\vec{r})$. This is consistent with the finding in Figure 7.2b that at lower V_G the QD has weaker confinement.

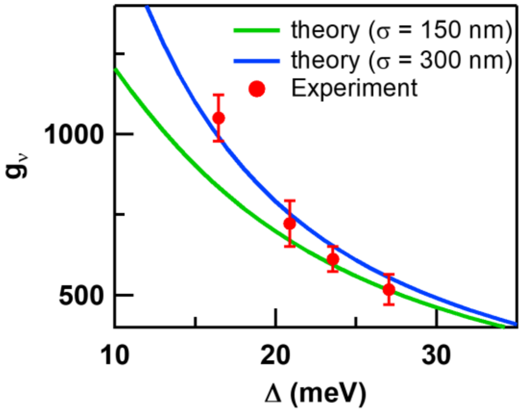

Figure 7.15 Comparison between experimental and theoretical g_v as a function of Δ.

7.5 Conclusions

In this work, we demonstrated the existence of a giant and gate tunable g_v for tip induced TLG QD states through gate, magnetic field and sublattice resolved STS measurements. Such a property of tip induced TLG QDs originates from the giant and gate tunable topological orbital magnetic moments that are hosted in TLG’s weakly gapped effective MLG bands. With sublattice resolved STS, we were able to pinpoint the effective MLG QD states in our experiments. Our work demonstrated the power of sublattice resolved STS on investigating multiband graphene systems. In addition, our work indicates TLG potentially can be a unique platform for fabricating valley-based quantum information devices and studying topological orbital magnetic moment related phenomena.

Chapter 8 Direct Visualization of Quantum Scars in Stadium Shaped MLG QDs

In chapters 5-7, we investigated some unique properties of the electronic structure and magnetic field response of QDs that are based on MLG, BLG and TLG. Although these studies were done on different graphene systems, one thing in common between them is that the QDs investigated there are all circularly shaped. In this chapter, on the other hand, I will show our recent experimental results on the electronic structure and magnetic field response of non-circular MLG QDs, more specifically, stadium shaped MLG QDs. Such change of the QD potential well shape, from circular shape to stadium shape, alters the corresponding classical dynamics of MLG QDs from integrable to non-integrable, which can have a significant consequence on the electronic structure of MLG QDs. One big motivation for this study is to directly visualize the long predicted scarred wavefunctions that can be hosted in quantum systems with non-integrable corresponding classical dynamics. The results I will show in this chapter have not yet been published in a peer reviewed journal and are under preparation towards a manuscript.

8.1 Introduction

The study of quantum classical correspondence can not only provide fundamental insights into the connections between classical and quantum mechanics, but also help achieve intuitive understandings of quantum phenomena. Among various systems studied before, the quantum classical correspondence in quantum systems with corresponding classical chaotic dynamics is of special interest[14,15,198-200]. One reason is that the required non-linearity for classical chaos (exponential sensitivity to initial conditions) is absent in quantum mechanics, so it is of fundamental interest to understand in what form classical chaos will be manifested in quantum systems. Previous studies showed that, instead of exponential sensitivity to initial conditions, signatures of corresponding classical chaos can be revealed in the energy level statistics of a quantum system[14,15,198-200]. Apart from this, wavefunction scarring, which refers to the enhancement of quantum probability density in the vicinity of unstable classical periodic orbits of a chaotic system, is another common feature shared among classically chaotic quantum systems[14,103,198,199,201]. Such wavefunctions with wavefunction scarring are commonly referred to as quantum scars, which are a visual demonstration of the quantum classical correspondence in classically chaotic quantum systems. Apart from appeals to fundamental physics, quantum scars also have potential importance in technological applications, such as in the chaos assisted directional emission in microcavity lasers[202-204] and the understanding of conductance fluctuations in open quantum dots[205,206]. More recently, the many-body version of quantum scars observed in quantum many-body systems also demonstrated their potential importance in quantum information[207,208].

Since the first prediction of quantum scars about 40 years ago[103], extensive experimental attempts have been carried out to directly image such states. Although analogue quantum scars have been clearly visualized in various classical wave experiments such as in microwave cavities[209,210], acoustic cavities[211] and fluid surface waves[212], the direct visualization of quantum scars in real quantum systems is still elusive[62,213-220]. Yet, the experimental verification of many new types of quantum scars proposed in recent years, such as relativistic quantum scars[201,221], perturbation induced quantum scars[222-225], and chiral quantum scars[226-228], demands experimental techniques that can directly visualize quantum scars with both high spatial and high energy resolutions.

To date, most experimental attempts for the direct visualization of quantum scars were done with the scanning gate microscopy (SGM) technique in QDs and quantum billiards with corresponding chaotic dynamics[213-219]. In these earlier works, features potentially linked to quantum scars were identified in the $LDOS$ maps acquired by SGM. However, it is ambiguous whether those identified features are indeed quantum scars due to the low experimental data quality in these previous SGM works. Compared to SGM, STM is an experimental tool more suitable for the direct visualization of quantum scars because STM can more directly acquire $LDOS$ maps. Additionally, STM can perform such mapping with atomic scale resolution, which is not possible with SGM. Yet only very few experimental works[62,220] have attempted using STM to directly visualize quantum scars and with no success. This is partly due to the incompatibility between STM and conventional electrostatically defined QDs and quantum billiards, which are typically buried in semiconductor heterojunctions, making them inaccessible to STM. But the recent advancements in the in-situ creation and probing of exposed graphene QDs with STM[53,57-60,62-64,69] solves the issue of incompatibility between STM and electrostatically defined QDs, thus offering an opportunity to directly and unambiguously visualize quantum scars in quantum systems. In this chapter, I will show our recent experimental results on the wavefunction mapping of stadium shaped MLG QDs in attempting to achieve the direct visualization of quantum scars.

8.2 In-situ Creation of Stadium Shaped MLG QDs

In this work, the stadium shaped MLG QDs were created with the two-step tip pulsing technique described in section 2.3.2 of chapter 2. Compared to the creation of circular MLG and BLG QDs as described in chapters 5 and 6, the creation of stadium shaped MLG QDs is a bit less straightforward and requires more careful tuning during the tip pulsing process. Because of this, I will briefly describe the steps on how we create stadium shaped MLG QDs as schematized in Figure 8.1 below.

To start creating a stadium shaped MLG QD, we typically will find a pristine MLG region with at least $400\ \text{nm} \times 200\ \text{nm}$ area. After finding a pristine MLG region that meets this requirement, we will first do three subsequent tip bias pulses around the center of the identified pristine MLG region at three locations separated by $100\ \text{nm}$ along a line as schematized in Figure 8.1a. During these tip bias pulses, the STM tip is kept relatively close to the sample surface $(\sim 1.1\ \text{nm})$ and a negative gate voltage $(V_G \sim -60\ \text{V})$ is applied. After this step, a large n-doped region that covers the whole identified pristine MLG area can be created.

Next, we will create smaller p-doped regions in this large n-doped background. To do so, in the following tip pulsing procedures, the STM tip will be kept relatively far away from the sample surface $(\sim 2.0\ \text{nm})$ and with a positive gate voltage $(V_G \sim 60\ \text{V})$ being applied during the tip bias pulse. As schematized in Figure 8.1b,c, we will first do two subsequent tip bias pulses at two locations separated by 150 nm around the center of identified pristine MLG region. During this procedure, a single circular p-doped region and a coupled double circular p-doped region can be created subsequently after each tip bias pulse. The doping patterns shown in Figure 8.1b,c are effectively the same as those single MLG QDs and coupled MLG QDs studied in chapter 5.

After achieving a coupled double circular p-doped region, we will perform three subsequent tip bias pulses to render the p-doped region to an approximate stadium shape as shown in Figure 8.1d-f. The locations of these three extra tip bias pulses are typically evenly distributed between the centers of the two circular p-doped regions created in the previous steps. In the most ideal situation, after completing these three extra tip pulsing steps, an approximately stadium shaped MLG QD can be created.

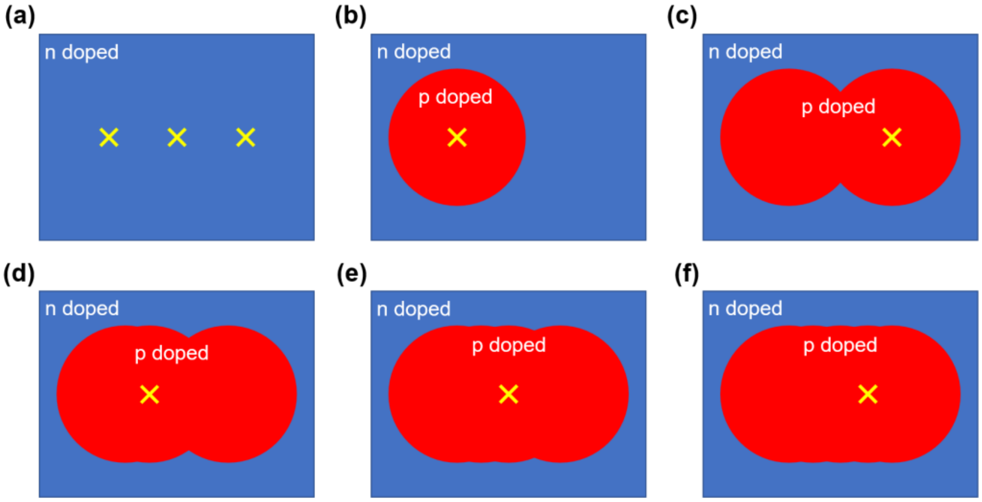

Figure 8.1 Schematic of the in-situ creation of a stadium shaped MLG QD. (a)-(f) The tip pulsing sequence to create a stadium shaped MLG QD and the resulting doping pattern after each step. The yellow cross indicates the location of the tip bias pulse. The blue and red colors represent n-doped and p-doped MLG regions, respectively.

After achieving a stadium shaped MLG QD with the tip pulsing technique, we can then probe its electronic structure with the conventional STM/STS technique as schematized in Figure 8.2a. During the measurements, a back gate voltage V_G can be applied to further tune and optimize the potential well of in-situ created stadium shaped MLG QD. In addition, an out of plane magnetic field can also be applied. Figure 8.2b shows a typical STM topography of a $400 \times 200\ \mathrm{nm}^2$ pristine MLG region where we created a stadium shaped MLG QD with the tip pulsing technique. Before performing wavefunction mapping, we characterize the potential well of in-situ created stadium shaped MLG QD. Figure 8.2c,d shows the experimentally measured $dI/dV_S(V_S, d)$ along the horizontal and vertical line across the stadium center at $V_G = -19\ \mathrm{V}$, respectively. The dark feature near $V_S = 0$ in Figure 8.2c,d corresponds to the phonon gap of graphene STS, which is discussed in section 2.1.1. A spatially varying dark envelope appears at positive V_S corresponds to the spatial energy variation of MLG band's Dirac point, which essentially gives us information about the potential well profile of our in-situ created stadium shaped MLG QD. Along the horizontal direction (Figure 8.2c), the potential well features a flat potential region near the stadium center, then the potential drops down near the stadium boundary. But along the vertical direction (Figure 8.2d), there is no flat potential region, and the potential well has an approximately quadratic shape. Based on this information, we can imagine the stadium shaped MLG QD in our experiment has a bathtub like potential well as depicted in Figure 8.3, which has a conduit-like shape around the stadium center and connected by two quadrant spheric-like shapes at the two ends.

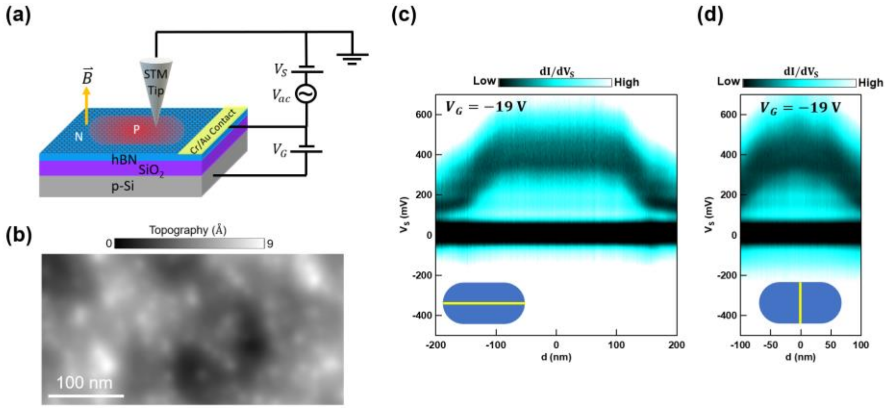

Figure 8.2 Characterizing the potential well of in-situ created stadium shaped MLG QD. (a) Schematic of the experimental set up. (b) STM topography of a $400 \times 200\ \mathrm{nm}^2$ pristine MLG region where a stadium shaped MLG QD was created. The scanning parameters used to acquire the data were $I = 0.72\ \mathrm{nA}, V_S = -18\ \mathrm{mV}$. (c)-(d) Experimentally measured $dI/dV_S(V_S, d)$ at $V_G = -19\ \mathrm{V}$ across the stadium center along the horizontal (c) and vertical (d) directions. The inset shows the schematic of the measurement direction.

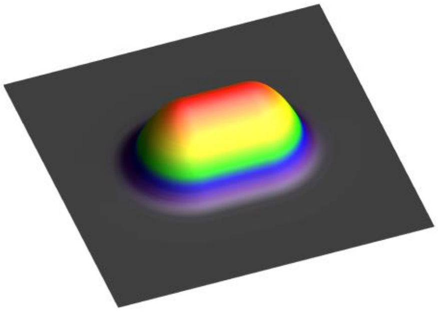

Figure 8.3 Schematic of the 3D representation of the potential well of the stadium shaped MLG QD in our experiment.

8.3 Wavefunction Mapping for In-situ Created Stadium Shaped MLG QDs

After characterizing the potential well of our in-situ MLG QDs, we now perform constant bias dI/dV_S map measurements to probe their wavefunctions. Figure 8.4 shows the dI/dV_S maps measured at $V_S = -18\ \mathrm{mV}$ at various V_G for the in-situ created stadium shape MLG QD shown in Figure 8.2c,d. At more positive V_G, we can see our in-situ created MLG QD indeed has an approximate stadium shape. We also notice the size of the in-situ created MLG QD generally becomes larger at more negative V_G, which is a result of the tuning of the potential well sharpness and Fermi level relative to the QD potential well when changing V_G. At more positive V_G, the potential well is generally sharper and the QD Fermi level is closer to the potential well bottom where the p-n junction boundary is smaller, these can both lead to a smaller QD size in the constant bias dI/dV_S map measurements. More interestingly, we clearly see enhanced dI/dV_S signals along certain closed trajectories, which mimics quantum scars. For example, enhanced dI/dV_S along a figure-eight trajectory (similar to the so called bow tie scar[212]) is observed at $V_G = -22$ V, -19 V and 10 V, then enhanced dI/dV_S along vertical trajectories (similar to the co called bouncing ball scar[212]) is observed at $V_G = -18$ V, -5 V, 0 V and 5 V.

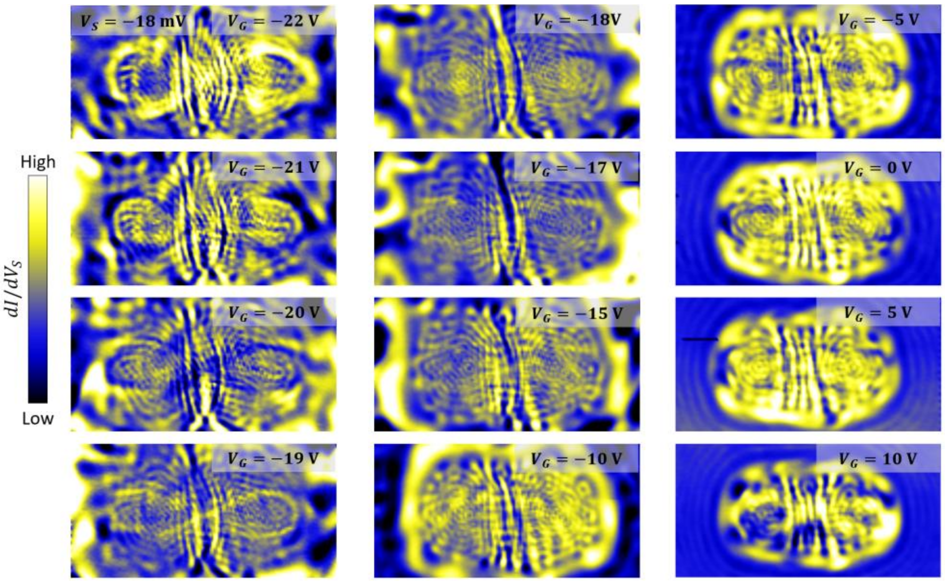

Figure 8.4 V_G dependence of dI/dV_S maps for in-situ created stadium shaped MLG QD. All dI/dV_S maps were acquired at $V_S = -18$ mV with a 2 mV ac modulation, the applied V_G for each dI/dV_S map are labeled at the top right corner of each image. The scanning window size is 400 nm × 200 nm.

To better characterize these observed features that are potentially quantum scars, we next perform dI/dV_S map measurements at a constant V_G but at different V_S.

Compared to dI/dV_S map measurements at a constant V_S with varying V_G, dI/dV_S maps measured at a constant V_G with varying V_S can keep the doping and potential well of the stadium shaped MLG QD unchanged, thus disentangling changes in QD states from a changing confinement potential profile and revealing the energy dependence of the QD wavefunctions. Figure 8.5 shows the experimentally measured dI/dV_S maps at $V_G = -19$ V at V_S between -18 mV and -8 mVand between 6 mV and 16 mV with a 2 mV interval. At $V_S = -18$ mV, enhanced dI/dV_S is observed along a figure-eight trajectory. When increasing V_S, we can see the enhancement of dI/dV_S along the figure-eight trajectory will decrease ($V_S = -16$ mV) and can even reverse to a reduction ($V_S = -14$ mV) before an enhancement is observed again ($V_S = -12$ mV). A similar behavior is observed for the enhanced dI/dV_S along a vertical trajectory, an enhancement is observed at $V_S = 6$ mV, then the enhancement gradually reduces ($V_S = 8$ mV, 10 mV) and reverses to a reduction ($V_S = 12$ mV), finally an enhancement redevelops ($V_S = 14$ mV) until a strong enhancement similar to that at $V_S = 6$ mV is observed again ($V_S = 16$ mV).

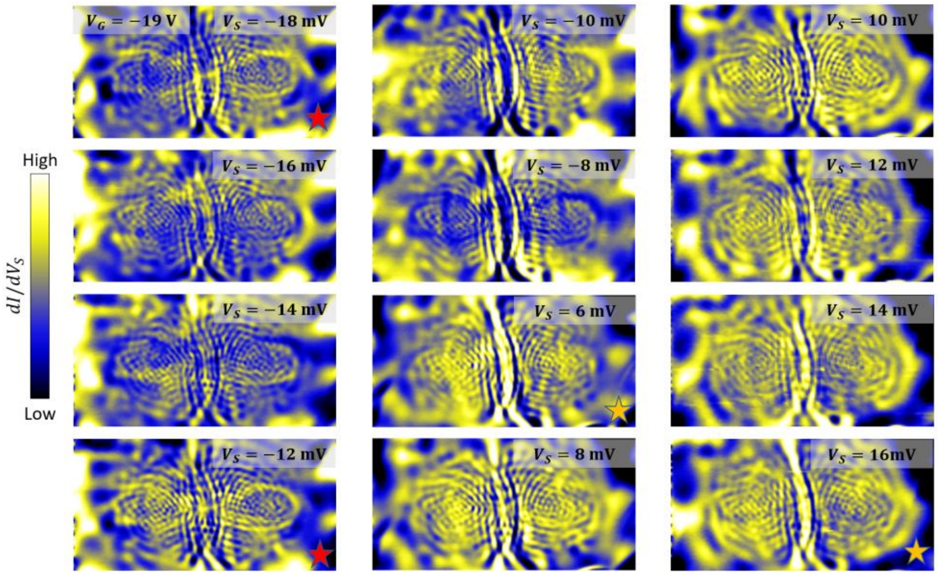

Figure 8.5 V_S dependence of dI/dV_S maps for in-situ created stadium shaped MLG QD. All dI/dV_S maps were acquired at $V_G = -19$ V with a 2 mV ac modulation, the applied V_S for each dI/dV_S map are labeled at the top right corner of each image. The scanning window size is 400 nm × 200 nm. The red and yellow star marks the energy at which a strong enhancement along figure-eight and vertical trajectories is observed, respectively.

By performing dI/dV_S map measurements at more bias voltages and with $V_G = -19$ V, we find the enhanced dI/dV_S along the figure-eight and vertical trajectories can keep reoccurring at additional different energies. The enhancement of dI/dV_S along the figure-eight trajectory recurs with every 6 meV (Figure 8.6a), but the enhancement of dI/dV_S along the vertical trajectory recures with every 10 meV (Figure 8.6b). Notably, such equal energy spacing recurrence is also expected for relativistic quantum scars[201]. Because we used MLG as a platform to create stadium shaped QDs, we expect the quantum scars in our experiments, if there are any, will be relativistic. Thus, the observed equal energy spacing recurrence for these enhanced

dI/dV_S patterns along closed trajectories further suggests these features are potentially quantum scars.

More quantitatively, it is predicted that the recurrence energy ΔE for a relativistic quantum scar is related to the length L of its corresponding classical closed orbit as[201] $\Delta E = hv_F/L$, where h is Planck's constant and $v_F \approx 10^6$ m/s is MLG's Fermi velocity. With the high spatial resolution of our dI/dV_S maps, we can directly get the length of the observed figure-eight and vertical trajectories by fitting them with short straight lines as shown by the red dashed lines in Figure 8.6a,b, respectively. From such fitting, we get L is around 668 nm and 401 nm for the figure eight trajectory and vertical trajectory, respectively. With the extracted L, we can estimate ΔE to be around 6.2 meV and 10.3 meV for the figure-eight and vertical trajectories, respectively, which are both in good agreement with our experimental observation. This further suggests that the enhanced dI/dV_S pattern observed in our experiment along the figure-eight and vertical trajectories are potentially quantum scars.

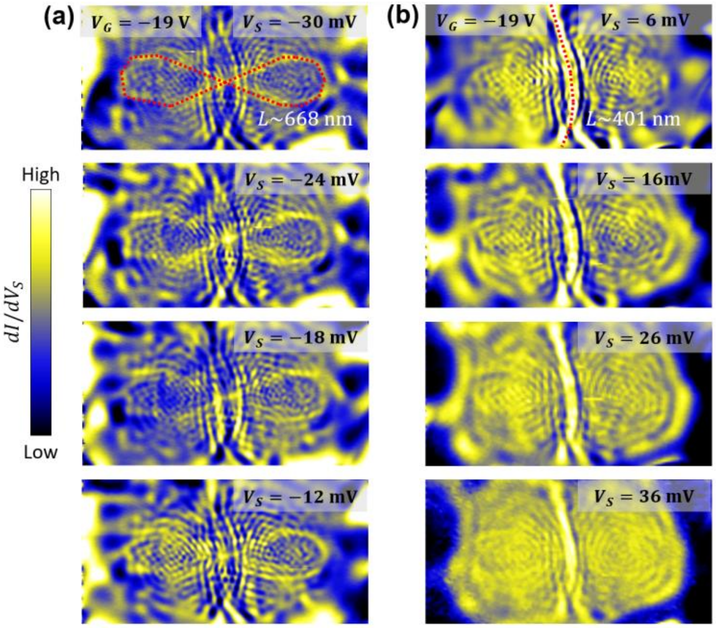

Figure 8.6 Connection between recurrence energy ΔE and trajectory length L. (a)-(b) Experimental dI/dV_S maps at $V_G = -19$ V that show an enhanced dI/dV_S along figure-eight (a) and vertical (b) trajectories. The corresponding V_S for each map is shown at the top right corner of each map. The red dashed line in the top most map in (a) and (b) corresponds to the fitted figure-eight and vertical trajectories, respectively. The extracted length L is shown next to the fitted trajectory. The scanning window size is 400 nm × 200 nm for all maps.

Such quantitative connection between ΔE and L for both the figure-eight and vertical trajectories is also observed at other gate voltages. Figure 8.7 shows the experimentally measured dI/dV_S maps that have an enhanced dI/dV_S along a figure-eight trajectory at $V_G = -22$ V, 0 V and 10 V. The observed recurrence energy is around 6 meV, 8 meV and 10 meV for $V_G = -22$ V, 0 V and 10 V, respectively. The length of the extracted figure-eight trajectory at $V_G = -22$ V, 0 V and 10 V (indicated by red dashed lines in Figure 8.7a-c, respectively) is around 757 nm, 532 nm and 550 nm, respectively. This leads to a theoretical recurrence energy around 5.5 meV, 7.8 meV and 7.5 meV for $V_G = -22$ V, 0 V and 10 V, respectively, which is in good agreement with experimentally observed recurrence energy at each V_G. Figure 8.8 shows the experimentally measured dI/dV_S maps that have an enhanced dI/dV_S along vertical trajectories at $V_G = -10$ V, 0 V and 10 V. A recurrence energy of 12 meV, 14 meV and 16 meV is observed at $V_G = -10$ V, 0 V and 10 V, respectively. By doing similar analysis as for the figure-eight trajectories, we can get the theoretical recurrence energy for vertical trajectories to be around 11.7 meV, 14.4 meV and 16.1 meV at $V_G = -10$ V, 0 V and 10 V, respectively, which is also in good agreement with the experimentally observed recurrence energy at each V_G. These observations all suggest the experimentally observed connection between ΔE and L is not simply a coincidence, which again solidifies the likelihood that the enhanced dI/dV_S along the figure-eight and vertical trajectories observed in our experiments correspond to quantum scars.

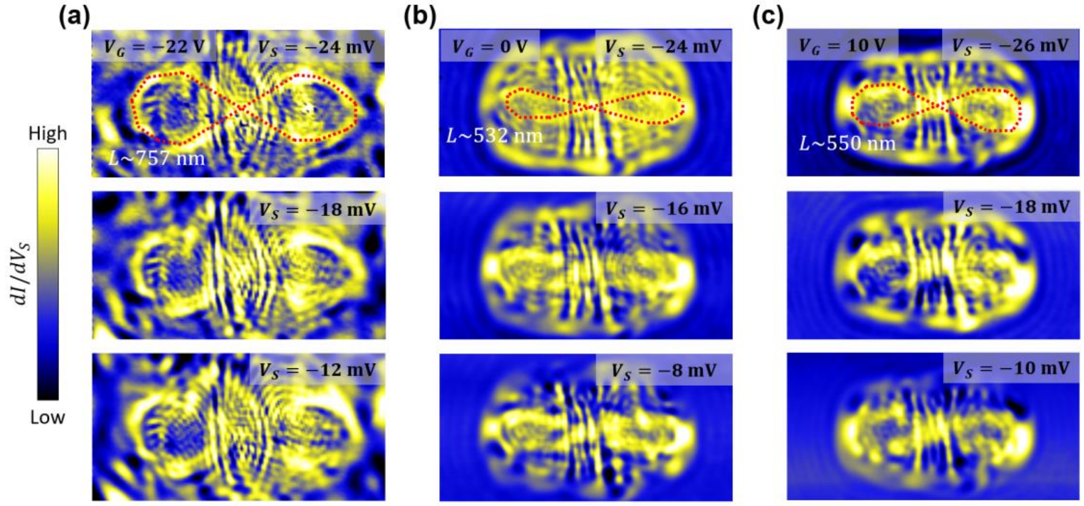

Figure 8.7 Connection between ΔE and L for figure-eight trajectories at more V_G. (a)-(c) Experimental dI/dV_Smaps at $V_G = -22$ V (a), 0 V (b) and 10 V (c) that show an enhanced dI/dV_S along figure-eight trajectories. The corresponding V_S for each map is shown at the top right corner of each map. The red dashed line in the top most map in (a)-(c) corresponds to the fitted figure-eight trajectory. The extracted length L is shown next to the fitted trajectory. The scanning window size is 400 nm × 200 nm for all maps.

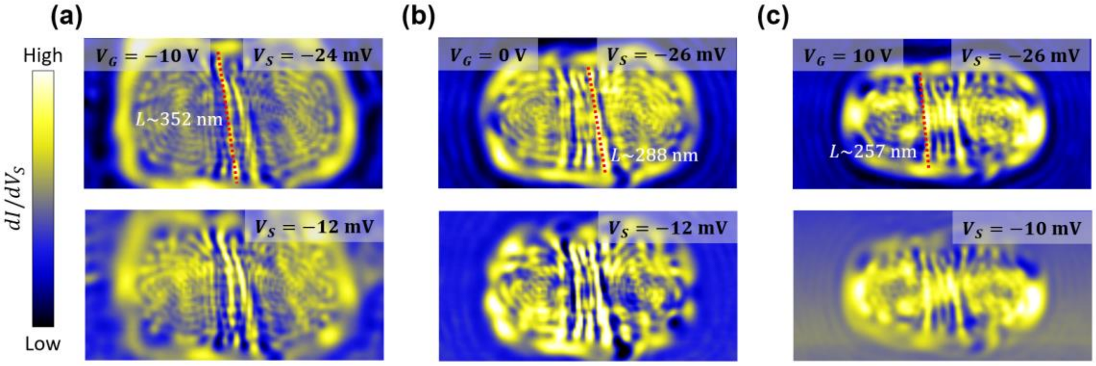

Figure 8.8 Connection between ΔE and L for vertical trajectories at more V_G. (a)-(c) Experimental dI/dV_S maps at $V_G = -10$ V (a), 0 V (b) and 10 V (c) that show an enhanced dI/dV_S along vertical trajectories. The corresponding V_S for each map is shown at the top right corner of each map. The red dashed line in the top most map in (a)-(c) corresponds to the fitted vertical trajectory. The extracted length L is shown next to the fitted trajectory. The scanning window size is 400 nm × 200 nm for all maps.

8.4 Quantum Classical Correspondence in Stadium Shaped MLG QDs

To understand our experimental findings more concretely, we perform combined TB and classical dynamics simulations for a stadium shaped MLG QD similar to those in our experiment. Figure 8.9a shows the potential well of the stadium shaped MLG QD used in our simulations, it has a shape similar to the one shown in Figure 8.3. To compare the similarity between the potential well used in our simulations and the actual potential well of stadium shaped MLG QD in our experiments, we overlay potential line cuts from Figure 8.9a to experimental $d^2I/dV_S^2(V_S, d)$ data taken from the corresponding direction, such comparisons are shown in Figure 8.9b,c. The $d^2I/dV_S^2(V_S, d)$ plot shown in Figure 8.9b,c are from the same stadium shape MLG QD shown in Figure 8.2c,d at $V_G = -19$ V along the horizontal and vertical directions across the stadium center, respectively. Here we use $d^2I/dV_S^2(V_S, d)$ plot instead of $dI/dV_S(V_S, d)$ plot to better identify the energy position of the local minimum in the

dI/dV_S spectra, which corresponds to MLG's Dirac point. Evidently, in Figure 8.9b,c, the line cut of the simulation potential generally is very similar to the experimental potential line cut along both the horizontal (Figure 8.9b) and vertical (Figure 8.9c) directions.

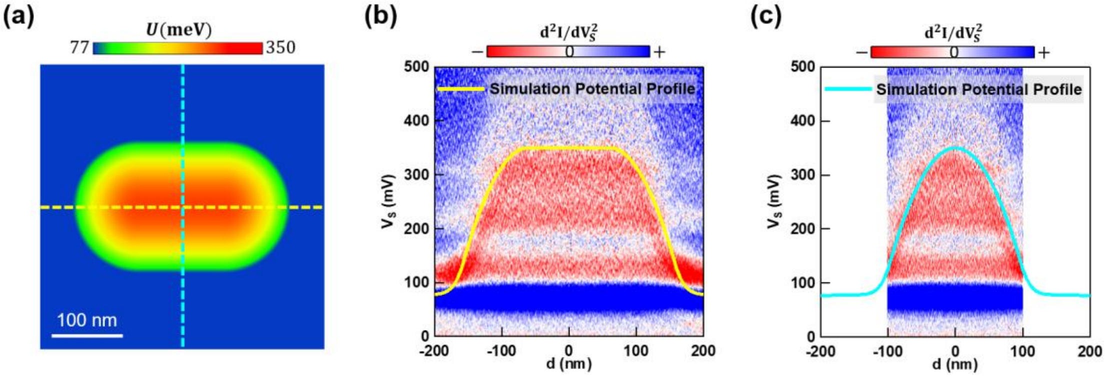

Figure 8.9 Comparison between the stadium potential well in simulation and in experiment. (a) Color plot of the potential well used in our TB and classical dynamics simulations for a stadium shaped MLG QD. (b)-(c) $d^2I/dV_S^2(V_S, d)$ plot numerically derived from the $dI/dV_S(V_S, d)$ data shown in Figure 8.2c,d, respectively. The yellow and blue solid lines in (b) and (c) are the potential line cuts from the potential well shown in (a) along the yellow and blue dashed lines, respectively.

With the potential well as defined in Figure 8.9a, we first proceed to analyze the corresponding classical dynamical properties for MLG QDs with such a potential well. To do so, it is useful to calculate the Poincaré surface of section (PSS) for this dynamical system. The definition of the PSS in our calculations is schematized in Figure 8.10. The energy of the PSS (denoted as E_{PSS}) is defined as the energy between the potential well bottom and the energy cut as schematized in Figure 8.10a, and the x coordinate and momentum angle θ with respect to $y = 0$ axis is recorded every time the particle crosses the $y = 0$ axis (Figure 8.10b). Figure 8.11 shows the calculated PSS for a MLG QD with the potential well shown in Figure 8.9a (calculation method in Appendix F). As we can see, although at low E_{PSS} the system seems to be purely chaotic (Figure 8.11a), the system quickly develops into a mixed dynamics with multiple stable islands as E_{PSS} increases (Figure 8.11b-f). Comparing with the energies of our experimental dI/dV_S maps with respect to the potential well bottom, those calculated PSS at higher E_{PSS} should be more relevant to our experimental results. So different from our original expectations, the corresponding classical dynamics of our in-situ created stadium shaped MLG QDs is mixed instead of purely chaotic around the energies we probed their QD wavefunctions.

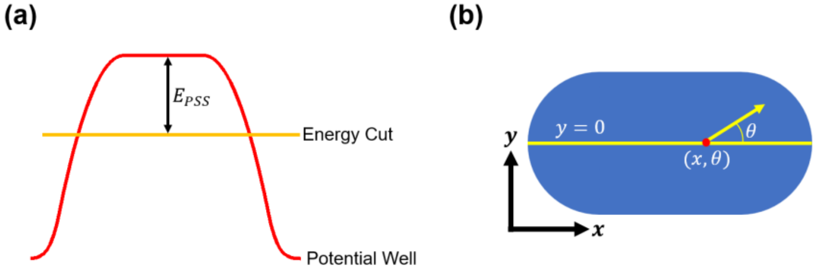

Figure 8.10 The definition of Poincaré surface of section (PSS) in our calculations. (a) Schematic of the energy cut for PSS. (b) Schematic of the spatial cut for PSS, which is indicated by the yellow line. The yellow arrow depicts the momentum direction when particle crosses the yellow line.

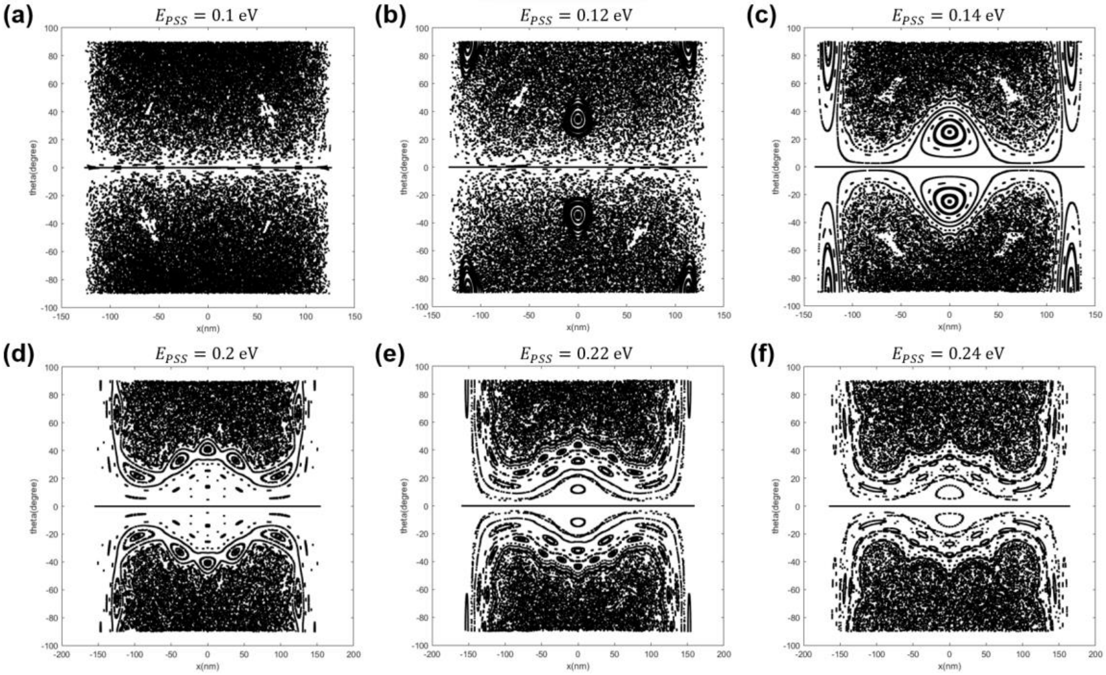

Figure 8.11 PSS for stadium shaped MLG QD. (a)-(f) Calculated PSS for a stadium shaped MLG QD with the potential well shown in Figure 8.9a. The energy cut of each PSS is shown at the top of each map.

After understanding the general classical dynamical properties of the stadium shaped MLG QD in our experiments, we next try to identify classical periodic orbit that exists in the model stadium shaped MLG QD that looks similar to the figure-eight and vertical trajectories observed in our experiments. As shown in Figure 8.12, we find there indeed exists a vertical periodic orbit (Figure 8.12b) and a figure-eight periodic orbit (Figure 8.12c) that looks similar to those observed in our experiments. By tracing their origin in the corresponding PSS, we find the figure-eight orbit is a stable periodic orbit, which corresponds to a stable island in PSS. On the other hand, the vertical orbit is buried in the chaotic sea, which is an unstable periodic orbit. Such information on the stability of the classical periodic orbit is important for the identification of quantum scars because according to the definition, quantum scar corresponds to states with enhanced wavefunction intensity along unstable but not stable periodic orbits[14,103,198-200]. As a result, according to our classical dynamics simulation, the figure-eight patterns observed in our experiments are not quantum scars. However, the enhanced dI/dV_S along vertical trajectories should be quantum scars.

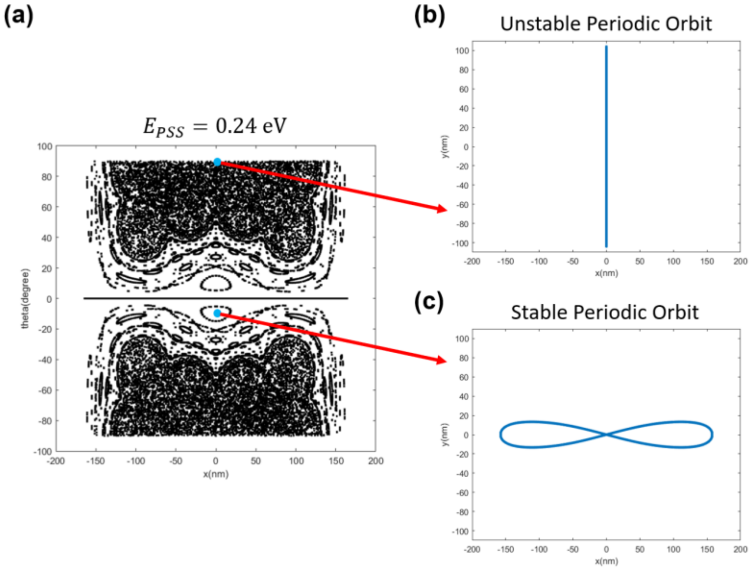

Figure 8.12 Classical periodic orbits in stadium shaped MLG QD. (a) PSS at $E_{PSS} = 0.24$ eV for a stadium shaped MLG QD with the potential well shown in Figure 8.9a. (b) An unstable vertical periodic orbit exists in a stadium shaped MLG QD with the potential well shown in Figure 8.9a at $E_{PSS} = 0.24$ eV. (c) A stable figure-eight periodic orbit exists in a stadium shaped MLG QD with the potential well shown in Figure 8.9a at $E_{PSS} = 0.24$ eV.

After conducting the classical dynamics simulations, we next use the TB method as described in section 4.1 to simulate dI/dV_S maps in a model stadium shaped MLG QD. The potential well used in the TB simulation is the same as that in the classical dynamics simulations, which is shown in Figure 8.9a. As shown in Figure 8.13, the experimentally observed enhanced dI/dV_S along the figure eight and vertical trajectories and their equal energy spacing recurrence are both reproduced in our simulation results. One thing to note is that here the energy E is different from E_{PSS}, with the potential well used in our simulations, these two energies are related as $E_{PSS} = 350\ \text{meV} - \text{E}$. With the classical periodic orbits obtained from our classical dynamics simulations, we can further analyze the connection between the recurrence energy ΔE and orbital length L similar to what we did for our experimental data. The calculated vertical and figure-eight periodic orbits at $E = 113$ meV is overlaid to the simulated dI/dV_S map at $E = 113$ meV in Figure 8.13a,b, respectively. The size and shape of these two classical orbits both generally matches the vertical and figure-eight patterns in the simulated dI/dV_S map, accordingly.

We can next analyze the connection between the recurrence energy ΔE and periodic orbit length L with our combined TB and classical dynamics simulation results. From the classical dynamics simulation, we extracted the length L of the vertical and figure-eight periodic orbit to be around 412 nm and 651 nm at $E = 113$ meV, respectively. Then similar to the analysis we did to our experimental data, by using the relation $\Delta E = hv_F/L$, we can estimate the recurrence energy ΔE to be around 10.0 meV and 6.4 meV for the enhanced dI/dV_S pattern along the vertical and figure-eight orbits, respectively. These two values are both in good agreement with the ΔE observed in our simulation results. With the classical dynamics simulations, we can further calculate the classical action ($S = \oint \vec{p} \cdot d\vec{q}$) of the vertical and figure-eight periodic orbits at the energy of each simulated dI/dV_S map, their values are listed at the top left corner of each map in Figure 8.13. We observe an approximate $2\pi\hbar$ difference for both the vertical and figure-eight orbits when the vertical or figure-eight pattern in the simulated dI/dV_S recurs, which is expected from semiclassical quantization conditions[198,199].

Interestingly, we also notice a difference between the exact semiclassical quantization conditions for the vertical orbit and figure-eight orbit. The vertical pattern appears at S with half integer values of $2\pi\hbar$, on the other hand, the figure-eight pattern appears at S with integer values of $2\pi\hbar$. The slight deviations from exact half-integer or integer values of $2\pi\hbar$ in Figure 8.13 is most likely due to the energies we choose is slightly deviated from the optimal quantization energy. Our understanding for the quantization condition difference between the vertical and figure-eight periodic orbits is still in progress, but I think it is likely related to the difference between the Maslov indices[198,199] associated these two orbits. In the 1D case, with the Wentzel–Kramers–Brillouin (WKB) approximation, the semiclassical quantization condition is given as[198,199]:

$$S = \oint p(x)dx = 2\pi\hbar(n + \beta_1 + \beta_2), n \in \mathbb{N}_0 \tag{8.1}$$

, where β_1 and β_2 are the Maslov indices associated with the two turning points of a classical orbit. And the value of β can be determined as following[198,199]:

$$\beta = \begin{cases} \frac{1}{4}\ for\ soft\ reflection \\ \frac{1}{2}\ for\ hard\ reflection \end{cases} \tag{8.2}$$

If we assume equation 8.2 still holds for relativistic systems, and we treat the vertical periodic orbit in our stadium shaped MLG QD as a 1D problem, the two soft reflections of this orbit will lead to a quantization condition of $S = 2\pi\hbar(n + 1/2)$, which agrees with our simulation results (Figure 8.13a). Currently, I am not totally clear how to assign the Maslov indices to the 2D figure-eight periodic orbit in our stadium shaped QD. If we assume its total Maslov indices is zero and the semiclassical quantization condition given in Equation 8.1 is still suitable for such a 2D orbit, then the semiclassical quantization condition observed in our simulation can be explained.

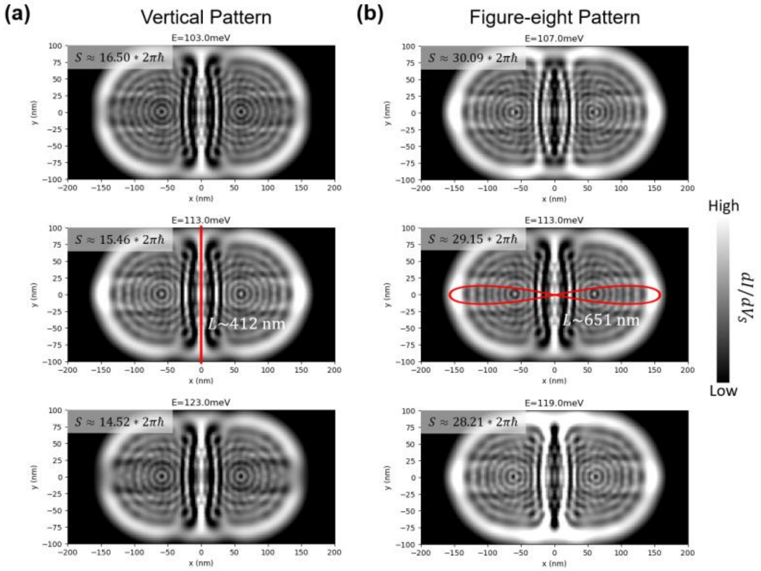

Figure 8.13 Simulated dI/dV_S maps for a stadium shaped MLG QD. (a)-(b) Simulated dI/dV_S maps with an enhanced dI/dV_S along the vertical and figure-eight periodic orbits, respectively. The energy of each dI/dV_S map is listed above each map. The top left corner in (a) and (b) shows the calculated classical action at the dI/dV_S map's energy for the vertical and figure-eight periodic orbits, respectively.

8.5 Magnetic Field Response of Stadium Shaped MLG QDs' Wavefunctions

After getting a relatively thorough understanding of the vertical and figure-eight patterns observed in the dI/dV_S maps of our stadium shaped MLG QDs, we next investigate their response to external magnetic fields. Figure 8.14 shows the experimental measured dI/dV_S maps for the same stadium shaped MLG QD shown in Figure 8.5 at $V_G = -19$ V in $B = 0$ T, 0.1 T, 0.2 T, 0.3 T and 0.4 T at some selected

V_S that shows a vertical or figure-eight pattern in $B = 0$ T. We find the figure-eight pattern with enhanced dI/dV_S gradually disappears when B increases (Figure 8.14a,b), but the vertical pattern can switch between enhanced dI/dV_S and reduced dI/dV_S when B increases (Figure 8.14c,d). In addition, we notice an additional curved pattern (marked by a red box in Figure 8.14c) with enhanced dI/dV_S appears in $B = 0.4$ T.

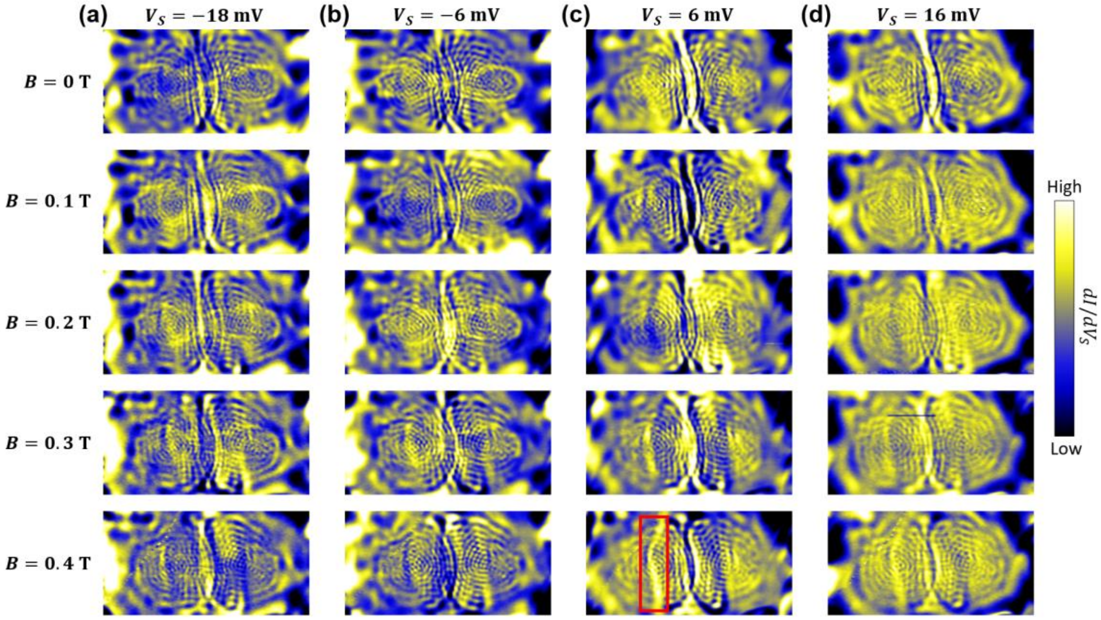

Figure 8.14 Magnetic field response of the enhanced dI/dV_S pattern along the vertical and figure-eight trajectories. (a)-(d) Experimental dI/dV_S maps for the same stadium shaped MLG shown in Figure 8.5 measured at $V_S = -18$ mV, -6 mV, 6 mV and 16 mV in different B, respectively. The value of the applied B for each row is shown at the left side of this figure. The red box indicates the new curved pattern with an enhanced dI/dV_S.

To compared with our experimental observations, we first performed TB calculations to simulate dI/dV_S maps in the stadium shaped MLG QD with different B applied. Figure 8.15 shows the simulated dI/dV_S maps at $E = 113$ meV in $B =$ 0 T, 0.1 T, 0.2 T, 0.3 T and 0.4 T. At this selected energy, the simulated dI/dV_S map shows enhanced dI/dV_S along both the vertical and figure-eight periodic orbits (Figure

8.15a). When B increases, the simulated dI/dV_S maps qualitatively reproduce all our experimental observations, namely, the gradual disappearance of the figure-eight pattern and the oscillating enhancement or reduction of dI/dV_S intensity for the vertical pattern. In addition, the simulated dI/dV_S map in $B = 0.4$ T also shows two addition curved patterns with enhanced dI/dV_S, which is similar to what was seen in our experiment.

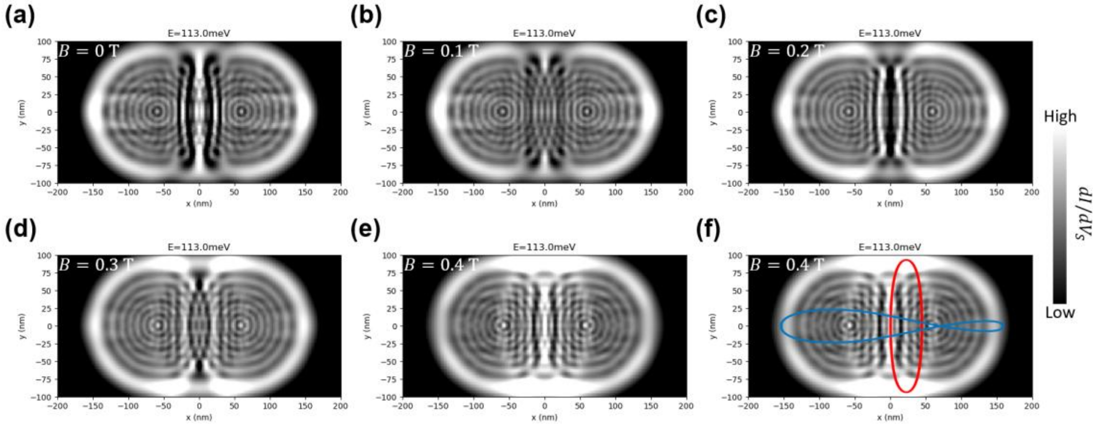

Figure 8.15 Simulated dI/dV_S maps for a stadium shaped MLG QD in different B. (a)-(e), dI/dV_S maps calculated based on a TB model for a stadium shaped MLG QD at $E = 113$ meV in $B = 0$ T, 0.1 T, 0.2 T, 0.3 T and 0.4 T, respectively. The potential well shown in Figure 8.9a is used in the model. (f) The same simulated dI/dV_S map as shown in (e) with the calculated classical stable (blue line) and unstable (red line) periodic orbits overlaid on top.

To better understand the magnetic field response of the wavefunctions in stadium shaped MLG QD, we analyze the classical dynamics of the stadium shaped MLG QD with a magnetic field applied. Figure 8.16a shows the PSS at $E_{PSS} = 0.24$ eV for the stadium shaped MLG QD at $B = 0.4$ T, similar to the $B = 0$ case (Figure 8.11a), there still exists some stable islands in the PSS at $B = 0.4$ T, but the dynamics is generally more chaotic than the $B = 0$ T case. Figure 8.16b,c shows an unstable periodic orbit and a stable periodic orbit that exists in the stadium shaped MLG QD at

$B = 0.4$ T, respectively. The two orbits shown in Figure 8.16b,c are evolved from the vertical and figure-eight orbits in $B = 0$ T, respectively. One thing to note is that there also exists a mirror symmetric orbit with respect to the $x = 0$ axis for both the unstable and stable orbits shown in Figure 8.16b,c.

With these understandings of the classical dynamics of the stadium shaped MLG QD at non-zero B in hand, we can get a qualitative understanding of the magnetic field response of the vertical and figure-eight patterns. The gradual disappearance of the figure-eight patterns in dI/dV_S maps when increasing B can be understood as its corresponding symmetric classical figure-eight orbit gradually disappears when increasing B. As shown in Figure 8.15f, we can actually roughly see a correspondence between the simulated dI/dV_S pattern and the distorted figure-eight orbit (blue line) in $B = 0.4$ T. The reason we did not see such a new correspondence pattern in our experiment could be the signal to noise ratio in our experiment is not high enough.

Then to explain the oscillating dI/dV_S intensity along the vertical trajectory and the newly appeared curved pattern, we consider the unstable loop shaped orbit in B. The oscillating dI/dV_S intensity along the vertical trajectory can be understood as the initial line shaped vertical periodic orbit transitioning into a loop shape when B is applied. Such a loop shaped orbit can pick up an Aharonov–Bohm (AB) phase in B as discussed in section 5.3.3 for circular MLG QDs. This additional AB phase can lead to the quantization condition change at the same energy, which can give rise to an oscillating enhanced or reduced dI/dV_S along the vertical trajectory as seen both in our experiment and TB simulation. As for the newly appeared curved pattern observed in

$B = 0.4$ T (Figure 8.14c), it can be understood as a result of the quantum classical correspondence of the newly developed loop shaped unstable periodic orbit in $B = 0.4$ T. A comparison between the curved pattern in simulated dI/dV_S map and this loop shaped unstable periodic orbit (red line) is shown in Figure 8.15f, their shapes and sizes generally agree with each other.

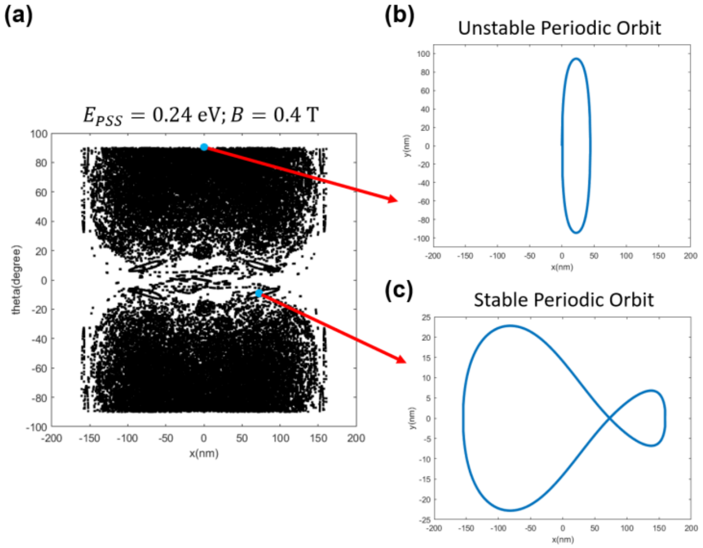

Figure 8.16 Classical periodic orbits in stadium shaped MLG QD with an applied B. (a) PSS at $E_{PSS} = 0.24$ eV in $B = 0.4$ T for a stadium shaped MLG QD with the potential well shown in Figure 8.9a. (b) An unstable periodic orbit that exists in the stadium shaped MLG QD at $E_{PSS} = 0.24$ eV in $B = 0.4$ T. (c) A stable periodic orbit that exists in the stadium shaped MLG QD at $E_{PSS} = 0.24$ eV in $B = 0.4$ T. The red arrows indicate the corresponding positions of each periodic orbit in the PSS.

8.6 Conclusions

In summary, we used the two-step tip pulsing technique successfully created a stadium shaped MLG QD with a deep and sharp potential well. By performing constant bias dI/dV_S mapping, we observed vertical and figure-eight patterns with enhanced dI/dV_S that can recur with equal energy spacing in our in-situ created stadium shaped MLG QD in $B = 0$ T. With a combined TB and classical dynamics simulations, we demonstrated these experimentally observed vertical and figure-eight patterns correspond to an unstable vertical periodic orbit and a stable figure-eight periodic orbit that exist in our stadium shaped MLG QD, respectively. And the recurrence property is a result of the relativistic nature of MLG QD systems. With such an understanding, the vertical patterns observed in our experiments should be quantum scars, which is also relativistic. I believe this is the first unambiguous direct visualization of quantum scars in a real quantum system. We further investigated the magnetic field response of the vertical and figure-eight patterns observed in our experiments, a good quantum classical correspondence is also demonstrated there. Our findings prove STM can be a powerful tool for investigating quantum scars, our work also opens the possibility of successful visualization of chiral quantum scars[222-225] and perturbation induced quantum scars[226-228] with in-situ created graphene QD systems in the future.

Chapter 9 Summary and Outlook

My dissertation focused on studying the electronic structure and magnetic field response of QDs that are electrostatically defined in graphene systems (including MLG, BLG and TLG). Conventionally, electrostatically defined QDs are studied with transport measurements. During my Ph.D. study, I instead investigated electrostatic graphene QDs with STM/STS by utilizing a very new in-situ graphene QD creation and probing technique that I described in chapter 2. This novel approach allowed us to gain both atomic spatial resolution and meV energetic resolution of graphene QD states at the same time; such capability cannot be achieved by any other experimental techniques currently and allowed us to be the first to observe many unique quantum phenomena in graphene QDs. This includes the observation of giant orbital magnetic moments and paramagnetic shift in MLG QDs due to the relativistic nature of their massless Dirac fermions (chapter 5), the effect of Berry curvature on the spatial distribution of BLG QD wavefunctions (chapter 6), giant valley Zeeman splitting in TLG QDs due to the giant topological orbital magnetic moment hosted in this system (chapter 7), and the unambiguous direct visualization of the quantum scars in stadium shaped MLG QDs (chapter 8). These results demonstrated that very rich physics can be studied with STM by creating artificial nanostructures with the in-situ local doping technique that I described in chapter 2.

One fruitful research direction could be pursued following the works presented in this dissertation is to use the in-situ local doping technique described in chapter 2 to create nanostructures or interfaces in materials that host richer quantum phases compared to MLG, BLG and TLG. These new types of nanostructures or interfaces can potentially give rise to many interesting emergent phenomena. Below I provide two examples of 2D material systems that host rich quantum phases and may still be compatible with the in-situ local doping technique described in chapter 2 to create artificial nanostructures or interfaces.

The first example is the recently discovered magical angle twisted bilayer graphene (MATBG), which can host varieties of gate tunable topological and correlated quantum phases, including superconductivity[188,229,230], orbital ferromagnetism[188,189,231], and Chern insulators[231-236]. Since MATBG devices are very similar to the graphene devices that I studied during my Ph.D. years, it is expected that the in-situ local doping technique I used should still work there. Many unique quantum phenomena can potentially be investigated in this system by creating electrostatically defined artificial nanostructures and interfaces with the in-situ local doping technique that I used for my Ph.D. studies. For example, φ_0-JJs and Majorana zero modes, which both have potential importance in quantum computation[237,238], have been recently proposed in MATBG and spin-orbital coupling proximitized MATBG with local electrostatic gating, respectively[239,240]. In addition, topologically protected chiral edge states with gate tunable chirality and channel numbers can also potentially be realized in MATBG by creating Chern insulator regions with different Chern numbers through local electrostatic gating[241]. Finally, with the in-situ local doping technique that I used in my Ph.D. studies, MATBG also offers a rare platform to realize electrostatically defined Andreev billiards[242,243], which utilizes the special retro-Andreev reflection (retro-AR) at the normal metal-superconductor (NS) interface. Such Andreev billiards is predicted to host unique quantum classical correspondence[242-244] compared to conventional quantum billiards that relies on the common specular reflection at the billiard boundary. For example, different from conventional quantum billiards, Andreev billiards are always integrable with any billiard shapes due to the retro-ARs at the NS boundaries if it is fully surrounded by superconducting regions. But a small magnetic field can turn on quantum chaos[242] in such Andreev billiards, which offers a precise control of the on and off of quantum chaos. And for Andreev billiards with partial NS boundaries, the imprints of classical chaotic dynamics can directly show up in level density as a hard gap instead of only in level spacing statistics as for conventional quantum billiards[243,244].

Another attractive material platform for studying artificial nanostructures and interfaces with the in-situ local doping and probing technique is the monolayer 1T'-WTe_2, which can host both superconductivity[245,246] and quantum spin hall states[247-249]. The topological insulator and superconductor phases in this material can be conveniently tuned from one to another through electrostatic doping. As a result, topological insulator-superconductor interfaces can potentially be created in this material through the in-situ local doping technique that I used in my previous studies. Topological insulator-superconductor interfaces have achieved a significant amount of attention in recent years because they can potentially be used to realize 1-D topological superconductivity and Majorana zero modes[250], which has potential importance in fault-tolerant topological quantum computation[238,251].

Chapter 10 Appendix Section

10.1 Appendix A: Python Scripts for Automated STM/STS Measurements

10.1.1 Gate Sweep

The python script below performs dI/dV_S spectra measurement at the top center of a scan window with 256×256 pixel numbers from $V_G = -50$ V to $V_G = 50$ V with a 0.1 V interval then brings V_G back to 0 V after the measurement is done.

```
''' ___ RUN MEGASWEEP___ '''
import visa
import win32com.client
import datetime
import calendar
import time
import numpy as np
ts = time.time()
ts = datetime.datetime.fromtimestamp(ts).strftime('%Y%m%d_%H%M%S')
stm=win32com.client.Dispatch("pstmafm.stmafmrem")
rm = visa.ResourceManager()
rm.list_resources()
itc4 = rm.open_resource("COM6")
#INPUT in Pixels
x_position = 127.99;
y_position = 0;
j=0
for i in np.arange(-50,50+0.0001,0.1): #np.arange(Initial_Voltage, Final_Voltage, Steps)
    itc4.write(":SOUR:VOLT %s" % (i))
    stm.stmbeep()
    time.sleep(0.15)
    stm.btn_vertspec(x_position,y_position)
    stm.savevertfilename='gs_' + ts + "_" + str(j).zfill(4)+".VERT"
    stm.vertsave()
    time.sleep(0.15)
    j+=1
for i in np.arange(50,0-0.001,-0.1):
    #stm.stmbeep()
    itc4.write(":SOUR:VOLT %s" % (i))
    time.sleep(0.1)
```

```
print "done"
```

10.1.2 Line Scan

The python script below performs a series of dI/dV_S spectra along the topmost horizontal line of a scan window with 256×256 pixel numbers.

```
''' ___ TAKE A LINESCAN ___ '''
import visa
import win32com.client
import datetime
import calendar
import time
import numpy as np
ts = time.time()
ts = datetime.datetime.fromtimestamp(ts).strftime('%Y%m%d_%H%M%S')
stm=win32com.client.Dispatch("pstmafm.stmafmrem")
rm = visa.ResourceManager()
rm.list_resources()
itc4 = rm.open_resource("COM6")

#INPUT in Pixels
x_start = 0;
y_start = 0;
x_end = 255;
y_end = 0;
stm.stmbeep()
stm.btn_vertspec_line(x_start,y_start,x_end,y_end)
print('1 done')
time.sleep(60)
```

10.1.3 dI/dV_S Mapping

The python script below performs a series of dI/dV_S maps at selected bias voltages ($V_S = -30\text{ mV}, -25\text{ mV}, -15\text{ mV}$ and -10 mV), the feedback tunneling current at each V_S is adjusted to make the tunneling junction resistance be $100\text{ M}\Omega$.

```
''' ___ SERIES of dI/dV images at various bias voltage ___ '''
```

```
import visa
import win32com.client
import datetime
import calendar
import time
import numpy as np
ts = time.time()
ts = datetime.datetime.fromtimestamp(ts).strftime('%Y%m%d_%H%M%S')
stm=win32com.client.Dispatch("pstmafm.stmafmrem")
rm = visa.ResourceManager()
rm.list_resources()
itc4 = rm.open_resource("COM6")
volts_init = -30
volts_final = -10
step= 1
a=np.array([-30, -25, -15, -10]) #list of gate voltages to measure
b=0
for i in np.arange(volts_init,volts_final+0.01*np.sign(step),step):
    stm.setparam('FBLogIset',i*10)
    time.sleep(0.005)
    if abs(i-a[b])<0.0001:
        print(i)
        stm.stmbeep()
        time.sleep(3)
        stm.scanstart()
        time.sleep(1*3600+30*60+8)
        stm.scanstop()
        time.sleep(3)
        b=b+1
```

10.1.4 Magnetic Field Sweep

The python script below performs a series of dI/dV_S spectra measurement from $B = 0$ T to $B = 0.4$ T with a 1 mT interval. The tip position adjusts after each measurement to compensate the relative drift between the STM tip and sample in magnetic fields.

```
''' ___ RUN B-field SWEEP with drift correction___ '''
import visa
import win32com.client
```

```
import datetime
import calendar
import time
import numpy as np
stm=win32com.client.Dispatch("pstmafm.stmafmrem")
rm = visa.ResourceManager()
rm.list_resources()
itc4 = rm.open_resource("COM6")
ts = time.time()
ts = datetime.datetime.fromtimestamp(ts).strftime('%Y%m%d_%H%M%S')
Vi=1*0.000019*42*0
Vf=1*0.000019*42*200
res=400
step=(Vf-Vi)/res
j=0
for i in np.arange(Vi,Vf+step,step): #np.arange(Initial_Voltage, Final_Voltage, Steps)
    if i==Vi:
        startamplitude=i
    else:
        startamplitude=i-step
    endamplitude=i
    rampstep=0.000019*2
    rampdelay=0.1
    DACgain=1
    DACoffset=-0.0001
    value=startamplitude
    DACvalue=value*DACgain+DACoffset

    if (startamplitude < endamplitude):
        while (value < endamplitude):
            stm.setdacvalf(1, 4, DACvalue)
            value+=rampstep
            DACvalue=value*DACgain+DACoffset
            time.sleep(rampdelay)
    else:
        while (value >= endamplitude):
            stm.setdacvalf(1, 4, DACvalue)
            value-=rampstep
            DACvalue=value*DACgain+DACoffset
            time.sleep(rampdelay)
    stm.stmbeep()
    if j<res/2:
        stm.move_tip_imagecoord(128-50*j/res,102*j/res,128-
50*(j+1)/res,102*(j+1)/res,100,50)
```

```
        time.sleep(5+12*j/res)
    else:
        stm.move_tip_imagecoord(206-206*j/res,-153+408*j/res,206-206*(j+1)/res,-
153+408*(j+1)/res,100,50)
        time.sleep(5+12*j/res)
    stm.vertspectrum()
    stm.savevertfilename='BS_' + ts + "_" + str(j).zfill(4)+".VERT"
    stm.vertsave()
    j=j+1
print "done"
```

10.2 Appendix B: Codes for Graphene QDs Simulation with TB Model

10.2.1 MLG QD

The Python code below can simulate the $LDOS$ spectra in the -400 meV to 400 meV energy range with a 2 meV energy resolution for a MLG QD in 0.4 T along a line across the QD center between $x = -100$ nm and $x = 100$ nm with a 1 nm spatial resolution. The MLG QD is defined on a 450 nm radius MLG sheet with a parabolic confinement potential well $V(r) = -0.2r^2\ \mathrm{meV/nm^2} + 100\ \mathrm{meV}$.

```
import multiprocessing
from multiprocessing import Pool
import time
import pybinding as pb
import numpy as np
import matplotlib.pyplot as plt
from math import sqrt, pi
from pybinding.constants import phi0
num_cores = 24 #multiprocessing.cpu_count()
start = list(range(-100,100,1))
block=int(len(start)/num_cores)+1
for j in np.arange(0,block,1):
    inputs = list(range(start[0+num_cores*j],start[0+num_cores*j]+num_cores,1))
    def initiate_pool(max_threads):
        if len(inputs) < max_threads:
            max_threads = len(inputs)
        args = list()
        # generate exhaustive list of arguments to be sent to each thread
```

```
                for input in inputs:
                        args.append([input])
                # initiate threading
                with Pool(processes=max_threads) as pool:
                        pool.starmap(sweep, args)
def monolayer_graphene():
a = 0.24595    # [nm] unit cell length
a_cc = 0.142  # [nm] carbon-carbon distance
t0 = -3.1      # [eV] nearest neighbour hopping
lat = pb.Lattice(a1=[a, 0],
              a2=[a/2, a*sqrt(3)/2])
lat.add_sublattices(('A', [0.1*a_cc, -a_cc+0.1*a_cc, 0]),
                ('B', [0.1*a_cc, 0.1*a_cc, 0]))
lat.add_hoppings(
   # inside the main cell
   ([0,  0], 'A', 'B', t0),
   # between neighboring cells
   ([-1, 1], 'B', 'A', t0),
   ([0, 1], 'B', 'A', t0),
)
lat.min_neighbors = 2
return lat
        def circle(radius):
                def contains(x, y, z):
                        return np.sqrt(x**2 + y**2) < radius
                return pb.FreeformShape(contains, width=[2*radius, 2*radius])
        def constant_magnetic_field(B):
                @pb.hopping_energy_modifier
                def function(energy, x1, y1, x2, y2):
                        # the midpoint between two sites
                        y = 0.5 * (y1 + y2)
                        # scale from nanometers to meters
                        y *= 1e-9
                        # vector potential along the x-axis
                        A_x = B * y
                        # integral of (A * dl) from position 1 to position 2
                        peierls = A_x * (x1 - x2)
                        # scale from nanometers to meters (because of x1 and x2)
                        peierls *= 1e-9
                        # the Peierls substitution
                        return energy * np.exp(1j * 2*pi/phi0 * peierls)
                return function
        def wavy(delta):
                @pb.onsite_energy_modifier
```

```
        def f(sub_id,x,y):
            if sub_id == 'A':
                return -2e-5*(x**2+y**2)+0.1+delta
            if sub_id == 'B':
                return -2e-5*(x**2+y**2)+0.1-delta
        return f
    def sweep(d):
        model = pb.Model(monolayer_graphene(), circle(radius=450)
        , wavy(delta=0)
        , constant_magnetic_field(B=0.4)
        )
        kpm = pb.kpm(model)
        ldos = kpm.calc_ldos(energy=np.linspace(-0.4, 0.4, 4000),
broadening=0.002, position=[d, 0], sublattice='A')
        g=np.array(ldos.data)
        f = open('LDOS1_A1'+str(d+101).zfill(4)+'.dat', "w")
        for i in range(0,4000,1):
            print(g[i],file=f)
            i=i+1
        f.close()
    if __name__ == "__main__":
        initiate_pool(max_threads=num_cores)
```

10.2.2 BLG QD

The Python code below can simulate the $LDOS$ spectra for sublattice A_1 in the -200 meV to 200 meV energy range with a 2 meV energy resolution for a BLG QD along a line across the QD center between $x = -200$ nm and $x = 200$ nm with a 1 nm spatial resolution. The BLG QD is defined on a 250 nm radius BLG sheet with a circularly symmetric parabolic confinement potential well $V(r) = -0.1r^2$ meV/nm^2 and 60 meV band gap. The trigonal warping is considered in the BLG QD TB model, but the conduction band and valence band asymmetry due to the γ_4 hopping is not included.

```
import multiprocessing
from multiprocessing import Pool
```

```
import pybinding as pb
import numpy as np
import matplotlib.pyplot as plt
from math import sqrt, pi
num_cores = 24 #multiprocessing.cpu_count()
start = list(range(-200,200,1))
block=int(len(start)/num_cores)+1
for j in np.arange(0,block,1):
    inputs = list(range(start[0+num_cores*j],start[0+num_cores*j]+num_cores,1))
    def initiate_pool(max_threads):
        if len(inputs) < max_threads:
            max_threads = len(inputs)
        args = list()
        # generate exhaustive list of arguments to be sent to each thread
        for input in inputs:
            args.append([input])
        # initiate threading
        with Pool(processes=max_threads) as pool:
            pool.starmap(sweep, args)
    a = 0.24595   # [nm] unit cell length
    a_cc = 0.142  # [nm] carbon-carbon distance
    def bilayer_graphene_BA():
        t0 = -3.16      # [eV] nearest neighbour hopping
        t2 = 0.381
        t3 = 0.38           # -0.38
        t4 = 0.14
        lat = pb.Lattice(a1=[a, 0],
                        a2=[a/2, a/2 * np.sqrt(3)])
        lat.add_sublattices(('A1', [0, -a_cc, 0]),
                            ('B1', [0, 0, 0]),
                            ('A2', [0, 0, -0.335]),
                            ('B2', [0, a_cc, -0.335]))
        lat.add_hoppings(
            # inside the main cell
            ([0,  0], 'A1', 'B1', t0),
            ([0,  0], 'A2', 'B2', t0),
            ([0,  0], 'A2', 'B1', t2),
            # between neighboring cellsd
            ([-1, 1], 'B1', 'A1', t0),
            ([0, 1], 'B1', 'A1', t0),
            ([-1, 1], 'B2', 'A2', t0),
            ([0, 1], 'B2', 'A2', t0),
            #t3
            ([0,  -1], 'A1', 'B2', t3),
```

```
                ([1,  -1], 'A1', 'B2', t3),
                ([1,  -2], 'A1', 'B2', t3),
                #t4
                #([0,  0], 'B1', 'B2', t4),
                #([0,  -1], 'B1', 'B2', t4),
                #([1,  -1], 'B1', 'B2', t4),
            )
            lat.min_neighbors = 2
            return lat
    def circle(radius):
            def contains(x, y, z):
                return np.sqrt(x**2 + y**2) < radius
            return pb.FreeformShape(contains, width=[2*radius, 2*radius])
    def wavy(delta):
            @pb.onsite_energy_modifier
            def f(sub_id,x,y):
                if sub_id == 'A1':
                        return -1e-5*(x**2+y**2)+delta/2
                if sub_id == 'B1':
                        return -1e-5*(x**2+y**2)+delta/2
                if sub_id == 'A2':
                        return -1e-5*(x**2+y**2)-delta/2
                if sub_id == 'B2':
                        return -1e-5*(x**2+y**2)-delta/2
            return f
    def sweep(d):
            model = pb.Model(bilayer_graphene_BA(), circle(radius=250),
wavy(delta=0.06))
            kpm = pb.kpm(model)
            ldos = kpm.calc_ldos(energy=np.linspace(-0.2, 0.2, 3000),
broadening=0.002, position=[d,0], sublattice='A1')
            g=np.array(ldos.data)
            f = open('LDOS1_A1'+str(d+201).zfill(4)+'.dat', "w")
            for i in range(0,3000,1):
                print(g[i],file=f)
                i=i+1
            f.close()
    if __name__ == "__main__":
            initiate_pool(max_threads=num_cores)
```

10.2.3 TLG QD

The Python code below can simulate the $LDOS$ spectra for sublattice A_1 in the -200 meV to 200 meV energy range with a 2 meV energy resolution for a TLG QD along a line across the QD center between $x = -100$ nm and $x = 100$ nm with a 1 nm spatial resolution. The TLG QD is defined on a 250 nm radius BLG sheet with a circularly symmetric parabolic confinement potential well $V(r) = -0.1r^2$ meV/nm^2. $\gamma_0, \gamma_1, \gamma_2, \gamma_3$ and γ_5 hoppings are included in the model, but γ_4 hopping and interlayer potential difference is not included in the model.

```
import multiprocessing
from multiprocessing import Pool
import pybinding as pb
import numpy as np
import matplotlib.pyplot as plt
from math import sqrt, pi
num_cores = 24 #multiprocessing.cpu_count()
start = list(range(-100,100,1))
block=int(len(start)/num_cores)+1
for j in np.arange(0,block,1):
	inputs = list(range(start[0+num_cores*j],start[0+num_cores*j]+num_cores,1))
	def initiate_pool(max_threads):
		if len(inputs) < max_threads:
			max_threads = len(inputs)
		args = list()
		# generate exhaustive list of arguments to be sent to each thread
		for input in inputs:
			args.append([input])
		# initiate threading
		with Pool(processes=max_threads) as pool:
			pool.starmap(sweep, args)
	a = 0.24595   # [nm] unit cell length
	a_cc = 0.142  # [nm] carbon-carbon distance
	def trilayer_graphene_ABA():
		t0 = -3.16      # [eV] nearest neighbour hopping
		t1 = 0.39
		t2 = -0.028
		t3 = 0.315
```

```
t4 = 0.04
t5 = -0.06
lat = pb.Lattice(a1=[a, 0],
a2=[a/2, a/2 * sqrt(3)])
lat.add_sublattices(('A1', [0, -a_cc, 0.335]),
                                            ('B1', [0, 0, 0.335]),
                                            ('A2', [0, 0, 0]),
                                            ('B2', [0, a_cc, 0]),
                                            ('A3', [0, -a_cc, -0.335]),
                                            ('B3', [0, 0, -0.335]))
lat.add_hoppings(
        #t0
        ([0,  0], 'B1', 'A1', t0),
        ([-1, 1], 'B1', 'A1', t0),
        ([0, 1], 'B1', 'A1', t0),
        ([0,  0], 'B2', 'A2', t0),
        ([-1, 1], 'B2', 'A2', t0),
        ([0, 1], 'B2', 'A2', t0),
        ([0,  0], 'B3', 'A3', t0),
        ([-1, 1], 'B3', 'A3', t0),
        ([0, 1], 'B3', 'A3', t0),
        #t1
        ([0, 0], 'B1', 'A2', t1),
        ([0, 0], 'A2', 'B3', t1),
        #t2
        ([0, 0], 'A1', 'A3', t2),
        #t3
        ([0,  1], 'B2', 'A1', t3),
        ([-1,  1], 'B2', 'A1', t3),
        ([-1,  2], 'B2', 'A1', t3),
        ([0,  1], 'B2', 'A3', t3),
        ([-1,  1], 'B2', 'A3', t3),
        ([-1,  2], 'B2', 'A3', t3),
        #t4
        #([0,  0], 'A1', 'A2', t4),
        #([1,  -1], 'A1', 'A2', t4),
        #([0,  -1], 'A1', 'A2', t4),
        #([0,  0], 'B1', 'B2', t4),
        #([0,  -1], 'B1', 'B2', t4),
        #([1,  -1], 'B1', 'B2', t4),
        #([0,  0], 'A3', 'A2', t4),
        #([1,  -1], 'A3', 'A2', t4),
        #([0,  -1], 'A3', 'A2', t4),
        #([0,  0], 'B3', 'B2', t4),
```

```
                #([0,  -1], 'B3', 'B2', t4),
                #([1,  -1], 'B3', 'B2', t4),
                #t5
                ([0,  0], 'B1', 'B3', t5)
            )
            lat.min_neighbors =2
            return lat
        def circle(radius):
            def contains(x, y, z):
                return np.sqrt(x**2 + y**2) < radius
            return pb.FreeformShape(contains, width=[2*radius, 2*radius])
        def wavy(delta):
            @pb.onsite_energy_modifier
            def f(sub_id,x,y):
                if sub_id == 'A1':
                    return -1e-5*(x**2+y**2)+delta/2
                if sub_id == 'B1':
                    return -1e-5*(x**2+y**2)+delta/2
                if sub_id == 'A2':
                    return -1e-5*(x**2+y**2)
                if sub_id == 'B2':
                    return -1e-5*(x**2+y**2)
                if sub_id == 'A3':
                    return -1e-5*(x**2+y**2)-delta/2
                if sub_id == 'B3':
                    return -1e-5*(x**2+y**2)-delta/2
            return f
        def sweep(d):
            model = pb.Model(trilayer_graphene_ABA(), circle(radius=250),
    wavy(delta=0))
            kpm = pb.kpm(model)
            ldos = kpm.calc_ldos(energy=np.linspace(-0.2, 0.2, 2000),
    broadening=0.002, position=[0, d], sublattice='A1')
            g=np.array(ldos.data)
            f = open('LDOS1_A1'+str(d+101).zfill(4)+'.dat', "w")
            for i in range(0,2000,1):
                print(g[i],file=f)
            f.close()
        if __name__ == "__main__":
            initiate_pool(max_threads=num_cores)
```

10.3 Appendix C: Codes for Graphene QDs Simulation with Continuum Model

10.3.1 MLG QD

The Python code below can calculate spatially resolved $LDOS$ for $m = \pm 5.5$ MLG QD states in $B = 0.3$ T based on the continuum model. The MLG QD potential well used in the simulation is a circularly symmetric parabolic potential well with $V(r) = -0.03r^2$ meV/nm^2.

```
import numpy as np
import matplotlib.pyplot as plt
from math import sqrt, pi, floor, exp
import scipy
from scipy.sparse.linalg import eigs
from scipy.linalg import eig
from matplotlib.pyplot import pcolormesh
from matplotlib import cm
L=500 #calculation range (nm)
N=1200 #mesh points
h=L/(N-1)
hbar=658.2 #value of hbar*Vf in meV,nm unit
gamma1=381*0 #gamma1 hopping (meV)
delta=0 #inter layer potential difference
kappa=-0.03 #parabolic potential U(r)=kappa*r**2 in meV,nm unit
B=0.3 #e*B*Vf in meV,nm unit
left=1
right=200
E_min=-260    #meV
E_max=-60     #meV
pixels=150
LDOS_All=np.zeros((pixels,right-left+1))
for m in np.arange(-5.5,5.5+0.1,11):
        H=np.zeros((2*N,2*N))
        for i in range(0,2*N,1):
                r=h*floor(i/2)+0.0001
                if i<2:
                        if i%2==0:
                                H[i,i+1]=-hbar/(1*h)
                                H[i,i]=0.5*delta+kappa*r**2
                                H[i,i+1]=hbar*m/r-0.5*B*r
                                H[i,i+3]=hbar/(1*h)
```

```
        else:
            H[i,i-1]=hbar/(1*h)
            H[i,i-1]=hbar*m/r-0.5*B*r
            H[i,i]=0.5*delta+kappa*r**2
            H[i,i+1]=-hbar/(1*h)
    elif 2*N-i<3:
        if i%2==0:
            H[i,i-1]=-hbar/(1*h)
            H[i,i]=0.5*delta+kappa*r**2
            H[i,i+1]=hbar*m/r-0.5*B*r
            H[i,i+1]=hbar/(1*h)
        else:
            H[i,i-3]=hbar/(1*h)
            H[i,i-1]=hbar*m/r-0.5*B*r
            H[i,i]=0.5*delta+kappa*r**2
            H[i,i-1]=-hbar/(1*h)
    else:
        if i%2==0:
            H[i,i-1]=-hbar/(2*h)
            H[i,i]=0.5*delta+kappa*r**2
            H[i,i+1]=hbar*m/r-0.5*B*r
            H[i,i+3]=hbar/(2*h)
        else:
            H[i,i-3]=hbar/(2*h)
            H[i,i-1]=hbar*m/r-0.5*B*r
            H[i,i]=0.5*delta+kappa*r**2
            H[i,i+1]=-hbar/(2*h)
[E,psi]=eig(H)
np.save('E_m='+str(m),E)
np.save('psi_m='+str(m),psi)
E=np.load('E_m='+str(m)+'.npy')
psi=np.load('psi_m='+str(m)+'.npy')
index=np.argsort(E)
x = np.linspace(0,L,N)
y = np.linspace(E_min,E_max,pixels)
LDOS_A1=np.zeros((pixels,right-left+1))
LDOS_B1=np.zeros((pixels,right-left+1))
selected=[]
for i in range(0,2*N,1):
    if E[index[i]]>E_min and E[index[i]]<E_max:
        selected.append(index[i])
print(len(selected))
psi_A1=np.zeros((N,len(selected)))
psi_B1=np.zeros((N,len(selected)))
```

```
    for i in range(0,len(selected),1):
        for j in range(0,2*N,1):
            if j%2==0:
    psi_A1[floor(j/2),i]=psi[j,selected[i]]*np.conjugate(psi[j,selected[i]])/(x[floor(
j/2)]+0.001)*100
            else:
    psi_B1[floor(j/2),i]=psi[j,selected[i]]*np.conjugate(psi[j,selected[i]])/(x[floor(
j/2)]+0.001)*100
    sigmas=round(2/h)
    smooth=np.array([exp(-i**2/2/sigmas**2)/(sqrt(2*pi)*sigmas) for i in range(-
3*sigmas,3*sigmas)])
    psi_A1_smooth=np.apply_along_axis(lambda m: np.convolve(m, smooth,
mode='same'), axis=0, arr=psi_A1)
    psi_B1_smooth=np.apply_along_axis(lambda m: np.convolve(m, smooth,
mode='same'), axis=0, arr=psi_B1)
    gammas=4
    for i in range(0,pixels,1):
        print(i)
        for j in range(left,right+1,1):
            temp_A1=0
            temp_B1=0
            for k in range(0,len(selected),1):
                if abs(E[selected[k]]-y[i])<3*gammas:
    temp_A1=temp_A1+psi_A1_smooth[j,k]*0.5*gammas/pi/((E[selected[k]]-
y[i])**2+(0.5*gammas)**2)#/x[j]*100
    #temp_B1=temp_B1+psi_B1_smooth[j,k]*0.5*gammas/pi/((E[selected[k]]-
y[i])**2+(0.5*gammas)**2)#/x[j]*100
            LDOS_A1[i,j-left]=temp_A1
            #LDOS_B1[i,j-left]=temp_B1
    LDOS_All=LDOS_All+LDOS_A1
plt.title('A1_m='+str(m))
plt.xlabel('r (nm)')
plt.ylabel('E (meV)')
pcolormesh(x[left:right+1],y,LDOS_All,cmap='viridis')
plt.clim(0,0.004)
ax=plt.gca()
ax.set_aspect(aspect=0.5)
plt.savefig('A1_m='+str(m)+'.png', bbox_inches='tight',pad_inches = 0.1)
#plt.clf()
plt.show()
```

10.3.2 BLG QD

The Python code below can calculate spatially resolved $LDOS$ on the four sublattices of BLG for $m = 1$ BLG QD state in $B = 0$ T based on the BLG QD continuum model. The BLG QD potential well used in the simulation is a circularly symmetric parabolic potential well with $V(r) = -0.01\ \mathrm{meV/nm^2}$ and a 30 meV band gap.

```
import numpy as np
import matplotlib.pyplot as plt
from math import sqrt, pi, floor, exp
import scipy
from scipy.sparse.linalg import eigs
from scipy.linalg import eig
from matplotlib.pyplot import pcolormesh
from matplotlib import cm
L=500 #calculation range (nm)
N=800 #mesh points
h=L/(N-1)
hbar=673.076676 #value of hbar*Vf in meV,nm unit (gamma1=-3.16eV)
gamma1=381 #gamma1 hopping (meV)
delta=30 #inter layer potential difference
kappa=-0.01 #parabolic potential U(r)=kappa*r**2 in meV,nm unit
m=1 #angular quantum number
H=np.zeros((4*N,4*N))
for i in range(0,4*N,1):
    r=h*floor(i/4)+0.0001
    #print(r)
    if i<4:
        if i%4==0:
            H[i,i+1]=hbar/(1*h)
            H[i,i]=0.5*delta+kappa*r**2
            H[i,i+1]=-hbar*(m-0.5)/r
            H[i,i+5]=-hbar/(1*h)
        elif i%4==1:
            H[i,i-1]=-hbar/(1*h)
            H[i,i-1]=-hbar*(m-0.5)/r
            H[i,i]=0.5*delta+kappa*r**2
            H[i,i+1]=gamma1
```

```
        H[i,i+3]=hbar/(1*h)
    elif i%4==2:
        H[i,i+1]=-hbar/(1*h)
        H[i,i-1]=gamma1
        H[i,i]=-0.5*delta+kappa*r**2
        H[i,i+1]=hbar*(m+0.5)/r
        H[i,i+5]=hbar/(1*h)
    else:
        H[i,i-1]=hbar/(1*h)
        H[i,i-1]=hbar*(m+0.5)/r
        H[i,i]=-0.5*delta+kappa*r**2
        H[i,i+3]=-hbar/(1*h)
elif 4*N-i<5:
    if i%4==0:
        H[i,i-3]=hbar/(1*h)
        H[i,i]=0.5*delta+kappa*r**2
        H[i,i+1]=-hbar*(m-0.5)/r
        H[i,i+1]=-hbar/(1*h)
    elif i%4==1:
        H[i,i-5]=-hbar/(1*h)
        H[i,i-1]=-hbar*(m-0.5)/r
        H[i,i]=0.5*delta+kappa*r**2
        H[i,i+1]=gamma1
        H[i,i-1]=hbar/(1*h)
    elif i%4==2:
        H[i,i-3]=-hbar/(1*h)
        H[i,i-1]=gamma1
        H[i,i]=-0.5*delta+kappa*r**2
        H[i,i+1]=hbar*(m+0.5)/r
        H[i,i+1]=hbar/(1*h)
    else:
        H[i,i-5]=hbar/(1*h)
        H[i,i-1]=hbar*(m+0.5)/r
        H[i,i]=-0.5*delta+kappa*r**2
        H[i,i-1]=-hbar/(1*h)
else:
    if i%4==0:
        H[i,i-3]=hbar/(2*h)
        H[i,i]=0.5*delta+kappa*r**2
        H[i,i+1]=-hbar*(m-0.5)/r
        H[i,i+5]=-hbar/(2*h)
    elif i%4==1:
        H[i,i-5]=-hbar/(2*h)
        H[i,i-1]=-hbar*(m-0.5)/r
```

```
            H[i,i]=0.5*delta+kappa*r**2
            H[i,i+1]=gamma1
            H[i,i+3]=hbar/(2*h)
        elif i%4==2:
            H[i,i-3]=-hbar/(2*h)
            H[i,i-1]=gamma1
            H[i,i]=-0.5*delta+kappa*r**2
            H[i,i+1]=hbar*(m+0.5)/r
            H[i,i+5]=hbar/(2*h)
        else:
            H[i,i-5]=hbar/(2*h)
            H[i,i-1]=hbar*(m+0.5)/r
            H[i,i]=-0.5*delta+kappa*r**2
            H[i,i+3]=-hbar/(2*h)
[E,psi]=eig(H)
index=np.argsort(E)
left=1
right=round(100/h)
x = np.linspace(0,L,N)
E_min=-80     #meV
E_max=-20     #meV
pixels=100
y = np.linspace(E_min,E_max,pixels)
LDOS_A1=np.zeros((pixels,right-left+1))
LDOS_B1=np.zeros((pixels,right-left+1))
LDOS_A2=np.zeros((pixels,right-left+1))
LDOS_B2=np.zeros((pixels,right-left+1))
selected=[]
for i in range(0,4*N,1):
    if E[index[i]]>E_min and E[index[i]]<E_max:
        selected.append(index[i])
psi_A1=np.zeros((N,len(selected)))
psi_B1=np.zeros((N,len(selected)))
psi_A2=np.zeros((N,len(selected)))
psi_B2=np.zeros((N,len(selected)))
for i in range(0,len(selected),1):
    for j in range(0,4*N,1):
        if j%4==0:
psi_A1[floor(j/4),i]=psi[j,selected[i]]*np.conjugate(psi[j,selected[i]])/(x[floor(j/4)]+0.
0001)*100
        elif j%4==1:
psi_B1[floor(j/4),i]=psi[j,selected[i]]*np.conjugate(psi[j,selected[i]])/(x[floor(j/4)]+0.
0001)*100
        elif j%4==2:
```

```
psi_A2[floor(j/4),i]=psi[j,selected[i]]*np.conjugate(psi[j,selected[i]])/(x[floor(j/4)]+0.0001)*100
        else:
psi_B2[floor(j/4),i]=psi[j,selected[i]]*np.conjugate(psi[j,selected[i]])/(x[floor(j/4)]+0.0001)*100
sigmas=round(2/h)
smooth=np.array([exp(-i**2/2/sigmas**2)/(sqrt(2*pi)*sigmas) for i in range(-3*sigmas,3*sigmas)])
psi_A1_smooth=np.apply_along_axis(lambda m: np.convolve(m, smooth, mode='same'), axis=0, arr=psi_A1)
psi_B1_smooth=np.apply_along_axis(lambda m: np.convolve(m, smooth, mode='same'), axis=0, arr=psi_B1)
psi_A2_smooth=np.apply_along_axis(lambda m: np.convolve(m, smooth, mode='same'), axis=0, arr=psi_A2)
psi_B2_smooth=np.apply_along_axis(lambda m: np.convolve(m, smooth, mode='same'), axis=0, arr=psi_B2)
gammas=3
for i in range(0,pixels,1):
    #print(i)
    for j in range(left,right+1,1):
        temp_A1=0
        temp_B1=0
        temp_A2=0
        temp_B2=0
        for k in range(0,len(selected),1):
            if abs(E[selected[k]]-y[i])<3*gammas:
                temp_A1=temp_A1+psi_A1_smooth[j,k]*0.5*gammas/pi/((E[selected[k]]-y[i])**2+(0.5*gammas)**2)
                temp_B1=temp_B1+psi_B1_smooth[j,k]*0.5*gammas/pi/((E[selected[k]]-y[i])**2+(0.5*gammas)**2)
                temp_A2=temp_A2+psi_A2_smooth[j,k]*0.5*gammas/pi/((E[selected[k]]-y[i])**2+(0.5*gammas)**2)
                temp_B2=temp_B2+psi_B2_smooth[j,k]*0.5*gammas/pi/((E[selected[k]]-y[i])**2+(0.5*gammas)**2)
        LDOS_A1[i,j-left]=temp_A1
        LDOS_B1[i,j-left]=temp_B1
        LDOS_A2[i,j-left]=temp_A2
        LDOS_B2[i,j-left]=temp_B2
plt.title('A1_m='+str(m))
plt.xlabel('r (nm)')
plt.ylabel('E (meV)')
pcolormesh(x[left:right+1],y,LDOS_A1,cmap='viridis')
plt.clim(0,0.01)
ax=plt.gca()
```

```
ax.set_aspect(aspect=1.5)
plt.savefig('A1_m='+str(m)+'.png', bbox_inches='tight',pad_inches = 0.1)
plt.show()
```

10.4 Appendix D: Single and Coupled MLG QDs Creation Procedure

10.4.1 Create Single Circular MLG QDs

1. Set $V_S = 0.5$ V and $I = 0.5$ nA, then bring V_G to ~ -60 V.

2. Open the STM feedback loop.

3. Withdraw the STM tip by $\Delta z \sim 1.1 - 1.2$ nm.

4. Increase V_s to $+5$ V.

5. Wait 2 minutes.

6. Decrease V_s to 0.5 V.

7. Close the STM feedback loop.

8. Bring V_G to $\sim +60$ V.

9. Open the STM feedback loop.

10. Withdraw the STM tip by $\Delta z \sim 1.9 - 2.1$ nm.

11. Increase V_S to $+5$ V.

12. Wait 1 minute.

13. Decrease V_S to 0.5 V.

14. Close the STM feedback loop.

10.4.2 Create Double Circular MLG QDs

1. Repeat processes 1-7 of creating single circular graphene pn junctions at three points along a line that are equally separated by 100 nm.

2. Repeat processes 8-14 of creating single circular graphene junctions at the two points in process 1 that are separated by 150 nm or 200 nm for coupled double dot and decoupled double dot, respectively.

10.5 Appendix E: P-type and N-type BLG QDs Creation Procedure

In our experiments, BLG QDs with p-type and n-type central doping can be created at the same BLG region. For example, a p-type BLG QD can be first created and investigated, we can then erase the p-type BLG QD and create a n-type BLG QD at the same region. Below I will describe the tip bias pulsing procedure we use for the creation of p-type and n-type BLG QDs, and how to erase BLG QDs.

10.5.1 P-type BLG QD Creation

1. Set $V_S = 0.5$ V and $I = 0.5$ nA, then bring V_G to -80 V.
2. Open the STM feedback loop.
3. Withdraw the STM tip by $\Delta z \sim 1.1 - 1.2$ nm.
4. Increase V_s to $+5$ V.
5. Wait 2 minutes.
6. Decrease V_s to 0.5 V.
7. Close the STM feedback loop.
8. Bring V_G to $+60$ V or +80 V.
9. Open the STM feedback loop.
10. Withdraw the STM tip by $\Delta z \sim 1.9 - 2.1$ nm.
11. Increase V_S to $+5$ V.
12. Wait 1 minute.
13. Decrease V_S to 0.5 V.
14. Close the STM feedback loop.

10.5.2 N-type BLG QD Creation

1. Set $V_S = 0.5$ V and $I = 0.5$ nA, then bring V_G to $+60$ V or +80 V.
2. Open the STM feedback loop.
3. Withdraw the STM tip by $\Delta z \sim 1.1 - 1.2$ nm.

4. Increase V_s to $+5$ V.

5. Wait 2 minutes.

6. Decrease V_s to 0.5 V.

7. Close the STM feedback loop.

8. Bring V_G to -80 V.

9. Open the STM feedback loop.

10. Withdraw the STM tip by $\Delta z \sim 1.9 - 2.1$ nm.

11. Increase V_S to $+5$ V.

12. Wait 1 minute.

13. Decrease V_S to 0.5 V.

14. Close the STM feedback loop.

10.5.3 BLG QD "Erasing"

1. Set $V_S = 0.5$ V and $I = 0.5$ nA, then bring V_G to 0 V.

2. Open the STM feedback loop.

3. Withdraw the STM tip by $\Delta z \sim 1.1 - 1.2$ nm.

4. Increase V_s to $+5$ V.

5. Wait 2 minutes.

6. Decrease V_s to 0.5 V.

7. Close the STM feedback loop.

10.6 Appendix F: Classical Dynamics Simulation for Stadium Shaped MLG QDs

The classical Hamiltonian for a stadium shaped MLG QD with confined holes can be expressed as

$$H = v_F \sqrt{\left(p_x + \frac{eBy}{2}\right)^2 + \left(p_y - \frac{eBx}{2}\right)^2} + V(x,y) \qquad (9.1)$$

Here v_F is MLG's Fermi velocity and $V(x, y)$ is the potential well of the stadium shaped MLG QD. The potential well shown in Figure 8.9a is used in the model. Then classical dynamics of the stadium shaped MLG QD can be simulated by solving Hamilton's equations with numerical techniques. Below I give example MATLAB codes that can be used to calculate the classical orbits and Poincaré surface of section (PSS) for the stadium shaped MLG QD in our experiment.

10.6.1 MATLAB Code for Simulating Classical Orbits

```
clc
clear all
hbar=1.0545718*10^(-34);
e=1.602176487*10^(-19);
vf=1.00337*10^(6);
pi=3.14159265358;
B=0; %magnetic field
L=120*10^(-9); %potential flat region legnth

%initial conditions
t=0;
E=0.237*e; %energy
x=0*10^(-9);
y=0*10^(-9);
% p_x=hbar*3.5685*10^8;
% p_y=sqrt(((E-U(x,y,L))/vf)^2-p_x^2);
theta=10.81; %velocity angle
p_x=sqrt(((E-U(x,y,L))/vf)^2)*cosd(theta)-0.5*e*B*y;
p_y=sqrt(((E-U(x,y,L))/vf)^2)*sind(theta)+0.5*e*B*x;

n=1000000;
dt=1*10^(-16);
x1=zeros(n,1);
y1=zeros(n,1);
p_x1=zeros(n,1);
p_y1=zeros(n,1);
v_x1=zeros(n,1);
v_y1=zeros(n,1);
T=zeros(n,1);

for i=1:n
    k1_x=f_x(x,y,p_x,p_y,B);
    k1_y=f_y(x,y,p_x,p_y,B);
    k1_p_x=f_p_x(x,y,p_x,p_y,B,L);
    k1_p_y=f_p_y(x,y,p_x,p_y,B,L);
```

```
k2_x=f_x(x+0.5*dt*k1_x,y+0.5*dt*k1_y,p_x+0.5*dt*k1_p_x,p_y+0.5*dt*k1_p_y,B)
;

k2_y=f_y(x+0.5*dt*k1_x,y+0.5*dt*k1_y,p_x+0.5*dt*k1_p_x,p_y+0.5*dt*k1_p_y,B)
;

k2_p_x=f_p_x(x+0.5*dt*k1_x,y+0.5*dt*k1_y,p_x+0.5*dt*k1_p_x,p_y+0.5*dt*k1_p_
y,B,L);
k2_p_y=f_p_y(x+0.5*dt*k1_x,y+0.5*dt*k1_y,p_x+0.5*dt*k1_p_x,p_y+0.5*dt*k1_p_
y,B,L);
k3_x=f_x(x+0.5*dt*k2_x,y+0.5*dt*k2_y,p_x+0.5*dt*k2_p_x,p_y+0.5*dt*k2_p_y,B)
;
k3_y=f_y(x+0.5*dt*k2_x,y+0.5*dt*k2_y,p_x+0.5*dt*k2_p_x,p_y+0.5*dt*k2_p_y,B)
;
k3_p_x=f_p_x(x+0.5*dt*k2_x,y+0.5*dt*k2_y,p_x+0.5*dt*k2_p_x,p_y+0.5*dt*k2_p_
y,B,L);
k3_p_y=f_p_y(x+0.5*dt*k2_x,y+0.5*dt*k2_y,p_x+0.5*dt*k2_p_x,p_y+0.5*dt*k2_p_
y,B,L);
    k4_x=f_x(x+dt*k3_x,y+dt*k3_y,p_x+dt*k3_p_x,p_y+dt*k3_p_y,B);
    k4_y=f_y(x+dt*k3_x,y+dt*k3_y,p_x+dt*k3_p_x,p_y+dt*k3_p_y,B);
    k4_p_x=f_p_x(x+dt*k3_x,y+dt*k3_y,p_x+dt*k3_p_x,p_y+dt*k3_p_y,B,L);
    k4_p_y=f_p_y(x+dt*k3_x,y+dt*k3_y,p_x+dt*k3_p_x,p_y+dt*k3_p_y,B,L);
    k_x=(k1_x+2*k2_x+2*k3_x+k4_x)/6;
    k_y=(k1_y+2*k2_y+2*k3_y+k4_y)/6;
    k_p_x=(k1_p_x+2*k2_p_x+2*k3_p_x+k4_p_x)/6;
    k_p_y=(k1_p_y+2*k2_p_y+2*k3_p_y+k4_p_y)/6;
    x1(i,1)=x;
    y1(i,1)=y;
    p_x1(i,1)=p_x+0.5*e*B*y;
    p_y1(i,1)=p_y-0.5*e*B*x;
    v_x1(i,1)=(p_x+0.5*e*B*y)/sqrt((p_x+0.5*e*B*y)^2+(p_y-0.5*e*B*x)^2);
    v_y1(i,1)=(p_y-0.5*e*B*x)/sqrt((p_x+0.5*e*B*y)^2+(p_y-0.5*e*B*x)^2);
    T(i,1)=-vf*sqrt((p_x+0.5*e*B*y)^2+(p_y-0.5*e*B*x)^2);
    x=x+k_x*dt;
    y=y+k_y*dt;
    p_x=p_x+k_p_x*dt;
    p_y=p_y+k_p_y*dt;
end

plot(x1*1e9,y1*1e9,'LineWidth',3)
xlabel('x(nm)')
ylabel('y(nm)')
xlim([-200,200])
ylim([-110,110])

%--------------------------------------------------------------
function [a]=f_x(x,y,p_x,p_y,B)
    vf=10^6;
    e=1.602176487*10^(-19);
    a=vf*(p_x+0.5*e*B*y)/sqrt((p_x+0.5*e*B*y)^2+(p_y-0.5*e*B*x)^2);
end
```

```
function [a]=f_y(x,y,p_x,p_y,B)
    vf=10^6;
    e=1.602176487*10^(-19);
    a=vf*(p_y-0.5*e*B*x)/sqrt((p_x+0.5*e*B*y)^2+(p_y-0.5*e*B*x)^2);
end

function [a]=f_p_x(x,y,p_x,p_y,B,L)
    vf=10^6;
    e=1.602176487*10^(-19);
    c10=2.6274*e;
    c11=-2.6274*e;
    c12=334.06764*10^(-9);
    c20=0.274277*e;
    c21=-0.049089*e;
    c22=11.766*10^(-9);
    if abs(x)<0.5*L
        if abs(y)<100*10^(-9)
            a=vf*e*B*0.5*(p_y-0.5*e*B*x)/sqrt((p_x+0.5*e*B*y)^2+(p_y-
0.5*e*B*x)^2);
        else
            a=vf*e*B*0.5*(p_y-0.5*e*B*x)/sqrt((p_x+0.5*e*B*y)^2+(p_y-
0.5*e*B*x)^2);
        end
    else
        if sqrt((abs(x)-0.5*L)^2+y^2)<100*10^(-9)
            a=vf*e*B*0.5*(p_y-0.5*e*B*x)/sqrt((p_x+0.5*e*B*y)^2+(p_y-
0.5*e*B*x)^2)+2*c11*(abs(x)-0.5*L)*sign(x)*exp(-((abs(x)-
0.5*L)^2+y^2)/c12^2)/c12^2;
        else
            a=vf*e*B*0.5*(p_y-0.5*e*B*x)/sqrt((p_x+0.5*e*B*y)^2+(p_y-
0.5*e*B*x)^2)+c21*(abs(x)-0.5*L)*sign(x)/(c22*sqrt((abs(x)-
0.5*L)^2+y^2))*exp(-(sqrt((abs(x)-0.5*L)^2+y^2)-100*10^(-9))/c22);
        end
    end
end

function [a]=f_p_y(x,y,p_x,p_y,B,L)
    vf=10^6;
    e=1.602176487*10^(-19);
    c10=2.6274*e;
    c11=-2.6274*e;
    c12=334.06764*10^(-9);
    c20=0.274277*e;
    c21=-0.049089*e;
    c22=11.766*10^(-9);
    if abs(x)<0.5*L
        if abs(y)<100*10^(-9)
            a=-vf*e*B*0.5*(p_x+0.5*e*B*y)/sqrt((p_x+0.5*e*B*y)^2+(p_y-
0.5*e*B*x)^2)+2*c11*y*exp(-y^2/c12^2)/c12^2;
        else
            a=-vf*e*B*0.5*(p_x+0.5*e*B*y)/sqrt((p_x+0.5*e*B*y)^2+(p_y-
0.5*e*B*x)^2)+c21*sign(y)*exp(-(abs(y)-100*10^(-9))/c22)/c22;
```

```
        end
    else
        if sqrt((abs(x)-0.5*L)^2+y^2)<100*10^(-9)
            a=-vf*e*B*0.5*(p_x+0.5*e*B*y)/sqrt((p_x+0.5*e*B*y)^2+(p_y-
0.5*e*B*x)^2)+2*c11*y*exp(-((abs(x)-0.5*L)^2+y^2)/c12^2)/c12^2;
        else
            a=-vf*e*B*0.5*(p_x+0.5*e*B*y)/sqrt((p_x+0.5*e*B*y)^2+(p_y-
0.5*e*B*x)^2)+c21*y/(c22*sqrt((abs(x)-0.5*L)^2+y^2))*exp(-(sqrt((abs(x)-
0.5*L)^2+y^2)-100*10^(-9))/c22);
        end
    end
end

function [a]=U(x,y,L)
    vf=10^6;
    e=1.602176487*10^(-19);
    c10=2.6274*e;
    c11=-2.6274*e;
    c12=334.06764*10^(-9);
    c20=0.274277*e;
    c21=-0.049089*e;
    c22=11.766*10^(-9);
    if abs(x)<0.5*L
        if abs(y)<100*10^(-9)
            a=c10+c11*exp(-y^2/c12^2);
        else
            a=c20+c21*exp(-(abs(y)-100*10^(-9))/c22);
        end
    else
        if sqrt((abs(x)-0.5*L)^2+y^2)<100*10^(-9)
            a=c10+c11*exp(-((abs(x)-0.5*L)^2+y^2)/c12^2);
        else
            a=c20+c21*exp(-(sqrt(((abs(x)-0.5*L)^2+y^2))-100*10^(-9))/c22);
        end
    end
end
```

10.6.2 MATLAB Code for Simulating PSS

```
clc
clear all
hbar=1.0545718*10^(-34);
e=1.602176487*10^(-19);
vf=1*10^(6);
pi=3.14159265358;
B=0;
L=120*10^(-9);
H=0.24*e;
x0=0*10^(-9);
y0=0*10^(-9);
initial=-1*(H-U(x0,y0,L))/vf;
```

```
final=1*(H-U(x0,y0,L))/vf;
interval=(final-initial)/60;

for l=initial:interval:final
    (l-initial)/interval
    t=0;
    x=x0;
    y=y0;
    E=H;
    p_x=l;
    p_y=sqrt(((E-U(x,y,L))/vf)^2-p_x^2);
    n=1000000;
    dt=1*10^(-16);
    x1=zeros(n,1);
    y1=zeros(n,1);
    p_x1=zeros(n,1);
    p_y1=zeros(n,1);
    for i=1:n
        k1_x=f_x(x,y,p_x,p_y,B);
        k1_y=f_y(x,y,p_x,p_y,B);
        k1_p_x=f_p_x(x,y,p_x,p_y,B,L);
        k1_p_y=f_p_y(x,y,p_x,p_y,B,L);
k2_x=f_x(x+0.5*dt*k1_x,y+0.5*dt*k1_y,p_x+0.5*dt*k1_p_x,p_y+0.5*dt*k1_p_y,B)
;
k2_y=f_y(x+0.5*dt*k1_x,y+0.5*dt*k1_y,p_x+0.5*dt*k1_p_x,p_y+0.5*dt*k1_p_y,B)
;
k2_p_x=f_p_x(x+0.5*dt*k1_x,y+0.5*dt*k1_y,p_x+0.5*dt*k1_p_x,p_y+0.5*dt*k1_p_
y,B,L);
k2_p_y=f_p_y(x+0.5*dt*k1_x,y+0.5*dt*k1_y,p_x+0.5*dt*k1_p_x,p_y+0.5*dt*k1_p_
y,B,L);
k3_x=f_x(x+0.5*dt*k2_x,y+0.5*dt*k2_y,p_x+0.5*dt*k2_p_x,p_y+0.5*dt*k2_p_y,B)
;
k3_y=f_y(x+0.5*dt*k2_x,y+0.5*dt*k2_y,p_x+0.5*dt*k2_p_x,p_y+0.5*dt*k2_p_y,B)
;
k3_p_x=f_p_x(x+0.5*dt*k2_x,y+0.5*dt*k2_y,p_x+0.5*dt*k2_p_x,p_y+0.5*dt*k2_p_
y,B,L);
k3_p_y=f_p_y(x+0.5*dt*k2_x,y+0.5*dt*k2_y,p_x+0.5*dt*k2_p_x,p_y+0.5*dt*k2_p_
y,B,L);
        k4_x=f_x(x+dt*k3_x,y+dt*k3_y,p_x+dt*k3_p_x,p_y+dt*k3_p_y,B);
        k4_y=f_y(x+dt*k3_x,y+dt*k3_y,p_x+dt*k3_p_x,p_y+dt*k3_p_y,B);
        k4_p_x=f_p_x(x+dt*k3_x,y+dt*k3_y,p_x+dt*k3_p_x,p_y+dt*k3_p_y,B,L);
        k4_p_y=f_p_y(x+dt*k3_x,y+dt*k3_y,p_x+dt*k3_p_x,p_y+dt*k3_p_y,B,L);
        k_x=(k1_x+2*k2_x+2*k3_x+k4_x)/6;
        k_y=(k1_y+2*k2_y+2*k3_y+k4_y)/6;
        k_p_x=(k1_p_x+2*k2_p_x+2*k3_p_x+k4_p_x)/6;
        k_p_y=(k1_p_y+2*k2_p_y+2*k3_p_y+k4_p_y)/6;
        x1(i,1)=x;
        y1(i,1)=y;
        p_x1(i,1)=p_x+0.5*e*B*y;
        p_y1(i,1)=p_y-0.5*e*B*x;
        x=x+k_x*dt;
        y=y+k_y*dt;
```

```
        p_x=p_x+k_p_x*dt;
        p_y=p_y+k_p_y*dt;
    end
    s_q=zeros(0);
    s_p=zeros(0);
    s_theta=zeros(0);

    j=0;
    for i=1:n
        if abs(y1(i,1))<5*10^(-11) %&& p_y1(i,1)>0
            s_q(length(s_q)+1)=x1(i,1);
            s_p(length(s_p)+1)=p_x1(i,1);
            s_theta(length(s_theta)+1)=atand(p_y1(i,1)/p_x1(i,1));
            j=j+1;
        end
    end

    hold on
    plot(s_q*10^9,s_theta,'k.')
    xlabel('x(nm)')
    ylabel('theta(degree)')
    set(gcf, 'Position',  [50, 150, 1400, 550])
end

%----------------------------------------------------------------
function [a]=f_x(x,y,p_x,p_y,B)
    vf=10^6;
    e=1.602176487*10^(-19);
    a=vf*(p_x+0.5*e*B*y)/sqrt((p_x+0.5*e*B*y)^2+(p_y-0.5*e*B*x)^2);
end

function [a]=f_y(x,y,p_x,p_y,B)
    vf=10^6;
    e=1.602176487*10^(-19);
    a=vf*(p_y-0.5*e*B*x)/sqrt((p_x+0.5*e*B*y)^2+(p_y-0.5*e*B*x)^2);
end

function [a]=f_p_x(x,y,p_x,p_y,B,L)
    vf=10^6;
    e=1.602176487*10^(-19);
    c10=2.6274*e;
    c11=-2.6274*e;
    c12=334.06764*10^(-9);
    c20=0.274277*e;
    c21=-0.049089*e;
    c22=11.766*10^(-9);
    if abs(x)<0.5*L
        if abs(y)<100*10^(-9)
            a=vf*e*B*0.5*(p_y-0.5*e*B*x)/sqrt((p_x+0.5*e*B*y)^2+(p_y-
0.5*e*B*x)^2);
        else
```

```
            a=vf*e*B*0.5*(p_y-0.5*e*B*x)/sqrt((p_x+0.5*e*B*y)^2+(p_y-
0.5*e*B*x)^2);
        end
    else
        if sqrt((abs(x)-0.5*L)^2+y^2)<100*10^(-9)
            a=vf*e*B*0.5*(p_y-0.5*e*B*x)/sqrt((p_x+0.5*e*B*y)^2+(p_y-
0.5*e*B*x)^2)+2*c11*(abs(x)-0.5*L)*sign(x)*exp(-((abs(x)-
0.5*L)^2+y^2)/c12^2)/c12^2;
        else
            a=vf*e*B*0.5*(p_y-0.5*e*B*x)/sqrt((p_x+0.5*e*B*y)^2+(p_y-
0.5*e*B*x)^2)+c21*(abs(x)-0.5*L)*sign(x)/(c22*sqrt((abs(x)-
0.5*L)^2+y^2))*exp(-(sqrt((abs(x)-0.5*L)^2+y^2)-100*10^(-9))/c22);
        end
    end
end

function [a]=f_p_y(x,y,p_x,p_y,B,L)
    vf=10^6;
    e=1.602176487*10^(-19);
    c10=2.6274*e;
    c11=-2.6274*e;
    c12=334.06764*10^(-9);
    c20=0.274277*e;
    c21=-0.049089*e;
    c22=11.766*10^(-9);
    if abs(x)<0.5*L
        if abs(y)<100*10^(-9)
            a=-vf*e*B*0.5*(p_x+0.5*e*B*y)/sqrt((p_x+0.5*e*B*y)^2+(p_y-
0.5*e*B*x)^2)+2*c11*y*exp(-y^2/c12^2)/c12^2;
        else
            a=-vf*e*B*0.5*(p_x+0.5*e*B*y)/sqrt((p_x+0.5*e*B*y)^2+(p_y-
0.5*e*B*x)^2)+c21*sign(y)*exp(-(abs(y)-100*10^(-9))/c22)/c22;
        end
    else
        if sqrt((abs(x)-0.5*L)^2+y^2)<100*10^(-9)
            a=-vf*e*B*0.5*(p_x+0.5*e*B*y)/sqrt((p_x+0.5*e*B*y)^2+(p_y-
0.5*e*B*x)^2)+2*c11*y*exp(-((abs(x)-0.5*L)^2+y^2)/c12^2)/c12^2;
        else
            a=-vf*e*B*0.5*(p_x+0.5*e*B*y)/sqrt((p_x+0.5*e*B*y)^2+(p_y-
0.5*e*B*x)^2)+c21*y/(c22*sqrt((abs(x)-0.5*L)^2+y^2))*exp(-(sqrt((abs(x)-
0.5*L)^2+y^2)-100*10^(-9))/c22);
        end
    end
end

function [a]=U(x,y,L)
    vf=10^6;
    e=1.602176487*10^(-19);
    c10=2.6274*e;
    c11=-2.6274*e;
    c12=334.06764*10^(-9);
    c20=0.274277*e;
```

```
    c21=-0.049089*e;
    c22=11.766*10^(-9);
    if abs(x)<0.5*L
        if abs(y)<100*10^(-9)
            a=c10+c11*exp(-y^2/c12^2);
        else
            a=c20+c21*exp(-(abs(y)-100*10^(-9))/c22);
        end
    else
        if sqrt((abs(x)-0.5*L)^2+y^2)<100*10^(-9)
            a=c10+c11*exp(-((abs(x)-0.5*L)^2+y^2)/c12^2);
        else
            a=c20+c21*exp(-(sqrt(((abs(x)-0.5*L)^2+y^2))-100*10^(-9))/c22);
        end
    end
end
```

References

1 Edvinsson, T. Optical quantum confinement and photocatalytic properties in two-, one-and zero-dimensional nanostructures. *Royal society open science* **5**, 180387 (2018).

2 Kouwenhoven, L. P., Austing, D. & Tarucha, S. Few-electron quantum dots. *Reports on Progress in Physics* **64**, 701 (2001).

3 Shulman, M. D. *et al.* Demonstration of entanglement of electrostatically coupled singlet-triplet qubits. *science* **336**, 202-205 (2012).

4 Beenakker, C. W. Theory of Coulomb-blockade oscillations in the conductance of a quantum dot. *Physical Review B* **44**, 1646 (1991).

5 Chakraborty, T. Quantum Dots: A survey of the properties of artificial atoms. (1999).

6 Reimann, S. M. & Manninen, M. Electronic structure of quantum dots. *Reviews of modern physics* **74**, 1283 (2002).

7 Tarucha, S., Austing, D., Honda, T., Van der Hage, R. & Kouwenhoven, L. P. Shell filling and spin effects in a few electron quantum dot. *Physical Review Letters* **77**, 3613 (1996).

8 Fock, V. Bemerkung zur Quantelung des harmonischen Oszillators im Magnetfeld. *Zeitschrift für Physik* **47**, 446-448 (1928).

9 Darwin, C. G. in *Mathematical Proceedings of the Cambridge Philosophical Society*. 86-90 (Cambridge University Press).

10 Holleitner, A. W., Blick, R. H., Huttel, A. K., Eberl, K. & Kotthaus, J. P. Probing and controlling the bonds of an artificial molecule. *Science* **297**, 70-72 (2002).

11 Oosterkamp, T. *et al.* Microwave spectroscopy of a quantum-dot molecule. *Nature* **395**, 873-876 (1998).

12 Kouwenhoven, L. Coupled quantum dots as artificial molecules. *Science* **268**, 1440-1441 (1995).

13 Schedelbeck, G., Wegscheider, W., Bichler, M. & Abstreiter, G. Coupled quantum dots fabricated by cleaved edge overgrowth: From artificial atoms to molecules. *Science* **278**, 1792-1795 (1997).

14 Stöckmann, H.-J. (American Association of Physics Teachers, 2000).

15 Nakamura, K. & Harayama, T. *Quantum chaos and quantum dots*. Vol. 3 (Oxford University Press on Demand, 2004).

16 Alhassid, Y. The statistical theory of quantum dots. *Reviews of Modern Physics* **72**, 895 (2000).

17 Marcus, C., Rimberg, A., Westervelt, R., Hopkins, P. & Gossard, A. Conductance fluctuations and chaotic scattering in ballistic microstructures. *Physical review letters* **69**, 506 (1992).

18 Chatterjee, A. *et al.* Semiconductor qubits in practice. *Nature Reviews Physics* **3**, 157-177 (2021).

19 Petersson, K., Petta, J., Lu, H. & Gossard, A. Quantum coherence in a one-electron semiconductor charge qubit. *Physical Review Letters* **105**, 246804 (2010).

20 Cao, G. *et al.* Ultrafast universal quantum control of a quantum-dot charge qubit using Landau–Zener–Stückelberg interference. *Nature Communications* **4**, 1401 (2013).

21 Kim, D. *et al.* Microwave-driven coherent operation of a semiconductor quantum dot charge qubit. *Nature nanotechnology* **10**, 243-247 (2015).

22 Malinowski, F. K. *et al.* Spectrum of the nuclear environment for GaAs spin qubits. *Physical review letters* **118**, 177702 (2017).

23 Zajac, D. M. *et al.* Resonantly driven CNOT gate for electron spins. *Science* **359**, 439-442 (2018).

24 Hendrickx, N. W. *et al.* A four-qubit germanium quantum processor. *Nature* **591**, 580-585 (2021).

25 Veldhorst, M. *et al.* A two-qubit logic gate in silicon. *Nature* **526**, 410-414 (2015).

26 Loss, D. & DiVincenzo, D. P. Quantum computation with quantum dots. *Physical Review A* **57**, 120 (1998).

27 Hanson, R., Kouwenhoven, L. P., Petta, J. R., Tarucha, S. & Vandersypen, L. M. Spins in few-electron quantum dots. *Reviews of modern physics* **79**, 1217 (2007).

28 Hensgens, T. *et al.* Quantum simulation of a Fermi–Hubbard model using a semiconductor quantum dot array. *Nature* **548**, 70-73 (2017).

29 Ponomarenko, L. A. *et al.* Chaotic Dirac billiard in graphene quantum dots. *Science* **320**, 356-358 (2008).

30 Eich, M. *et al.* Spin and valley states in gate-defined bilayer graphene quantum dots. *Physical Review X* **8**, 031023 (2018).

31 Goossens, A. M. *et al.* Gate-defined confinement in bilayer graphene-hexagonal boron nitride hybrid devices. *Nano letters* **12**, 4656-4660 (2012).

32 Allen, M. T., Martin, J. & Yacoby, A. Gate-defined quantum confinement in suspended bilayer graphene. *Nature communications* **3**, 934 (2012).

33 Kurzmann, A. *et al.* Charge detection in gate-defined bilayer graphene quantum dots. *Nano letters* **19**, 5216-5221 (2019).

34 Banszerus, L. *et al.* Gate-defined electron–hole double dots in bilayer graphene. *Nano letters* **18**, 4785-4790 (2018).

35 Banszerus, L. *et al.* Single-electron double quantum dots in bilayer graphene. *Nano letters* **20**, 2005-2011 (2020).

36 Kurzmann, A. *et al.* Excited states in bilayer graphene quantum dots. *Physical review letters* **123**, 026803 (2019).

37 Tong, C. *et al.* Tunable valley splitting and bipolar operation in graphene quantum dots. *Nano Letters* **21**, 1068-1073 (2021).

38 Garreis, R. *et al.* Shell filling and trigonal warping in graphene quantum dots. *Physical Review Letters* **126**, 147703 (2021).

39 Kurzmann, A. *et al.* Kondo effect and spin–orbit coupling in graphene quantum dots. *Nature Communications* **12**, 6004 (2021).

40 Tong, C. *et al.* Pauli Blockade of Tunable Two-Electron Spin and Valley States in Graphene Quantum Dots. *Physical Review Letters* **128**, 067702 (2022).

41 Gächter, L. M. *et al.* Single-shot spin readout in graphene quantum dots. *PRX Quantum* **3**, 020343 (2022).

42 Garreis, R. *et al.* Counting statistics of single electron transport in bilayer graphene quantum dots. *Physical Review Research* **5**, 013042 (2023).

43 Garreis, R. *et al.* Long-lived valley states in bilayer graphene quantum dots. *arXiv preprint arXiv:2304.00980* (2023).

44 Banszerus, L. *et al.* Pulsed-gate spectroscopy of single-electron spin states in bilayer graphene quantum dots. *Physical Review B* **103**, L081404 (2021).

45 Banszerus, L. *et al.* Dispersive sensing of charge states in a bilayer graphene quantum dot. *Applied Physics Letters* **118**, 093104 (2021).

46 Banszerus, L. *et al.* Spin-valley coupling in single-electron bilayer graphene quantum dots. *Nature Communications* **12**, 5250 (2021).

47 Möller, S. *et al.* Probing two-electron multiplets in bilayer graphene quantum dots. *Physical Review Letters* **127**, 256802 (2021).

48 Banszerus, L. *et al.* Spin relaxation in a single-electron graphene quantum dot. *Nature Communications* **13**, 3637 (2022).

49 Banszerus, L. *et al.* Particle-hole symmetry protects spin-valley blockade in graphene quantum dots. *arXiv preprint arXiv:2303.10201* (2023).

50 Zhao, Y. *et al.* Creating and probing electron whispering-gallery modes in graphene. *Science* **348**, 672-675 (2015).

51 Freitag, N. M. *et al.* Electrostatically confined monolayer graphene quantum dots with orbital and valley splittings. *Nano letters* **16**, 5798-5805 (2016).

52 Freitag, N. M. *et al.* Large tunable valley splitting in edge-free graphene quantum dots on boron nitride. *Nature nanotechnology* **13**, 392-397 (2018).

53 Lee, J. *et al.* Imaging electrostatically confined Dirac fermions in graphene quantum dots. *Nature Physics* **12**, 1032-1036 (2016).

54 Gutiérrez, C., Brown, L., Kim, C.-J., Park, J. & Pasupathy, A. N. Klein tunnelling and electron trapping in nanometre-scale graphene quantum dots. *Nature Physics* **12**, 1069-1075 (2016).

55 Jiang, Y. *et al.* Tuning a circular p–n junction in graphene from quantum confinement to optical guiding. *Nature nanotechnology* **12**, 1045-1049 (2017).

56 Liu, Y.-W., Hou, Z., Li, S.-Y., Sun, Q.-F. & He, L. Movable valley switch driven by berry phase in bilayer-graphene resonators. *Physical review letters* **124**, 166801 (2020).

57 Ghahari, F. *et al.* An on/off Berry phase switch in circular graphene resonators. *Science* **356**, 845-849, doi:10.1126/science.aal0212 (2017).

58 Gutiérrez, C. *et al.* Interaction-driven quantum Hall wedding cake–like structures in graphene quantum dots. *Science* **361**, 789-794 (2018).

59 Quezada-López, E. A. *et al.* Comprehensive Electrostatic Modeling of Exposed Quantum Dots in Graphene/Hexagonal Boron Nitride Heterostructures. *Nanomaterials* **10**, 1154 (2020).

60 Ge, Z. *et al.* Visualization and manipulation of bilayer graphene quantum dots with broken rotational symmetry and nontrivial topology. *Nano letters* **20**, 8682-8688 (2020).

61 Ge, Z. *et al.* Control of giant topological magnetic moment and valley splitting in trilayer graphene. *Physical Review Letters* **127**, 136402 (2021).

62 Ge, Z. *et al.* Imaging quantum interference in stadium-shaped monolayer and bilayer graphene quantum dots. *Nano Letters* **21**, 8993-8998 (2021).

63 Ge, Z. *et al.* Giant orbital magnetic moments and paramagnetic shift in artificial relativistic atoms and molecules. *Nature Nanotechnology* **18**, 250-256 (2023).

64 Velasco Jr, J. *et al.* Visualization and control of single-electron charging in bilayer graphene quantum dots. *Nano letters* **18**, 5104-5110 (2018).

65 Fu, Z.-Q. *et al.* Relativistic artificial molecules realized by two coupled graphene quantum dots. *Nano Letters* **20**, 6738-6743 (2020).

66 Ren, Y.-N., Cheng, Q., Sun, Q.-F. & He, L. Realizing Valley-Polarized Energy Spectra in Bilayer Graphene Quantum Dots via Continuously Tunable Berry Phases. *Physical Review Letters* **128**, 206805 (2022).

67 Zheng, Q., Zhuang, Y.-C., Sun, Q.-F. & He, L. Coexistence of electron whispering-gallery modes and atomic collapse states in graphene/WSe2 heterostructure quantum dots. *Nature Communications* **13**, 1597 (2022).

68 Walkup, D. *et al.* Tuning single-electron charging and interactions between compressible Landau level islands in graphene. *Physical Review B* **101**, 035428, doi:10.1103/PhysRevB.101.035428 (2020).

69 Behn, W. A. *et al.* Measuring and Tuning the Potential Landscape of Electrostatically Defined Quantum Dots in Graphene. *Nano Letters* **21**, 5013-5020 (2021).

70 Tong, C. *et al.* Pauli Blockade of Tunable Two-Electron Spin and Valley States in Graphene Quantum Dots. *Physical Review Letters* **128**, 067702, doi:10.1103/PhysRevLett.128.067702 (2022).

71 Banszerus, L. *et al.* Particle–hole symmetry protects spin-valley blockade in graphene quantum dots. *Nature*, doi:10.1038/s41586-023-05953-5 (2023).

72 Eich, M. *et al.* Coupled quantum dots in bilayer graphene. *Nano letters* **18**, 5042-5048 (2018).

73 Neto, A. C., Guinea, F., Peres, N. M., Novoselov, K. S. & Geim, A. K. The electronic properties of graphene. *Reviews of modern physics* **81**, 109 (2009).

74 Trauzettel, B., Bulaev, D. V., Loss, D. & Burkard, G. Spin qubits in graphene quantum dots. *Nature Physics* **3**, 192-196 (2007).

75 Novoselov, K. S. *et al.* Electric field effect in atomically thin carbon films. *science* **306**, 666-669 (2004).

76 Novoselov, K. S. *et al.* Two-dimensional gas of massless Dirac fermions in graphene. *nature* **438**, 197-200 (2005).

77 Zhang, Y., Tan, Y.-W., Stormer, H. L. & Kim, P. Experimental observation of the quantum Hall effect and Berry's phase in graphene. *Nature* **438**, 201-204 (2005).

78 Young, A. F. & Kim, P. Quantum interference and Klein tunnelling in graphene heterojunctions. *Nature Physics* **5**, 222-226 (2009).

79 Novoselov, K. S., Mishchenko, A., Carvalho, o. A. & Castro Neto, A. 2D materials and van der Waals heterostructures. *Science* **353**, aac9439 (2016).

80 Wallace, P. R. The band theory of graphite. *Physical review* **71**, 622 (1947).

81 McCann, E. Electronic properties of monolayer and bilayer graphene. *Graphene Nanoelectronics: Metrology, Synthesis, Properties and Applications*, 237-275 (2012).

82 McCann, E. & Koshino, M. The electronic properties of bilayer graphene. *Reports on Progress in physics* **76**, 056503 (2013).

83 Thaller, B. *The dirac equation*. 39-41 (Springer Science & Business Media, 2013).

84 Xiao, D., Chang, M.-C. & Niu, Q. Berry phase effects on electronic properties. *Reviews of Modern Physics* **82**, 1959 (2010).

85 Berry, M. V. Quantal phase factors accompanying adiabatic changes. *Proceedings of the Royal Society of London. A. Mathematical and Physical Sciences* **392**, 45-57 (1984).

86 Anandan, J. The geometric phase. *Nature* **360**, 307-313 (1992).

87 Varlet, A. *et al.* Band gap and broken chirality in single-layer and bilayer graphene. *physica status solidi (RRL)–Rapid Research Letters* **10**, 46-57 (2016).

88 Katsnelson, M., Novoselov, K. & Geim, A. Chiral tunnelling and the Klein paradox in graphene. *Nature physics* **2**, 620-625 (2006).

89 Knothe, A. & Fal'ko, V. Influence of minivalleys and Berry curvature on electrostatically induced quantum wires in gapped bilayer graphene. *Physical Review B* **98**, 155435 (2018).

90 Varlet, A. *et al.* Fabry-Pérot interference in gapped bilayer graphene with broken anti-Klein tunneling. *Physical review letters* **113**, 116601 (2014).

91 Du, R. *et al.* Tuning anti-Klein to Klein tunneling in bilayer graphene. *Physical review letters* **121**, 127706 (2018).

92 Koshino, M. & McCann, E. Gate-induced interlayer asymmetry in ABA-stacked trilayer graphene. *Physical Review B* **79**, 125443 (2009).

93 Zhang, F., Sahu, B., Min, H. & MacDonald, A. H. Band structure of A B C-stacked graphene trilayers. *Physical Review B* **82**, 035409 (2010).

94 Mak, K. F., Shan, J. & Heinz, T. F. Electronic Structure of Few-Layer Graphene: Experimental Demonstration of Strong Dependence on Stacking Sequence. *Physical Review Letters* **104**, 176404, doi:10.1103/PhysRevLett.104.176404 (2010).

95 Bao, W. *et al.* Stacking-dependent band gap and quantum transport in trilayer graphene. *Nature Physics* **7**, 948-952, doi:10.1038/nphys2103 (2011).

96 Zibrov, A. A. *et al.* Emergent Dirac Gullies and Gully-Symmetry-Breaking Quantum Hall States in ABA Trilayer Graphene. *Physical Review Letters* **121**, 167601, doi:10.1103/PhysRevLett.121.167601 (2018).

97 Taychatanapat, T., Watanabe, K., Taniguchi, T. & Jarillo-Herrero, P. Quantum Hall effect and Landau-level crossing of Dirac fermions in trilayer graphene. *Nature Physics* **7**, 621-625, doi:10.1038/nphys2008 (2011).

98 Grüneis, A. *et al.* Tight-binding description of the quasiparticle dispersion of graphite and few-layer graphene. *Physical Review B* **78**, 205425, doi:10.1103/PhysRevB.78.205425 (2008).

99 Campos, L. C. *et al.* Landau Level Splittings, Phase Transitions, and Nonuniform Charge Distribution in Trilayer Graphene. *Physical Review Letters* **117**, 066601, doi:10.1103/PhysRevLett.117.066601 (2016).

100 Dresselhaus, M. S. & Dresselhaus, G. Intercalation compounds of graphite. *Advances in Physics* **30**, 139-326, doi:10.1080/00018738100101367 (1981).

101 Xiao, D., Yao, W. & Niu, Q. Valley-Contrasting Physics in Graphene: Magnetic Moment and Topological Transport. *Physical Review Letters* **99**, 236809, doi:10.1103/PhysRevLett.99.236809 (2007).

102 Dean Moldovan, M. A., & Francois Peeters. pybinding v0.9.5: a Python package for tight-binding calculations (v0.9.5). Zenodo. https://doi.org/10.5281/zenodo.4010216. (2020).

103 Heller, E. J. Bound-State Eigenfunctions of Classically Chaotic Hamiltonian Systems: Scars of Periodic Orbits. *Physical Review Letters* **53**, 1515-1518, doi:10.1103/PhysRevLett.53.1515 (1984).

104 Bardeen, J. Tunnelling from a Many-Particle Point of View. *Physical Review Letters* **6**, 57-59, doi:10.1103/PhysRevLett.6.57 (1961).

105 Tersoff, J. & Hamann, D. R. Theory and Application for the Scanning Tunneling Microscope. *Physical Review Letters* **50**, 1998-2001, doi:10.1103/PhysRevLett.50.1998 (1983).

106 Tersoff, J. & Hamann, D. R. Theory of the scanning tunneling microscope. *Physical Review B* **31**, 805-813, doi:10.1103/PhysRevB.31.805 (1985).

107 Luryi, S. Quantum capacitance devices. *Applied Physics Letters* **52**, 501-503, doi:10.1063/1.99649 (1988).

108 Song, S. M., Park, J. K., Sul, O. J. & Cho, B. J. Determination of Work Function of Graphene under a Metal Electrode and Its Role in Contact Resistance. *Nano Letters* **12**, 3887-3892, doi:10.1021/nl300266p (2012).

109 Zhang, Y. *et al.* Giant phonon-induced conductance in scanning tunnelling spectroscopy of gate-tunable graphene. *Nature Physics* **4**, 627-630, doi:10.1038/nphys1022 (2008).

110 Wehling, T. O., Grigorenko, I., Lichtenstein, A. I. & Balatsky, A. V. Phonon-Mediated Tunneling into Graphene. *Physical Review Letters* **101**, 216803, doi:10.1103/PhysRevLett.101.216803 (2008).

111 Mohr, M. *et al.* Phonon dispersion of graphite by inelastic x-ray scattering. *Physical Review B* **76**, 035439, doi:10.1103/PhysRevB.76.035439 (2007).

112 Wong, D. *Tuning Electrostatic Potentials for Imaging the Quantum Properties of Massless Dirac Fermions in Graphene*. (University of California, Berkeley, 2017).

113 Chen, W., Madhavan, V., Jamneala, T. & Crommie, M. F. Scanning Tunneling Microscopy Observation of an Electronic Superlattice at the Surface of Clean Gold. *Physical Review Letters* **80**, 1469-1472, doi:10.1103/PhysRevLett.80.1469 (1998).

114 Velasco, J., Jr. *et al.* Nanoscale Control of Rewriteable Doping Patterns in Pristine Graphene/Boron Nitride Heterostructures. *Nano Letters* **16**, 1620-1625, doi:10.1021/acs.nanolett.5b04441 (2016).

115 Wong, D. *et al.* Characterization and manipulation of individual defects in insulating hexagonal boron nitride using scanning tunnelling microscopy. *Nature Nanotechnology* **10**, 949-953, doi:10.1038/nnano.2015.188 (2015).

116 Zomer, P. J., Dash, S. P., Tombros, N. & van Wees, B. J. A transfer technique for high mobility graphene devices on commercially available hexagonal boron nitride. *Applied Physics Letters* **99**, 232104, doi:10.1063/1.3665405 (2011).

117 Quezada-Lopez, E. A. *Exploring the Graphene/Hexagonal Boron Nitride Heterostructure from the Bottom to the Top*. (University of California, Santa Cruz, 2020).

118 Davenport II, J. L. *Planar Tunneling Spectroscopy of Graphene and Bilayer Graphene*. (University of California, Santa Cruz, 2020).

119 Wang, L. *et al.* One-Dimensional Electrical Contact to a Two-Dimensional Material. *Science* **342**, 614-617, doi:10.1126/science.1244358 (2013).

120 Pizzocchero, F. *et al.* The hot pick-up technique for batch assembly of van der Waals heterostructures. *Nature Communications* **7**, 11894, doi:10.1038/ncomms11894 (2016).

121 Photo Etch Technology http://stencil.com/.

122 Schweizer, P. *et al.* Mechanical cleaning of graphene using in situ electron microscopy. *Nature Communications* **11**, 1743, doi:10.1038/s41467-020-15255-3 (2020).

123 Lin, Y.-C. *et al.* Graphene Annealing: How Clean Can It Be? *Nano Letters* **12**, 414-419, doi:10.1021/nl203733r (2012).

124 Kretinin, A. V. *et al.* Electronic Properties of Graphene Encapsulated with Different Two-Dimensional Atomic Crystals. *Nano Letters* **14**, 3270-3276, doi:10.1021/nl5006542 (2014).

125 Goossens, A. M. *et al.* Mechanical cleaning of graphene. *Applied Physics Letters* **100**, 073110, doi:10.1063/1.3685504 (2012).

126 Lanczos, C. An Iteration Method for the Solution of the Eigenvalue Problem of Linear Differential and Integral Operators. *Journal of Research of the National Bureau of Standards* **45**, 255-282 (1950).

127 Weiße, A., Wellein, G., Alvermann, A. & Fehske, H. The kernel polynomial method. *Reviews of Modern Physics* **78**, 275-306, doi:10.1103/RevModPhys.78.275 (2006).

128 Lehoucq, R. B., Sorensen, D. C. & Yang, C. *ARPACK users' guide: solution of large-scale eigenvalue problems with implicitly restarted Arnoldi methods*. (SIAM, 1998).

129 Groth, C. W., Wimmer, M., Akhmerov, A. R. & Waintal, X. Kwant: a software package for quantum transport. *New Journal of Physics* **16**, 063065 (2014).

130 Moldovan, D. *Electronic properties of strained graphene and supercritical charge centers*, University of Antwerp, (2016).

131 *https://hummingbird.ucsc.edu/*.

132 Hofstadter, D. R. Energy levels and wave functions of Bloch electrons in rational and irrational magnetic fields. *Physical Review B* **14**, 2239-2249, doi:10.1103/PhysRevB.14.2239 (1976).

133 Liu, M.-H. *et al.* Scalable Tight-Binding Model for Graphene. *Physical Review Letters* **114**, 036601, doi:10.1103/PhysRevLett.114.036601 (2015).

134 Matulis, A. & Peeters, F. M. Quasibound states of quantum dots in single and bilayer graphene. *Physical Review B* **77**, 115423, doi:10.1103/PhysRevB.77.115423 (2008).

135 Rodriguez-Nieva, J. F. & Levitov, L. S. Berry phase jumps and giant nonreciprocity in Dirac quantum dots. *Physical Review B* **94**, 235406, doi:10.1103/PhysRevB.94.235406 (2016).

136 Pereira, J. M., Vasilopoulos, P. & Peeters, F. M. Tunable Quantum Dots in Bilayer Graphene. *Nano Letters* **7**, 946-949, doi:10.1021/nl062967s (2007).

137 Knothe, A. & Fal'ko, V. Quartet states in two-electron quantum dots in bilayer graphene. *Physical Review B* **101**, 235423, doi:10.1103/PhysRevB.101.235423 (2020).

138 Wang, Y. *et al.* Observing Atomic Collapse Resonances in Artificial Nuclei on Graphene. *Science* **340**, 734-737, doi:doi:10.1126/science.1234320 (2013).

139 Lu, J. *et al.* Frustrated supercritical collapse in tunable charge arrays on graphene. *Nature Communications* **10**, 477, doi:10.1038/s41467-019-08371-2 (2019).

140 Chen, S. *et al.* Electron optics with p-n junctions in ballistic graphene. *Science* **353**, 1522-1525, doi:doi:10.1126/science.aaf5481 (2016).

141 Cheianov, V. V., Fal'ko, V. & Altshuler, B. L. The Focusing of Electron Flow and a Veselago Lens in Graphene <i>p-n</i> Junctions. *Science* **315**, 1252-1255, doi:doi:10.1126/science.1138020 (2007).

142 Cheianov, V. V. & Fal’ko, V. I. Selective transmission of Dirac electrons and ballistic magnetoresistance of $n\text{\ensuremath{-}}p$ junctions in graphene. *Physical Review B* **74**, 041403, doi:10.1103/PhysRevB.74.041403 (2006).

143 Liu, M.-H., Gorini, C. & Richter, K. Creating and Steering Highly Directional Electron Beams in Graphene. *Physical Review Letters* **118**, 066801, doi:10.1103/PhysRevLett.118.066801 (2017).

144 Lodahl, P., Mahmoodian, S. & Stobbe, S. Interfacing single photons and single quantum dots with photonic nanostructures. *Reviews of Modern Physics* **87**, 347-400, doi:10.1103/RevModPhys.87.347 (2015).

145 Bai, K.-K. *et al.* Generating atomically sharp $p\ensuremath{-}n$ junctions in graphene and testing quantum electron optics on the nanoscale. *Physical Review B* **97**, 045413, doi:10.1103/PhysRevB.97.045413 (2018).

146 Bethe, H. A. & Salpeter, E. E. *Quantum mechanics of one-and two-electron atoms*. (Springer Science & Business Media, 2012).

147 Rinaldi, R. *et al.* Zeeman effect in parabolic quantum dots. *Physical review letters* **77**, 342 (1996).

148 Paskov, P. *et al.* Magnetoluminescence of highly excited InAs/GaAs self-assembled quantum dots. *Physical Review B* **62**, 7344 (2000).

149 Raymond, S. *et al.* Excitonic energy shell structure of self-assembled InGaAs/GaAs quantum dots. *Physical review letters* **92**, 187402 (2004).

150 Lenz, J. & Edelstein, S. Magnetic sensors and their applications. *IEEE Sensors journal* **6**, 631-649 (2006).

151 Degen, C. L., Reinhard, F. & Cappellaro, P. Quantum sensing. *Reviews of modern physics* **89**, 035002 (2017).

152 Davenport, J. L. *et al.* Probing the electronic structure of graphene near and far from the Fermi level via planar tunneling spectroscopy. *Applied Physics Letters* **115**, 163504 (2019).

153 Ashcroft, N. W. & Mermin, N. D. *Solid state physics*. (Cengage Learning, 2022).

154 Arimondo, E., Ciampini, D. & Rizzo, C. in *Advances In Atomic, Molecular, and Optical Physics* Vol. 65 1-66 (Elsevier, 2016).

155 Ambegaokar, V. & Eckern, U. Coherence and persistent currents in mesoscopic rings. *Physical review letters* **65**, 381 (1990).

156 Bleszynski-Jayich, A. *et al.* Persistent currents in normal metal rings. *Science* **326**, 272-275 (2009).

157 Mooij, J. *et al.* Josephson persistent-current qubit. *Science* **285**, 1036-1039 (1999).

158 Nisoli, C., Moessner, R. & Schiffer, P. Colloquium: Artificial spin ice: Designing and imaging magnetic frustration. *Reviews of Modern Physics* **85**, 1473 (2013).

159 Basov, D., Averitt, R. & Hsieh, D. Towards properties on demand in quantum materials. *Nature materials* **16**, 1077-1088 (2017).

160 Liu, X. & Hersam, M. C. 2D materials for quantum information science. *Nature Reviews Materials* **4**, 669-684 (2019).

161 Bockrath, M. Unprecedented charge state control in graphene quantum dots. *Nano Letters* (2020).

162 Lee, Y. *et al.* Tunable valley splitting due to topological orbital magnetic moment in bilayer graphene quantum point contacts. *Physical review letters* **124**, 126802 (2020).

163 Tarucha, S., Yamamoto, M., Oiwa, A., Choi, B.-S. & Tokura, Y. in *Principles and Methods of Quantum Information Technologies* 541-567 (Springer, 2016).

164 Recher, P., Nilsson, J., Burkard, G. & Trauzettel, B. Bound states and magnetic field induced valley splitting in gate-tunable graphene quantum dots. *Physical Review B* **79**, 085407 (2009).

165 Zarenia, M., Partoens, B., Chakraborty, T. & Peeters, F. Electron-electron interactions in bilayer graphene quantum dots. *Physical Review B* **88**, 245432 (2013).

166 Hou, Z., Zhou, Y.-F., Xie, X. & Sun, Q.-F. Berry phase induced valley level crossing in bilayer graphene quantum dots. *Physical Review B* **99**, 125422 (2019).

167 Lauffer, P. *et al.* Atomic and electronic structure of few-layer graphene on SiC (0001) studied with scanning tunneling microscopy and spectroscopy. *Physical Review B* **77**, 155426 (2008).

168 Kim, K. S. *et al.* Visualizing atomic-scale negative differential resistance in bilayer graphene. *Physical review letters* **110**, 036804 (2013).

169 Ju, L. *et al.* Topological valley transport at bilayer graphene domain walls. *Nature* **520**, 650 (2015).

170 Joucken, F. *et al.* Determination of the trigonal warping orientation in Bernal-stacked bilayer graphene via scanning tunneling microscopy. *Physical Review B* **101**, 161103 (2020).

171 Dutreix, C. *et al.* Measuring the Berry phase of graphene from wavefront dislocations in Friedel oscillations. *Nature* **574**, 219-222, doi:10.1038/s41586-019-1613-5 (2019).

172 Shimazaki, Y. *et al.* Generation and detection of pure valley current by electrically induced Berry curvature in bilayer graphene. *Nature Physics* **11**, 1032 (2015).

173 Mak, K. F., McGill, K. L., Park, J. & McEuen, P. L. The valley Hall effect in MoS2 transistors. *Science* **344**, 1489-1492 (2014).

174 Xu, S.-Y. *et al.* Electrically switchable Berry curvature dipole in the monolayer topological insulator WTe 2. *Nature Physics* **14**, 900-906 (2018).

175 Weng, H., Fang, C., Fang, Z., Bernevig, B. A. & Dai, X. Weyl semimetal phase in noncentrosymmetric transition-metal monophosphides. *Physical Review X* **5**, 011029 (2015).

176 Xu, S.-Y. *et al.* Discovery of a Weyl fermion semimetal and topological Fermi arcs. *Science* **349**, 613-617 (2015).

177 Lv, B. *et al.* Experimental discovery of Weyl semimetal TaAs. *Physical Review X* **5**, 031013 (2015).

178 Wu, S. *et al.* Electrical tuning of valley magnetic moment through symmetry control in bilayer MoS 2. *Nature Physics* **9**, 149-153 (2013).

179 Aivazian, G. *et al.* Magnetic control of valley pseudospin in monolayer WSe 2. *Nature Physics* **11**, 148-152 (2015).

180 Komatsu, K. *et al.* Observation of the quantum valley Hall state in ballistic graphene superlattices. *Science advances* **4**, eaaq0194 (2018).

181 Overweg, H. *et al.* Topologically nontrivial valley states in bilayer graphene quantum point contacts. *Physical review letters* **121**, 257702 (2018).

182 Moriya, R. *et al.* Emergence of orbital angular moment at van Hove singularity in graphene/h-BN moiré superlattice. *Nature communications* **11**, 1-6 (2020).

183 Li, Y. *et al.* Valley splitting and polarization by the Zeeman effect in monolayer MoSe 2. *Physical review letters* **113**, 266804 (2014).

184 MacNeill, D. *et al.* Breaking of valley degeneracy by magnetic field in monolayer MoSe 2. *Physical review letters* **114**, 037401 (2015).

185 Srivastava, A. *et al.* Valley Zeeman effect in elementary optical excitations of monolayer WSe 2. *Nature Physics* **11**, 141-147 (2015).

186 Kraft, R. *et al.* Valley Subband splitting in bilayer graphene quantum point contacts. *Physical review letters* **121**, 257703 (2018).

187 Wang, T. *et al.* Giant valley-Zeeman splitting from spin-singlet and spin-triplet interlayer excitons in WSe2/MoSe2 heterostructure. *Nano letters* **20**, 694-700 (2019).

188 Lu, X. *et al.* Superconductors, orbital magnets and correlated states in magic-angle bilayer graphene. *Nature* **574**, 653-657 (2019).

189 Sharpe, A. L. *et al.* Emergent ferromagnetism near three-quarters filling in twisted bilayer graphene. *Science* **365**, 605-608 (2019).

190 He, W.-Y., Goldhaber-Gordon, D. & Law, K. T. Giant orbital magnetoelectric effect and current-induced magnetization switching in twisted bilayer graphene. *Nature communications* **11**, 1-8 (2020).

191 Zhu, J., Su, J.-J. & MacDonald, A. H. Voltage-Controlled Magnetic Reversal in Orbital Chern Insulators. *Physical Review Letters* **125**, 227702 (2020).

192 Polshyn, H. *et al.* Electrical switching of magnetic order in an orbital Chern insulator. *Nature* **588**, 66-70, doi:10.1038/s41586-020-2963-8 (2020).

193 Yankowitz, M., Ma, Q., Jarillo-Herrero, P. & LeRoy, B. J. van der Waals heterostructures combining graphene and hexagonal boron nitride. *Nature Reviews Physics* **1**, 112-125 (2019).

194 Que, Y. *et al.* Stacking-dependent electronic property of trilayer graphene epitaxially grown on Ru (0001). *Applied Physics Letters* **107**, 263101 (2015).

195 Zhang, Y., Qiao, J.-B., Yin, L.-J. & He, L. High-resolution tunneling spectroscopy of ABA-stacked trilayer graphene. *Physical Review B* **98**, 045413 (2018).

196 Yankowitz, M., Wang, F., Lau, C. N. & LeRoy, B. J. Local spectroscopy of the electrically tunable band gap in trilayer graphene. *Physical Review B* **87**, 165102 (2013).

197 Yankowitz, M. *et al.* Electric field control of soliton motion and stacking in trilayer graphene. *Nature materials* **13**, 786-789 (2014).

198 Sandro, W. *Nonlinear Dynamics and Quantum Chaos: An Introduction*. (Berlin: Springer, 2014).

199 Gutzwiller, M. C. *Chaos in classical and quantum mechanics*. Vol. 1 (Springer Science & Business Media, 2013).

200 Haake, F. *Quantum signatures of chaos*. (Springer, 1991).

201 Huang, L., Lai, Y.-C., Ferry, D. K., Goodnick, S. M. & Akis, R. Relativistic Quantum Scars. *Physical Review Letters* **103**, 054101, doi:10.1103/PhysRevLett.103.054101 (2009).

202 Gmachl, C. *et al.* High-power directional emission from microlasers with chaotic resonators. *Science* **280**, 1556-1564 (1998).

203 Shinohara, S. *et al.* Chaos-Assisted Directional Light Emission from Microcavity Lasers. *Physical Review Letters* **104**, 163902, doi:10.1103/PhysRevLett.104.163902 (2010).

204 Nöckel, J. U. & Stone, A. D. Ray and wave chaos in asymmetric resonant optical cavities. *Nature* **385**, 45-47 (1997).

205 Ferry, D. K. *et al.* Open quantum dots—probing the quantum to classical transition. *Semiconductor science and technology* **26**, 043001 (2011).

206 Bird, J. *et al.* Interference and interactions in open quantum dots. *Reports on Progress in Physics* **66**, 583 (2003).

207 Bernien, H. *et al.* Probing many-body dynamics on a 51-atom quantum simulator. *Nature* **551**, 579-584 (2017).

208 Serbyn, M., Abanin, D. A. & Papić, Z. Quantum many-body scars and weak breaking of ergodicity. *Nature Physics* **17**, 675-685 (2021).

209 Stein, J. & Stöckmann, H. J. Experimental determination of billiard wave functions. *Physical Review Letters* **68**, 2867-2870, doi:10.1103/PhysRevLett.68.2867 (1992).

210 Sridhar, S. Experimental observation of scarred eigenfunctions of chaotic microwave cavities. *Physical Review Letters* **67**, 785-788, doi:10.1103/PhysRevLett.67.785 (1991).

211 Chinnery, P. A. & Humphrey, V. F. Experimental visualization of acoustic resonances within a stadium-shaped cavity. *Physical Review E* **53**, 272-276, doi:10.1103/PhysRevE.53.272 (1996).

212 Kudrolli, A., Abraham, M. C. & Gollub, J. P. Scarred patterns in surface waves. *Physical Review E* **63**, 026208, doi:10.1103/PhysRevE.63.026208 (2001).

213 Crook, R. *et al.* Imaging Fractal Conductance Fluctuations and Scarred Wave Functions in a Quantum Billiard. *Physical Review Letters* **91**, 246803, doi:10.1103/PhysRevLett.91.246803 (2003).

214 Martins, F. *et al.* Imaging Electron Wave Functions Inside Open Quantum Rings. *Physical Review Letters* **99**, 136807, doi:10.1103/PhysRevLett.99.136807 (2007).

215 Hackens, B. *et al.* Imaging and controlling electron transport inside a quantum ring. *Nature Physics* **2**, 826-830 (2006).

216 Burke, A. *et al.* Imaging scarred states in quantum dots. *Journal of Physics: Condensed Matter* **21**, 212201 (2009).

217 Burke, A. M. *et al.* Periodic Scarred States in Open Quantum Dots as Evidence of Quantum Darwinism. *Physical Review Letters* **104**, 176801, doi:10.1103/PhysRevLett.104.176801 (2010).

218 Aoki, N. *et al.* Direct Imaging of Electron States in Open Quantum Dots. *Physical Review Letters* **108**, 136804, doi:10.1103/PhysRevLett.108.136804 (2012).

219 Cabosart, D. *et al.* Recurrent quantum scars in a mesoscopic graphene ring. *Nano letters* **17**, 1344-1349 (2017).

220 Heller, E., Crommie, M., Lutz, C. & Eigler, D. Scattering and absorption of surface electron waves in quantum corrals. *Nature* **369**, 464-466 (1994).

221 Huang, L., Xu, H.-Y., Grebogi, C. & Lai, Y.-C. Relativistic quantum chaos. *Physics Reports* **753**, 1-128 (2018).

222 Keski-Rahkonen, J., Luukko, P. J. J., Kaplan, L., Heller, E. J. & Räsänen, E. Controllable quantum scars in semiconductor quantum dots. *Physical Review B* **96**, 094204, doi:10.1103/PhysRevB.96.094204 (2017).

223 Keski-Rahkonen, J., Ruhanen, A., Heller, E. J. & Räsänen, E. Quantum Lissajous Scars. *Physical Review Letters* **123**, 214101, doi:10.1103/PhysRevLett.123.214101 (2019).

224 Luukko, P. J. *et al.* Strong quantum scarring by local impurities. *Scientific reports* **6**, 1-6 (2016).

225 Keski-Rahkonen, J., Luukko, P., Åberg, S. & Räsänen, E. Effects of scarring on quantum chaos in disordered quantum wells. *Journal of Physics: Condensed Matter* **31**, 105301 (2019).

226 Xu, H., Huang, L., Lai, Y.-C. & Grebogi, C. Chiral Scars in Chaotic Dirac Fermion Systems. *Physical Review Letters* **110**, 064102, doi:10.1103/PhysRevLett.110.064102 (2013).

227 Wang, C.-Z., Huang, L. & Chang, K. Scars in Dirac fermion systems: the influence of an Aharonov–Bohm flux. *New Journal of Physics* **19**, 013018 (2017).

228 Song, M.-Y., Li, Z.-Y., Xu, H.-Y., Huang, L. & Lai, Y.-C. Quantization of massive Dirac billiards and unification of nonrelativistic and relativistic chiral quantum scars. *Physical Review Research* **1**, 033008, doi:10.1103/PhysRevResearch.1.033008 (2019).

229 Cao, Y. *et al.* Unconventional superconductivity in magic-angle graphene superlattices. *Nature* **556**, 43-50 (2018).

230 Yankowitz, M. *et al.* Tuning superconductivity in twisted bilayer graphene. *Science* **363**, 1059-1064 (2019).

231 Serlin, M. *et al.* Intrinsic quantized anomalous Hall effect in a moiré heterostructure. *Science* **367**, 900-903 (2020).

232 Saito, Y. *et al.* Hofstadter subband ferromagnetism and symmetry-broken Chern insulators in twisted bilayer graphene. *Nature Physics* **17**, 478-481 (2021).

233 Nuckolls, K. P. *et al.* Strongly correlated Chern insulators in magic-angle twisted bilayer graphene. *Nature* **588**, 610-615 (2020).

234 Wu, S., Zhang, Z., Watanabe, K., Taniguchi, T. & Andrei, E. Y. Chern insulators, van Hove singularities and topological flat bands in magic-angle twisted bilayer graphene. *Nature materials* **20**, 488-494 (2021).

235 Das, I. *et al.* Symmetry-broken Chern insulators and Rashba-like Landau-level crossings in magic-angle bilayer graphene. *Nature Physics* **17**, 710-714 (2021).

236 Choi, Y. *et al.* Correlation-driven topological phases in magic-angle twisted bilayer graphene. *Nature* **589**, 536-541 (2021).

237 Ioffe, L. B., Geshkenbein, V. B., Feigel'Man, M. V., Fauchere, A. L. & Blatter, G. Environmentally decoupled sds-wave Josephson junctions for quantum computing. *Nature* **398**, 679-681 (1999).

238 Nayak, C., Simon, S. H., Stern, A., Freedman, M. & Sarma, S. D. Non-Abelian anyons and topological quantum computation. *Reviews of Modern Physics* **80**, 1083 (2008).

239 Xie, Y.-M., Efetov, D. K. & Law, K. Valley-Polarized State Induced φ_0-Josephson Junction in Twisted Bilayer Graphene. *arXiv preprint arXiv:2202.05663* (2022).

240 Thomson, A., Sorensen, I. M., Nadj-Perge, S. & Alicea, J. Gate-defined wires in twisted bilayer graphene: From electrical detection of intervalley coherence to internally engineered Majorana modes. *Physical Review B* **105**, L081405 (2022).

241 Hasan, M. Z. & Kane, C. L. Colloquium: topological insulators. *Reviews of modern physics* **82**, 3045 (2010).

242 Kosztin, I., Maslov, D. L. & Goldbart, P. M. Chaos in Andreev billiards. *Physical review letters* **75**, 1735 (1995).

243 Beenakker, C. in *Quantum Dots: a Doorway to Nanoscale Physics* 131-174 (Springer, 2005).

244 Melsen, J., Brouwer, P., Frahm, K. & Beenakker, C. Induced superconductivity distinguishes chaotic from integrable billiards. *EPL (Europhysics Letters)* **35**, 7 (1996).

245 Fatemi, V. *et al.* Electrically tunable low-density superconductivity in a monolayer topological insulator. *Science* **362**, 926-929 (2018).

246 Sajadi, E. *et al.* Gate-induced superconductivity in a monolayer topological insulator. *Science* **362**, 922-925 (2018).

247 Fei, Z. *et al.* Edge conduction in monolayer WTe2. *Nature Physics* **13**, 677-682 (2017).

248 Tang, S. *et al.* Quantum spin Hall state in monolayer 1T'-WTe2. *Nature Physics* **13**, 683-687 (2017).

249 Wu, S. *et al.* Observation of the quantum spin Hall effect up to 100 kelvin in a monolayer crystal. *Science* **359**, 76-79 (2018).

250 Alicea, J. New directions in the pursuit of Majorana fermions in solid state systems. *Reports on progress in physics* **75**, 076501 (2012).

251 Kitaev, A. Y. Fault-tolerant quantum computation by anyons. *Annals of Physics* **303**, 2-30 (2003).